Microstructure and Charge Transport in Composite Cathodes for Solid State Batteries

Dem Fachbereich Biologie und Chemie
der Justus-Liebig-Universität Gießen

vorgelegte Dissertation zur Erlangung
des akademischen Grades
Doktor der Naturwissenschaften
– Dr. rer. Nat. –

Philip Minnmann

Dezember 2024

1. Gutachter / 1st Reviewer: Prof. Dr. Dr. h.c. Jürgen Janek
(Justus-Liebig-Universität Gießen)

2. Gutachterin / 2nd Reviewer: Prof. Dr. Nella Vargas-Barbosa
(Universität Bayreuth)

3. Prüferin / 3rd Reviewer: Prof. Dr. Matthias Elm
(Justus-Liebig-Universität Gießen)

4. Prüferin / 4th Reviewer: Prof. Dr. Maren Lepple
(Justus-Liebig-Universität Gießen)

Eingereicht / submitted: 18.12.2024

Disputation: 07.03.2025

Eidesstattliche Erklärung,

Die vorliegende Arbeit wurde im Zeitraum vom 01.11.2018 bis 30.09.2023 am Physikalisch-Chemischen Institut der Justus-Liebig-Universität Gießen unter Betreuung von Prof. Dr. Jürgen Janek angefertigt.

Ich erkläre: Ich habe die vorgelegte Dissertation selbstständig und ohne unerlaubte fremde Hilfe und nur mit den Hilfen angefertigt, die ich in der Dissertation angegeben habe.

Alle Textstellen, die wörtlich oder sinngemäß aus veröffentlichten Schriften entnommen sind, und alle Angaben, die auf mündlichen Auskünften beruhen, sind als solche kenntlich gemacht. Ich stimme einer evtl. Überprüfung meiner Dissertation durch eine Antiplagiat-Software zu. Bei den von mir durchgeführten und in der Dissertation erwähnten Untersuchungen habe ich die Grundsätze guter wissenschaftlicher Praxis, wie sie in der "Satzung der Justus-Liebig-Universität Gießen zur Sicherung guter wissenschaftlicher Praxis" niedergelegt sind, eingehalten.

Erklärung zur Nutzung von KI-Tools

Für die sprachliche Ausformulierung der englischen Textstellen wurde ChatGPT-4 (https://chat.openai.com/) benutzt, um eine bessere Lesbarkeit des Manuskriptes zu hervorzurufen. Dabei wurden die Textstellen kapitelweise mit dem prompt: "*Please improve the following section for better readability. Do not change its content or style*" versehen. Alle Textpassagen wurden anschließend von mir editiert und auf inhaltliche Richtigkeit mit der ursprünglichen Textstelle abgeglichen und gegebenenfalls angepasst. Während des Schreibprozesses wurden einzelne Sätze mittels des KI-Tools DeepL übersetzt, um die sprachliche Richtigkeit zu gewährleisten.

Gießen, 12.12.2024

Philip Minnmann

Abstract

Rechargeable batteries play a central role in the transformation of the mobility sector from combustion engines to sustainable technologies such as electric motors. In the pursuit of batteries with higher energy density, improved safety and extended service life, solid-state batteries are regarded as promising next generation battery technology. Higher energy density can increase vehicle range potentially leading to greater acceptance of electric vehicles. In solid-state batteries, solid ion-conducting materials replace liquid organic electrolytes providing advantageous properties such as mechanical resistance and a lithium-ion transfer number close to one. These can enable the use of lithium metal anodes or higher charging rates. Among solid-state electrolytes the lithium argyrodite Li_6PS_5Cl, which is used in this study, is one of the most intensively investigated materials, due to its high conductivity. Despite intensive research activities, solid-state batteries using this material class are not yet ready for commercialization with persisting challenges in electrode architecture and production.

In conventional Li-ion batteries, porous cathodes can be easily infiltrated by liquid electrolytes; however, the particulate nature of solid electrolytes requires a homogeneous distribution in the cathode during the manufacturing process. This requirement becomes increasingly challenging as the proportion of active materials increases and has a significant influence on the charge transport within the cathode and, correspondingly, on the kinetics. Thus, the experimental investigation of the charge transport of cathodes was the primary focus of this dissertation. Composite cathodes composed of sulfide based solid electrolytes and Ni-rich active materials were fabricated and characterized using electrochemical measurements. By comparing charge transport data with results obtained by microscopic imaging techniques, microstructure parameters were elucidated and quantified. Findings revealed that, in addition to limitations in percolation networks, the particle size distribution of the solid electrolyte significantly impacts electrode porosity and homogeneity. Overall, this work extended the insight into key electrode microstructure parameters and their effects on cell performance. From these findings, guidelines for electrode optimization can be derived aiming to enhance both energy density and power density.

Zusammenfassung

In der Transformation des Mobilitätssektors von Verbrennungsmotoren zu nachhaltigen Technologien wie Elektromotoren spielen Batterien eine zentrale Rolle. Im Zuge der Suche nach Batterien mit höherer Energiedichte, Sicherheit und Lebensdauer werden Festkörperbatterien als vielversprechende Batterietechnologie der nächsten Generation gehandelt. Eine höhere Energiedichte ermöglicht dabei eine größere Reichweite der Fahrzeuge und kann somit zu einer höheren Akzeptanz von Elektrofahrzeugen führen. Bei Festkörperbatterien werden flüssige organische Elektrolyte durch feste ionenleitende Materialien ersetzt. Aufgrund des festen Charakters des Elektrolyten ergeben sich dadurch Eigenschaften wie ein mechanischer Widerstand und eine Lithium-Ionen Transferzahl nahe eins. Diese können den Einsatz von Lithium-Metallanoden beziehungsweise höhere Ladegeschwindigkeiten ermöglichen. Einer der am intensivsten untersuchten Festkörperelektrolyte ist dabei der Lithium-Argyrodit Li_6PS_5Cl, welcher hohe Leitfähigkeiten besitzt und in dieser Studie verwendet wurde. Trotz intensiver Forschungsaktivitäten sind Festkörperbatterien dieser Materialklasse noch nicht massenmarkttauglich und es existieren weiterhin Herausforderungen bezüglich der Elektrodenarchitektur und Herstellung.

Während in konventionellen Li-Ionen Batterien die porösen Kathoden durch flüssige Elektrolyte infiltriert werden können, erzeugt der partikuläre Charakter von Festelektrolyten die Notwendigkeit diese möglichst homogen in der Kathode bereits beim Herstellungsprozess zu verteilen. Dies wird mit zunehmendem Anteil an Aktivmaterialien immer herausfordernder, und hat einen signifikanten Einfluss auf den Ladungstransport innerhalb der Kathode und entsprechend auf die Kinetik. Die experimentelle Untersuchung des Ladungstransportes von Kathoden stand aus diesem Grund im Vordergrund dieser Dissertation. Hierfür wurden Kathoden aus sulfid-basierten Festelektrolyten und Ni-reichen Aktivmaterialien hergestellt und mittels elektrochemischer Messmethoden charakterisiert. Durch den Vergleich der Ladungstransportdaten mit Informationen aus bildgebender Mikroskopie konnten Mikrostrukturparameter aufgeklärt und quantifiziert werden. Neben Limitierungen in Perkolationsnetzwerken konnte ein Einfluss der Partikelgrößenverteilung des Festelektrolyten auf die Porosität und die Homogenität der Elektrode bestimmt werden. Insgesamt erweitert diese Arbeit das Verständnis der relevanten Parameter der Elektrodenmikrostruktur und der daraus resultierenden Zellleistung. Aus diesen können Richtlinien zur Elektrodenoptimierung abgeleitet werden, welche dazu dienen Energiedichte und Leistungsdichte weiter zu steigern.

List of symbols and abbreviations

AAM	anode active material
BEV	battery electric vehicle
BSE	back scattered electrons
CAM	cathode active material
CT	X-ray computed tomography
DC	direct current
EIS	electrochemical impedance spectroscopy
FIB-SEM	focused ion beam - scanning electron microscopy
LE	liquid electrolyte
LIB	lithium-ion battery
OCV	open circuit voltage
OEM	original equipment manufacturer
SE	solid electrolyte
SEL	secondary electrons
SSB	solid state battery

Chemicals

NCM	$LiNi_xCo_yMn_zO_2$
NCM622	$LiNi_{0.6}Co_{0.2}Mn_{0.2}O_2$
LPSCl	Li_6PS_5Cl

Symbols

A	interface area (m^2)
l_{eff}	effective pathway length (m)
l_0	electrode thickness (m)
σ_{eff}	effective conductivity ($S\ cm^{-1}$)
σ_0	bulk conductivity ($S\ cm^{-1}$)
ε	porosity (vol.-%)
φ	volumetric phase content (vol.-%)
κ	tortuosity factor
τ	tortuosity
j	exchange current density

i	net charge flux
Z_{ct}	charge transfer impedance
Z_{ohm}	ohmic impedance
$\widetilde{D}_{\mathrm{Li}}$	chemical diffusion coefficient of lithium
R	resistance (Ω)
T	temperature (K)
E	specific energy (Wh kg^{-1})
W	energy density (Wh l^{-1})
ρ	specific resistance (Ω m^{-2})
X_{eff}	effective material property

Table of Contents

1. Introduction and Motivation

The paradigm shift from fossil fuels to renewable energy sources places high demands on the infrastructure for energy generation, conversion, and storage. The mobility sector, in particular, faces challenges in ensuring that battery electric vehicles (BEVs) have sufficient accessible energy for acceleration and movement.[1] In classic fuels like gasoline and diesel, chemically stored energy is irreversibly released through combustion. However, electromobility relies on reversible electrochemical reactions within galvanic cells. In a more general context, the collective term "battery" is mostly used, which describes several electrochemical cells that are arranged together in a compound.[2]

Each cell consists of integral components: the negative electrode (anode), the positive electrode (cathode) a separator, which electronically isolates the electrodes to prevent a short circuit, and an electrolyte. During discharging, lithium is oxidized at the anode side and migrates to the cathode where it is reduced. During charge, the entire process is reversed. Lithium-ion batteries (LIBs), an important type of rechargeable battery, have revolutionized modern life, enabling the wireless world we live in today, with most devices now being mobile. LIBs gained commercial success in the early 1990s due to pioneering work from Sony Corp. and have since seen massive improvements in performance coupled with significant cost reductions.[3] However, physicochemical limitations will soon likely inhibit further advancements in conventional liquid electrolyte (LE) based LIBs.[4,5]

Compared to fossil fuels, LIBs have a significantly lower specific energy and energy density, meaning that more mass and volume are required to store the same amount of (reversibly) available chemical energy.[6] This creates a challenge for vehicles where limited volumes are available and leads to the fact that the range of BEVs is still lower than that of vehicles with internal combustion engines. This limitation, along with safety concerns and high prices, has hindered high acceptance rates of BEVs in the broader social spectrum.[7] To address this, there is intense competition within academic researchers, startups, established cell manufacturers, and OEMs, to further increase the energy density and thus extend the range of BEVs.[8]

In conventional LIBs, the LE consists of a specific mixture of organic carbonates and dissolved lithium salts, each component affecting the overall performance of the cell.[9] However, the low lithium-ion transference number of the LE and the resulting concentration polarization impede charge transport at high rates and prevent the use of thicker electrodes.[10,11] Additionally, LEs lack the mechanical resistance necessary to prevent the dendrite formation in lithium metal anodes[12], can dissolve integral components of active materials[13] and will be easily oxidized by high voltage cathode active materials.[14] To overcome these limitations, solid state batteries are heavily researched as a potential next-generation technology. Their key difference to conventional LIBs is the use of a solid, ion-conducting material with negligible conductivity, known as the "solid electrolyte (SE)".

Theoretically, SEs can be viewed as LEs in which the salt content is increased to a point where no liquid remains. In SEs, usually only one type of ion is mobile, making them single ion conductors. This single-ion conductivity eliminates concentration polarization at higher current densities, a potential advantage of SEs over LEs with similar conductivity. Among the different type of SEs, thiophosphates have attracted significant attention because their ionic conductivities at room temperature can compete with those of LEs[15] with values of up to 25 mS cm^{-1} reported for thio-SEs processed by cold pressing and even higher for sintered samples.[16–20] Thio-SEs can be crystalline or "glassy" and are often composed of P-S polyhedra which create the immobile backbone of the molecular structure of these materials.[15,21] However, these polyhedra can participate in electrochemical reactions at the interface to cathode or anode active materials (CAM, AAM). While oxidation reactions at the cathode side lead to the formation of phosphates, sulfates and poly-sulfides[22], at the anode side binary phases (i.e., Li_2S, Li_3P) are often the reaction products.[23,24]

The electrochemical stability window, i.e., the range of the chemical potential of lithium (i.e., the range of electrode potential) in which these thio-SEs remain stable is relatively narrow[25,26] (e.g. 1.7 - 3.0 V vs. Li^+/Li for Li_6PS_5Cl) necessitating protection concepts prevent constant degradation.[27] One such strategy involves coating materials, which have low electronic conductivity to prevent electron transfer and redox rections.[28] However, these coating materials and their processing are usually expensive, and alternative protection concepts could involve SEs that degrade but form electron blocking phases, leading to a self-limiting reaction.

Another challenge when using SEs is manufacturing of dense electrodes with fast kinetics.[29] On the anode side, lithium metal electrodes are preferred (ideally formed "*in-situ*" after assembly), but the situation is different on the cathode side. Here, particulate CAMs are employed which are the component, which is actually storing the charge. From a thermodynamic point of view, the fraction of CAM in the electrode and in the cell is consequently desired to be maximized to achieve the highest energy density possible but kinetic performance is equally important to achieve high power release and fast charging capabilities.[10,30] This raises the question: How can cell kinetics be optimized without compromising energy density? Considering the nature of the composite cathode and the processes that govern its kinetics, the working hypothesis of this thesis was that the microstructure of the composite cathode plays a crucial role, with charge transport properties being a primary contributor to the overpotential during cell operation. However, the quantification of these transport processes, and experimental evidence of kinetic limitations was scarce. Data on the influence of composition, particle size and porosity were largely not accessible, and validation of models consequently remained difficult.

In my first publication "*Quantifying the impact of charge transport bottlenecks of composite cathodes for all-solid-state batteries*"[31], I focused on the charge transport properties of composite cathodes and examined their impact on cell performance metrics. Selectively blocking electrodes and impedance spectroscopy were used to determine effective conductivities and tortuosity factors. By adjusting the CAM and SE content, the electrode microstructure was carefully altered and correlations between the obtained charge transport properties and cell performance metrics obtained from electrochemical cycling were investigated. This work validated the approach of using partial conductivites for detection of charge transport limitations and is closely related to simulations performed by *Bielefeld et al.*[32] Distinct electronic and ionic limitations at low and high CAM contents were identified, respectively, underscoring the need for balanced partial conductivities of both charge carriers. In a first attempt to improve electrode design, ionic transport limitations were reduced by decreasing the SE particle size, leading to the question: How does the actual microstructure of composite cathodes look like and where are the limiting bottlenecks located?

Answering this question requires 3D models or representations of the actual cathode microstructure. The hypothesis was that smaller SE particles would lead to a more homogeneous distribution of the respective phases and better fill residual voids than larger particles. Using focused ion beam – scanning electron microscopy (FIB-SEM) tomography 3D reconstructions of the cathode microstructure were obtained and microstructural features were compared to cell performance and charge transport properties in my second publication entitled: "*Visualizing the Impact of the Composite Cathode Microstructure and Porosity on Solid-State Battery Performance"*[33]. By varying milling conditions in SE synthesis, different particle sizes could be obtained. Smaller SE particles were found to result in better SE distribution and improved charge transport properties coupled with better cell performance. Interestingly, it was observed that the results of charge transport measurements and charge transport modelling differed, revealing that additional contributions such as contact resistance or nanopores, not detected in the 3D reconstruction, may be affecting performance.

As a result, the SE particle size must be tailored to the specific CAM that is being used, opening the question of what additional parameters need to be optimized for improved electrodes. This depends certainly on the base chemistry, SE and battery application that is targeted. I compiled a comprehensive overview of key parameters that one may need to take into account in my third publication: "*Designing Cathodes and Cathode Active Materials for Solid State Batteries*"[34]. Here I showed that CAM particle size design should target certain factors, such as the chemical diffusion coefficient, volume change during cycling and the applied protective coating. This affects not only CAM processing, but also the overall electrode design including parameters like CAM content and SE particle size.

In summary, the studies presented here progress from the empirical identification of electrode charge transport properties to the visualization of electrode microstructures and conduction pathways culminating in a guideline for electrode design. While the focus has been on composite positive electrodes, key findings are also applicable to composite negative electrodes and provide important insights into understanding and optimizing kinetic performance of solid-state batteries. To facilitate understanding and application of this knowledge **Chapter 2** offers a brief introduction to composite electrodes, **Chapter 3** outlines recommended methods for charge transport and microstructure investigation and **Chapter 4** summarizes and reviews the current state of research highlighting limitations and open questions.

2. Fundamentals of Charge Transport and Electrode Kinetics

When seeking to improve the performance of SSB cathodes an immediate question arises: where to start? Of course, the respective materials must meet certain properties, but after all it is their combination that creates the unique performance characteristics of the cathode. Therefore, the next chapters will focus on the following topics:

- What determines transport processes in composite cathodes?
- Which tools can be used to identify and characterize these processes?
- How can correlations between these processes be found?
- How can the components or their arrangement be tailored to achieve a certain effect?

The chapter will start by exploring the working principle of an electrode and how it is related to microstructure. Understanding the microstructure of an electrode is essential for comprehending the kinetics of a cell[35–37]. To be able to design better electrodes, it is essential to understand the core parameters and how to describe them. The following section lays the foundation by introducing the definition and the features of microstructures. These features are later investigated and quantified to develop design principles for SSB cathodes.

2.1 Composite Electrode Microstructure

A combination of at least two materials is typically referred to as composite[38]. In composites, multiple phases and materials coexist each one serving a specific purpose. These phases naturally possess different properties in all regards and the overall properties of the composite are strongly influenced by the individual components. However, the properties of the composite are also highly dependent on how these phases are arranged. In materials science, this arrangement is commonly referred to as microstructure, as most of the relevant features (grains, secondary phases, 2D and 3D defects) are on the micrometer scale. That said, it has to be noted that features at other length scales can be play a role as well, namely the mesostructured (larger than microstructure) and the nanostructure (within the nanometer range). For simplification in material science, the term microstructure can encompass features at the meso- and nanostructure referring broadly to a spatial arrangement of phases (materials)[39]. As it describes spatial arrangement, the microstructure is investigated in terms of geometry and geometric descriptors, regardless of the specific material system or application. In battery research. numerous relevant descriptors are introduced, and their importance varies depending on the respective property under investigation.[35]

2.2 Kinetics of Solid-State Composite Battery Electrodes

The kinetics of battery electrodes are primarily determined by the individual resistance contributions along the charge carriers pathway[40]. Please note that for simplification, a basic assumption is the absence of major influences from phase transition kinetics of active materials during (de-)intercalation and no inductive effects from migrating ions or electrons. Within this simplified framework, three major contributions of the electrode resistance (or impedance Z for alternating currents) can be identified. These determine the polarization (or overpotential) of a cell during operation (c.f**. Figure 1**).[6]

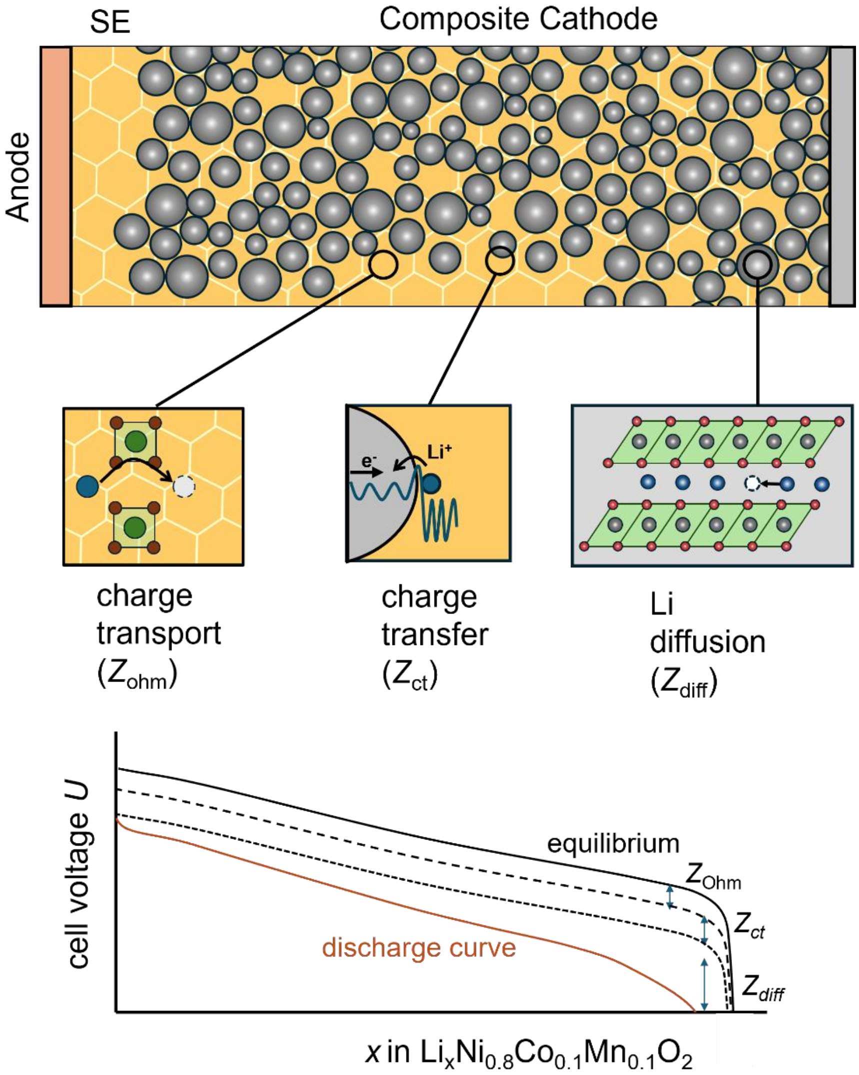

Figure 1. Top: visualization of kinetic contributions to electrode resistance during discharge divided into charge transport through the SE phase, charge transfer at the interface between CAM and SE and diffusion of lithium inside a transition metal oxide CAM. During charge, the directions are reversed. Bottom: implications of the resistance contributions on the cell discharge curve over various states of charge. While charge transport and charge transfer are usually generating a constant voltage drop, the diffusion resistance is highly depending on the Li concentration inside the active material. Its limiting character is commonly highest towards the end of discharge.

The larger the resistance, the greater the polarization. During charging this leads to an increase in voltage and during discharge a voltage drop occurs. These voltage changes negatively influence cell power and also cause the cut-off to be reached earlier, reducing the available capacity. For fast charging and discharging, low cell impedance is crucial, and each individual resistance component must be minimized. These components can be classified as:

1. Charge Transport Impedance Z_{Ohm}: This is also referred to as ohmic resistance and results from ions migrating through the solid electrolyte and electrons migrating through the electronically conductive network. Using Ohms law, this can be approximated to:

   $$Z_{\mathrm{Ohm}} = \frac{l}{\sigma \cdot A_{\mathrm{el}}} \qquad \text{(Equation 1)}$$

   with l being the pathway length, σ being the specific conductivity and A_{el} being the electrode cross-sectional area. Consequently shorter transport pathways and higher conductivities result in lower impedance.
2. Charge Transfer Impedance Z_{ct}: This arises from the potential barrier that must be overcome by ions transferring between the SE to the CAM, sometimes referred to as activation. It is related to the charge transfer resistance R_{ct} which can be calculated by[10]:

   $$Z_{ct} = \frac{R_{\mathrm{ct}}}{A} = \frac{RT}{zFjA} \qquad \text{(Equation 2)}$$

   with R as gas constant, T as temperature, F as Faraday constant, j as exchange current density and A as interface area. A higher interface area and lower potential barriers reduce this impedance.

3. Diffusion Impedance Z_{diff}: This is caused by the chemical diffusion of Li inside of the CAM from or towards the center of the particle. Diffusion creates a concentration gradient inside the CAM during operation. Upon discharge, Li concentration is depleted at the CAM|SE interface during operation. Conversely during charging, the CAM|SE interface becomes enriched of Li which decreases the number of vacancies available for ion mobility. Both scenarios negatively affect the chemical diffusion coefficient $\widetilde{D}_{\mathrm{Li}}$. Increased diffusion coefficients and shortening of diffusion length can reduce the diffusion impedance.

While all of the above listed impedance components primarily affect ions, the same principles apply to electrons. However, electronic conduction and charge transfer generally occur faster than ionic processes and, in most models, it is assumed that Li-ions are reduced immediately after entering the active material by electrons provided by the current collector. For charge transport percolation, however, electronic conduction can become significant, which will be described in detail later.

Conclusion: To enhance cell kinetics, the resistance contributions of charge transport, charge transfer and diffusion need to be minimized.

2.2.1 Charge Transport in Solid Materials

Charge transport in solids differs significantly from that in liquids. In solid-state materials, there are roughly five distinct classes: electrical insulators, metallic conductors, semiconductors, mixed-ionic-electronic conductors (MIECs), and single ion conductors[41]. Lithium solid electrolytes fall into the category of single-ion conductors. In these materials, Li-ions move via a hopping mechanism, transitioning from an occupied lattice site (in crystalline materials) to an unoccupied site (vacancy or interstitial)[21]. Since the anion network is rigid and immobile, no strong concentration gradient can form, and only Li-ions contribute to the net charge flux i, represented by the equation:

$$i = \sigma_{ion} \cdot \vec{E} \qquad \text{(Equation 3)}$$

where $\vec{E}$ is the applied electric field. In most relevant crystalline thio-solid electrolytes, a conductivity of 0.1–10 mS cm^{-1} can be achieved[15]. However, this typically refers to the "bulk" conductivity within a single crystallite. In macroscopic samples and applications, grain boundaries play a crucial role. Grain boundaries are formed between particles or crystallites with different crystallographic orientations. They are highly defective, featuring accumulations of 0D and 1D defects such as vacancies and dislocations. Due to the high concentration of these defects, a space charge layer can form, posing a significant barrier for charge carriers and contributing to Z_{ohm}. This effect is even more pronounced when the contact area between individual particles is low, leading to current constriction phenomena. Reducing grain boundary resistance is therefore desirable and often attempted through mechanical fusion of particles at high pressures and elevated temperatures.[42]

In contrast to solid electrolytes, most cathode active materials (CAMs) are MIECs. These materials must conduct both electrons and ions to be electrochemically active and store large amounts of charge. Since both charge carriers contribute to the total net flux, Equation 3 is modified to:

$$i = \sigma_{\mathrm{tot}} \cdot \vec{E} \qquad \text{(Equation 4)}$$

with $\sigma_{\mathrm{tot}} = \sigma_{\mathrm{ion}} + \sigma_{\mathrm{el}}$ being the total conductivity. Transition metal oxides, such as NCM (used in this study), can provide electronic transport via p-type polarons[43,44]. Polarons are quasiparticles and can be described by lattice distortions around electrons and electron holes in the band structure. The conductivity is described by:

$$\sigma_{\mathrm{el}} = \mathrm{e} \cdot p \cdot \mu_{\mathrm{p}} \qquad \text{(Equation 5)}$$

where e is the elementary charge, p is the charge carrier (hole) density and μ_{p} is the hole mobility.[41] Because of the p-type conduction mechanism, electronic conductivity increases during delithiation, as more electrons (complementary to Li-ions) are removed, increasing the hole density in the valence band[43]. Similarly, the Li-ion conductivity increases during delithiation, due to the insertion of vacancies which enhance Li-ion mobility and, hence, the apparent Li-diffusion coefficient. At low states of charge (SOC), the conductivity decreases again, due to a significantly lower Li-ion concentration. The low Li-mobility in NCM at high SOC was leveraged in Publication 1 and Publication 2 to separate ionic and electronic conductivity under the assumption that in fully lithiated NCM, the ionic transport and charge transfer across the CAM|SE interface is negligible.

2.2.2 Charge Transport in Composite Electrodes

To enable a lithium-ion to enter or exit the CAM particle, an active interface to the SE phase is essential. However, charge neutrality requires that an electron must also enter or leave the CAM particle. That is only possible if the CAM particle is connected to a network of electronic conductors, which protrude uninterrupted from the particle to the cathode's current collector.[45] This requirement applies of course for all CAM particles involved in charging and discharging. Similarly, the SE phase, which facilitates the Li-ion transfer, must be connected to a network of SE phase extending to the separator (and ultimately to the anode) to allow the Li-ion to move towards or away from the anode.

In general, a phase that forms a continuous network through the electrode (from the current collector to separator) is called a percolating network. For achieving highest energy density, all CAM particles must be in contact with ionic AND electronic percolating networks. Achieving this in particle-based composites can be challenging and the percentage of CAM particles that meet these criteria is referred to as utilization level[32]. Maximizing this utilization level is therefore one of the key targets to avoid material waste, which would not only increase costs, but also reduce the achievable energy density.[32]

While the percolating networks described above determine how much charge can be stored in the electrode under ideal conditions, the length of the charge transport pathway dictates the resistance Z_{ohm}, experienced by these charge carriers and therefore the efficiency of these networks. Considering **Equation 1**, the resistance increases proportionally with the length of the transport pathways. On a cell level, in most cases the goal is to maximize specific energy and power and to reduce the cells internal resistance to a bare minimum. Transport resistance is a significant contribution to this total cell resistance and one effective way to reduce it is by shortening transport pathways.

Conclusion: Short charge transport pathways for ions and electrons are desirable to reduce the overall resistance of the cell.

2.2.3 Tortuosity

While the effective pathway length l_{eff} ideally corresponds to the thickness of the electrode $l_{\mathrm{electrode}}$, real microstructures result in larger values. Charge carriers cannot take the "direct" route, but are transported along more complex, tortuous pathways. The respective descriptor of this phenomenon is called geometric tortuosity τ and is quantified by the ratio $l_{\mathrm{eff}}/l_{\mathrm{electrode}}$, it is therefore a measure of how "twisted" or elongated a specific transport pathway is. The concept is illustrated for Li ion transport in **Figure 2, case A**.

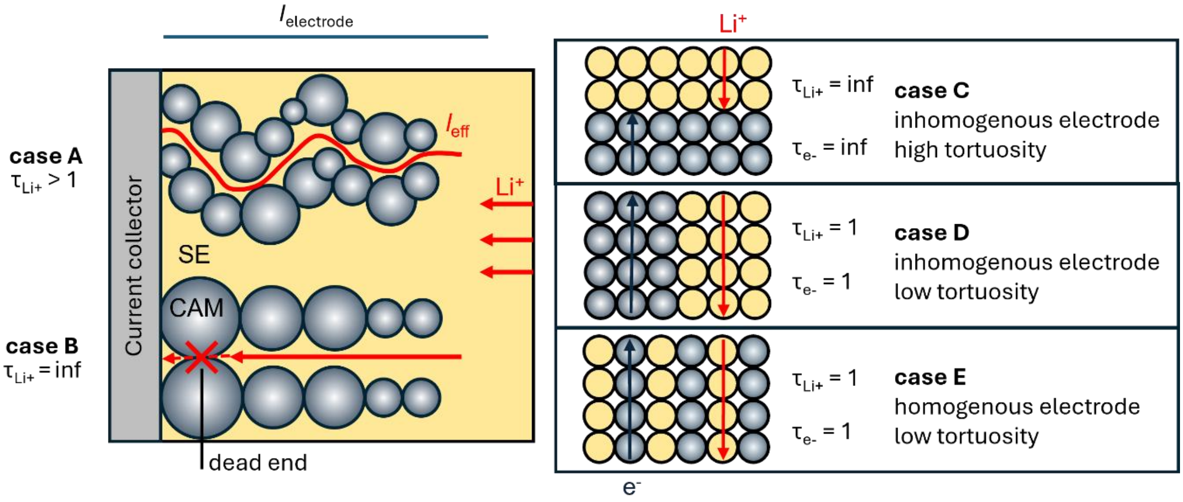

Figure 2: Concept of tortuosity visualized, and implications of different microstructures shown in separate cases. Case A: Tortuosity means elongated pathways for charge carriers, due to obstacles in their way of movement. Case B: tortuosity does not consider dead ends for charge carriers, even though they can contribute to the electrochemical performance of the electrode. Layered, inhomogeneous electrodes can exhibit high tortuosities perpendicular to the layers (Case C) because charge carriers cannot move through the entire electrode. However, they can also exhibit low tortuosities parallel to the layers but because they have low interfacial area, even low tortuosity does not result in sufficient charge transport. Only in Case D, low tortuosities and high interface area are present, marking an ideal electrode microstructure.

There are, however, various definitions of "tortuosity", which differ based on how they are determined[46,47]. Here the focus is on the tortuosity factor κ commonly used for battery electrodes. For very simple systems (like cylindric capillaries) κ can be approximated by:[47]

$$\kappa = \tau^2 \qquad \text{(Equation 6)}$$

However, this approximation is not accurate for Li-ion battery electrodes given their 3D nature but is often applied to this topic. This tortuosity factor relates effective properties of composite materials to bulk properties of its constituents such as[48]:

$$X_{\mathrm{eff}} = \varphi \cdot X_{\mathrm{bulk}} / \kappa \qquad \text{(Equation 7)}$$

Where X_{eff} and X_{bulk} represent the effective and bulk intrinsic transport property respectively, and φ is the volumetric content of a given phase. Consequently, the number of tortuosity factors that can be determined corresponds to the number of phases present in an electrode. In the context of batteries, the tortuosity factor of both the electron conducting phase and the ion conducting phase are particularly important.

It is also important to note, that the concept of tortuosity (and empirical extensions such as the Bruggemann relation[49]) are not always universally applicable and are controversially discussed in the battery context[46–48]. Tortuosity factors are typically used to describe "flow-through like" transport properties in heterogeneous materials. In the battery field, however, the charge carriers do not necessarily need to travel through the whole electrode, but only reach all available CAM-SE interfaces. The implications are detailed in **Figure 2, case B and C**. Even though in both cases the Li-ion conductive phase does not form a continuous path through the whole electrode and ends in a dead-end, still charge carriers can be transported to the interface between CAM and SE. As a result, the cells performance will likely be limited by the solid-state diffusion within the CAM rather than by the charge transport resistance.

Regardless of the definition used, all tortuosity concepts share one key idea: a higher value indicates longer transport pathways, which should be avoided. However, a low tortuosity does not necessarily imply that an electrode is homogenous as shown in **Figure 2, case D**. Therefore, it is important to consider that homogenous electrodes are required for tortuosity to be used effectively as a geometric descriptor. Nevertheless, this is true for most of the SSB cathodes of interest and in my first two publications the concept of tortuosity factors could be used to quantify the efficiency of charge transport.

Conclusion: Percolating pathways and low tortuosities for all conducting phases are essential for effective charge transport.

2.2.4 Interface Area

The specific interface area $A_{\mathrm{CAM|SE}}$ determines the number of reaction sites available for the (de-)intercalation of Li-ions and it influences the global charge transfer resistance.[50] While in general the interfacial resistance is a function of the two materials in contact (as well as experimental conditions, such as temperature and pressure), the charge transfer impedance Z_{ct} of a composite electrode is determined by the charge transfer resistance R_{ct} and $A_{\mathrm{CAM|SE}}$. In other words, a larger interface area results in a lower global charge transfer impedance. Additionally, lithium diffusion through the CAM particle is affected by the interface area. Low coverage can constrict transport pathways increasing diffusion resistance, whereas higher CAM surface coverage results in more homogenous diffusion profiles.[50–52]

Conclusion: A large interface area between SE and CAM is therefore desired from a kinetic perspective.[a]

In this chapter, microstructural features are examined in detail and their requirements defined: high interfacial area, high utilization level, and short transport pathways. The implications of these requirements are visualized in **Figure 3**. If the utilization level is low, a large portion of CAM will be isolated, and the inactive material will result in a lower achievable capacity. Conversely, if charge transport pathways are too long or the interface area is too small, kinetic limitations will significantly reduce the cell's power, and achievable capacity.

Now the question remains: how can the parameters be investigated that control these features and electrode like the one depicted in **Figure 2 case E** be designed? And can these descriptors be quantified to gain a better understanding of the microstructure and its influence on kinetics? These questions will be explored in Chapter 3.

---

[a] Please note that due to the instability of CAM and ISE, a surface area that is too high could result in excessive degradation and fast cell failure. It is therefore imperative to find either stabilizing solutions or to balance the active interface area in terms of resistance and degradation.

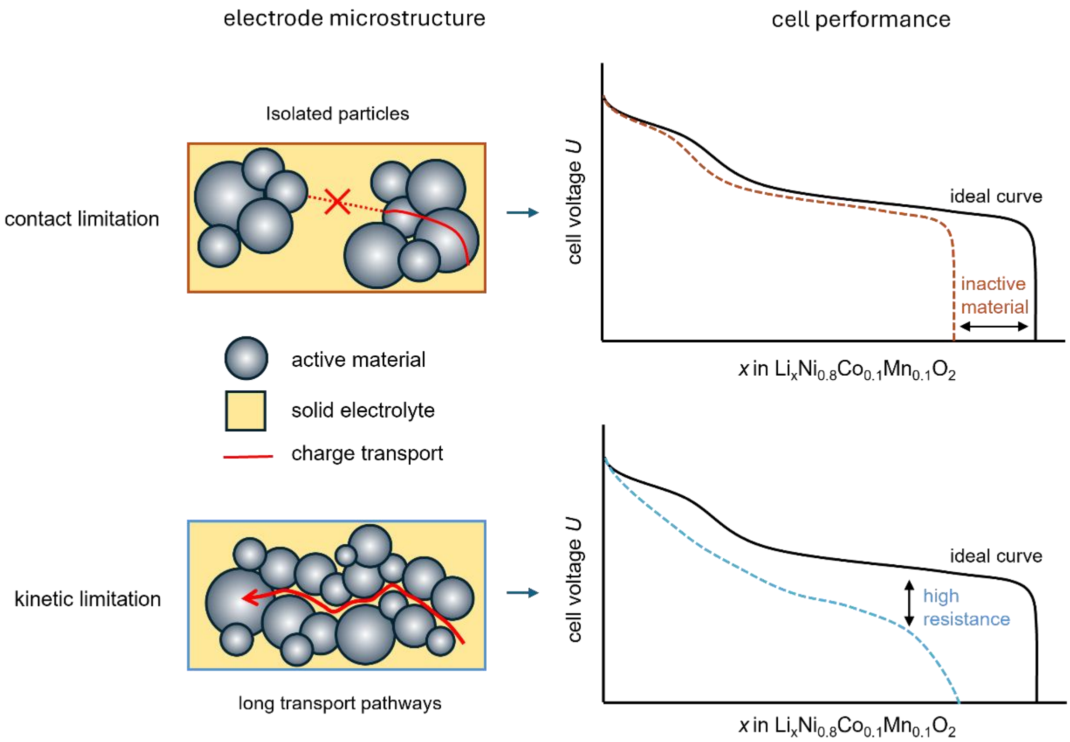

Figure 3: Representation of the two modes of charge transport limitation within composite electrode microstructures. Top: contact limitation (percolation). If no sufficiently percolating networks are formed, CAM particles remain isolated (in the depicted case: electronically isolated) and hence electrochemically inactive. This will result in a lower achievable capacity, regardless of the applied charging rate. Bottom: Kinetic limitation. If percolating networks are formed for ions and electrons, their efficiency determines the cell performance. If charge carriers have to travel long distances to reach all electrochemically active sites, high resistance and consequently higher overpotential can be observed. This is highly dependent on the applied charging rate and a larger effect is present at higher charging rates.

3. Characterization

3.1.Charge transport measurement techniques

One of the simplest ways to assess the charge transport and length of respective transport pathways, is by measuring the charge transport resistance of the electrode. This method produces valuable data since charge transport resistance directly contributes to the cell's internal resistance thus affecting its kinetic performance. However, this approach involves strong approximations making it difficult to quantify the actual transport pathway length and typically yields only an average effective value, while, in reality a distribution of transport pathway lengths is more likely.

To determine the charge transport resistance, two widely used techniques are steady-state current measurements and electrochemical impedance spectroscopy (EIS). Both techniques have their advantages in terms of measurement setup requirements, data acquisition and processing, but fundamentally they should provide the same result. The key difference is the ease of measuring, extracting the values of interest and handling of the respective underlying model. The following sections will introduce these techniques as well as the different possibilities of contacting setups used in this thesis and provide guidelines of when to select which technique.

3.1.1 Steady-state current:

In steady-state current measurements, a constant bias voltage is applied to the sample to create an electric driving force for charge carriers. The resulting current of charge carriers can be measured, but this concept requires at least one charge carrier to be transferred to and from the respective electrode terminals, while blocking the other. This setup is usually referred to as "selectively blocking contacts". Initially, the charge flow is higher as all charge carriers contribute, but over time, a concentration gradient forms due to blocked charge carriers, which reduces the current. Once steady-state conditions are reached ($t \rightarrow \infty$), only one charge carrier moves through the sample, and the current depends on the charge transport resistance of the sample for that charge carrier, as well as the charge transfer resistance at the current collector-sample interface.

The advantages of this technique include its simple setup (applying voltage and measuring current over time). However, drawbacks include the long measurement times needed to reach steady-state conditions and the superposition of at least two resistances. In practice, it is possible to separate the charge transfer resistance (Z_{ct}) from the ohmic resistance (Z_{Ohm}) through parameter variations like changing the contact area or sample thickness, but this requires additional experiments. This method is therefore mainly used to validate results from impedance spectroscopy.

3.1 2 Electrochemical impedance spectroscopy

In EIS, an alternating sinusoidal signal (either current or voltage) is applied to the sample, and the response (voltage or current, respectively) is measured across a frequency range. This produces a spectrum that acts as a Fourier transform of steady-state measurements, allowing for easy visualization of both resistive and capacitive contributions. Results are often displayed in a Nyquist plot (imaginary vs. real impedance), where different processes can be identified and modeled using equivalent circuit models that represent the physical processes. Additionally, the Bode plot (real/imaginary impedance vs. frequency) provides the possibility to identify processes based on their excitation frequency. At higher frequencies, fast, short range transport processes with low respective capacitance dominate, while at lower frequencies slower processes with higher capacitance dominate the signal. Typically, impedance spectra of batteries are modelled by equivalent circuits consisting of serial or parallel units of resistors and capacitors, each one of these units representing a respective process. For composite or porous media, more sophisticated models, such as the transmission line model (TLM), are required[53]. This model describes charge transport in different media connected through interfaces, making it the most accurate model for describing composite battery electrodes.

The benefits of EIS include short measurement times and the ability to separate different processes easily, even with blocking terminals, charge carriers can still move at sufficiently high frequencies, allowing measurements in various configurations. However, the drawbacks include expensive equipment, such as frequency modulators, impedance analyzers, special cables, and the need for specialized training to interpret the results accurately. In this work, the investigation of charge transport required an extensive study with wide parameter variation and model validation, and hence EIS is the preferred method.

For EIS measurements, two different measuring configurations can be employed **(Figure 4)**. In a full blocking setup, two composite electrodes sandwich a solid electrolyte layer, as employed by *Kaiser et al.*[54] Neither ions, nor electrons can move freely through the cell, assuming that the electrode materials are either fully lithiated or fully delithiated. Delithiated electrodes have no Li-reservoir and cannot provide ions to follow an electric force. Lithiated electrodes do not provide lattice vacancies for Li-ions to be inserted to and are thus blocking charge transfer at the interface. The central solid electrolyte layer allows movement of ions, but not electrons and is therefore electronically separating the two electrode layers. In total no charge can flow through the cell in steady state conditions (i.e. $\omega \rightarrow 0$, with ω being the angular frequency) and the electrochemical behavior becomes purely capacitive. From a mathematical point of view, the transmission line model equation can be simplified to $Re(Z)_{\omega \rightarrow 0} = R_{\mathrm{Ohm}}/3$. This setup has been used by several groups for electrodes in SSBs[55,56] and LIBs[57,58] and is generally easier to apply.

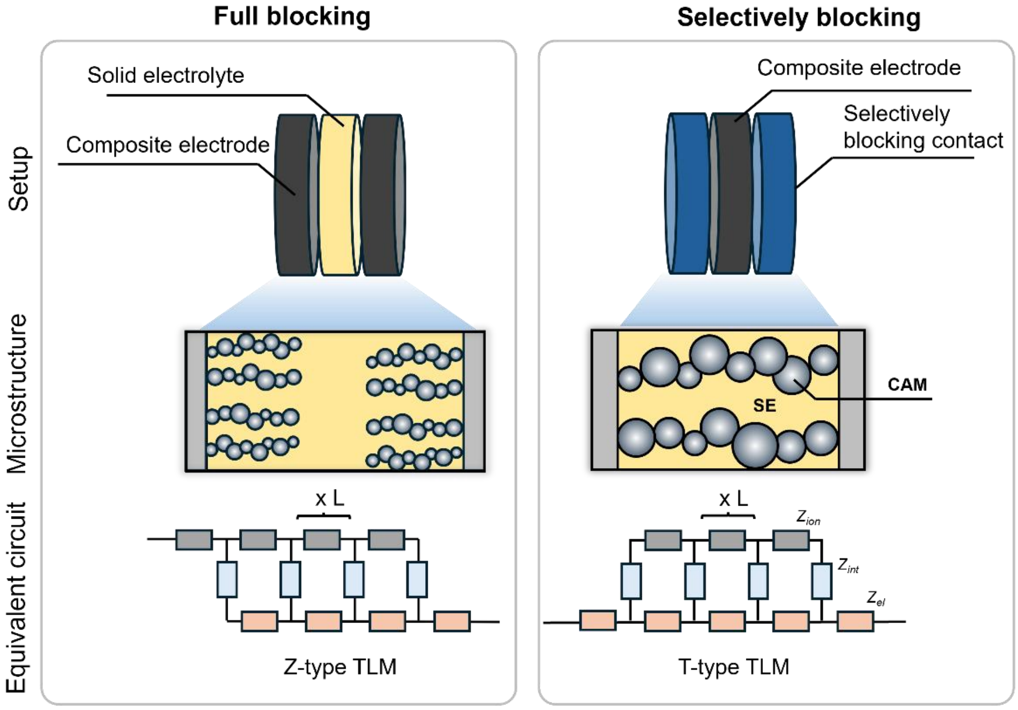

Figure 4: Impedance measurements setups that allow determination of charge transport properties of composite electrodes. In full blocking setups (left), two composite cathodes are sandwiching a solid electrolyte layer. Correspondingly, the transmission line model has one ionic and one electronic terminal. In selectively blocking setups (right), a composite cathode is sandwiched by two selectively blocking contacts. The transmission line model correspondingly has two symmetric terminals. Please note that while the electronic terminal is depicted, ionic terminals can be chosen, too.

In contrast to full blocking setups, selectively blocking contacts restrict certain charge carriers, while allowing transfer of others. In the context of SSB cathodes, this means that either electrons are transmitted, and ions are blocked or vice versa. For ion blocking contacts, metal terminals, like stainless steel are typically used and a composite material can be characterized by sandwiching it between the two metal contacts.[59–64] For electron-blocking contacts, the picture is more complex. These setups not only require electron-blocking, ion conducting layers, but also Li-ion reservoirs, which allow for steady state flow of charge carriers. Usually this is done by sandwiching the composite between two layers of solid electrolyte and then enclosing this stack between Li-reservoir containing contacts, such as Li-metal or Li-alloys.[31,54,60,61,63,64] Although this approach can be prone to errors, it has the advantage of allowing impedance data collection, and "quasi-steady-state" charge flow through the cell, by extrapolating the data as the frequency approaches zero. However, the use of several contributing resistances in the overall impedance spectrum demands careful validation of the equivalent circuit models employed. In these models, parameters such as interfacial resistance and impedance of the solid electrolyte layers must be determined accurately.

3.2 Evaluating results of charge transport measurements

Both steady-state and EIS measurements yield a resistance value which can be used to determine the conductivity σ of the investigated sample. By deconvoluting the electronic and ionic contributions, partial conductivities σ_{el} and σ_{ion} are determined. These can then be used to calculate the tortuosity factor of the sample. This parameter is always an average value, which compares the determined "effective conductivity", to the theoretically expected value. For instance, in a homogeneous mixture of a conductive and an insulating phase, one would expect a 50% drop in conductivity for a sample containing only 50% of the conductive phase, relative to the bulk conductivity σ_{bulk} of that phase. However, tortuosity increases the length of the charge transport pathway, leading to lower effective conductivites than anticipated. This relationship can be described mathematically by adjusting **Equation 7**:

$$\sigma_{\mathrm{i\ eff}} = \sigma_{\mathrm{i\ bulk}} \cdot \varphi_{\mathrm{i}} / \kappa_{\mathrm{i}} \qquad \text{(Equation 8)}$$

where φ is the volumetric phase content of the conductive phase, σ_{eff} is the effective conductivity of the composite and the index i representing the respective charge carriers (i.e., *el* for electrons and *ion* for ions). Due to the omission of important factors, such as contact resistances or current constriction the tortuosity factor determined through transport measurements is often larger than the corresponding geometric tortuosity factor, as discussed for LIB electrodes by *Cooper et al.*[46] and *Landesfeind et al.*[57] Similar observations have been made in Publication 2 where an imaging based technique i.e., tomography, is applied to determine the tortuosity of battery electrode microstructures.

3.3 Tomography

Tomography is an analytical method that involves sequentially imaging a series of 2D slices with certain information, which are then combined to create a 3D object. This technique provides spatially resolved information about phase distribution and arrangement, making it a key tool across multiple fields of research and industry. The 3D object created can be used for visualizing certain arrangements, or integrated into simulations to model how the object's structure impacts its properties. Several methods are used to generate tomography data, each with its advantages and disadvantages. In the context of batteries, the two most important methods are FIB-SEM tomography and X-ray computer tomography (CT).[65] Below, the fundamentals and benefits of each technique will be discussed.

3.3.1 X-ray Computed Tomography (CT)

X-ray CT uses X-rays to penetrate a sample. These X-rays are absorbed and scattered by the different components of the sample. By detecting the spatially resolved intensity of the absorption or scattering, a 3D model can be generated. The main advantages of this method are its ability to investigate relatively large sample volumes, up to several hundred cubic centimeters, and its non-destructive character, making it suitable for quality control and *operando* measurements.[65] However, in the context of battery research it has certain limitations, such as low phase contrast—weakly diffracting elements like lithium are hard to distinguish from pore spaces, which do not diffract at all.[66] Additionally, the method's resolution is limited to several tens of micrometers, which makes it less suitable for detecting local arrangements of phases in battery electrodes. However, it is effective for detecting large-scale production errors and inhomogeneities in electrodes.

As a relatively new technique, nano-CT has undergone significant improvements in recent years. Nano-CT employs focused high energy X-ray beams, which reduce the spot size and improve resolution. Depending on the sample size, resolutions of < 100 nm are achievable. However, the tradeoff for improved resolution is a significantly reduced sample volume, often limited to a few cubic micrometers, compared to traditional CT.

3.3.2 FIB-SEM Tomography

FIB-SEM tomography involves two different beam sources that work in tandem. The focused ion beam (FIB) prepares a cross-section of the sample and then removes layer by layer, creating 3D information[67]. The scanning electron microscope (SEM) is used to image the sample, generating phase contrast and enabling differentiation between the various constituents. SEM achieves very high resolutions, with a spot size of just a few nanometers[65], making FIB-SEM tomography the highest resolution technique discussed here.

Because FIB-SEM removes material from the sample, it is a destructive technique; each sample volume can only be investigated once. Additionally, the FIB may cause material to redeposit in pores, meaning that the porosity observed in FIB-SEM data of SSB cathodes is often a lower limit.

The SEM operates in two modes: the secondary electron (SEL) and backscattered electron (BSE) mode. SEL provides information about the sample’s topography, while BSE mode is influenced primarily by the sample's elemental composition, such as the distribution of light and heavy elements. Consequently, SEL mode is better for detecting porosity, while BSE mode excels at identifying different material phases.[68] In Publication 2 both modes were combined to distinguish between void space and material phase which proved to be a powerful approach for accounting for all phases in a composite electrode. However, it is important to note that FIB-SEM tomography is only applicable to samples that are stable under high vacuum conditions and do not decompose or alter under the electron or ion beam.

4. Rate Limitations of SSB Cathodes

The previous chapters provide a comprehensive understanding of how cathodes are ideally constructed, the key metrics used to describe the electrodes and how to determine them. Based on this, in the following chapter, factors that influence cathode performance and strategies to optimize and change them are explored. Several research groups have focused on this topic, and insight from other fields of study can also be applied. Even though SSB cathodes typically consist of just three to four materials, there exist several factors that are drastically changing how the microstructure looks like and have vast implications for the resulting performance. The next chapter will provide an overview of the knowledge that has been gained in this field, by extensive efforts of multiple groups. Within each subsection a factor as well as possible approaches to optimize it will be discussed in terms of cathodes with better performance.

4.1 Composition

As mentioned in Section 1, the CAM in modern batteries is ultimately determining the maximum capacity that can be stored, i.e., dictating the upper energy density limit. To maximize energy density the goal is to incorporate as much CAM as possible. **Figure 5a** illustrates the effect of vol.-% of CAM in a cathode on the achieved energy density of the cell.

However, most CAM materials typically do not exhibit sufficient ionic conductivity, leading to an ionic charge transport resistance within the material. Thus, a balance must be found between optimizing charge transport and energy density. While most SSB studies report cathodes with around 50 vol.-% of CAM[51,63,69–75], some studies have shown that higher fractions are indeed feasible.[76–79] Please note that Publication 1 and Publication 2 too, investigate microstructures with roughly 50 vol.-% CAM, because these allow a proper determination of cycling performance without using sophisticated and often inaccessible methods for preparing the electrodes.

A modeling study by *Bielefeld et al.* focusing on cathode active material content in composite cathodes identified two limiting regimes, ionic and electronic.[32] Percolating networks of CAM form at volumetric contents above 45-55 %. depending on the particle size. When the CAM content is lower, the electronic transport from particle to particle is hindered because most particles remain isolated from each other. As CAM content increases, more and more particles are connected to percolating networks thereby increasing utilization level. However, when CAM content exceeds a certain level, the likelihood of SE particles forming ionic percolating networks decreases. This is accompanied by a drop in the specific interface area between CAM and SE. In the first publication**:** "*Quantifying the impact of charge transport bottlenecks in composite cathodes for solid state batteries"* the results by *Bielefeld et al.* were experimentally validated through charge transport measurements and demonstrated the correlation between these effects and cell cycling performance.[31] Building on these results, subsequent studies showed charge transport limitations in different material systems.[55,63,64,79,80] It is worth mentioning, that in most of these studies the use of conductive additives is avoided due to severe degradation when carbon additives contact sulfide based SEs.[81–83] However, a limited use of carbon may be beneficial for electronic charge transport, particularly low aspect ratio fibers still benefit electronic charge transport.[69,84]

In conclusion: a certain amount of CAM is necessary for required energy densities and (in case of NCMs) electronic charge transport properties. However, excessively high CAM content leads to ionic limitations. Higher CAM content reduces electronic tortuosity but increases ionic tortuosity. A balance must be found between the effective conductivities.

4.2 Porosity

Porosity, or void space, is a critical parameter for charge transport and charge transfer.[51,85,86] In battery context: voids refer to regions that are not occupied by active materials, electrolytes or additives. Since they do not conduct ions or electrons, nor store charge, their location can significantly influence the kinetic performance of the electrodes and cells.[51] Additionally, the total quantity of voids can negatively influence volumetric performance metrics, such as the energy density of the cathodes and the resulting cells. **Figure 5** illustrates how porosity, as a function of CAM fraction and areal loading, affects energy density. The energy density is calculated for a cell, with an architecture similar to one reported by *Lee et al.* of Samsung SDI.[78] As CAM content or loading increases, the energy density of electrodes and consequently cells increase, too. However, the effect of porosity becomes more pronounced at higher cathode loading, which is only intuitive as higher loading increases the volumetric phase fraction of the cathode relative to the total volume of the cell. Since high loadings are required to achieve the ambitious targets of SSB manufacturers, the pore volume becomes even more critical.

Please note that the data presented in **Figure 5** only reflects the effect of pores on the achievable (thermodynamic) maximum energy density. In real cells, kinetic limitations caused by pores will be even more pronounced, due to larger charge transport pathways, lower specific interface area and current constriction phenomena[51,87]. This is evident from the plotted data reported by

Lee et al.[78] which has a reported cathode density of < 5 %, but still falls short of achieving full capacity.

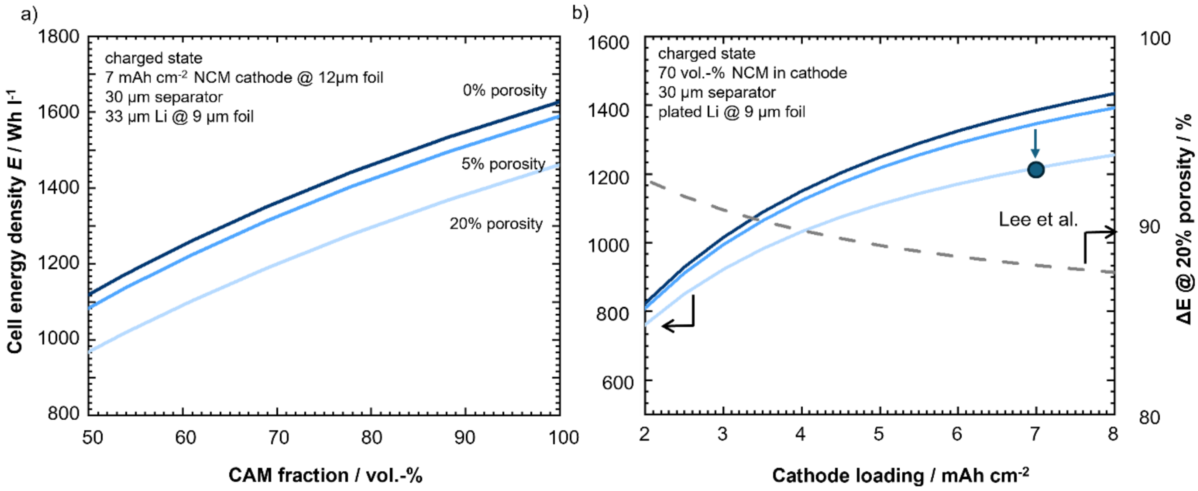

Figure 5: Calculated cell level energy density for composite cathodes using a) different fractions of CAM at constant loading and b) using different loading at constant CAM fraction. In both cases, the impact of porosity within the cathode is displayed, ranging from 0% to 20%. In most academic literature reports, porosity is stated to range from 10-15 %. As a reference, the reported cell energy density of Lee et al. is depicted, with a reported cathode porosity of around 5 %. From the displayed data can be observed, that reducing porosity is especially important for thick cathodes, having high loadings, as the relative portion of the cathode to cell volume increases with increasing loading.

While cathode voids have for a long time been overlooked in SSB research, recent attention has been drawn to their importance. *Bielefeld et al.* found that both the position of a void and also its size can significantly affect the charge transfer properties of the CAM/SE interface[51]. *Yamamoto et al.* demonstrated that pores can have a massive impact on charge transport and cell performance.[88] *Kodama et al.* showed, that even with high resolution µ-CT not all pores are detectable.[86,89] Voids may be distributed randomly or preferentially, and their size and location can impact SSB kinetics in various ways. In Publication 2 three different techniques were therefore applied to characterize the microstructure, including pores and the impact on charge transport properties was determined to show correlations between imaging and electrochemistry, as well as deviations.

Voids in SSBs originate from insufficient densification of powder-based cell components. In LIBs, voids are intentionally created during the slurry coating and drying process and their volume is carefully controlled during calendaring to ensure a certain desired electrolyte volume and percolation within the electrode[90]. It is worth noting that while voids are desired during fabrication of the electrodes, once the electrolyte is infiltrated, voids are almost eliminated in LIBs. In contrast, voids are completely undesired in SSBs, and advanced methods are required to minimize them.

One common approach is powder densification through applying high pressures of up to 1 GPa. Void space in ASSBs components can range from 5% to 25%, depending on the pressure and material used[85,86,88,91,92]. When considering pressurization, two mechanical force mechanisms have to be differentiated **(Figure 6)**. Uniaxial pressing involves densifying the components through applying mechanical force along a single axis (**Figure 6, left**). Here the pressure is highest at the contact points with the pressing tool, and it decreases along the walls of the pressing die due to wall friction. The uniaxial nature of the pressure can also cause particle rearrangement and a texturing of composite materials. Furthermore, the force vectors acting along a single axis may mechanically damage the materials. This has been reported by *Doerrer et al.* for CAM particles being pressed at pressures > 500 MPa.[76]

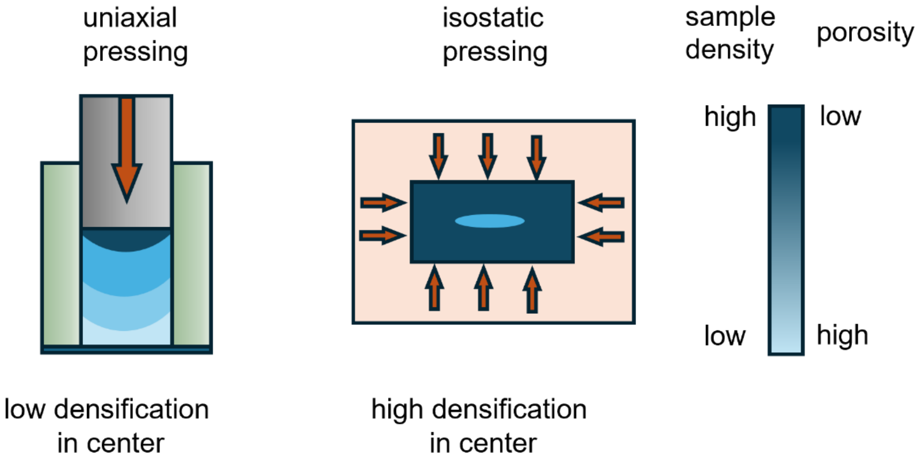

Figure 6: Schematic representation of the pressure distribution in uniaxially (left) and isostatically (right) pressed powder samples. While during uniaxial pressing, the compaction is highest at the contact to the piston, the pressure decreases due to wall friction effects towards the center of the sample. During isostatic pressing, a much more homogeneous pressure profile can be observed due to the fact that forces are acting from all sides, leading to in total higher densification.

Another consolidating method is isostatic pressing, where the components are sealed in a flexible, yet tight and evacuated container (such as a pouch bag) and placed in a vessel filled with a pressurization medium, often mineral oil, water or gas. During isostatic pressing, pressure is applied uniformly from all direction and the sample is evenly densified, without particle reorientation.[42] *Lee et al.* demonstrated, that indeed very low void fractions of < 5% can be achieved through the application of "warm-isostatic" pressing without damaging SE or CAM materials[78]. It is important to note that while these methods are effective on a lab scale level, sophisticated and scalable methods of pressurization are needed for SSBs to compete with LIBs.

4.3 Particle Size / Shape and Morphology

Naturally, large CAM particles require Li to diffuse long distances from surface to particle center, while small particles exhibit much shorter diffusion lengths. *Ruess et al.* found that a pathway can even increase within particles due to mechanical damage like cracking which has profound effects on cell performance.[70] Additionally, *Strauss et al.* found that smaller CAM particles provide higher effective conductivity of electrodes though no significant influence was observed for the ionic network[60]. Cells utilizing the smaller CAM particles demonstrated higher specific capacities and higher utilization level. In cells with larger CAM particles, X-ray diffraction could identify larger amounts of inactive material, proving the direct impact of percolation to utilization. They concluded that smaller CAM particles can create more electronic percolation pathways within the composite and are thus preferred over larger particles, which has been supported by other reports.[75,79,80]

However, one must take into account that smaller particles also have a much higher surface area at a given mass or volume. This can be advantageous for charge transfer, but also means more degradation and faster cell failure in case of (electro-)chemical instabilities.[93] As with many aspects of battery design, a balance must be achieved between charge transport, manufacturability, and stability.

Drawing from these reports, in Publication 1, ball milling was employed to reduce the SE particle size and overcome ionic limitations at high CAM loadings[31]. This reduction significantly improved effective ionic conductivity as well as the cell's performance. Results, that were later supported by observations from *Schlautmann et al.*, and others[64,94,95]. However, the real effect that these smaller SEs had on the microstructure remained unclear and was thus the motivation for the detailed investigation and visualization in the second publication.

Both CAM and SE particle sizes play crucial roles in influencing cathode microstructures. A study by *Shi et al*. explored the interplay between CAM and SE particle size through combined modelling and experiment identifying an optimal regime of CAM:SE particle size ratio to be around 1.4. This ratio can serve as a guideline to design the particle size of new materials targeting optimized charge transport in composites. However, when looking at the solid electrolyte particle size, one has to take into account that using smaller particles results in more particle-particle contacts (sometimes generalized under the term grain boundaries) which have an additional effect on the ionic charge transport. Several studies have shown that, while smaller particles can enhance the ionic conductivity of composites, they may reduce the bulk conductivity of the SE.[31,42,64,94–96] Thus, there appears to exist a natural limit of how small SE particles can be before further reductions cease to improve conductivity.

Besides particle size, particle morphology is also important[97]. Most NCM based CAMs are synthesized as spherical particles for their low aspect ratio and high packing density. However, they consist of smaller, single crystalline primary particles, and the grain boundaries are mechanical weak spots, prone to cracking[88,98]. In LIB, these cracks shorten diffusion pathways, but SEs cannot infiltrate these cracks leading to performance losses. Single crystalline CAM can mitigate this issue, as they lack intra-particle boundaries and are less prone to mechanical fatigue upon cycling[99–101]. *Ruess et al.* found no significant difference in cycling performance between single crystalline and polycrystalline NCMs in LIBs, but in SSBs, single-crystalline CAMs outperformed their polycrystalline counterparts.[102] They could demonstrate that this is related to reduced mechanical fatigue and a lower amount of “loss of active material” caused by interparticle cracks.

To conclude: particle sizes of CAM and SE must be carefully matched, and smaller particles are generally preferred. However smaller particles can increase the interface area and especially in the case of SEs, the effective ionic conductivity of the material typically decreases upon particle size reduction.

5. Results and Discussion

Composite electrodes for solid-state batteries (SSBs) are complex systems, with their performance — particularly kinetics — depending on several design factors. The aim of this work was to identify kinetic bottlenecks in composite cathodes and offer guidelines for optimization strategies. Although microstructural modeling is a powerful tool for quickly screening various architectures, it requires reliable reference data for benchmarking. Additionally, this approach constructs "ideal" electrodes, which can overlook influences such as material processing and component interactions. Therefore, experimental determination of charge transport and cell kinetics remains crucial for validating simulation guided cathode design and optimization methods.

In this chapter, three publications will be presented that focus on improving the understanding of composite cathodes for solid-state batteries. These studies primarily examine a combination of intercalation-type cathode active materials (CAMs) and thiophosphate-based solid electrolytes (SEs), as they allow for the simple and rapid creation of composite cathodes via mechanical mixing and room-temperature densification. While core concepts can be applied to other material combinations, certain parameters may vary. For instance, high-temperature sintering of oxide-based solid electrolytes can produce dense microstructures, provided that suitable protection strategies are in place to prevent interdiffusion between SE and CAM elements.

In Publication 1 and Publication 2, composite cathode microstructures are systematically varied and extensively characterized through charge transport measurements and electrochemical cell cycling. These studies progress in complexity from identifying bottlenecks in charge transport and their impact on cell performance to visualizing the cathode microstructure, emphasizing the importance of particle size and residual void space in affecting cell kinetics. In Publication 3, the results are comprehensively summarized and contextualized within the current solid-state battery (SSB) literature, identifying key properties and design factors for cathode active materials in SSB applications.

In these publications, laboratory-based manufacturing techniques were used, and it is important to consider that electrode processing plays a crucial role in shaping the resulting microstructure. While the findings highlight general trends and effects that must be addressed, the examples provided are not the only ways to overcome limitations. For each system, bottlenecks must be identified before optimization strategies are implemented

5.1 Publication 1 - Quantifying the impact of charge transport bottlenecks of composite cathodes for all solid-state batteries.

The baseline for Publication 1 was set by aiming to understand how charge transport can be measured, quantified, and used to identify the mechanisms limiting solid-state battery (SSB) performance. While initial simulations highlighted the importance of the geometric microstructure[32], and pioneering work explored the use of impedance spectroscopy to characterize charge transport[54,61], a comprehensive study with systematic microstructure variation was missing. In this work[31], a model system for composite cathodes was used, containing Li_6PS_5Cl as SE and NCM622 as CAM. By varying the CAM ratio, different microstructures were created and subsequently analyzed using impedance spectroscopy and a transmission line model. Selectively blocking contacts enabled reliable deconvolution of ionic and electronic partial conductivities, which were used to identify performance bottlenecks.

The study found that as the amount of SE decreased, the partial conductivity of the composite dropped dramatically, leading to high tortuosity factors. Complementary electrochemical cell cycling showed that reduced ionic partial conductivity correlated with lower C-rate capability, indicating kinetic limitations. However, increasing the SE content improved C-rate capability while reducing performance at lower C-rates, which was accompanied by a drop in electronic partial conductivity. The study demonstrated that percolation limitations in CAM networks, which increase inactive mass, could be addressed using carbon additives. This effect was not observed in cells with high CAM content, as the percolating networks already ensured sufficient electronic partial conductivity.

Interestingly, the study also showed that reducing solid electrolyte particle size led to better performance and higher ionic conductivities at low SE content. Therefore, microstructure design, particularly through controlling SE and CAM particle sizes, is crucial for optimizing SSB kinetics. These findings have been used in multiple studies to validate simulation results and have been confirmed in other SE/CAM systems as well.

The study design was developed by J. Janek, and me and the experimental concept created by all authors. The manuscript was written by me and edited by all authors. Reprinted with permission under CC BY from:

Minnmann, P.; Quillman, L.; Burkhardt, S.; Richter, F. H.; Janek, J. Editors’ Choice—Quantifying the Impact of Charge Transport Bottlenecks in Composite Cathodes of All-Solid-State Batteries. *J. Electrochem. Soc.* **2021**, *168* (4), 040537. https://doi.org/10.1149/1945-7111/abf8d7.

Journal of The Electrochemical Society, 2021 **168** 040537

Editors' Choice—Quantifying the Impact of Charge Transport Bottlenecks in Composite Cathodes of All-Solid-State Batteries

Philip Minnmann,[1,2] **Lars Quillman,**[1,2] **Simon Burkhardt,**[1,2] **Felix H. Richter,**[1,2] **and Jürgen Janek**[1,2,z]

[1] *Institute of Physical Chemistry, Justus-Liebig-University Giessen, D-35392 Giessen, Germany*
[2] *Center for Materials Research (LaMa), Justus-Liebig-University Giessen, D-35392 Giessen, Germany*

All-solid-state lithium batteries have the potential to provide increased energy and power density compared to conventional lithium-ion batteries with a liquid electrolyte. The charge transport within solid electrolyte-based composite cathodes determines the C-rate capability and ultimately the overall performance of a solid-state cell, making it one of the key remaining challenges. In this study, the charge transport in composite cathodes composed of Li_6PS_5Cl and NCM-622 is analyzed and characterized in terms of the effective ionic and electronic partial conductivities. The correlations between these effective conductivities, the microstructure of the composite cathodes, and the all-solid-state cell performance are revealed. By quantifying these correlations, bottlenecks for charge transport in composite cathodes are identified and strategies to optimize the cell performance are developed. The optimization potential of these strategies is demonstrated exemplarily by tuning electronic and ionic charge transport pathways using high active material loadings and an adjusted solid electrolyte particle size, respectively. The results will help to further increase energy and power density of all-solid-state batteries.

Manuscript submitted February 22, 2021; revised manuscript received April 1, 2021. Published April 27, 2021.

Supplementary material for this article is available online

High energy lithium-ion batteries are considered an enabler for the paradigm shift from fossil fuels-powered mobility toward more environmentally-friendly electric propulsion of vehicles.[1,2] However, physicochemical limitations will soon slow down the improvement of liquid electrolyte-based lithium-ion batteries.[3] Driven by the demand for safe and reliable energy storage devices with high power and energy density, all-solid-state batteries (ASSBs) have received increased attention in recent years.[4] The inherent non-flammable nature of the solid electrolyte as well as the projected ability to employ lithium metal anodes have made them a promising candidate for next-generation batteries to be used in consumer electronics and automotive applications.[5]

The key component of ASSBs—next to the active materials—is a chemically stable solid electrolyte providing an ionic conductivity that exceeds values of several mS cm^{-1} to achieve the performance of conventional lithium-ion batteries.[6] To date, intensive research has identified a multitude of material classes of solid electrolytes, such as oxides, thiophosphates, halides, or phosphidosilicates, some of which overcome this threshold.[7–12] The materials exhibiting by far the highest conductivities reported are lithium thiophosphates, some of which are reaching values above 20 mS cm^{-1}.[8,13] Besides the high conductivity of such materials, a further advantage for their application in ASSBs is their malleable nature, caused by low Young's moduli, enabling low-temperature processing and cell preparation.[14,15]

However, there are remaining challenges that have to be addressed, such as chemo-mechanical volume changes of the cathode active material (CAM) during electrochemical cycling,[16] dendrite formation at the lithium metal anode,[4] and interfacial stability issues.[17–21] Furthermore, high energy and power density require an appropriate microstructural design of composite cathodes to ensure sufficient charge transport pathways throughout the composite. For lithium-ion batteries with liquid electrolytes, the cathode is typically manufactured as a porous layer. This enables an easy and pore-free infiltration of the liquid electrolyte, and thus, good ionic percolation. This is typically expressed by a high effective ionic conductivity of the cathode, often described by a low tortuosity. In contrast, composite cathodes for ASSBs require homogeneous mixing of the solid electrolyte and CAM powders, unavoidably forming pores that lower the effective ionic conductivity.[22] In an ideal composite cathode, sufficient charge transport pathways are accessible to both, ions and electrons, and the influence of porosity and electrically insulating polymer binder is minimized.[23] Additionally, CAM loading should be as high as feasible to maximize the energy density of the cell.

Few studies have dealt yet with the microstructural design of thiophosphate-based composite cathodes. In contrast to oxide- or polymer-based solid electrolytes, thiophosphates can be processed by powder mixing at ambient temperature. So far, the optimization of charge transport pathways has only in few cases been based on microstructural parameters, such as tortuosity or effective conductivity.[24–30] Bielefeld et al. modelled the influence of different CAM fractions and particle size distributions on the CAM utilization and the tortuosity of ionic charge transport and Neumann et al. investigated transport bottlenecks of charge-discharge cycles of a cathode structure based on tomography data.[6,24,31] Recently, Shi et al. combined microstructural modelling and experimental work to determine an optimal solid electrolyte-to-CAM particle size ratio for the ionic charge transport through the solid electrolyte.[28]

Siroma et al. and Kaiser et al. demonstrated that the effective ionic conductivity, and thus tortuosity, can be derived from impedance spectra of composite cathodes.[25,26,32] Asano et al. correlated the CAM loading with charge transport properties of $LiNi_{0.33}Co_{0.33}Mn_{0.33}O_2$ - Li_3PS_4 composite cathodes and their performance in cell cycling.[27] Kato et al. developed an elegant method to determine effective ionic conductivities and tortuosities by fitting cell cycling data to a reaction-zone-front based model and discussed the impacts of these quantities on the cell performance.[33] Dewald et al. used DC polarization to investigate the influence of solid electrolyte and conductive additive fractions on charge transport in lithium-sulfur cathodes and the respective electrochemical cell performance.[34] Recent work highlights the formation of space charge layers at the cathode interfaces, but their quantitative impact on the cathode performance needs to be explored yet.[35] However, a comprehensive study correlating microstructural parameters and battery cell performance by compositional tuning and/or particle size adjustment is still lacking.

Therefore, we show in the following that the microstructure of cathode composites for ASSBs employing $LiNi_{0.6}Co_{0.2}Mn_{0.2}O_2$

---

[z] E-mail: juergen.janek@pc.jlug.de

(NCM-622) and chloride argyrodite Li_6PS_5Cl (LPSCl) can be optimized based on effective partial conductivities derived from impedance spectra of composite cathodes and galvanostatic battery cycling. We demonstrate that a high CAM loading eliminates the necessity for carbon additives often used to provide sufficient electronic conductivity in the composite. By reducing the size of the solid electrolyte particles in the composite cathode, the direct correlation between improved cell performance and a higher effective ionic conductivity is revealed.

Experimental

Preparation of composite cathodes for impedance evaluation.—If not mentioned otherwise, all experimental procedures were carried out in an argon-filled glovebox (*LabMaster*, MBraun, Garching, Germany), with $p(O_2)$ and $p(H_2O)$ <1 ppm.

Li_6PS_5Cl solid electrolyte was purchased from NEI Corporation (Somerset, NY, USA) and exhibited an ionic conductivity of 1.6 mS cm^{-1} at 25 °C and an electronic conductivity of less than 10^{-6} S cm^{-1} (measured by impedance spectroscopy and DC polarization, respectively) $LiNi_{0.6}Co_{0.2}Mn_{0.2}O_2$ (NCM-622) with a typical particle size of 3 μm was provided by BASF SE (Ludwigshafen, Germany) and dried overnight in a BÜCHI vacuum drying oven at 200 °C prior to the transfer into the glovebox. The NCM-622 exhibits an electronic partial conductivity of 10 mS cm^{-1} (Supplementary Information, Table S2 (available online at stacks.iop.org/JES/168/040537/mmedia)).

For the preparation of the composite cathodes, the solid electrolyte and CAM powders were thoroughly mixed by hand in an agate mortar for 15 min. A solid electrolyte with smaller particles was produced by milling 2 g of Li_6PS_5Cl (LPSCl) powder in a wet-milling process. Anhydrous heptane (Sigma Aldrich) and dibutylether (Sigma Aldrich) served as milling additives in a volume ratio of 8:1. The milling media-to-powder weight ratio was 30:1 and the powder-to-solvent weight ratio was 9:1. Planetary ball milling was conducted in a Fritsch *Pulverisette 7* at a rotational speed of 200 rpm with a 20 min milling and 10 min resting-cycle for a total of 30 cycles (for 10 h of absolute milling time).

For the measurement of the electronic conductivity of the composite cathodes, electronically conducting and ionically blocking electrodes were used as terminals (electronically terminated cathodes). For this purpose, 100 mg of the powder mixture was transferred into a polyether-ether-ketone cell casing with an inner diameter of 10 mm and was compacted with an uniaxial pressure of 380 MPa for 3 min at room temperature. The specially designed cell setup used for this has been described in a previous publication.[36] The volume fraction of the CAM was adjusted between 25 % and 61 %. For the calculation of the corresponding weight ratios of CAM and catholyte in the composite cathodes, bulk densities of LPSCl and NCM-622 have been assumed to be 1.87 g cm^{-3} and 4.65 g cm^{-3}, respectively. Stainless steel rods served as contacts.

For the measurement of the ionic conductivity of the composite cathodes, the electronically contacted cells were disassembled and approx. 60 mg of solid electrolyte powder were added to each side of the cathode composite. The whole setup was again compacted with a uniaxial pressure of 380 MPa for 3 min at room temperature. $In/(InLi)_x$ alloys ($x \approx 0.3$), prepared by pressing together indium foil (100 μm thickness, 9 mm diameter, 99.999 % Chempur, Germany) and lithium foil (120 μm thickness, 6 mm diameter), served as lithium reservoirs on each side.

For the preparation of ASSB cells, 60 mg of solid electrolyte were compacted with a uniaxial pressure of 100 MPa as a separator layer of approximately 200–300 μm thickness. Subsequently, 12 mg of the composite cathode powder mixtures (equivalent to approx. 15.3 mg cm^{-2}, corresponding to a CAM loading of 214 mAh cm^{-2}) were applied to one side of the SE layer and the resulting bilayer pellet was consolidated with a uniaxial pressure of 380 MPa for 3 min. The anode, an $In/(InLi)_x$ two-phase mixture, was prepared as described above and was attached to the opposite side of the SE layer to provide a stable anode potential of 0.62 V vs Li^+/Li.[37]

Electrochemical impedance spectroscopy (EIS).—The impedance of composite cathodes was measured at room temperature using a *Biologic VMP 300* potentiostat (BioLogic, Seyssinet-Pariset, France) with an amplitude of 10 mV. The impedance was typically measured in a frequency range from 7 MHz to 50 mHz. A constant pressure of approx. 40 MPa was applied to the pellets during the measurements. A specially designed cell setup comprising a force sensor to adjust the force (and thus the pressure) and a spring to compensate for pressure relaxation caused by elastic deformations of individual components was used. The impedance spectra were fitted using the *RelaxIS 3* software package (rhd Instruments, Darmstadt, Germany). Each impedance spectrum was tested for stationarity using the *Kramers-Kroning* test and the frequency range was adjusted accordingly.

Cell cycling.—For each experiment, a total of two ASSB cells were tested in a *MACCOR*® (Maccor, Tusla, OK, USA) battery cycler at 25 °C using a constant current charge-discharge profile. During cycling, a pressure of about 40 MPa was applied. For the C-rate calculation, a theoretical capacity of the CAM of 200 mAh g^{-1} was assumed.

Results and Discussion

Analysis of the ionic and electronic partial effective conductivity of composite cathodes.—Composite cathodes contain at least two different materials that fulfill the fundamental requirements of storing and transporting charge. These materials usually show different charge transport properties, as the solid electrolyte ensures ionic charge transport, while charge storage and electronic charge transport are ensured by the CAM and carbon additives. This simplified differentiation neglects the mixed-conducting properties of each material as the partial conductivity of one charge carrier is usually several orders of magnitude higher than that of the other. While mixed-conduction in the individual materials of the composite cathode can therefore be neglected, both electronic and ionic conduction are essential for understanding and describing the charge transport in the composite cathode as a whole.

Typical methods for the experimental investigation of charge transport in mixed-conducting systems are impedance spectroscopy and DC polarization with ion- or electron-blocking electrodes. An essential aspect for the practical application of both methods is the choice of the electrode materials that connect the sample to the measurement system. These should be either ionically or electronically insulating, e.g. stainless steel or LPSCl, respectively, in order to block one charge carrier at low frequencies.[26] Therefore, we built two types of symmetrical cells. For studies on electronic charge transport, electron-conducting and lithium-ion-blocking stainless steel electrodes were employed. For studies on ionic charge transport, ion-conducting and electron-blocking layers of LPSCl solid electrolyte were attached to both sides of the composite cathode. Because this electrolyte is not stable against lithium metal,[38] In/InLi reversible electrodes were used as lithium reservoirs and to avoid low-frequency polarization. The respective cell stacks are schematically depicted in Fig. 1.

Electrochemical impedance spectroscopy was conducted to determine the effective conductivity of the composite cathodes. Figure 1 shows representative impedance spectra of the respective cells with either ion-blocking (blue circles) or electron-blocking (orange circles) electrodes. The volume fraction of the CAM in both composite cathodes was approx. 42 vol.-% and the composite cathode amount was 100 mg.

In general, the shape of the Nyquist plots depicted in Fig. 1 is caused by impedance contributions originating from both charge carriers, and is characteristic for composite cathodes. Because of the respective termination, the composite cathode impedance $Z_{CC}(\omega)$ in

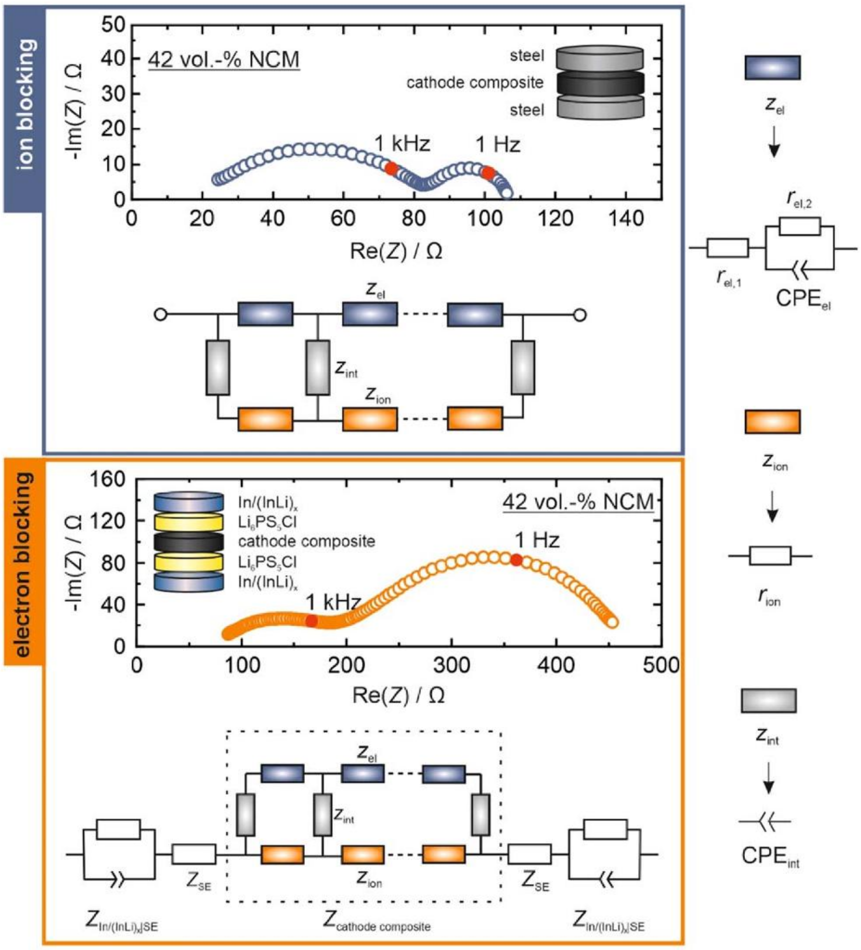

Figure 1. Schematic illustration of the measurement setup with electron-blocking (top) and ion-blocking (bottom) electrodes as well as representative impedance spectra. The corresponding transmission line model used for fitting the impedance spectra measured in these different cases is displayed in a simplified way. The exact equivalent circuit elements used to model the impedance contributions of electronic (blue), ionic (orange), and interfacial (grey) processes are depicted at the bottom of the figure. The two resistor elements $r_{el,\ 1}$ and $r_{el,\ 2}$ in the electronic transport process are attributed to electronic bulk transport and interfacial charge transfer, respectively.

the low-frequency part ($\omega \rightarrow 0$ Hz) is purely resistive in both cases. Composite cathodes are composed of multiple phases and charge transport can not only take place in either of these phases, but also across the interface between these phases. The impedance spectra of composite cathodes can, therefore, not be described by a simple parallel arrangement of electrical circuit elements, as is typically used for mixed conducting materials.[39] It is thus necessary to employ a transmission line model (TLM), which usually describes mass transport in a porous membrane, but can also model composite cathodes.[26,32,40,41]

To account for the symmetric contact configuration of the cells, the "T-type" TLMs with the equivalent circuit components depicted in Fig. 1 were used to fit the impedance data. In both cases, non-faradaic behavior is assumed for the interface, as fully lithiated NCM-622 (0 % SoC) exhibits a comparably high charge transfer resistance, which is caused by diffusion limitations inside the CAM. Details on the corresponding TLM are given in the Supplementary Information, Section 1.

Equation 1 is the mathematical description for the impedance of a T-type TLM, as derived by Siroma et al. (see Table 3 in Ref. 32, condition "open-open").[26,32] It describes how the cell impedance $Z_{CC}(\omega)$ depends on the impedance z_{el} of the electron conducting phase, the impedance z_{ion} of the ion conducting phase and the impedance z_{int} of the interface that is formed by these phases. Please note, the dimensions of z_{el} and z_{ion} are given in [Ω m] and z_{int} is given in [Ω m^{-1}], while the scaling parameter L is given in [m] and is referring to the composite cathode thickness.

$$Z_{CC}(\omega) = \frac{z_{ion} z_{el}}{z_{ion} + z_{el}} L + \frac{2\, z_{el}{}^{2} \sqrt{z_{int}}}{(z_{ion} + z_{el})^{\frac{3}{2}}} \cdot \frac{\cosh\left(L\sqrt{\frac{z_{ion}+z_{el}}{z_{int}}}\right) - 1}{\sinh\left(L\sqrt{\frac{z_{ion}+z_{el}}{z_{int}}}\right)} \qquad [1]$$

This equation was fitted to the measured impedance data to obtain the respective electronic and ionic resistance contributions R_{el} and R_{ion}. More information on the respective equivalent circuit elements that were used to model z_{ion}, z_{el} and z_{int} can be found in the Supplementary Information, Section 1. It has to be considered, that

Eq. 1 describes the impedance response of a composite cathode with ion-blocking electrodes materials. For electron-blocking electrodes, z_{ion} and z_{el} have to be interchanged.The effective conductivity $\sigma_{i,\mathrm{eff}}$ of a charge carrier *i* being transported through a composite cathode describes the average conductivity of the charge transporting material in this configuration. It is affected by the distribution and the properties of the respective charge transporting materials. In this case, the effective conductivity is calculated by using the geometrical thickness *L* and area *A* of the cylindrical composite cathode and the calculated resistances R_{el} and R_{ion} obtained from the impedance analysis (Eq. 2).

The distribution of the materials determines the trajectories of charge carriers through the composite cathode. The geometric tortuosity τ_i of a trajectory is the ratio of the length of the shortest charge transport pathway l_i to the shortest distance l_0 between two points according to Eq. 3:

$$\sigma_{i,\mathrm{eff}} = \frac{L}{R_i A} \qquad [2]$$

$$\tau_i = \frac{l_i}{l_0} \qquad [3]$$

In conventional lithium-ion batteries with a liquid electrolyte, the tortuosity is a parameter typically used to describe ion diffusion in porous composite cathodes and to optimize e.g. processing parameters and compositions.[42] Recently, the tortuosity of the electronic and ionic transport pathways in composite cathodes has also gained importance for the design of thiophosphate based all-solid-state cathodes.[6,25,27,43]

In composite cathodes containing a solid electrolyte, the tortuosity factor τ_i^2 can be calculated according to Eq. 4,[6] using the respective effective partial conductivity $\sigma_{i,\mathrm{eff}}$, the partial (bulk) conductivity $\sigma_{i,0}$ and the volume fraction ϕ_i of the respective material,

$$\tau_i^{\,2} = \frac{\sigma_{i,\mathrm{eff}}}{\sigma_{i,0}}\phi_i \qquad [4]$$

This equation neglects the effects originating from current constriction, cathode-electrolyte-interphase (CEI) formation, interface polarizations, and space charge layers. Therefore, the determined tortuosity factor might deviate from the "true" geometrical tortuosity factor. The effective partial conductivities $\sigma_{\mathrm{el,eff}}$ and $\sigma_{\mathrm{ion,eff}}$ as well as the tortuosity factors τ^2_{el} and τ^2_{ion} of the composite cathodes were calculated according to Eqs. 2 and 4, respectively.

The high-frequency offset in the real part of the impedance Re[$Z(\omega \rightarrow \infty)$] of composite cathodes studied with electron-blocking electrodes can be attributed to the resistivity of solid electrolyte separator layers. Impedance contributions originating from the In/(InLi)$_x$-LPSCl interfaces are considered based on impedance measurements in symmetric cells (In/(InLi)$_x$ | LPSCl | In/(InLi)$_x$) as illustrated in Fig. S3.

By fitting the transmission line model to the impedance spectra shown in Fig. 1 for cathode composites with approx. 42 vol.-% of CAM, resistances of $R_{\mathrm{el}} = 107\ \Omega$, and $R_{\mathrm{ion}} = 360\ \Omega$ are obtained. With a measured thickness of 470 μm and a calculated area of 0.785 cm^2, the respective effective conductivities are $\sigma_{\mathrm{el,\ eff}} = 5.6 \cdot 10^{-4}$ S cm^{-1} and $\sigma_{\mathrm{ion,\ eff}} = 1.7 \cdot 10^{-4}$ S cm^{-1}. Using the volume fractions of the respective phases and the bulk conductivities specified in the experimental section, the tortuosity factors yield $\tau_{\mathrm{el}}^{\,2} = 7.4$ and $\tau_{\mathrm{ion}}^{\,2} = 4.3$.

Variation of the volume fraction of NCM-622 in the composite cathode.—A variation of the composition of the composite cathodes inherently leads to changes in microstructure and, therefore, has a direct impact on the charge transport properties. Figure 2 displays the changes in effective ionic and electronic conductivity and tortuosity factors for composite cathodes with 25 to 61 vol.-% of NCM-622 determined with the method described above. For the calculation of the respective volume fractions, an average porosity of 14 % is assumed. Details on the calculation, as well as the derivation of this average porosity, can be found in the Supplementary Information, Section 3. Data for the individual materials was obtained from impedance spectroscopy of pure samples of these materials.

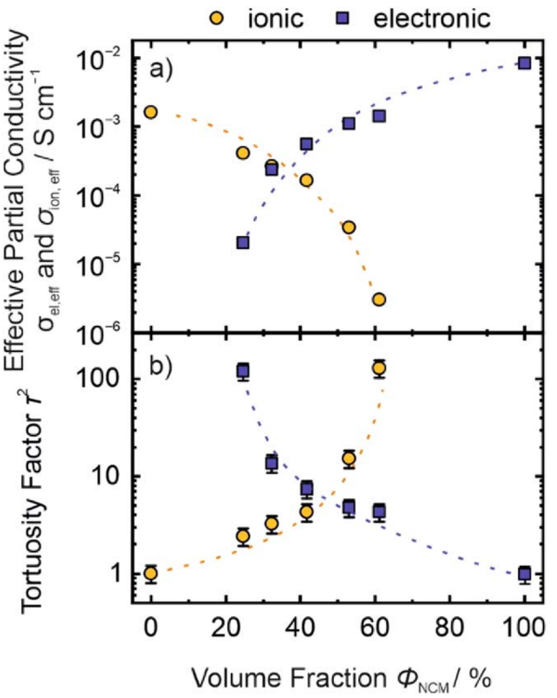

Figure 2. (a) Effective partial ionic (orange) and electronic (blue) conductivity of composite cathodes with different volume fractions of CAM obtained from impedance spectroscopy. Electronic conductivities were obtained using ion-blocking electrodes, and ionic conductivities were obtained using electron-blocking electrodes. Volume fractions were calculated with an average porosity of 14 vol.-%. (b) Calculated tortuosity factors of the composites. The ionic bulk conductivity of the solid electrolyte is 1.6 mS cm^{-1} and the electronic bulk conductivity of the CAM is 10 mS cm^{-1}. Dashed lines are guides to the eye only.

As expected, the electronic partial conductivity increases with increasing CAM volume fraction, while the ionic conductivity decreases. This trend is portrayed inversely by the respective tortuosity factors, as these are inversely proportional to the effective conductivities. The composite cathodes exhibit effective partial conductivities between 10^{-6} to 10^{-3} S cm^{-1} for both charge carriers in the investigated volume fraction range. For lower CAM volume fractions, the ionic partial conductivity exceeds the electronic one, while at higher volume fractions, the electronic partial conductivity exceeds the ionic one.

At approx. 42 vol.-% CAM the effective ionic conductivity of the composite is about four times lower than the ionic conductivity of the bulk solid electrolyte. However, because of the high bulk ionic conductivity of the employed chloride argyrodite (1.6 mS cm^{-1}), the effective ionic conductivity of the composite cathode is still 0.17 mS cm^{-1}. This is comparable to the bulk ionic conductivity of other solid electrolytes such as e.g. β-Li$_3$PS$_4$, which is still capable of being employed in ASSB cells with specific charges as high as 124 mAh g^{-1}.[44]

Figure 2a shows that the effective ionic conductivity decreases further for higher CAM fractions, which are desired to improve the

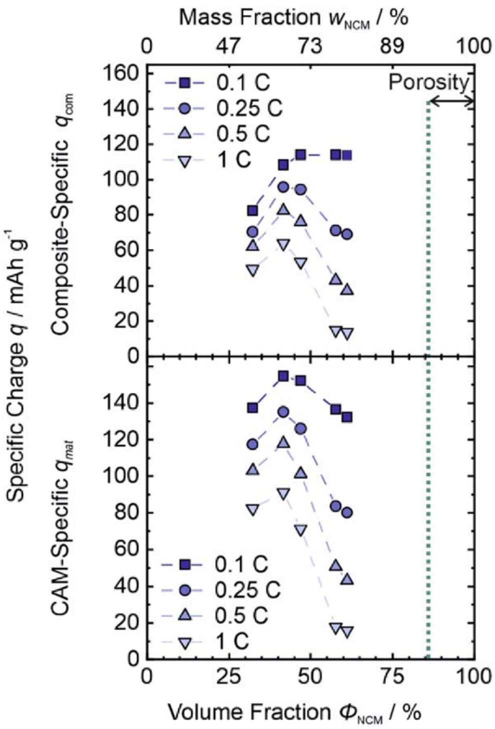

Figure 3. Influence of different CAM fractions on the specific charge of ASSB cathode composites and CAM during the discharge step. The obtained specific charge is normalized to the mass of the cathode composite (top) and the mass of the CAM (bottom). Dashed lines are guides to the eye only. The dashed vertical line illustrates the boundary of a pure NCM cathode with 14 % porosity. The specific charge increases with increasing CAM fraction for low and medium fractions—independent of the C-rate. The ionic charge transport becomes a major limiting factor in composite cathodes with high CAM fractions.

energy density of composite cathodes.[45] The ionic tortuosity factor (Fig. 2b) of the composite cathodes increases from a value of approx. 2.4 at 25 vol.-% NCM to a value of approx. 15.3 at 53 vol.-%, which is slightly higher than microstructural models generated by Bielefeld et al. have predicted.[6]

An increase of the volume fraction of NCM from 25 vol.-% to 33 vol.-% leads to an increase of the effective electronic partial conductivity by one order of magnitude from $2.1 \cdot 10^{-5}$ S cm^{-1} to $2.4 \cdot 10^{-4}$ S cm^{-1}. This increase of the effective electronic conductivity is accompanied by a decrease in effective ionic conductivity. A reduced effective electronic conductivity of composites with low volume fractions of CAM can be explained by a smaller number of electronic conduction paths through the composite. This insufficient electronic percolation lowers the effective electronic conductivity of such composites.

The electronic partial conductivity of the employed and fully lithiated NCM (10 mS cm^{-1}) is one order of magnitude higher than the ionic conductivity of the solid electrolyte. Additionally, it has been reported, that the electronic conductivity of NCM increases upon delithiation, hinting that the electronic limitation will be even lower upon cell cycling.[46] To obtain a possible predictor for cell performance, it is necessary to compare both, the tortuosity factors of the two charge carriers and the effective conductivities as microstructural descriptors. The electronic tortuosity factor decreases from a value of 120 at 25 vol.-% NCM to approx. 4.3 at 61 vol.-% NCM. This could imply that a high CAM fraction in the cathode composite provides sufficient electronic percolation through the cathode composite even without the use of carbon additives. Thus, ASSB cells with high CAM loading could omit the use of carbon additives, which in turn leads to a fundamental and conceptual difference between composite cathodes required for conventional LIBs and ASSBs. Carbon additives can improve the electronic conductivity throughout composite cathodes with low volume fractions of NCM and also the performance of ASSB cells. However, as the electronic potential of the carbon additives is comparable to that of the CAM, potential-related degradation of the solid electrolyte at the surfaces of carbon additives and CAM are more likely to occur.[47–50]

Whether carbon additives improve the performance of ASSBs depends on the electronic tortuosity of the composite cathode and thus on the CAM fraction. Typically, the reported volume fraction of CAM in thiophosphate-based ASSB is around 42 %.[9,16,22,27,36,47,51–56] For this volume fraction, the electronic tortuosity factor is above eight. Hence, we assume that not all CAM particles are connected to the electronically conducting network.[24] This would explain the beneficial effects of using carbon additives that have been reported for thiophosphate ASSB cells.[47,48,57]

Cycling performance of the composite cathodes with different volume fraction of NCM-622.—To elucidate the impact of the obtained microstructural parameters on the cell performance, we assembled and tested ASSB cells at different C-rates. The composite cathode mass was kept constant which in turn leads to different thicknesses and areal capacities (Table SII) for the different CAM volume fractions. However, by keeping the composite mass constant, a direct comparison of the gravimetric specific charge, is feasible. Figure 3 displays the specific charge obtained from the aforementioned composite cathodes with varying CAM fraction. If not mentioned otherwise, all specific charges refer to the discharge step.

The specific charge is normalized to either the cathode composite mass (composite-specific charge) or the CAM mass (material-specific charge). Both plots show an inverse U-shape, indicating that an optimum in specific charge can be obtained between the low and high limits of the CAM volume fractions. As expected, the specific charge decreases with increasing C-rate for all samples. However, certain differences are observed, when comparing the different compositions. The decrease in specific charge for increasing C-rates is lowest for the lowest CAM volume fraction and highest for the highest NCM volume fraction.

For a CAM fraction of 33 vol.-% NCM, a CAM-specific charge of 137 mAh g^{-1} was obtained at 0.1C, which drops by 40 % to 83 mAh g^{-1} at 1C. The composite cathode with the highest CAM fraction of around 61 vol.-% NCM provides a CAM-specific charge of 132 mAh g^{-1} at 0.1C, which drops by 88 % to 16 mAh g^{-1} at 1C. The highest CAM-specific charge at all C-rates was obtained at an NCM fraction of about 42 vol.-% with 154 mAh g^{-1} at 0.1C and 91 mAh g^{-1} at 1C. This observation is in line with previous results on $LiCoO_2/Li_{10}GeP_2S_{12}$ systems and NCM/Li_3PS_4-based systems. This may also explain the dominance of this composition in ASSB literature for thiophosphate-based systems.[9,16,22,27,36,47,51–56]

An increase in the energy density of ASSB cells on the composite cathode level is generally governed by two competing parameters, which are the CAM fraction in the composite cathode and the CAM utilization level. The utilization level describes how many CAM particles are connected to the ionic and electronic percolation network.[31] Both connections are necessary as isolated particles cannot be addressed electrochemically during charge and discharge.[58] At lower CAM fractions, improvements in energy density can be achieved by increasing the CAM fraction without affecting the utilization level negatively. This changes when CAM fractions exceed a certain threshold, above which additional CAM particles are isolated from the ion-conducting phase and remain inactive during operation. Thus, any further increase of the CAM fraction leads to a lower CAM utilization.

As observed for the CAM-specific charge, the composite-specific charge increases if the NCM fraction increases from 33 vol.-% to 42 vol.-%. In contrast to the CAM-specific charge, the composite-specific charge increases even beyond 42 vol.-% NCM at low C-rates. It saturates at around 115 mAh g^{-1} for NCM fractions between 42 vol.-% and 61 vol.-% at a C-rate of 0.1C. However, a similar behavior as for the CAM-specific charge can be observed in the C-rate capability, meaning the reduction of the composite-specific charge due to increasing C-rates from 0.1C to 1C. The composite-specific charge of composite cathodes with 33 vol.-% and 61 vol.-% NCM is lowered by 40 % (33 mAh g^{-1}) and 88 % (100 mAh g^{-1}), respectively.

The results indicate an important differentiation between different charge transport limiting effects, whose dominance depends on the composition of the composite cathode. At low CAM fractions, the electronic percolation becomes the limiting factor due to a low electronic CAM utilization. At high CAM fractions, the low effective ionic conductivity has a significant impact on the C-rate performance. When comparing the effective ionic conductivities and tortuosity factors, it becomes evident that high NCM fractions lead to highly tortuous pathways for ions. The ionic tortuosity factor at 61 vol.-% NCM is approx. 130, leading to large IR-drops at higher C-rates. This is also displayed by the charge-discharge curves shown Fig. S2. This highlights the need for solid electrolytes with conductivities beyond 10 mS cm^{-1}, as well as improved microstructural architectures for composite cathodes.[6] Additionally, the porosity in the composite cathode needs to be reduced as much as possible. Porosity is volume that is not contributing to electronic or ionic transport, thus, decreasing the effective conductivity of the composite cathode.

Because of the high solid electrolyte fraction, the C-rate performance at low CAM fractions is better than at high CAM fractions. This was also reported by Asano et al. for cathodes containing Li_3PS_4 solid electrolyte and NCM-111 CAM. The authors concluded that ionic limitation is the major issue to be solved in the microstructural design of composite cathodes containing high amounts of CAM.[27] Although, the electronic conductivity of the composite cathodes at 0 % SoC was much lower in the cited study than in our case, the cell performance at 49 vol.-% NCM (neglecting porosity) was highest for all C-rates, which is in line with our results.

Overcoming electronic limitations in composite cathodes.—Improving the effective electronic conductivity at high CAM fractions does not necessarily lead to a higher CAM utilization and conductive additives may not be necessary at all. To demonstrate this, we added conductive additives (vapor grown carbon fibers, VGCF) to cathode composites with CAM fractions of 33 vol.-% and 61 vol.-% (1 mg of VGCF per 100 mg of cathode composite). Conductive additives increase the electronic percolation at lower CAM fractions and act as electronic "wires" in the composite. Each composite was tested in ASSB cells and the specific charges obtained were compared to cells without the conductive additives as depicted in Fig. 4.

For the composite cathodes with a CAM fraction of 33 vol.-%, the addition of VGCF increases the material-specific charge by 13 % at a C-rate of 0.1C. However, for the cell in which a composite cathode with a CAM fraction of 61 vol.-% was used, no improvements in the specific charge were observed. At higher C-rates, the performance of the composite cathode with a high CAM fraction is even slightly lower compared to the composite cathode without VGCF. This may be caused by degradation at the carbon-solid electrolyte interface during cycling which can lead to changes in the ion transport pathways and increased ionic tortuosity. Because of the higher ionic tortuosity at higher CAM-fractions the decomposition of the solid electrolyte at the CAM-SE carbon-SE interface will affect the ionic charge transport in these cathode composites even more severely.

The addition of VGCF to the cathode composite with a low CAM fraction increased its material-specific charge during charging (Table SIV) and discharging by 10–20 mAh g^{-1} at all C-rates. This indicates that this improvement is mainly caused by creating additional contacts to CAM particles that would have been isolated without the use of carbon additives. At lower C-rates, higher composite-specific charges can be obtained by using composite cathodes with higher CAM fractions, even without carbon additives. This is due to the lower total amount of CAM in composite cathodes with low CAM fractions. At higher C-rates, however, composite cathodes with low CAM fractions outperform the ones with high CAM fractions because of the higher fraction of solid electrolyte in the composite and the resulting superior ionic percolation.

Consequently, a higher CAM fraction is required to achieve higher energy densities in ASSB cells while a lower CAM fraction enables higher current densities and may be used for high power density cells. The ionic limitation in composite cathodes with high CAM fractions has been found for $LiNi_{0.33}Co_{0.33}Mn_{0.33}O_2$, $LiCoO_2$, and $Li_4Ti_7O_{11}$-based composites.[25,27,36] Because ASSB cells need to provide both, high energy and high power density, these results show the need for an improved microstructural design of composite cathodes.

Overcoming ionic limitation in composite cathodes.—While testing with constant C-rates is important for the practical assessment of cell performance, using constant current densities is the more suitable approach to investigate the impact of the effective ionic conductivity within the composite cathodes. C-rate tests are used in ASSB research because the potential drop caused by the charge transfer resistance at the CAM-solid electrolyte-interface is kept constant, regardless of cathode mass or composition. By multiplying the C-rate with the theoretical specific capacity of the CAM, C-rates can also be written as specific current in units of mA g^{-1}. These are well suited to investigate the properties of CAM and CAM interfaces. However, when studying the ionic charge transport in composite cathodes at a certain C-rate, changes in the CAM itself and/or the CAM fraction of a composite cathode usually lead to changes in the current densities as well. Higher currents influence the charge transport IR-drop and additionally the charge transfer overpotentials from the anode side, which makes it difficult to assess the influence of the current density on cathode performance indicators such as cycling stability and specific charge. Figure 5 shows the specific charge obtained from composite cathodes with different CAM fractions as a function of the applied current density. The current density is determined by dividing the applied current through the geometric area of the cell.

The results show that increasing the CAM fraction leads to a stronger decay of the specific charge with increasing current density. This can be attributed to the decrease in effective ionic conductivity of the composite cathode. Additionally, as for the C-rates, the highest material-specific charge for all current densities was obtained from an ASSB cell with a cathode composite containing 42 vol.-% NCM. It is this composition that showed both, good electronic and good ionic effective conductivity. The results underline the importance of increasing the effective ionic conductivity in composite cathodes with high CAM fractions. Additionally, it can be observed that at similar current densities the composite cathodes with different CAM-fractions exhibit a different performance. As the anode is the same in all full cell tests, differences in the kinetic limitations observed in cell tests at similar current densities must correspond to kinetic limitations originating from the cathode.

Previous reports have demonstrated that reducing the solid electrolyte particle size may increase the performance of ASSB cells.[28,52,54] Thus, the influence of an additional grinding procedure of the solid electrolyte powder before fabrication of the cathode composite on charge transport was investigated. Using this approach, additional influence from amorphization of solid electrolyte particles typically seen in high energy ball milling steps can be minimized.[34] However, a direct comparison of the impedance

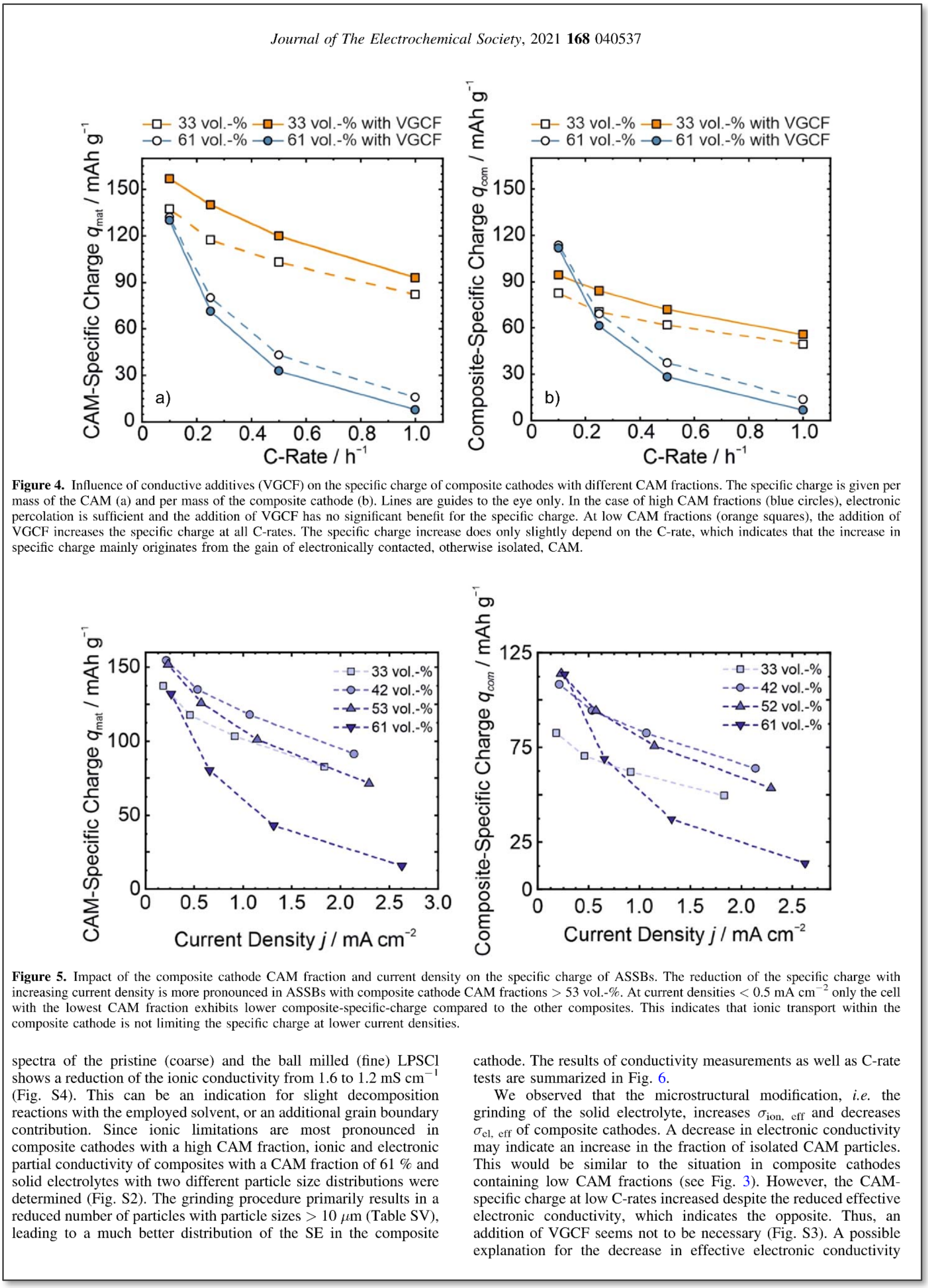

Journal of The Electrochemical Society, 2021 **168** 040537

Figure 4. Influence of conductive additives (VGCF) on the specific charge of composite cathodes with different CAM fractions. The specific charge is given per mass of the CAM (a) and per mass of the composite cathode (b). Lines are guides to the eye only. In the case of high CAM fractions (blue circles), electronic percolation is sufficient and the addition of VGCF has no significant benefit for the specific charge. At low CAM fractions (orange squares), the addition of VGCF increases the specific charge at all C-rates. The specific charge increase does only slightly depend on the C-rate, which indicates that the increase in specific charge mainly originates from the gain of electronically contacted, otherwise isolated, CAM.

Figure 5. Impact of the composite cathode CAM fraction and current density on the specific charge of ASSBs. The reduction of the specific charge with increasing current density is more pronounced in ASSBs with composite cathode CAM fractions > 53 vol.-%. At current densities < 0.5 mA cm^{-2} only the cell with the lowest CAM fraction exhibits lower composite-specific-charge compared to the other composites. This indicates that ionic transport within the composite cathode is not limiting the specific charge at lower current densities.

spectra of the pristine (coarse) and the ball milled (fine) LPSCl shows a reduction of the ionic conductivity from 1.6 to 1.2 mS cm^{-1} (Fig. S4). This can be an indication for slight decomposition reactions with the employed solvent, or an additional grain boundary contribution. Since ionic limitations are most pronounced in composite cathodes with a high CAM fraction, ionic and electronic partial conductivity of composites with a CAM fraction of 61 % and solid electrolytes with two different particle size distributions were determined (Fig. S2). The grinding procedure primarily results in a reduced number of particles with particle sizes > 10 μm (Table SV), leading to a much better distribution of the SE in the composite cathode. The results of conductivity measurements as well as C-rate tests are summarized in Fig. 6.

We observed that the microstructural modification, *i.e.* the grinding of the solid electrolyte, increases $\sigma_{\mathrm{ion,\ eff}}$ and decreases $\sigma_{\mathrm{el,\ eff}}$ of composite cathodes. A decrease in electronic conductivity may indicate an increase in the fraction of isolated CAM particles. This would be similar to the situation in composite cathodes containing low CAM fractions (see Fig. 3). However, the CAM-specific charge at low C-rates increased despite the reduced effective electronic conductivity, which indicates the opposite. Thus, an addition of VGCF seems not to be necessary (Fig. S3). A possible explanation for the decrease in effective electronic conductivity

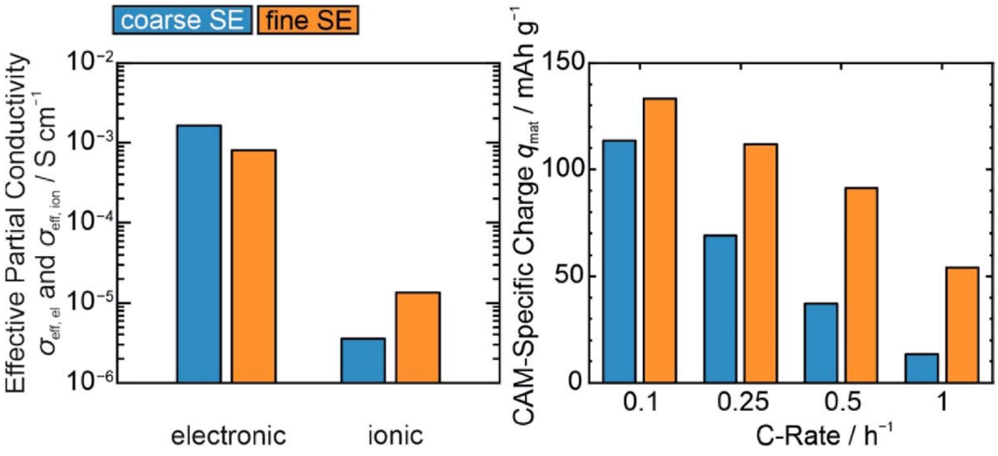

Figure 6. Influence of a reduced solid electrolyte particle size on the ionic and electronic charge transport in a composite cathode with a CAM fraction of 61 vol.-% (left) and the respective C-rate capability of ASSB cells with composite cathode containing the different solid electrolytes (right). Decreasing the solid electrolyte particle size leads to a more homogeneous distribution of the materials, less clustering of CAM particles, and improved contact between the solid electrolyte and the CAM. Although the effective electronic partial conductivity is decreased, a higher C-rate capability is observed, because of lower ionic transport IR drops.

could be a less pronounced clustering of the CAM particles. In such a scenario, solid electrolyte and CAM particles would be distributed more homogeneously, which would also explain the significant increase in the CAM-specific charge for the smaller SE particle size.

Similar observations have been made by Noh et al. and Shi et al. who demonstrated improved discharge capacities in ASSB cells containing $LiCoO_2$[52] and NCM,[28] respectively. The authors decreased the particle size of the thiophosphate SE particles through a ball milling approach. The results of our work show the direct correlation between effective partial conductivities of composite cathodes and the electrochemical performance of these composite cathodes in ASSB cells. Effective partial conductivities derived by impedance spectroscopy may thus be a suitable, easily accessible, and meaningful descriptor for the microstructural optimization of composite cathodes.

As a consequence of our results we propose to focus on the following aspects when optimizing the charge transport in composite cathodes:

- Reduction of porosity: We found that, although the determination of exact porosity values is difficult, composite cathodes prepared by a dry mixing process with subsequent uniaxial consolidation exhibit a high porosity of 13 %–17 % (Table SIII), which is comparable to values reported in literature.[43] This porosity not only decreases the volumetric energy- and power-density, it also blocks ionic and electronic charge transport. A result are low effective conductivities and highly tortuous charge transport pathways. One solution to reduce porosity can be improved processing techniques, such as warm-isostatic pressing. Lee et al. demonstrated that this approach can result in low single-digit porosity values.[59] Alternatively, infiltration of the pores by low-viscosity liquid or polymer electrolytes may be beneficial, provided there will be no detrimental interfacial reactions between either of the components.[60]
- Increasing solid electrolyte conductivity and simultaneously decreasing solid electrolyte particle size: Using highly conductive solid electrolytes with small particle size is necessary to increase the effective ionic conductivity in composite cathodes with high active material volume fractions. The determined ionic tortuosity factors of a composite cathode with 61 vol. % and a fine SE is around 34 (Table SII). In contrast, tortuosity factors in liquid electrolyte based cathodes for lithium-ion-batteries (LIB) are approx. an order of magnitude lower.[61] Although some reduction of tortuosity may be feasible by improved processing of the cathodes, tortuosity will probably stay higher than in LIBs, posing a challenge for the optimization of composite cathodes for ASSBs. For instance, for that composite cathode, which showed the best C-rate performance in our experiments, an effective ionic conductivity of 0.4 mS cm^{-1} was determined. To achieve this value in a composite cathode with 61 vol.-% and a tortuosity factor of 34, the ionic conductivity of the employed solid electrolyte has to be at least 47 mS cm^{-1}. This is nearly twice as large as the highest conductivity reported so far for a lithium solid electrolyte.[8] However, if the tortuosity factor could be decreased to a value below 10, the necessary ionic conductivity would yield 16 mS cm^{-1}. These results are comparable to microstructural models reported by Bielefeld et al. In the cited study, the authors stated that conductivities of more than 10 mS cm^{-1} are required for composite cathodes with a similar cathode volume fraction than in our upper limit case, but at lower ionic tortuosity factors. Similar results have been reported by Kaiser et al.[25] These results further highlight the necessity of highly conductive solid electrolytes to achieve high effective ionic conductivities and, ultimately, a better electrochemical performance of composite cathodes for ASSBs.
- Careful introduction of polymer binders: All results shown in this study were obtained from dry mixed powders. In order to facilitate large scale fabrication of ASSBs, slurry based roll-to-roll processes may be necessary.[62] The slurries typically contain polymer binders to mechanically stabilize the electrodes, which are manufactured as layers of about 100 μm thickness (sheets). These binders are also blocking ionic and electronic transport and will, thus, decrease the respective effective conductivities even more. Possible concepts to address this problem could be the drastic reduction of the binder content, as demonstrated by Hippauf et al. or the complementary use of binders, that are ionically conductive and electronically conductive additives, as shown by Oh et al.[63,64]

Conclusions

Effective ionic and electronic partial conductivities as well as the corresponding tortuosity factors of composite cathodes with varying amounts of $LiNi_{0.6}Co_{0.2}Mn_{0.2}O_2$ and Li_6PS_5Cl were measured and evaluated. For this purpose, impedance spectra were recorded using either ion-blocking or electron-blocking electrodes. A transmission line model was used to fit the impedance spectra obtained and to

derive the equivalent resistances. With increasing CAM fraction, the effective ionic conductivity decreases, while the effective electronic conductivity increases. Comparing effective conductivities and discharge capacities from battery cycling, two types of charge transport limitations are identified, which reduce the specific charge of ASSB cells. At a low CAM fraction, electronically isolated CAM particles cannot contribute to the charge-discharge process manifesting itself in a reduced CAM utilization. At higher CAM fractions, low effective ionic conductivity and clustering of the CAM particles reduce the C-rate capability of ASSB cells. The use of carbon additives increases the material-specific charge only at low CAM fractions, while the reduction of the solid electrolyte particle size increases the C-rate capability at high CAM fractions. Based on these results, the influence of the microstructural properties of composite cathodes on the performance of ASSBs based on them is discussed.

Acknowledgments

Financial support from the Federal Ministry of Education and Research (BMBF) within the FESTBATT consortium (03XP0177A) is gratefully acknowledged. We thank Anja Bielefeld for helpful discussions, Moritz Hofer (iPat, Technical University of Braunschweig) for the particle-size measurements and BASF SE (Ludwigshafen, Germany) for the supply with cathode material.

ORCID

Philip Minnmann https://orcid.org/0000-0002-9646-0487
Jürgen Janek https://orcid.org/0000-0002-9221-4756

References

1. S. Chu and A. Majumdar, *Nature*, **488**, 294 (2012).
2. D. Larcher and J.-M. Tarascon, *Nat. Chem.*, **7**, 19 (2015).
3. J. Janek and W. G. Zeier, *Nat. Energy*, **1**, 1167 (2016).
4. Y. S. Jung, D. Y. Oh, Y. J. Nam, and K. H. Park, *Isr. J. Chem.*, **55**, 472 (2015).
5. T. Famprikis, P. Canepa, J. A. Dawson, M. S. Islam, and C. Masquelier, *Nat. Mater.*, **18**, 1278 (2019).
6. A. Bielefeld, D. A. Weber, and J. Janek, *ACS Appl. Mater. Interfaces*, **12**, 12821 (2020).
7. N. Kamaya et al., *Nat. Mater.*, **10**, 682 (2011).
8. Y. Kato, S. Hori, T. Saito, K. Suzuki, M. Hirayama, A. Mitsui, M. Yonemura, H. Iba, and R. Kanno, *Nat. Energy*, **1**, 652 (2016).
9. M. A. Kraft, S. Ohno, T. Zinkevich, R. Koerver, S. P. Culver, T. Fuchs, A. Senyshyn, S. Indris, B. J. Morgan, and W. G. Zeier, *J. Am. Chem. Soc.*, **140**, 16330 (2018).
10. L. Zhou, C. Y. Kwok, A. Shyamsunder, Q. Zhang, X. Wu, and L. F. Nazar, *Energy Environ. Sci.*, **13**, 2056 (2020).
11. X. Li et al., *Angew. Chem.*, **131**, 16579 (2019).
12. S. Strangmüller et al., *J. Am. Chem. Soc.*, **141**, 14200 (2019).
13. S. V. Patel, S. Banerjee, H. Liu, P. Wang, P.-H. Chien, X. Feng, J. Liu, S. P. Ong, and Y.-Y. Hu, *Chem. Mater.*, **33**, 1435 (2021).
14. A. Kato, M. Yamamoto, A. Sakuda, A. Hayashi, and M. Tatsumisago, *ACS Appl. Energy Mater.*, **1**, 1002 (2018).
15. M. Yamamoto, M. Takahashi, Y. Terauchi, A. Sakuda, Y. Kobayashi, and S. Ikeda, *J. Ceram. Soc. Japan*, **125**, 391 (2017).
16. R. Koerver, W. Zhang, L. de Biasi, S. Schweidler, A. O. Kondrakov, S. Kolling, T. Brezesinski, P. Hartmann, W. G. Zeier, and J. Janek, *Energy Environ. Sci.*, **11**, 2142 (2018).
17. J. Auvergniot, A. Cassel, J.-B. Ledeuil, V. Viallet, V. Seznec, and R. Dedryvère, *Chem. Mater.*, **29**, 3883 (2017).
18. S.-K. Jung, H. Gwon, S. Lee, H. Kim, J. C. Lee, J. Chung, S. Park, Y. Aihara, and D. Im, *J. Mater. Chem. A*, **7**, 22967 (2019).
19. S. P. Culver, R. Koerver, W. G. Zeier, and J. Janek, *Adv. Energy Mater.*, **9**, 1900626 (2019).
20. F. Walther, R. Koerver, T. Fuchs, S. Ohno, J. Sann, M. Rohnke, W. G. Zeier, and J. Janek, *Chem. Mater.*, **31**, 3745 (2019).
21. Y.-Q. Zhang, Y. Tian, Y. Xiao, L. J. Miara, Y. Aihara, T. Tsujimura, T. Shi, M. C. Scott, and G. Ceder, *Adv. Energy Mater.*, **10**, 1903778 (2020).
22. J. Kim, M. Eom, S. Noh, and D. Shin, *J. Power Sources*, **244**, 476 (2013).
23. R. E. Usiskin and J. Maier, *Phys. Chem. Chem. Phys.*, **20**, 16449 (2018).
24. A. Bielefeld, D. A. Weber, and J. Janek, *J. Phys. Chem. C*, **123**, 1626 (2019).
25. N. Kaiser, S. Spannenberger, M. Schmitt, M. Cronau, Y. Kato, and B. Roling, *J. Power Sources*, **396**, 175 (2018).
26. Z. Siroma, T. Sato, T. Takeuchi, R. Nagai, A. Ota, and T. Ioroi, *J. Power Sources*, **316**, 215 (2016).
27. T. Asano, S. Yubuchi, A. Sakuda, A. Hayashi, and M. Tatsumisago, *J. Electrochem. Soc.*, **164**, A3960 (2017).
28. T. Shi, Q. Tu, Y. Tian, Y. Xiao, L. J. Miara, O. Kononova, and G. Ceder, *Adv. Energy Mater.*, **2**, 1902881 (2019).
29. J. Y. Kim, J. Kim, S. H. Kang, D. O. Shin, M. J. Lee, J. Oh, Y.-G. Lee, and K. M. Kim, *ETRI J.*, **42**, 129 (2020).
30. J. Park, K. T. Kim, D. Y. Oh, D. Jin, D. Kim, Y. S. Jung, and Y. M. Lee, *Adv. Energy Mater.*, **10**, 2001563 (2020).
31. A. Neumann, S. Randau, K. Becker-Steinberger, T. Danner, S. Hein, Z. Ning, J. Marrow, F. H. Richter, J. Janek, and A. Latz, *ACS Appl. Mater. Interfaces*, **12**, 9277 (2020).
32. Z. Siroma, N. Fujiwara, S. Yamazaki, M. Asahi, T. Nagai, and T. Ioroi, *Electrochim. Acta*, **160**, 313 (2015).
33. Y. Kato, S. Shiotani, K. Morita, K. Suzuki, M. Hirayama, and R. Kanno, *The journal of physical chemistry letters*, **9**, 607 (2018).
34. G. F. Dewald, S. Ohno, J. G. C. Hering, J. Janek, and W. G. Zeier, *Batteries Supercaps*, **4**, 183 (2021).
35. L. Wang et al., *Nat. Commun.*, **11**, 5889 (2020).
36. W. Zhang et al., *ACS Appl. Mater. Interfaces*, **9**, 17835 (2017).
37. A. L. Santhosha, L. Medenbach, J. R. Buchheim, and P. Adelhelm, *Batteries Supercaps*, **2**, 524 (2019).
38. S. Wenzel, S. J. Sedlmaier, C. Dietrich, W. G. Zeier, and J. Janek, *Solid State Ionics*, **318**, 102 (2018).
39. R. A. Huggins, *Ionics*, **8**, 300 (2002).
40. P. Braun, C. Uhlmann, M. Weiss, A. Weber, and E. Ivers-Tiffée, *J. Power Sources*, **393**, 119 (2018).
41. J. Bisquert, *Phys. Chem. Chem. Phys.*, **2**, 4185 (2000).
42. J. Landesfeind, J. Hattendorff, A. Ehrl, W. A. Wall, and H. A. Gasteiger, *J. Electrochem. Soc.*, **163**, A1373 (2016).
43. D. Hlushkou, A. E. Reising, N. Kaiser, S. Spannenberger, S. Schlabach, Y. Kato, B. Roling, and U. Tallarek, *J. Power Sources*, **396**, 363 (2018).
44. R. Koerver, I. Aygün, T. Leichtweiß, C. Dietrich, W. Zhang, J. O. Binder, P. Hartmann, W. G. Zeier, and J. Janek, *Chem. Mater.*, **29**, 5574 (2017).
45. S. Randau et al., *Nat. Energy*, **5**, 259 (2020).
46. R. Amin and Y.-M. Chiang, *J. Electrochem. Soc.*, **163**, A1512 (2016).
47. W. Zhang, T. Leichtweiß, S. P. Culver, R. Koerver, D. Das, D. A. Weber, W. G. Zeier, and J. Janek, *ACS Appl. Mater. Interfaces*, **9**, 35888 (2017).
48. F. Strauss, D. Stepien, J. Maibach, L. Pfaffmann, S. Indris, P. Hartmann, and T. Brezesinski, *RSC Adv.*, **10**, 1114 (2020).
49. F. Walther, S. Randau, Y. Schneider, J. Sann, M. Rohnke, F. H. Richter, W. G. Zeier, and J. Janek, *Chem. Mater.*, **32**, 6123 (2020).
50. D. H. S. Tan, E. A. Wu, H. Nguyen, Z. Chen, M. A. T. Marple, J.-M. Doux, X. Wang, H. Yang, A. Banerjee, and Y. S. Meng, *ACS Energy Lett.*, **4**, 2418 (2019).
51. F. Strauss, T. Bartsch, L. de Biasi, A.-Y. Kim, J. Janek, P. Hartmann, and T. Brezesinski, *ACS Energy Lett.*, **3**, 992 (2018).
52. S. Noh, W. T. Nichols, C. Park, and D. Shin, *Ceram. Int.*, **43**, 15952 (2017).
53. C. Park, S. Lee, K. Kim, M. Kim, S. Choi, and D. Shin, *J. Electrochem. Soc.*, **166**, A5318 (2019).
54. A. Sakuda, T. Takeuchi, and H. Kobayashi, *Solid State Ionics*, **285**, 112 (2016).
55. S. Ito, S. Fujiki, T. Yamada, Y. Aihara, Y. Park, T. Y. Kim, S.-W. Baek, J.-M. Lee, S. Doo, and N. Machida, *J. Power Sources*, **248**, 943 (2014).
56. J.-M. Doux, H. Nguyen, D. H. S. Tan, A. Banerjee, X. Wang, E. A. Wu, C. Jo, H. Yang, and Y. S. Meng, *Adv. Energy Mater.*, **10**, 1903253 (2020).
57. T. Ates, M. Keller, J. Kulisch, T. Adermann, and S. Passerini, *Energy Storage Mater.*, **17**, 204 (2019).
58. T. Bartsch, A.-Y. Kim, F. Strauss, L. de Biasi, J. H. Teo, J. Janek, P. Hartmann, and T. Brezesinski, *Chem Commun (Camb)*, **55**, 11223 (2019).
59. Y.-G. Lee et al., *Nat. Energy*, **5**, 299 (2020).
60. M. Weiss, F. J. Simon, M. R. Busche, T. Nakamura, D. Schröder, F. H. Richter, and J. Janek, *Electrochem. Energ. Rev.*, **3**, 221 (2020).
61. J. Landesfeind, M. Ebner, A. Eldiven, V. Wood, and H. A. Gasteiger, *J. Electrochem. Soc.*, **165**, A469 (2018).
62. J. Schnell, T. Günther, T. Knoche, C. Vieider, L. Köhler, A. Just, M. Keller, S. Passerini, and G. Reinhart, *J. Power Sources*, **382**, 160 (2018).
63. D. Y. Oh, Y. J. Nam, K. H. Park, S. H. Jung, K. T. Kim, A. R. Ha, and Y. S. Jung, *Adv. Energy Mater.*, **22**, 1802927 (2019).
64. F. Hippauf, B. Schumm, S. Doerfler, H. Althues, S. Fujiki, T. Shiratsushi, T. Tsujimura, Y. Aihara, and S. Kaskel, *Energy Storage Materials*, **21**, 390 (2019).

5.2. Publication 2 - Visualizing the Impact of the Composite Cathode Microstructure and Porosity on Solid-State Battery Performance

With the revelation of the impact of SE particle size on charge transport properties, the question arose as to how these microstructures actually look like at the microscale. The connection between charge transport and the actual microstructure was largely made using artificially generated models. While these models are important and powerful tools, they have limitations, as they are primarily based on mathematical descriptors and often overlook particle agglomeration, residual porosity, and the effects of manufacturing techniques.

In Publication 2[33], this was addressed by using FIB-SEM tomography to create accurate digital twins of cathode microstructures with varying SE particle sizes. These 3D reconstructions allowed to locate particle agglomerations and porosity, and to simulate charge transport for both ions and electrons. The results were then compared to effective conductivities obtained from charge transport measurements. Smaller SE particles did indeed improve ionic charge transport, primarily through a better distribution of the SE phase, and, interestingly, through a reduction in porosity. This led to less distorted pathways, significantly impacting cell performance.

However, one key finding was the systematic difference between simulated and measured conductivities for both ions and electrons. Simulation results consistently showed higher conductivity, suggesting that either additional resistive factors were present in the measurements, or that porosity, which has a major impact on charge transport, was not sufficiently captured in the image segmentation. In either case, the methodology revealed that simulations sometimes overlook critical contributions to cell performance.

Nevertheless, the importance of homogeneous cathodes was demonstrated, as well as the need to control porosity, and that optimizing cathode microstructure through particle design can indeed be effective.

The study design was developed by J. Schubert and me, and the experimental concept was created all authors. J. Schubert and I contributed equally to this work. The manuscript was written by J. Schubert and me and edited by all authors. Reprinted with permission under CC BY from:

Minnmann, P.; Schubert, J.; Kremer, S.; Rekers, R.; Burkhardt, S.; Ruess, R.; Bielefeld, A.; Richter, F. H.; Janek, J. Editors' Choice—Visualizing the Impact of the Composite Cathode Microstructure and Porosity on Solid-State Battery Performance. *J. Electrochem. Soc.* **2024**, *171* (6), 060514. https://doi.org/10.1149/1945-7111/ad510e.

Journal of The Electrochemical Society, 2024 **171** 060514

Editors' Choice—Visualizing the Impact of the Composite Cathode Microstructure and Porosity on Solid-State Battery Performance

Philip Minnmann,[1,2,z] **Johannes Schubert,**[1,2,z] **Sascha Kremer,**[1,2] **René Rekers,**[1,2]
Simon Burkhardt,[1,2] **Raffael Ruess,**[1,2] **Anja Bielefeld,**[1,2] **Felix H. Richter,**[1] **and**
Jürgen Janek[1,2,3,z]

[1]*Institute for Physical Chemistry, Justus-Liebig-University Giessen, Germany*
[2]*Center for Materials Research, Justus-Liebig-University Giessen, Germany*
[3]*BELLA, Institute for Nanotechnology, Karlsruhe Institute of Technology, Karlsruhe, Germany*

The kinetics of composite cathodes for solid-state batteries (SSBs) relies heavily on their microstructure. Spatial distribution of the different phases, porosity, interface areas, and tortuosity factors are important descriptors that need accurate quantification for models to predict the electrochemistry and mechanics of SSBs. In this study, high-resolution focused ion beam-scanning electron microscopy tomography was used to investigate the microstructure of cathodes composed of a nickel-rich cathode active material (NCM) and a thiophosphate-based inorganic solid electrolyte (ISE). The influence of the ISE particle size on the microstructure of the cathode was visualized by 3D reconstruction and charge transport simulation. By comparison of experimentally determined and simulated conductivities of composite cathodes with different ISE particle sizes, the electrode charge transport kinetics is evaluated. Porosity is shown to have a major influence on the cell kinetics and the evaluation of the active mass of electrochemically active particles reveals a higher fraction of connected NCM particles in electrode composites utilizing smaller ISE particles. The results highlight the importance of homogeneous and optimized microstructures for high performance SSBs, securing fast ion and electron transport.

[DOI: 10.1149/1945-7111/ad510e]

Manuscript submitted March 24, 2024; revised manuscript received May 13, 2024. Published June 11, 2024.

Supplementary material for this article is available online

Since their commercialization more than 30 years ago, lithium-ion batteries (LIBs) have greatly influenced everyday life from enabling handheld electronic devices that can operate for days to the first electrified vehicles able to drive hundreds of kilometers on a single charge. However, this type of battery, even though still making progress, is slowly approaching fundamental physicochemical limitations in terms of energy density and power density.[1] For a further increase, new concepts are necessary. Among the most promising concepts are solid-state batteries (SSBs), which replace flammable organic electrolytes used in LIBs with a solid electrolyte.[2] To date, numerous classes of inorganic solid electrolytes (ISEs) have been explored and thiophosphate-based ISEs appear particularly promising due to their exceptionally high ionic conductivity exceeding 20 mS cm^{-1} and favorable mechanical properties, that allow room temperature operation and processing, respectively.[3–6] However, there are still challenges that limit the SSB performance and consequently their practical application.[7]

While on the anode side, mostly two-dimensional interfaces between the ISE and high-capacity anodes such as lithium metal or silicon are investigated,[8–10] three-dimensional composites are used as the cathode.[11–13] These composites consist of the cathode active material (CAM), the ISE, functional additives (such as polymer binders or carbons) and a (hardly avoidable) residual porosity. The arrangement of the individual constituents is denoted as microstructure of the cathode composite and is of paramount importance for the SSB performance.[14–16] In an ideal cathode, the porosity is minimized, the CAM content is maximized (it is the only constituent storing charge), and the ISE is distributed homogeneously forming low resistance charge transport pathways.[12,13,17] This means that the cathode microstructure must conduct ions and electrons and provide a large interfacial contact area between ISE and CAM to ensure rapid transfer of lithium during charging and discharging.[12] However, charge transport pathways are often tortuous and charge carriers must travel longer distances than one might initially assume based on the geometric dimensions. This can be quantified by "tortuosity factors," which correlate effective transport properties and bulk properties of the respective phases in a composite microstructure, and which have become an important metric in microstructural optimization[14,18] even though their proper determination and meaningfulness is still under debate.[19,20]

In LIBs, cathodes are manufactured as porous components, that can be infiltrated by liquid electrolyte, thus enabling sufficient wetting of the CAM in all cathode regions as well as short charge transport pathways.[21,22] In SSBs, however, the picture is different as the ISE is already a constituent of the cathode during the manufacturing process. Therefore, uniform distribution and intimate contact between CAM and ISE particles must be achieved during cell fabrication. Consequently, the microstructure of these cathodes is more complex than in LIBs. In this context, thiophosphate-based ISEs have unique mechanical properties that distinguishes them from other material classes. In particular, their malleability allows densification at low temperature without requiring energy intensive sintering.[23]

Several research groups have studied the cathode microstructure by modelling or electrical transport measurements.[14,15,18,24–36] Key findings include that cell microstructure and resulting properties depend on the employed materials, composition,[14,15,18,25,28,29,35] particle sizes[16,33,34,36–39] and manufacturing conditions.[40–43] For instance, Shi et al.[34] introduced the ratio of ISE to CAM as a determining metric and Cronau et al. expanded this concept to a detailed experimental study on the achievable capacity in SSBs.[44]

Additional to model-based approaches and electrochemical measurements, three-dimensional tomography and microstructural reconstruction are important to visualize and understand the real microstructure. Methods that allow such reconstructions are e.g. X-ray computed tomography (CT) and focused ion beam scanning electron microscopy (FIB-SEM). First studies have already reported such microstructures[45–50] and delivered valuable input for modelling groups that can use these reconstructions to simulate charge transport and battery operation on real models. For instance, chemo-mechanical failure of composite cathodes was investigated[51,52] and globally obtained data such as the charge transfer resistance of a cathode were

---

[z] E-mail: philip.minnmann@phys.chemie.uni-giessen.de; johannes.schubert@phys.chemie.uni-giessen.de; juergen.janek@phys.chemie.uni-giessen.de

correlated to the microscopic processes, i.e. areal resistance of the ISE-CAM interface.[47]

So far, there are few studies correlating actual charge transport measurements of thiophosphate-based SSB cathodes[35,50,53] with the microstructural information obtained from tomography. These investigate mostly only small volumes (in the range of a few thousands of μm^3) or larger volumes with lower resolution ($>$ 300 nm). Nevertheless, these studies provide valuable insight into the fundamental microstructural features that limit SSB cathode performance. Hlushkou et al. investigated the influence of pores on the charge transport in $LiCoO_2$-based electrodes and found that porosity has a significant effect on the ionic charge transport in such structures.[53] The same group reported detailed reconstructions and investigated the microstructure of $LiNi_xCo_yMn_zO_2$-based composite cathodes using ISEs (beta-Li_3PS_4 and Li_6PS_5Br) with different particle morphologies.[47] Iwamoto et al. used nano-CT to obtain cathode reconstructions and simulated charge transport parameters for three different ISE particle sizes ($75Li_2S$-$25P_2S_5$ glass).[48] They found that clustering of active material particles, which is one of the mechanisms that limits SSB performance, can be reduced by smaller ISE particles. However, due to the nature of the employed technique, they could not determine and consider porosity in their reconstructions.

A detailed study visualizing the influence of thiophosphate-based ISE particle size on the microstructure of composite cathodes and investigating the effects on charge transport is reported here for the first time, to the best of our knowledge. We compare experimental and simulated charge transport in composite cathodes composed of agglomerated single crystals of $LiNi_{0.83}Co_{0.11}Mn_{0.06}O_2$ (NCM) and the thiophosphate-based glassy ISE Li_3PS_4-0.5LiI with different particle sizes. We correlate the results to the microstructure obtained by highly resolved FIB-SEM tomography on large (several 10^5 μm^3) cathode volumes. A complementary investigation of the electrochemical performance, the utilization levels of CAM and the chemo-mechanics of these cathodes provides important information for modelling groups and are used to develop guidelines for the further optimization of the composite cathode.

Experimental

All solids used in this study were dried at 200 °C under dynamic vacuum for 12 h using a vacuum drying oven (Büchi, Switzerland). Unless stated otherwise, all experiments were performed under inert gas atmosphere; either in an Ar filled glovebox (LabMaster, MBraun, Germany) with H_2O and O_2 concentration below 0.1 ppm and N_2 concentration below 1 ppm, or by using sealed containers for components and materials filled with dry Ar atmosphere.

Synthesis.—Glassy Li_3PS_4-0.5LiI (ISE) was synthesized via a mechanochemical route using stochiometric amounts of P_2S_5 (Sigma Aldrich), LiI (Sigma Aldrich) and Li_2S (Sigma Aldrich) (2 g in total). Precursors were mixed in a planetary ball mill (Pulverisette 7, Fritsch, Germany) for 12 h with a rotational speed of 450 rpm using a 70 ml zirconia jar and 20 pieces of zirconia milling media of 10 mm diameter. Three batches of ISE powder were synthesized in this way. In order to obtain ISE powders with smaller particle sizes, additional milling steps were conducted for two of the batches. For this, the two batches were ground further for 4 h at 450 rpm using zirconia milling media of 3 mm diameter and 1 mm diameter, respectively, with a milling media-to-powder weight ratio of 30:1. To reduce the amount of powder adhering to the milling media, and hence, increasing the yield, five drops of anhydrous heptane were added into the jar prior to grinding. Mixing as well as grinding were suspended after every 15 min for 15 min to prevent overheating of the sample. After removal of the sample from the jar, all products were ground in an agate mortar for 5 min by hand to crush agglomerates of ISE. The ISE powders obtained from grinding with milling media of 10 mm, 3 mm and 1 mm diameter and composites prepared from these are referred to as BM10, BM03 and BM01 (BM corresponds to "ball milled"), respectively, in the following.

Cell fabrication and testing.—For SSB cell fabrication, an in house developed housing was used.[54] Initially, 60 mg of Li_6PS_5Cl (LPSCl) (NEI Corporation, Somerset, USA) were put into a 10 mm diameter polyetheretherketone (PEEK) cylinder and compacted by a hand press using stainless steel pistons. Cathode composites were prepared for each batch of ISE with differing particle sizes of the ISE powder. For this, agglomerated single-crystals of $LiNi_{0.83}Mn_{0.06}Co_{0.11}O_2$ (D_{50} = 3–5 μm, MSE Supplies, USA) and Li_3PS_4-0.5LiI in the weight ratio of 70:30 were thoroughly mixed for 15 min by hand in an agate mortar. 12 mg of composite material (equivalent to a CAM loading of 10.7 mg cm^{-2}) was homogeneously distributed on the LPSCl separator layer, and the resulting pellet was densified at room temperature by uniaxial pressure of approx. 380 MPa for 3 min. Finally, an indium foil disc (9 mm diameter, 100 μm, ChemPur, Germany) and a lithium foil disc (6 mm diameter, 100 μm, China Energy Lithium, PRC) were placed on the separator layer leading to an $In/(InLi)_x$ two-phase mixture that served as anode with a stable potential of 0.62 V vs Li^+/Li.[55]

All resulting SSB cells were cycled in a Maccor battery cycler at 25 °C with an applied stack pressure of 30 MPa. Galvanostatic charging and discharging was conducted between 2 V and 3.7 V with C-rates of 0.1 C, 0.2 C, 0.5 C, 1 C and 2 C (1 C = 200 mA g^{-1}) increasing every three cycles.

Conductivity measurements.—For measurements of the ionic conductivity of the synthesized ISEs an ion-blocking symmetric cell configuration was used in which the ISE was confined on both sides with steel pistons. For this, approx. 100 mg of ISE were filled in the PEEK cylinder and subsequently pressed at room temperature with uniaxial pressure of approx. 380 MPa.

For conductivity measurements of the cathode two types of symmetric cell configurations containing 50 mg or 100 mg of the composite cathode material were prepared. Please note that no conductive additive was added to avoid additional decomposition reactions.

For measurements of the electronic conductivity the composite was put into the PEEK cylinder, confined on both sides with steel pistons and subsequently compacted at 380 MPa for 3 min. For measurement of the ionic conductivity a LPSCl separator layer with a thickness of approx. 400 μm was formed by compaction of the powder at 380 MPa for 3 min. 25 mg or 50 mg of the composite cathode material were then distributed on both sides followed by a final densification step.

Electrochemical impedance spectroscopy was carried out with a *VMP*-300 potentiostat (Biologic, France) at ambient temperature. Cells were mounted in a steel frame which allowed to maintain a pressure of about 100 MPa throughout the measurement. Potentiostatic electrochemical impedance spectra (PEIS) of symmetric cells were recorded at open circuit voltage (OCV) in the frequency range of 3 MHz to 10 mHz with an amplitude of 10 mV.

Particle size analysis.—The particle size of the ISE was determined by laser scattering. A small amount of the respective sample was dispersed in a solution of polyisobutylene and anhydrous xylene. The dispersion was subsequently ultrasonicated for 15 min. Measurements were performed outside of a glovebox in a *HELOS* particle size analyzer (SympaTec GmbH, Germany). Due to a short timeframe of the measurement and the dispersion in xylene, we assume no significant change in the particle size and morphology.

FIB-SEM.—Plasma-FIB-SEM (PFIB-SEM) tomography of three composite pellets (differing ISE particle size and without carbon) was carried out on a *XEIA3* (Tescan, Czech Republic) using an Xe-plasma ion source. Pellets were coated with a thin platinum layer by sputter deposition and subsequently the region of interest was coated with 10–15 μm of platinum using the gas injection system of the instrument. A U-shaped trench was milled into the surface allowing for imaging of the cross-sectional area. To attenuate curtaining, a polishing step was carried out prior to tomography. Sectioning was performed automatically using the 3D acquisition wizard of the software with a current of 36 nA and with a slice distance of 100 nm. Secondary electron (SE) and back scattered electron (BSE) SEM images were recorded with a resolution of 100 nm, which results in cubic voxel dimensions. All sample transfers were conducted under vacuum or inert Ar-atmosphere using a *VCT* transfer module (LEICA, Germany).

Image processing and segmentation.—Processing of the images acquired by the BSE and the SE detectors was implemented with *Fiji ImageJ* and *Python* 3.7. First, in order to align all images of the image stacks properly, slight drifting of the imaged cross-section area throughout the measurement was corrected using the *MultiStackReg* plugin of *ImageJ*, enabling identical drift correction of BSE and SE image stacks. Potential inhomogeneous illuminations of images were reduced by division of the image with a strongly blurred version of itself. Finally, curtaining effects visible only in SE images were attenuated with the *Stripes Filter* function of the *Xlib* plugin and the image contrast was normalized.

As an attempt to improve segmentation of pores as well as interfaces, a segmentation method based on machine learning techniques was implemented. The employed machine learning model consists of the first two convolutional layers of a pre-trained *VGG16 CNN* model used for feature extraction and a random forest classifier used for the pixelwise classification task.[56] Details are described in Sect. S3. The implementation in *Python* was performed using *Keras* and *Scikit-learn*.[57,58] The segmented image was generated by combination of the segmentation of BSE and SE images. Several impurities of an unknown material (possibly fragments of a mortar) were observed in the BM01 sample. Since the volume fraction was small and fragments could be reliably identified by eye, the phase was segmented manually on the respective slices.

Microstructure analysis.—The three-dimensional reconstruction obtained from the segmented images and all subsequent methods for its microstructural analysis and characterization were implemented in Python. The volume fractions of CAM, ISE and pores were directly calculated from the reconstructed volume by counting all voxels belonging to the respective phase. Surface areas for each phase and respective interface areas were calculated using the marching cubes algorithm by *Scikit-learn*. With the surface areas S of each phase, the interface area $S_{\text{a-b}}$ between phases in a system containing three phases (a, b, c) was then calculated with Eq. 1.[59]

$$S_{\text{a}-\text{b}} = \frac{1}{2}(S_{\text{a}} + S_{\text{b}} - S_{\text{c}}) \tag{1}$$

Chord length distributions CLD of CAM and ISE phase were determined using the Python package *PoreSpy*.[60] Chords are linear segments lying inside the phase of interest and with both ends trimmed at the phase boundary.[61] Hence, the CLD may allow to draw conclusions on the morphology of the respective phase and with regard to the investigated composite, in particular, potential clustering of phases. Chords were applied along each axis of the volume with a distance of two voxels between adjacent chords. Chords intersecting the volume of interest boundaries were discarded as they are artificially truncated, and thus, would distort the distribution.

Determination of the tortuosity.—To further assess the influence of morphology on the transport properties, tortuosities of CAM and ISE phases were determined by random walk simulations using *Pytrax* and by a flux-based method using *GeoDict*.[62,63] For random walk simulations, initially, a total of 2000 walkers were randomly distributed in either the CAM phase or the ISE phase. Every timestep, the walkers were allowed to move in orthogonal directions to adjacent voxels and the respective mean square displacement (*MSD*) was recorded periodically. In order to prevent artificial confinement of the walker and introduction of an upper limit of the *MSD*, the reconstructed volume was extended on each side by mirroring, which allows the walker to leave the volume. Afterwards, the *MSD* was plotted as a function of time steps, resulting in a roughly linear curve, and the tortuosity was determined from the inverse slope considering that the slope of the respective curve is unity in free space. To ensure a sufficient number of time steps, simulations were performed multiple times with an increasing number of time steps for each simulation. For the flux-based method, *GeoDict's ConductoDict* module was used to determine the partial conductivities from which the tortuosities were subsequently calculated.

Results

Solid electrolyte particle size influences effective conductivity.—We prepared glassy Li_3PS_4-0.5LiI solid electrolyte with three different particle sizes (BM10, BM03, BM01) using solvent-assisted ball milling with three different milling media sizes. Figures 1a–1c compare the SEM images of these samples. We note that all three samples exhibit a similar particle morphology, which indicates that no severe damage was inflicted to the particles by ball milling. In a first qualitative assessment, it can be observed that the number of larger particles is reduced by the ball milling steps with 3 mm or 1 mm milling media, which results in a much larger number of smaller particles.

Using these SEM images, the particle size can be quantified, as shown in Figs. 1a–1c. Evidently, the particle size decreases when smaller milling media are employed, i.e. in the BM10 sample, several large particles with diameter $d > 20\ \mu$m can be observed, while in the BM03 sample only few larger particles are found. In contrast, the BM01 sample does not show particles with $d > 20\ \mu$m, however, the general particle size is slightly larger than the one in the BM03 sample. This is also evident in the particle size distribution (PSD) data obtained by laser diffraction. The d_{50} values decrease from $d_{50} = 7.41\ \mu$m for BM10 to $d_{50} = 4.93\ \mu$m for the BM03 sample. While with $d_{50} = 5.93\ \mu$m the BM01 sample also shows a decrease in particle size compared to the BM10 sample, the BM03 sample apparently exhibits overall the smallest particle sizes. Based on the SEM images (Fig. 1c), we attribute this observation to particle re-agglomeration in the suspension, which could not be avoided entirely and can be responsible for the additional change of slope around 10 μm in the PSD of the BM01 sample. Interestingly, the distribution of particle sizes becomes narrower for the BM03 and BM01 sample. A narrow PSD can result in more homogeneous microstructures of cathodes which may improve their charge transport properties.

The effective reduction of the particle sizes by use of smaller milling media can be explained by the increase of the collision frequency between the sample and the milling media. Smaller milling media are, at a given total mass, more numerous than larger milling media and can create more collisions per time unit than their larger counterparts. For a further reduction of the particle size, we assume that particle re-agglomeration must be avoided, for instance by use of dispersing agents and surfactants.

We determined the room temperature ionic conductivity to be $\sigma_{\text{ion}} = 2.0$ mS cm^{-1} for BM10, $\sigma_{\text{ion}} = 1.7$ mS cm^{-1} for BM03 and $\sigma_{\text{ion}} = 1.6$ mS cm^{-1} for BM01 (**cf** Fig. S1). Particles of BM03 and BM01 are on average smaller, thus, the decreasing ionic conductivity compared to BM10 indicates a higher contribution of the ionic contact resistance between individual particles, which is in line with other reports of this material class.[34,44] There are no changes observable in the X-ray diffractograms of all three samples depicted in Fig. 1e, which display largely glassy or glass-crystalline materials with some LiI impurity.

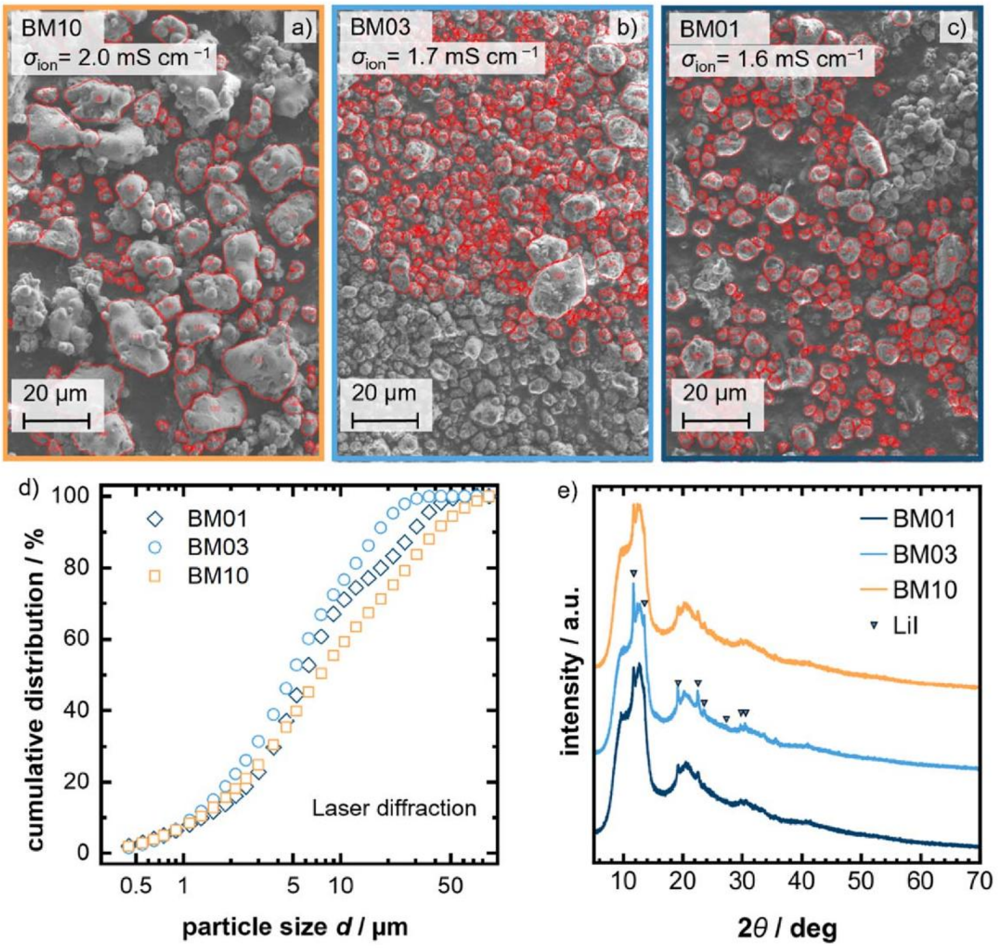

Figure 1. SEM images and analysis results of differently sized Li_3PS_4−0.5LiI solid electrolyte particles. Solid electrolytes were ball milled with (a) 10 mm (BM10), (b) 3 mm (BM03) and (c) 1 mm (BM01) milling media. Red boundaries indicate individual particles and were inserted manually. Smaller milling media lead to a reduction in particle size without significant loss of ionic conductivity. (d) Volume-weighted particle size distribution measured by laser diffraction. (e) XRD pattern of BM10, BM03 and BM01 samples showing characteristic patterns of glassy samples with some LiI impurity.

To investigate the influence of the different ISE particle sizes on cathode transport properties, we prepared composite electrodes by thoroughly mixing ISE and CAM. We subsequently determined the effective conductivities by impedance spectroscopy with two different experimental setups and corresponding transmission line models.

For the determination of the electronic partial conductivity, a composite electrode was embedded between two steel stamps that serve as current collector and block ionic transport. This cell concept known as *ion blocking electrodes* is typically used for mixed ionic-electronic conductors but can be applied to SSB cathodes, too.[18,25,28] While it is possible to determine the ionic conductivity from these impedance spectra, a large uncertainty exists, if ionic and electronic conductivity differ by orders of magnitude. Therefore, the ionic partial conductivity was measured in a different cell configuration, which we denote as *full blocking* (Fig. 2b), in which an ISE layer is sandwiched between two composite electrode layers. This setup has recently become increasingly popular in battery research.[27,64,65]

A transmission line model (TLM) is used to fit the impedance data of the composite electrode, i.e. the electronic and the ionic charge transport, and the interface between the two phases.[66] Analogous to our previous work,[18] the use of fully lithiated NCM means that lithium ion transfer cannot take place between NCM and ISE due to the very high charge transfer resistance. T-type and Z-type TLMs (Fig. S2) correspond to the different cell setups as described below. Detailed explanations of these models and their physical meaning can be found elsewhere.[66] From the resulting fits, the charge transport resistances R_{cc}, (c.c. being the respective charge carrier—"el" for electronic and "ion" for ionic transport) were obtained, and the respective effective partial conductivities $\sigma_{cc,eff}$ calculated according to Eq. 2:

$$\sigma_{cc,eff} = \frac{l}{R_{cc} \cdot A} \qquad [2]$$

with the electrode thickness l and the cell area A. In the case of the electron blocking cell setup, the obtained resistance corresponds to the sum of both electrode layers, and for the determination of the partial conductivity, the resistance was divided by a factor of two.

Figures 2a and 2b show representative impedance plots of the electrodes together with the corresponding cell setups. In the spectrum of the ion blocking setup (Fig. 2a, a large semicircle is

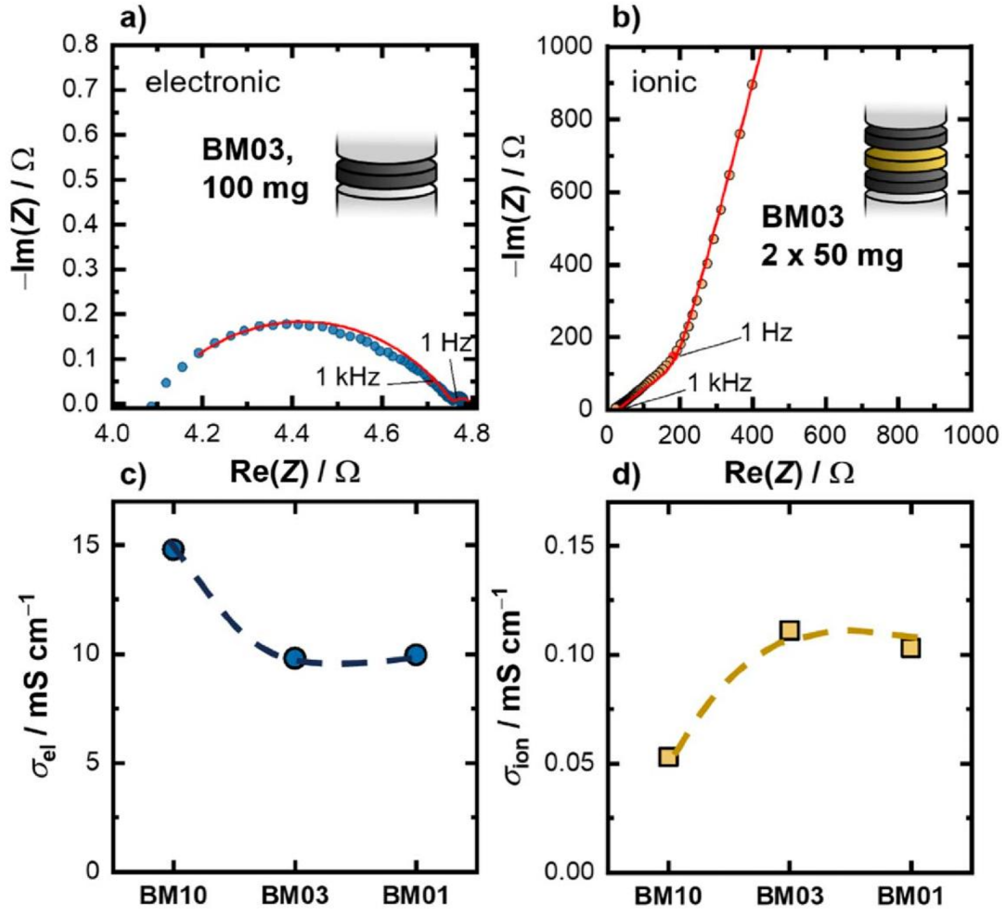

Figure 2. Evaluation of partial effective conductivities of composite cathodes containing 70 wt-% CAM and 30 wt-% ISE from impedance spectra using selectively blocking cell configurations. (a) Ion blocking cells (steel|cathode|steel) and respective impedance spectrum with fit (red line), and (b) full-blocking cell (steel|cathode|ISE|cathode|steel) and respective impedance spectrum with fit (red line). Effective conductivities of (c) electronic and (d) ionic charge carriers display an influence of the charge transport on the particle size of the solid electrolyte. While the effective electronic conductivity decreases with smaller ISE particles, the effective ionic conductivity increases, showing a more homogeneous distribution of both phases. Dashed lines are guides to the eye. Based on the uncertainty of the thickness determination, the influence of the applied pressure and the fit, we estimate the uncertainty of the data to be approx. 20%.

visible at high frequencies and a small semicircle is visible at low frequencies. At very low frequencies a purely resistive impedance can be observed. This shape is characteristic for T-type TLMs, in which two transport processes occur in parallel and in which one charge carrier is not blocked and can transfer across the current collector-sample interfaces. In contrast, the spectrum of the full blocking setup displays a 45° slope at high frequencies, which transitions into a much higher phase angle below 1 Hz. Such a shape is characteristic for a Z-Type TLM, in which interfaces are capacitive at low frequencies, which is the case for fully lithiated NCM.[27,66] In both cases, the employed models accurately fit the spectra with low residuals.

While $\sigma_{\mathrm{el,eff}}$ evidently decreases from 15 mS cm^{-1} for the BM10 sample to around 10 mS cm^{-1} for the BM03 and BM01 sample, $\sigma_{\mathrm{ion,eff}}$ increases by almost a factor of two, from 0.05 mS cm^{-1} to 0.11 mS cm^{-1} when using 3 mm instead of 10 mm milling media. This indicates improved ionic transport through the cathode and likely results from more and shorter ionic transport pathways and, thus, better percolation. The loss of $\sigma_{\mathrm{el,eff}}$ may be explained by reduced clustering of active material particles and therefore a better overall distribution, as discussed by Iwamoto et al.[48] CAM particle clusters serve as electronic "highways" with low R_{el}, but they do not necessarily lead to lower overall cell resistance in full cells since particles inside the cluster have low contact areas to the ISE phase, which hinders charge transfer and blocks ionic transport on a micrometer scale, which is evident from the measured $\sigma_{\mathrm{ion,eff}}$ values. Similar phenomenological observations were already made by several groups for other thiophosphate-based ISEs. As there is yet no quantitative model for these effects, this needs further investigation.[42,48]

ISE particle size determines cathode homogeneity and porosity.—As we intend to evaluate how particle clusters and the microstructure influences the kinetics of composite electrodes, we employed Xe-plasma FIB-SEM (PFIB-SEM) to measure the three-dimensional microstructure of the three composite cathodes to a cubic voxel size of 100 nm. The images obtained from PFIB-SEM tomography were segmented into CAM, ISE and pore phases, based on gray scale values of both secondary electron (SE) and back-scattered electron (BSE) images (Fig. 3). Subsequently, the collected images were transformed to three-dimensional reconstructions, which were used to carry out digital microstructural analyses.

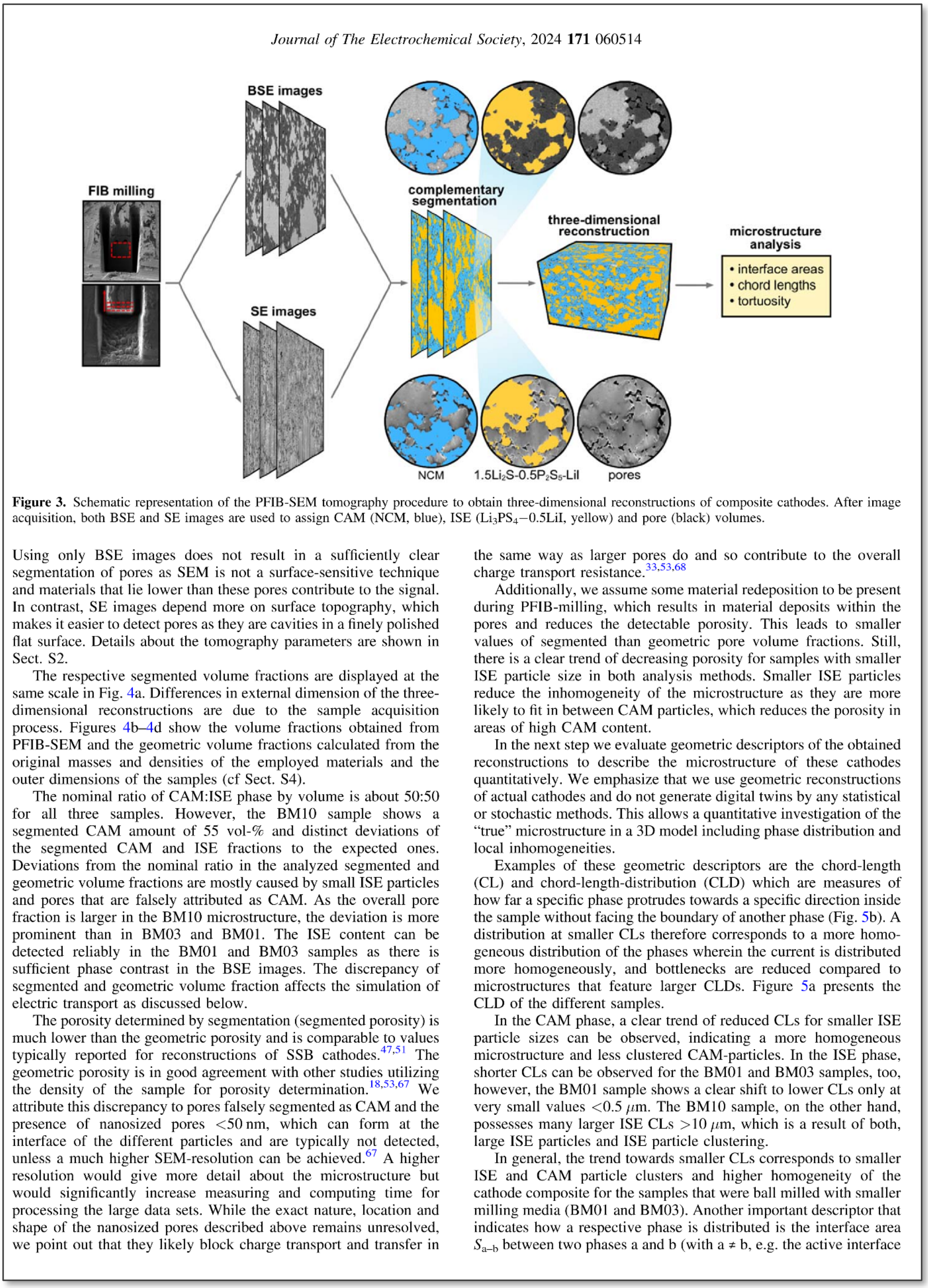

Figure 3. Schematic representation of the PFIB-SEM tomography procedure to obtain three-dimensional reconstructions of composite cathodes. After image acquisition, both BSE and SE images are used to assign CAM (NCM, blue), ISE ($Li_3PS_4-0.5LiI$, yellow) and pore (black) volumes.

Using only BSE images does not result in a sufficiently clear segmentation of pores as SEM is not a surface-sensitive technique and materials that lie lower than these pores contribute to the signal. In contrast, SE images depend more on surface topography, which makes it easier to detect pores as they are cavities in a finely polished flat surface. Details about the tomography parameters are shown in Sect. S2.

The respective segmented volume fractions are displayed at the same scale in Fig. 4a. Differences in external dimension of the three-dimensional reconstructions are due to the sample acquisition process. Figures 4b–4d show the volume fractions obtained from PFIB-SEM and the geometric volume fractions calculated from the original masses and densities of the employed materials and the outer dimensions of the samples (cf Sect. S4).

The nominal ratio of CAM:ISE phase by volume is about 50:50 for all three samples. However, the BM10 sample shows a segmented CAM amount of 55 vol-% and distinct deviations of the segmented CAM and ISE fractions to the expected ones. Deviations from the nominal ratio in the analyzed segmented and geometric volume fractions are mostly caused by small ISE particles and pores that are falsely attributed as CAM. As the overall pore fraction is larger in the BM10 microstructure, the deviation is more prominent than in BM03 and BM01. The ISE content can be detected reliably in the BM01 and BM03 samples as there is sufficient phase contrast in the BSE images. The discrepancy of segmented and geometric volume fraction affects the simulation of electric transport as discussed below.

The porosity determined by segmentation (segmented porosity) is much lower than the geometric porosity and is comparable to values typically reported for reconstructions of SSB cathodes.[47,51] The geometric porosity is in good agreement with other studies utilizing the density of the sample for porosity determination.[18,53,67] We attribute this discrepancy to pores falsely segmented as CAM and the presence of nanosized pores <50 nm, which can form at the interface of the different particles and are typically not detected, unless a much higher SEM-resolution can be achieved.[67] A higher resolution would give more detail about the microstructure but would significantly increase measuring and computing time for processing the large data sets. While the exact nature, location and shape of the nanosized pores described above remains unresolved, we point out that they likely block charge transport and transfer in the same way as larger pores do and so contribute to the overall charge transport resistance.[33,53,68]

Additionally, we assume some material redeposition to be present during PFIB-milling, which results in material deposits within the pores and reduces the detectable porosity. This leads to smaller values of segmented than geometric pore volume fractions. Still, there is a clear trend of decreasing porosity for samples with smaller ISE particle size in both analysis methods. Smaller ISE particles reduce the inhomogeneity of the microstructure as they are more likely to fit in between CAM particles, which reduces the porosity in areas of high CAM content.

In the next step we evaluate geometric descriptors of the obtained reconstructions to describe the microstructure of these cathodes quantitatively. We emphasize that we use geometric reconstructions of actual cathodes and do not generate digital twins by any statistical or stochastic methods. This allows a quantitative investigation of the "true" microstructure in a 3D model including phase distribution and local inhomogeneities.

Examples of these geometric descriptors are the chord-length (CL) and chord-length-distribution (CLD) which are measures of how far a specific phase protrudes towards a specific direction inside the sample without facing the boundary of another phase (Fig. 5b). A distribution at smaller CLs therefore corresponds to a more homogeneous distribution of the phases wherein the current is distributed more homogeneously, and bottlenecks are reduced compared to microstructures that feature larger CLDs. Figure 5a presents the CLD of the different samples.

In the CAM phase, a clear trend of reduced CLs for smaller ISE particle sizes can be observed, indicating a more homogeneous microstructure and less clustered CAM-particles. In the ISE phase, shorter CLs can be observed for the BM01 and BM03 samples, too, however, the BM01 sample shows a clear shift to lower CLs only at very small values $<0.5\ \mu m$. The BM10 sample, on the other hand, possesses many larger ISE CLs $>10\ \mu m$, which is a result of both, large ISE particles and ISE particle clustering.

In general, the trend towards smaller CLs corresponds to smaller ISE and CAM particle clusters and higher homogeneity of the cathode composite for the samples that were ball milled with smaller milling media (BM01 and BM03). Another important descriptor that indicates how a respective phase is distributed is the interface area S_{a-b} between two phases a and b (with a ≠ b, e.g. the active interface

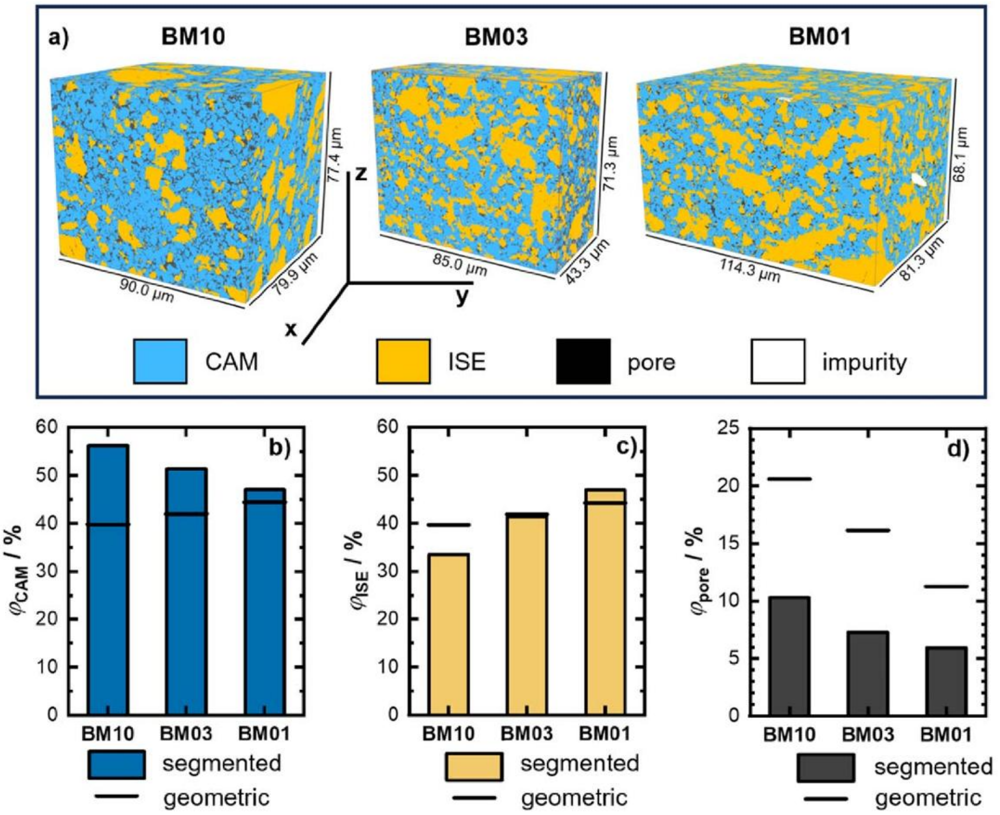

Figure 4. Segmented 3D reconstructions of cathode composites containing solid electrolyte that was treated with differently sized milling media. (a) Abbreviations indicating the employed milling media diameter: BM10 = 10 mm, BM03 = 3 mm, BM01 = 1 mm). All reconstructed volumes feature a voxel size of 100 nm. The reconstructed volume is segmented, and the corresponding volume fractions are determined for (b) CAM (NCM), (c) ISE ($Li_3PS_4-0.5LiI$) and (d) pores. Black horizontal bars indicate the expected values calculated with the employed masses, the material density, and the porosity determined from geometric dimensions of the sample.

between CAM and ISE, $S_{CAM\text{-}ISE}$). If particles of the same phase form clusters, only part of the surface area of the particles is available for interfaces with other phases and $S_{a\text{-}b}$ is reduced. The interface area between CAM and ISE is of particular importance for the cell performance, as this is where the transfer of lithium ions takes place. To allow for a low charge transfer impedance, a high interface area is required.

Figure 5c shows, that, compared to BM10, the BM03 and BM01 samples exhibit a larger contact area between CAM and ISE. Thus, less pores are in contact with the CAM and $S_{CAM\text{-}pore}$ is decreasing from 0.34 m^2 g^{-1} for BM10 to 0.16 m^2 g^{-1} for BM01, while simultaneously, $S_{CAM\text{-}ISE}$ increases from 0.11 to 0.24 m^2 g^{-1}. This observation can be explained by smaller CAM clusters. Voids between individual CAM particles can be filled by the smaller sized ISE during fabrication[48] as already observed in the measured total porosity. This penetration of pore space between CAM particles goes hand in hand with shorter diffusion lengths for lithium ions and better kinetics.[68] Assuming a specific surface area of 0.5 m^2g^{-1} for the CAM (as given by the supplier), this implies that the coverage of CAM particles by ISE increases from around 20% for BM10 to almost 50% for BM03 and BM01. However, half of the CAM surface area is still covered by pores (31%) and other CAM particles (19%). The high accumulation of pores at the interface can significantly affect the performance of the cathode as current constriction phenomena and high interfacial resistances will increase the overall cell resistance.[68] We point out, that the overall porosity of the sample is smaller for BM03 and BM01 than for BM10, which is in line with the results described above as ISE particles of reduced size can fill smaller void spaces.

Interestingly, $S_{ISE\text{-}pore}$ increases upon ISE particle size reduction from 0.05 to 0.09 m^2g^{-1} as well, which we assume to be caused by more point-to-point contacts between the respective ISE particles. The fact that the $S_{ISE\text{-}pore}$ values are in general much smaller than the $S_{CAM\text{-}pore}$ values can be explained by the mechanical properties of the employed materials.[50] The rigid CAM particles[69] tend not to deform significantly during densification, hence, any porosity between CAM particles cannot be closed, while the much more malleable ISE[70,71] allows for the removal of pores between individual ISE particles.

We conclude that a homogeneous distribution of the different phases, supported by small ISE particles, is crucial for homogeneous composite cathodes with high $S_{CAM\text{-}ISE}$ and low residual porosity. Sophisticated processing and careful selection of materials with matching properties are very important to produce cathodes that can deliver fast kinetics, as we present and discuss in the following chapter.

Charge transport is determined by microstructure.— Complementary to geometric descriptors, we carried out charge transport simulations to correlate microstructure and transport kinetics. The tortuosity factors κ_a of a respective phase a can be determined by comparison of the effective conductivities $\sigma_{a,eff}$ to the

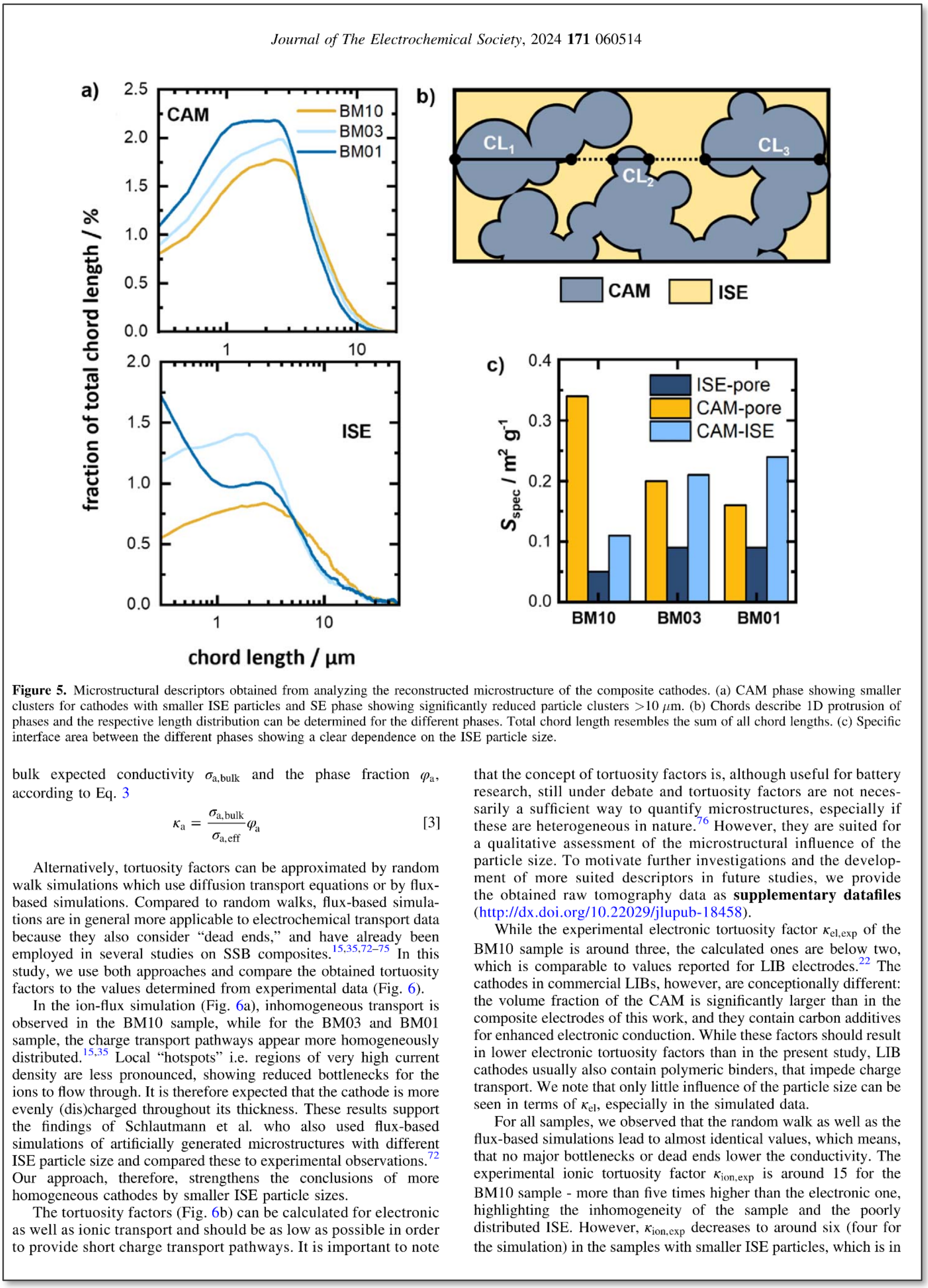

Journal of The Electrochemical Society, 2024 **171** 060514

Figure 5. Microstructural descriptors obtained from analyzing the reconstructed microstructure of the composite cathodes. (a) CAM phase showing smaller clusters for cathodes with smaller ISE particles and SE phase showing significantly reduced particle clusters >10 μm. (b) Chords describe 1D protrusion of phases and the respective length distribution can be determined for the different phases. Total chord length resembles the sum of all chord lengths. (c) Specific interface area between the different phases showing a clear dependence on the ISE particle size.

bulk expected conductivity $\sigma_{\mathrm{a,bulk}}$ and the phase fraction φ_{a}, according to Eq. 3

$$\kappa_{\mathrm{a}} = \frac{\sigma_{\mathrm{a,bulk}}}{\sigma_{\mathrm{a,eff}}}\varphi_{\mathrm{a}} \qquad [3]$$

Alternatively, tortuosity factors can be approximated by random walk simulations which use diffusion transport equations or by flux-based simulations. Compared to random walks, flux-based simulations are in general more applicable to electrochemical transport data because they also consider "dead ends," and have already been employed in several studies on SSB composites.[15,35,72–75] In this study, we use both approaches and compare the obtained tortuosity factors to the values determined from experimental data (Fig. 6).

In the ion-flux simulation (Fig. 6a), inhomogeneous transport is observed in the BM10 sample, while for the BM03 and BM01 sample, the charge transport pathways appear more homogeneously distributed.[15,35] Local "hotspots" i.e. regions of very high current density are less pronounced, showing reduced bottlenecks for the ions to flow through. It is therefore expected that the cathode is more evenly (dis)charged throughout its thickness. These results support the findings of Schlautmann et al. who also used flux-based simulations of artificially generated microstructures with different ISE particle size and compared these to experimental observations.[72] Our approach, therefore, strengthens the conclusions of more homogeneous cathodes by smaller ISE particle sizes.

The tortuosity factors (Fig. 6b) can be calculated for electronic as well as ionic transport and should be as low as possible in order to provide short charge transport pathways. It is important to note that the concept of tortuosity factors is, although useful for battery research, still under debate and tortuosity factors are not necessarily a sufficient way to quantify microstructures, especially if these are heterogeneous in nature.[76] However, they are suited for a qualitative assessment of the microstructural influence of the particle size. To motivate further investigations and the development of more suited descriptors in future studies, we provide the obtained raw tomography data as **supplementary datafiles** (http://dx.doi.org/10.22029/jlupub-18458).

While the experimental electronic tortuosity factor $\kappa_{\mathrm{el,exp}}$ of the BM10 sample is around three, the calculated ones are below two, which is comparable to values reported for LIB electrodes.[22] The cathodes in commercial LIBs, however, are conceptionally different: the volume fraction of the CAM is significantly larger than in the composite electrodes of this work, and they contain carbon additives for enhanced electronic conduction. While these factors should result in lower electronic tortuosity factors than in the present study, LIB cathodes usually also contain polymeric binders, that impede charge transport. We note that only little influence of the particle size can be seen in terms of κ_{el}, especially in the simulated data.

For all samples, we observed that the random walk as well as the flux-based simulations lead to almost identical values, which means, that no major bottlenecks or dead ends lower the conductivity. The experimental ionic tortuosity factor $\kappa_{\mathrm{ion,exp}}$ is around 15 for the BM10 sample - more than five times higher than the electronic one, highlighting the inhomogeneity of the sample and the poorly distributed ISE. However, $\kappa_{\mathrm{ion,exp}}$ decreases to around six (four for the simulation) in the samples with smaller ISE particles, which is in

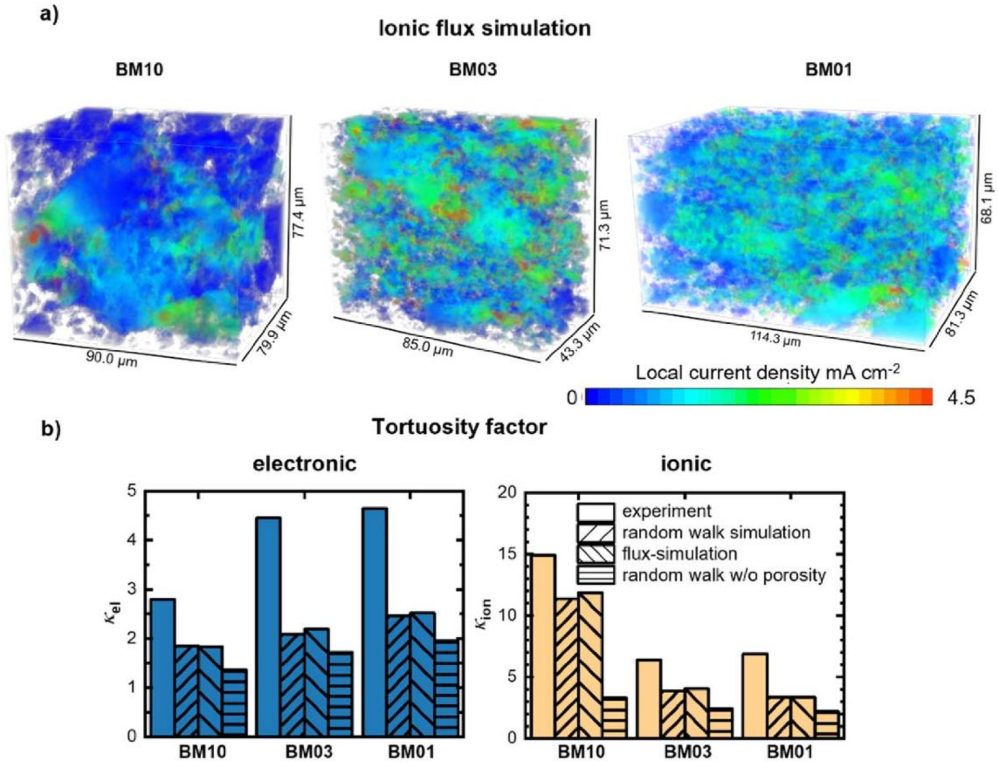

Figure 6. Simulation results of ionic-flux and comparison of experimentally determined and simulated tortuosities. (a) Ionic flux-distributions simulated for the three microstructure reconstructions with different ISE particle size. (b) Tortuosity factors of electronic and ionic transport determined from impedance spectra and from charge transport simulations on the reconstructed microstructures. A significant improvement of the ionic transport is visible for smaller ISE particles. Large differences between experimental and simulated charge transport indicate an influence of segmented porosity and particle-particle contact resistances.

line with the observation of a better distribution of ISE particles and a correspondingly homogenized microstructure. Note that the simulated tortuosity factors are, in general, very similar for all three dimensions in all reconstructions, except for κ_{ion} in the BM10 sample, which is significantly increased along the x-axis (cf Fig. S6). We attribute this observation to the presence of large CAM clusters, which effectively block the ionic transport along this direction.

In general, κ_{el} are lower than corresponding κ_{ion}. The experimentally obtained values are much higher than the calculated ones for both charge carriers. We assume that this discrepancy of experimental and simulated values is due to several reasons:

I. Contact resistances between the current collectors and the electrodes, and grain boundaries lower the determined conductivity[77] but cannot be resolved in our microstructure reconstructions.
II. Nanopores, that influence particle-particle contacts reduce the effective conductivity by current constriction but are not resolved in the SEM images and the resulting segmentation.[67]
III. Current constriction phenomena, that influence the total current distribution and disrupt the homogeneity of the electric field, leading to overpotentials are not considered. Additionally, high local current densities can result in high local temperatures and especially in case of narrow bottlenecks in a stronger degradation between ISE and CAM.

While these individual effects, or a superposition of them, can play a role for ionic transport, electronic transport or both, the general trend of improved ionic transport at reduced ISE particle sizes is reflected by both simulation and experiment. The increase in the electronic tortuosity with decreasing ISE particle size can be explained by the fact that these small ISE particles, can effectively break up CAM clusters, which slightly decreases effective electronic conductivity while simultaneously improving ionic conductivity. This observation is well in line with previous reports.[18,48]

As discussed above, porosity is an important factor impeding charge transport and transfer. Its influence was tested using random walk simulations in which transport properties of either the ISE or the CAM phase were attributed to the segmented porosity given. That allowed us to investigate the tortuosity factors that are theoretically attainable in a completely densified sample. Results are displayed in Fig. S7. Clearly, the "filling" of porosity has a significant effect on the ionic charge transport, while the effect on electronic transport is rather small. This observation is a strong indication for pores being predominantly present in CAM clusters, therefore preventing ionic transport in these areas. There is, however, no significant influence of the ISE particle size on the "pore-less" tortuosity factor, showing, that the porosity is the main inhibitor of the charge transport, and that the main contribution of the ISE particle size is on the homogeneity and reduction of porosity in SSB cathodes. Additionally, the results show, that with proper processing techniques that allow for full densification, i.e. warm isostatic pressing, tortuosity factors comparable to the ones of LIBs could be achieved, which is in line with recent experimental findings by Koenig et al.[39]

Overall, our observations demonstrate that the residual porosity is particularly harmful for the ionic transport, which is already a limiting factor, and we assume that pores would be even more severe in cathodes with higher CAM contents. Ultimately, charge transport must be tailored by particle size and strategies to reduce porosity and increase the effective ionic conductivity.

Homogeneous microstructures are necessary to improve cell performance.—SSB cells with cathodes featuring the three different ISE samples were investigated with In/(InLi)$_x$ alloy and Li_6PS_5Cl as anode and separator material, respectively. Galvanostatic cycling was performed within the voltage range of 2.62–4.32 V vs Li^+/Li for different C-rates to evaluate the kinetic influence of the microstructure of the cathode. It is important to mention that similar mass loadings and identical masses for the separators and anodes were used. The discharge capacities of the galvanostatic cycling are presented in Fig. 7a.

We find that the BM10 sample, which features large sized SE particles, performs much worse than the other two samples at low as well as at high C-rates: the sample achieves capacities of 92 mAh g^{-1} at 0.1 C, compared to 152 and 156 mAh g^{-1} for the BM01 and BM03 cells, respectively. This correlates well to findings by Shi et al.[34] and Schlautmann et al.[72] and is clearly showing the detrimental influence of the large SE particles on the microstructure. Similar information can be drawn from the *dQ*/*dV* plot (Fig. 7b), where the characteristic peaks of the CAM material are less explicit for BM10 compared to BM03 and BM01 curves. For the H2/H3 phase transition, this is a result of slower kinetics, caused by overall longer transport pathways. Additionally, the delayed onset of the "kinetic hindrance" peak is an indication for overall increased overpotentials, which can be correlated to the ionic tortuosity and the lower values in $S_{\text{CAM-ISE}}$. With increasing C-rates, the capacity drops further, which can be attributed to higher overpotentials, as shown in Figs. 7c and 7d. At 1 C, we find that for BM10 only 25% of the initial low C-rate capacity are retained, compared to 28% and 32% for BM01 and BM03, respectively. While this shows severe kinetic issues in the composite cathode, the sum of the results demonstrates the positive influence that homogeneous conduction pathways can have on the cell kinetics. At low C-rates, the influence of kinetics on the measured cell voltage is reduced and the total mass of electrochemically connected material, i.e. the material having access to percolating electronic and ionic charge transport pathways, determines the achievable capacity. In contrast, at high C-rates kinetics have a larger impact and the length of these pathways and, thus, the overpotential caused by their resistance dominates the capacity.[18] The low C-rate performance can be used as an identifier of significant inhomogeneities of the microstructure, while the high C-rate performance is an indication of the tortuosity of charge transport pathways and low interfacial contact between CAM and ISE.

Please note, that additional processes contribute to the full cell kinetics, i.e. the anode kinetics, charge transfer resistance at the interface between CAM and ISE, which depends on $S_{\text{CAM-ISE}}$ and the exchange current density. This is an additional process contributing to the poor performance of cells with large ISE particles.[68]

Interestingly, the 1st cycle *Coulomb* efficiency at 0.1 C (Fig. S8) is much higher for the BM03 and BM01 samples (η = 73% and 68%) compared to the BM10 sample (η = 58%) even though the higher interface area of the former samples results in more severe

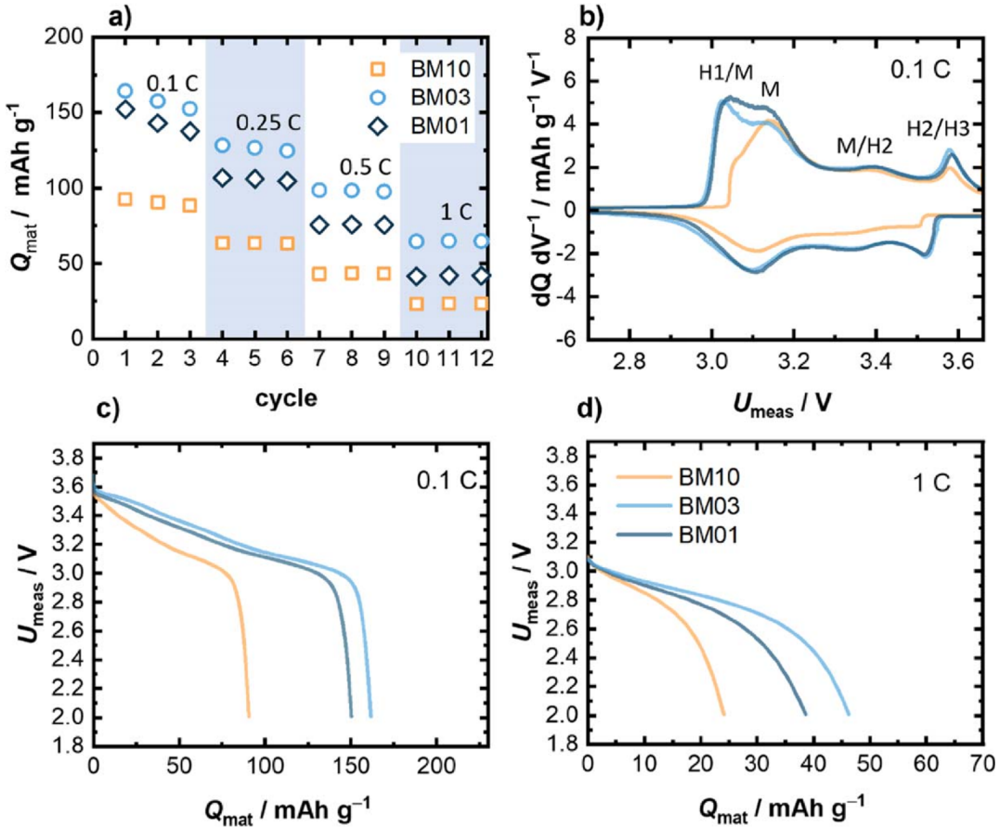

Figure 7. Electrochemical cycling performance of the analyzed cathodes in full cell configuration. Full cells were constructed using In|InLi anodes and a mass loading of 10.7 mg cm^{-2}. (a) Discharge C-rate capability, (b) differential capacity at 0.1 C and discharge curves of cells at (c) 0.1 C and (d) 1 C. Large ISE particles result in reduced capacity due to slower kinetics and higher overpotentials as well as particle clusters that reduce the charge transfer capabilities.

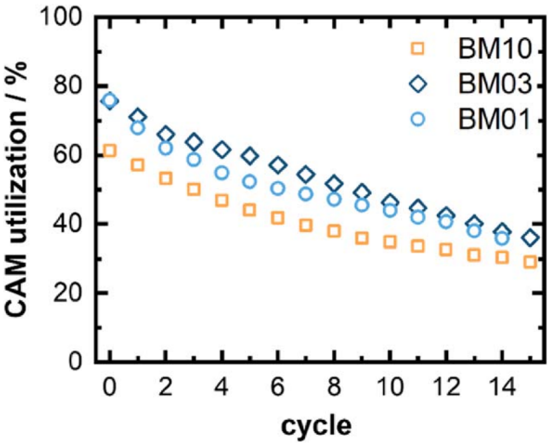

Figure 8. CAM utilization as a function of cycle number. Utilization was calculated by determining the active mass of the CAM phase. A much lower level of CAM utilization is observed for cathodes with large ISE particles showing the extent to which CAM clusters affect the electrochemical performance.

degradation. We attribute low *Coulomb* efficiency determined for all samples to interfacial degradation and chemo-mechanical losses within the first cycle.[78] These result from contact loss at the CAM-ISE interface[51,79] due to expansion and contraction of CAM particles during (dis-)charge, which are more severe in case of the BM10 sample as there are already smaller $S_{\text{CAM-ISE}}$ values.

Overall, the data obtained from the electrochemical performance is consistent with the information obtained from the segmentation, i.e. $S_{\text{CAM-ISE}}$, as well as with the simulated and measured tortuosity factors of the cathodes. Our results are, therefore, a clear indication that small SE particle sizes improve the cell performance, as they enable more homogeneous microstructures with favorable transport properties. Observations of improved cell performance for small ISE particles have also been made by Shi et al.,[34] Cronau et al.[44] and Schlautmann et al.[72] Comparing our results with the findings of both studies and using the proposed particle size ratio of CAM and ISE, i.e., $\lambda = d_{\text{CAM}}/d_{\text{ISE}}$, we find that BM10 with $\lambda = 0.7$ and BM03/BM01 with $\lambda = 1.0–1.2$ perform well within the predictions of this model. A low amount of electrochemically accessible material, which we denote as CAM utilization, in line with Bielefeld et al.[14] and Shi et al.,[34] is therefore the reason for the poor performance of the BM10 cells.

Smaller ISE particles lead to higher CAM utilization.—To further quantify the influence of the microstructure on loss of CAM utilization, we adapted the methodology of Ruess et al.[80] to determine the electrochemically active mass. This method utilizes a comparative measurement of the open circuit potential (OCP) in equilibrium as a function of lithium content and the relaxed OCP after (dis-)charge. Electrochemically inactive particles do not contribute to (dis-)charge processes and, respectively, not to the OCP of the cell. Details can be found in Fig. S9. The determined electrochemically active masses for 15 consecutive cycles allows to evaluate the chemo-mechanical degradation caused by the contact loss between CAM and ISE. The results are presented in Fig. 8.

Comparing the initial CAM utilization, we find that within the BM10 sample only 62% of the CAM mass is electrochemically active, which is an explanation for the low overall capacity that can be achieved. In contrast, the BM03 and BM01 samples exhibit significantly larger values of 77% CAM utilization. The visualization of the electronic conduction clusters of the reconstructed microstructures (cf Fig. S10) does not indicate a significant number of isolated CAM particles. Still, the experimentally determined utilization level indicates an increased clustering in BM10 resulting in a disconnection of CAM clusters from the ion percolating network. Consequently, a more pronounced CAM clustering due to larger ISE particles may lead to a reduced active mass. In contrast to the CAM network, however, the ISE network shows a clear increase for decreasing d_{ISE}, which may suggest a more important role of ionic percolation on the CAM utilization. These results are in line with Shi et al.[34] whose model showed a decrease of the percolating ISE network for increasing d_{ISE}, which led to a reduced fraction of CAM particles in direct contact with the ISE.

We assume the reduction of active mass is mainly caused by CAM particles close to the current collector without contact to the ionically percolating ISE network, as for these particles, ionic conduction paths are already much longer. These regions are included in the tomography data presented in this study. An additional aspect causing a reduced active mass in BM10 may be the smaller electrochemically active interface area as discussed above.

It is important to note that these conclusions are based on the reconstructed volume of pristine composites. Electrochemical cycling induces irreversible alterations of the microstructure, i.e. decomposition reactions[81] and chemo-mechanical volume changes of constituents can cause disconnections of CAM particles from the percolating network and an increase in porosity.[51] Significant capacity fading, particularly in the first cycle, was reported for thiophosphate-based ISE and was linked to a formation of high resistive interphases, which can lead to an insulation of CAM particles, as well as contact loss between CAM and ISE due to the contraction of CAM particles upon charging.[54,78]

Interestingly, during cycling all samples show a similar loss of active material and no clear trend can be observed regarding the influence of d_{ISE}. The decrease in CAM utilization can be explained by contact loss at the interface between CAM and ISE, effectively reducing the charge transfer sites. Additionally, mechanical fatigue mechanisms such as cracking within the single-crystalline CAM aggregates can lead to electronically isolated particles, that do not participate in the electrochemical cycling anymore. However, there seems to be no significant influence of d_{ISE} and we assume that the contact loss mentioned above takes place in CAM clusters, as well as in well distributed particles. A more detailed investigation of d_{ISE} on the role of chemo-mechanics, i.e., on the pressure evolution during cycling, however, is beyond the scope of this study and will be part of future investigations.

Shortcomings of this study and remaining challenges in cathode optimization.—Beyond the results discussed above, our study reveals the difficulties in reliably determining the porosity of composite cathodes for SSBs. First, the geometric porosity and the segmented porosity differ significantly, which affects the charge transport properties. Even with highly resolved PFIB-SEM images it is not always possible to detect pores by gray scale contrast. Since a detailed understanding of the microstructure can only be achieved if the resolution is higher than the smallest particle/pore size, it is essential to achieve a resolution in the range of 100 nm, as has been used in our study. This requires either synchrotron-based or electron beam-based techniques both of which are rather expensive and require a higher degree of automatization in order to obtain tomography data of large volumes of multiple samples.

Additional to the image acquisition, the processing of tomography data needs improvement. More sophisticated and more efficient image processing techniques are necessary. Considering the large amount of data (gigabytes of images that have to be segmented automatically) that need to be processed, machine learning algorithms could help to better segment images and to help understand the microstructure of composite cathodes.

Our study could not resolve the reason for the decreased (effective) conductivity of smaller ISE particle networks unequivocally, and a segmentation of particle contacts was not possible. In future work, these particle-particle interfaces need to be considered for charge transport and electrochemical simulations. This could be achieved either by a more sophisticated sample preparation, such as etching, or by artificially introducing these boundaries in a model based on the particle size distribution of the employed powders.[77] In any case, the grain boundary "design" of electrolytes with very high bulk conductivity appears to be necessary.

We showed that the residual porosity is still present in cold pressed composite cathodes and most likely responsible for the poor electrochemical performance of the composite cathodes. It is worth noting, that all electrochemical experiments were conducted under comparably high pressures, which is necessary to properly operate this type of SSBs. In contrast, image acquisition was performed under high vacuum conditions. We assume the pressure to have an influence on the microstructure, however the pressure will most likely result in decreased porosity, and contact resistance. Based on our results it is, therefore, even more necessary to densify SSB components and to optimize the charge transport of composite cathodes.

A careful selection of particle size distributions, mixing and densification techniques are crucial for reducing porosity to a minimum. Warm isostatic pressing is a promising option and has previously been used for full densification of well-performing cathodes.[8] Additionally, conductive additives, such as plastic polymer or liquid electrolytes could fill residual pores and contribute to the kinetics of the cathode, but these concepts have rarely been employed and need further investigation regarding practicability, also regarding the (chemical) stability of interfaces. These concepts of "hybridization" may be chemically difficult for sulfide-type SEs, as they tend to dissolve easily in polar solvents (and polymers),[82,83] thus causing the risk of severe chemical instability.

Besides porosity, carbon additives will influence the percolation and tortuosities. Since they are electronic conductors, a beneficial effect on the electronic tortuosity is expected, however as they are another non-ion conducting phase, they will most likely impede ionic charge transport and transfer. Their use should therefore be limited, especially if high CAM contents are used. Also, carbon additives are an additional source of SE degradation at high potentials, as first reported by Zhang et al.[84]

Conclusions

In this study, we analyze the three-dimensional microstructure of composite cathodes employing a sulfide-type ISE and a transition metal oxide-based CAM by FIB-SEM tomography and subsequent reconstruction. By varying the ISE particle size, we elucidate its direct influence on important microstructural descriptors and find correlations of these with the electrochemical data. A comparison of simulated and experimentally determined charge transport data shows that in microstructural modelling the effective conductivities are overestimated and tortuosities are underestimated. This is because the simulations rely on reconstructed microstructures that fail to reproduce the porosity values that are geometrically expected. The residual porosity plays a critical role in solid-state cathodes and additionally particle-particle contacts need to be considered. We further quantify the influence of the microstructure by analyzing the electrochemical performance of full cells. Based on our results, we conclude that small ISE particles are essential to obtain homogeneous cathodes, high interface area between CAM and ISE, low ionic tortuosity, and consequently, improved cycling and rate performance. The corresponding kinetic cell data highlight the necessity of optimizing the microstructure of cathodes for achieving solid-state batteries with high energy and power density. We hope that our results motivate further efforts in optimizing cathode microstructures by particle size adjustment, as well as investigations on the densification of cathodes by consolidation or the use of pore filling additives.

Acknowledgments

We acknowledge financial support within the FestBatt Cluster of Competence (BMBF, Bundesministerium für Bildung *u*nd Forschung) in the projects 03XP0177A, 03XP0430A, 03XP0346D, 03XP0428E, as well as the ProGral project (03XP0427). A.B. acknowledges financial support by the Hessian Ministry of Higher Education, Research, and the Arts (HMWK).

Author Contributions

Conceptualization, P.M. and J.S., Methodology, P.M., J.S., Formal Analysis, P.M., J.S., S.K., A.B., Investigation, P.M., J.S Re.R., Resources, S.B., J.J., Writing—Original Draft, P.M., J.S., Writing—Review & Editing, P.M., J.S., A.B., F.H.R., J.J., Funding Acquisition, S.B., J.J, Supervision, S.B., Ra.R., A.B., J.J., P.M. and J.S. contributed equally to this work.

Declaration of Interests

The authors declare no competing interests.

ORCID

Philip Minnmann https://orcid.org/0000-0002-9646-0487
Johannes Schubert https://orcid.org/0009-0003-3148-6672
Sascha Kremer https://orcid.org/0009-0009-3739-8749
Anja Bielefeld https://orcid.org/0000-0003-2193-8375
Jürgen Janek https://orcid.org/0000-0002-9221-4756

References

1. J. Janek and W. G. Zeier, "A solid future for battery development." *Nat. Energy*, **1**, 1167 (2016).
2. M. Weiss et al., "Fast charging of lithium-ion batteries: a review of materials aspects." *Adv. Energy Mater.*, **11**, 2101126 (2021).
3. J. Janek and W. G. Zeier, "Challenges in speeding up solid-state battery development." *Nat. Energy*, **8**, 230 (2023).
4. T. Famprikis, P. Canepa, J. A. Dawson, M. S. Islam, and C. Masquelier, "Fundamentals of inorganic solid-state electrolytes for batteries." *Nat. Mater.*, 1278 (2019).
5. Y. Kato, S. Hori, T. Saito, K. Suzuki, M. Hirayama, A. Mitsui, M. Yonemura, H. Iba, and R. Kanno, "High-power all-solid-state batteries using sulfide superionic conductors." *Nat. Energy*, **1**, 652 (2016).
6. N. Kamaya et al., "A lithium superionic conductor." *Nat. Mater.*, **10**, 682 (2011).
7. S. Randau et al., "Benchmarking the performance of all-solid-state lithium batteries." *Nat. Energy*, **5**, 259 (2020).
8. Y.-G. Lee et al., "High-energy long-cycling all-solid-state lithium metal batteries enabled by silver–carbon composite anodes." *Nat. Energy*, **5**, 299 (2020).
9. J. Doux, H. Nguyen, D. H.-S. Tan, A. Banerjee, X. Wang, E. A. Wu, C. Jo, H. Yang, and Y. S. Meng, "Stack pressure considerations for room–temperature all–solid–state lithium metal batteries." *Adv. Energy Mater.*, **10**, 1903253 (2020).
10. D. H.-S. Tan et al., "Carbon-free high-loading silicon anodes enabled by sulfide solid electrolytes." *Science*, **373**, 1494 (2021).
11. X. Yang, K. Doyle-Davis, X. Gao, and X. Sun, "Recent progress and perspectives on designing high-performance thick electrodes for all-solid-state lithium batteries." *eTransportation*, **11**, 100152 (2022).
12. G. Deysher, P. Ridley, S.-Y. Ham, J.-M. Doux, Y.-T. Chen, E. A. Wu, D. H.-S. Tan, A. Cronk, J. Jang, and Y. S. Meng, "Transport and mechanical aspects of all-solid-state lithium batteries." *Mater. Today Phys.*, **24**, 100679 (2022).
13. P. Minnmann et al., "Designing cathodes and cathode active materials for solid-state batteries." *Adv. Energy Mater.*, **12**, 2201425 (2022).
14. A. Bielefeld, D. A. Weber, and J. Janek, "Microstructural modeling of composite cathodes for all-solid-state batteries." *J. Phys. Chem. C*, **123**, 1626 (2019).
15. A. Bielefeld, D. A. Weber, and J. Janek, "Modeling effective ionic conductivity and binder influence in composite cathodes for all-solid-state batteries." *ACS Appl. Mater. Interfaces*, **12**, 12821 (2020).
16. A. Sakuda, T. Takeuchi, and H. Kobayashi, "Electrode morphology in all-solid-state lithium secondary batteries consisting of $LiNi_{1/3}Co_{1/3}Mn_{1/3}O_2$ and Li_2S-P_2S_5 solid electrolytes." *Solid-state Ion.*, **285**, 112 (2016).
17. A. Sakuda, "Favorable composite electrodes for all-solid-state batteries." *J. Ceram. Soc. Jpn.*, **126**, 675 (2018).
18. P. Minnmann, L. Quillman, S. Burkhardt, F. H. Richter, and J. Janek, "Editors' choice—quantifying the impact of charge transport bottlenecks in composite cathodes of all-solid-state batteries." *J. Electrochem. Soc.*, **168**, 040537 (2021).
19. F. L.-E. Usseglio-Viretta et al., "Resolving the discrepancy in tortuosity factor estimation for li-ion battery electrodes through micro-macro modeling and experiment." *J. Electrochem. Soc.*, **165**, A3403 (2018).
20. T.-T. Nguyen, A. Demortière, B. Fleutot, B. Delobel, C. Delacourt, and S. J. Cooper, "The electrode tortuosity factor: why the conventional tortuosity factor is not well suited for quantifying transport in porous li-ion battery electrodes and what to use instead." *NPJ Comput. Mater.*, **6**, 123 (2020).
21. J. Landesfeind, M. Ebner, A. Eldiven, V. Wood, and H. A. Gasteiger, "Tortuosity of battery electrodes: validation of impedance-derived values and critical comparison with 3D tomography." *J. Electrochem. Soc.*, **165**, A469 (2018).

22. J. Landesfeind, J. Hattendorff, A. Ehrl, W. A. Wall, and H. A. Gasteiger, "Tortuosity determination of battery electrodes and separators by impedance spectroscopy." *J. Electrochem. Soc.*, **163**, A1373 (2016).
23. M. Yamamoto, M. Takahashi, Y. Terauchi, A. Sakuda, Y. Kobayashi, S. Ikeda, and A. Sakuda, "Fabrication of composite positive electrode sheet with high active material content and effect of fabrication pressure for all-solid-state battery." *J. Ceram. Soc. Jpn.*, **125**, 391 (2017).
24. K. G. Naik, B. S. Vishnugopi, and P. P. Mukherjee, "Kinetics or transport: whither goes the solid-state battery cathode?" *ACS Appl. Mater. Interfaces*, **14**, 29754 (2022).
25. T. Asano, S. Yubuchi, A. Sakuda, A. Hayashi, and M. Tatsumisago, "Electronic and ionic conductivities of LiNi1/3Mn1/3Co 1/3O2 -Li3PS4 positive composite electrodes for all-solid-state lithium batteries." *J. Electrochem. Soc.*, **164**, A3960 (2017).
26. S. Randau et al., "On the additive microstructure in composite cathodes and alumina-coated carbon microwires for improved all-solid-state batteries." *Chem. Mater.*, **33**, 1380 (2021).
27. N. Kaiser, S. Spannenberger, M. Schmitt, M. Cronau, Y. Kato, and B. Roling, "Ion transport limitations in all-solid-state lithium battery electrodes containing a sulfide-based electrolyte." *J. Power Sources*, **396**, 175 (2018).
28. Z. Siroma, T. Sato, T. Takeuchi, R. Nagai, A. Ota, and T. Ioroi, "AC impedance analysis of ionic and electronic conductivities in electrode mixture layers for an all-solid-state lithium-ion battery." *J. Power Sources*, **316**, 215 (2016).
29. T. A. Hendriks, M. A. Lange, E. M. Kiens, C. Baeumer, and W. G. Zeier, "Balancing partial ionic and electronic transport for optimized cathode utilization of high-voltage LiMn$_2$O$_4$ /Li$_3$InCl$_6$ solid-state batteries." *Batter. Supercaps*, **6**, e202200544 (2023).
30. D. Shin, J. S. Nam, C. T. Linh Nguyen, Y. Jo, K. Lee, S. M. Hwang, and Y.-J. Kim, "Design of densified nickel-rich layered composite cathode *via* the dry-film process for sulfide-based solid-state batteries." *J. Mater. Chem. A*, **10**, 23222 (2022).
31. M. So, G. Inoue, R. Hirate, K. Nunoshita, S. Ishikawa, and Y. Tsuge, "Effect of mold pressure on compaction and ion conductivity of all-solid-state batteries revealed by the discrete element method." *J. Power Sources*, **508**, 230344 (2021).
32. M. Yamamoto, Y. Terauchi, A. Sakuda, A. Kato, and M. Takahashi, "Effects of volume variations under different compressive pressures on the performance and microstructure of all-solid-state batteries." *J. Power Sources*, **473**, 228595 (2020).
33. M. B. Dixit, A. Parejiya, N. Muralidharan, R. Essehli, R. Amin, and I. Belharouak, "Understanding implications of cathode architecture on energy density of solid-state batteries." *Energy Storage Mater.*, **40**, 239 (2021).
34. T. Shi, Q. Tu, Y. Tian, Y. Xiao, L. J. Miara, O. Kononova, and G. Ceder, "High active material loading in all–solid–state battery electrode via particle size optimization." *Adv. Energy Mater.*, **2**, 1902881 (2019).
35. J. Park, K. T. Kim, D. Y. Oh, D. Jin, D. Kim, Y. S. Jung, and Y. M. Lee, "Digital twin–driven all–solid–state battery: unraveling the physical and electrochemical behaviors." *Adv. Energy Mater.*, **10**, 2001563 (2020).
36. F. Strauss, T. Bartsch, L. de Biasi, A.-Y. Kim, J. Janek, P. Hartmann, and T. Brezesinski, "Impact of cathode material particle size on the capacity of bulk-type all-solid-state batteries." *ACS Energy Lett.*, **3**, 992 (2018).
37. C. Park, S. Lee, K. Kim, M. Kim, S. Choi, and D. Shin, "Electrochemical properties of composite cathode using bimodal sized electrolyte for all-solid-state batteries." *J. Electrochem. Soc.*, **166**, A5318 (2019).
38. Y. Yamada, K. Watanabe, H. Kim, K. Suzuki, S. Hori, R. Kanno, and M. Hirayama, "Microstructure control of LiCoO$_2$-Li$_{10}$GeP$_2$S$_{12}$ composite cathodes by adjusting the particle size distribution for the enhancement of all-solid-state batteries." *Batter. Supercaps*, **6**, e202300261 (2023).
39. C. König, V. Miß, L. Janin, and B. Roling, "Mitigating the ion transport tortuosity in composite cathodes of all-solid-state batteries by wet milling of the solid electrolyte particles." *ACS Appl. Energy Mater.*, **6**, acsaem.3c01242 (2023).
40. J. Kim, M. Eom, S. Noh, and D. Shin, "Effect of mixing method on the properties of composite cathodes for all-solid-state lithium batteries using Li2S–P2S5 solid electrolytes." *J. Power Sources*, **244**, 476 (2013).
41. S. Noh, W. T. Nichols, M. Cho, and D. Shin, "Importance of mixing protocol for enhanced performance of composite cathodes in all-solid-state batteries using sulfide solid electrolyte." *J. Electroceramics*, **40**, 293 (2018).
42. H. Nakamura, T. Kawaguchi, T. Masuyama, A. Sakuda, T. Saito, K. Kuratani, S. Ohsaki, and S. Watano, "Dry coating of active material particles with sulfide solid electrolytes for an all-solid-state lithium battery." *J. Power Sources*, **448**, 227579 (2020).
43. V. Laue, N. Wolff, F. Röder, and U. Krewer, "Modeling the influence of mixing strategies on microstructural properties of all-solid-state electrodes." *Energy Technol.*, **8**, 1801049 (2020).
44. M. Cronau, M. Duchardt, M. Szabo, and B. Roling, "Ionic conductivity versus particle size of ball-milled sulfide-based solid electrolytes: strategy towards optimized composite cathode performance in all-solid-state batteries." *Batter. Supercaps*, **5** (2022).
45. A. Neumann, S. Randau, K. Becker-Steinberger, T. Danner, S. Hein, Z. Ning, J. Marrow, F. H. Richter, J. Janek, and A. Latz, "Analysis of interfacial effects in all-solid-state batteries with thiophosphate solid electrolytes." *ACS Appl. Mater. Interfaces*, **12**, 9277 (2020).
46. M. Kodama, A. Ohashi, H. Adachi, T. Miyuki, A. Takeuchi, M. Yasutake, K. Uesugi, T. Kaburagi, and S. Hirai, "Three-dimensional structural measurement and material identification of an all-solid-state lithium-ion battery by X-ray nanotomography and deep learning." *J. Power Sources Adv.*, **8**, 100048 (2021).
47. M. Kroll, M. Duchardt, S. L. Karstens, S. Schlabach, F. Lange, J. Hochstrasser, B. Roling, and U. Tallarek, "Sheet-type all-solid-state batteries with sulfidic electrolytes: analysis of kinetic limitations based on a cathode morphology study." *J. Power Sources*, **505**, 230064 (2021).
48. S. Iwamoto, M. Kodama, K. Yanagi, Y. Haniu, Y. Fujii, M. Masuda, H. Higuchi, Y. Suetsugu, and S. Hirai, "Numerical simulations of all-solid-state batteries using specific contact area diameters for active materials determined by X-ray computed tomography." *J. Power Sources Adv.*, **21**, 100120 (2023).
49. M. Kodama, N. Horikawa, A. Ohashi, and S. Hirai, "Coupled nonlinear stress and electric field numerical simulation for all-solid-state lithium-ion batteries." *J. Power Sources Adv.*, **8**, 100049 (2021).
50. A. Ohashi, M. Kodama, N. Horikawa, and S. Hirai, "Effect of Young's modulus of active materials on ion transport through solid electrolyte in all-solid-state lithium-ion battery." *J. Power Sources*, **483**, 229212 (2021).
51. T. Shi, Y.-Q. Zhang, Q. Tu, Y. Wang, M. C. Scott, and G. Ceder, "Characterization of mechanical degradation in an all-solid-state battery cathode." *J. Mater. Chem. A*, **8**, 17399 (2020).
52. X. Gao et al., "Solid-state lithium battery cathodes operating at low pressures." *Joule*, **6**, 636 (2022).
53. D. Hlushkou, A. E. Reising, N. Kaiser, S. Spannenberger, S. Schlabach, Y. Kato, B. Roling, and U. Tallarek, "The influence of void space on ion transport in a composite cathode for all-solid-state batteries." *J. Power Sources*, **396**, 363 (2018).
54. W. Zhang et al., "Interfacial processes and influence of composite cathode microstructure controlling the performance of all-solid-state lithium batteries." *ACS Appl. Mater. Interfaces*, **9**, 17835 (2017).
55. A. L. Santhosha, L. Medenbach, J. R. Buchheim, and P. Adelhelm, "The indium-lithium electrode in solid-state lithium–ion batteries: phase formation, redox potentials, and interface stability." *Batter. Supercaps*, **414**, 359 (2019).
56. S. Bhattiprolu, 158b_transfer_learning_using_CNN_weights_VGG16_RF. https://github.com/bnsreenu/python_for_microscopists/blob/master/158b_transfer_learning_using_CNN_weights_VGG16_RF.py.
57. P. K. Charles, (2015), https://keras.io.
58. F. Pedregosa et al., "Scikit-learn: machine learning in python." *J. Mach. Learn. Res.*, **12**, 2825 (2011).
59. M. Ender, J. Joos, T. Carraro, and E. Ivers-Tiffée, "Quantitative characterization of LiFePO$_4$ cathodes reconstructed by FIB/SEM tomography." *J. Electrochem. Soc.*, **159**, A972 (2012).
60. J. Gostick, Z. Khan, T. Tranter, M. Kok, M. Agnaou, M. Sadeghi, and R. Jervis, "PoreSpy: a python toolkit for quantitative analysis of porous media images." *J. Open Source Softw.*, **4**, 1296 (2019).
61. S. Zhang and K. O. Findley, "Application of chords for quantitative characterization of multi-constituent microstructures." *Metallogr. Microstruct. Anal.*, **1**, 28 (2012).
62. T. G. Tranter, M. D.-R. Kok, M. Lam, and J. T. Gostick, "Pytrax: a simple and efficient random walk implementation for calculating the directional tortuosity of images." *SoftwareX*, **10**, 100277 (2019).
63. Math2Market GmbH, *GeoDict Simulation Software Release*, **2023** (2023).
64. S. Ohno, C. Rosenbach, G. F. Dewald, J. Janek, and W. G. Zeier, "Linking solid electrolyte degradation to charge carrier transport in the thiophosphate-based composite cathode toward solid-state lithium-sulfur batteries." *Adv. Funct. Mater.*, **31**, 2010620 (2021).
65. J. Y. Kim, J. Kim, S. H. Kang, D. O. Shin, M. J. Lee, J. Oh, Y. Lee, and K. M. Kim, "Efficient cell design and fabrication of concentration–gradient composite electrodes for high–power and high–energy–density all–solid–state batteries." *ETRI J.*, **42**, 129 (2020).
66. Z. Siroma, N. Fujiwara, S. Yamazaki, M. Asahi, T. Nagai, and T. Ioroi, "Mathematical solutions of comprehensive variations of a transmission-line model of the theoretical impedance of porous electrodes." *Electrochim. Acta*, **160**, 313 (2015).
67. M. Kodama, A. Takeuchi, M. Uesugi, T. Miyuki, H. Yasuda, and S. Hirai, "Nanoscale pore measurements in an all-solid-state lithium-ion battery with ultra-small-angle X-ray scattering (USAXS)." *J. Power Sources Adv.*, **12**, 100076 (2021).
68. A. Bielefeld, D. A. Weber, R. Rueß, V. Glavas, and J. Janek, "Influence of lithium ion kinetics, particle morphology and voids on the electrochemical performance of composite cathodes for all-solid-state batteries." *J. Electrochem. Soc.*, **169**, 020539 (2022).
69. E. J. Cheng, K. Hong, N. J. Taylor, H. Choe, J. Wolfenstine, and J. Sakamoto, "Mechanical and physical properties of LiNi0.33Mn0.33Co0.33O2 (NMC)." *J. Eur. Ceram. Soc.*, **37**, 3213 (2017).
70. A. Sakuda, A. Hayashi, and M. Tatsumisago, "Sulfide solid electrolyte with favorable mechanical property for all-solid-state lithium battery." *Sci Rep.*, **3**, 2261 (2013).
71. A. Kato, M. Yamamoto, A. Sakuda, A. Hayashi, and M. Tatsumisago, "Mechanical properties of Li 2 S–P 2 S 5 glasses with lithium halides and application in all-solid-state batteries." *ACS Appl. Energy Mater.*, **1**, 1002 (2018).
72. E. Schlautmann et al., "Impact of the solid electrolyte particle size distribution in sulfide-based solid-state battery composites." *Adv. Energy Mater.*, 2302309 (2023).
73. J. Lee, S. Byun, H. Lee, Y. Roh, D. Jin, J. Lim, J. Song, C. B. Dzakpasu, J. Park, and Y. M. Lee, "Digital-twin-driven structural and electrochemical analysis of Li$^+$ single-ion conducting polymer electrolyte for all-solid-state batteries." *Battery Energy*, **2**, 20220061 (2023).
74. J. Park et al., "Unraveling the limitations of solid oxide electrolytes for all-solid-state electrodes through 3D digital twin structural analysis." *Nano Energy*, **79**, 105456 (2021).
75. M. Rana, Y. Rudel, P. Heuer, E. Schlautmann, C. Rosenbach, M. Y. Ali, H. Wiggers, A. Bielefeld, and W. G. Zeier, "Toward achieving high areal capacity in silicon-based solid-state battery anodes: what influences the rate-performance?" *ACS Energy Lett.*, **8**, 3196 (2023).

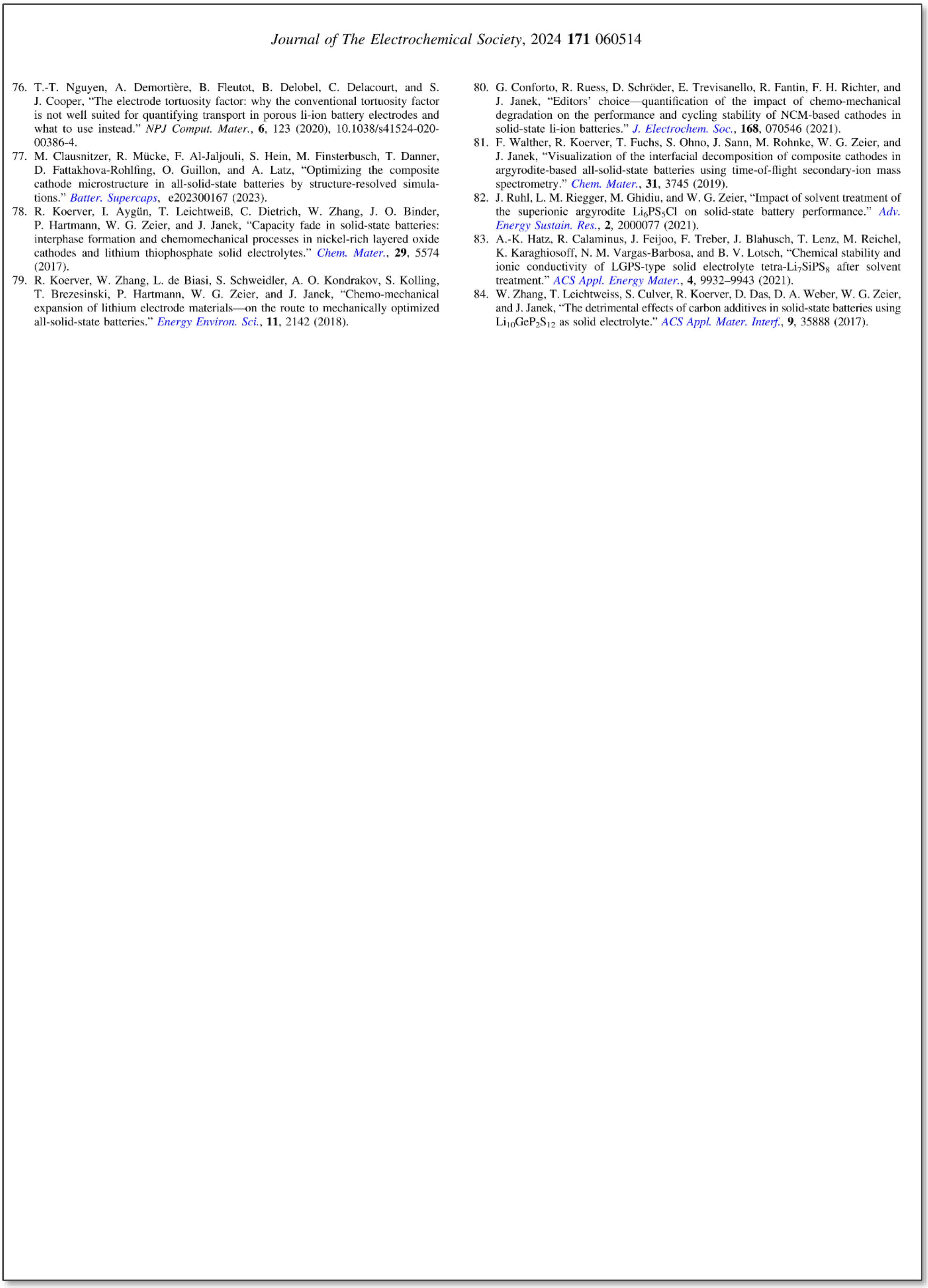

76. T.-T. Nguyen, A. Demortière, B. Fleutot, B. Delobel, C. Delacourt, and S. J. Cooper, "The electrode tortuosity factor: why the conventional tortuosity factor is not well suited for quantifying transport in porous li-ion battery electrodes and what to use instead." *NPJ Comput. Mater.*, **6**, 123 (2020), 10.1038/s41524-020-00386-4.
77. M. Clausnitzer, R. Mücke, F. Al-Jaljouli, S. Hein, M. Finsterbusch, T. Danner, D. Fattakhova-Rohlfing, O. Guillon, and A. Latz, "Optimizing the composite cathode microstructure in all-solid-state batteries by structure-resolved simulations." *Batter. Supercaps*, e202300167 (2023).
78. R. Koerver, I. Aygün, T. Leichtweiß, C. Dietrich, W. Zhang, J. O. Binder, P. Hartmann, W. G. Zeier, and J. Janek, "Capacity fade in solid-state batteries: interphase formation and chemomechanical processes in nickel-rich layered oxide cathodes and lithium thiophosphate solid electrolytes." *Chem. Mater.*, **29**, 5574 (2017).
79. R. Koerver, W. Zhang, L. de Biasi, S. Schweidler, A. O. Kondrakov, S. Kolling, T. Brezesinski, P. Hartmann, W. G. Zeier, and J. Janek, "Chemo-mechanical expansion of lithium electrode materials—on the route to mechanically optimized all-solid-state batteries." *Energy Environ. Sci.*, **11**, 2142 (2018).
80. G. Conforto, R. Ruess, D. Schröder, E. Trevisanello, R. Fantin, F. H. Richter, and J. Janek, "Editors' choice—quantification of the impact of chemo-mechanical degradation on the performance and cycling stability of NCM-based cathodes in solid-state li-ion batteries." *J. Electrochem. Soc.*, **168**, 070546 (2021).
81. F. Walther, R. Koerver, T. Fuchs, S. Ohno, J. Sann, M. Rohnke, W. G. Zeier, and J. Janek, "Visualization of the interfacial decomposition of composite cathodes in argyrodite-based all-solid-state batteries using time-of-flight secondary-ion mass spectrometry." *Chem. Mater.*, **31**, 3745 (2019).
82. J. Ruhl, L. M. Riegger, M. Ghidiu, and W. G. Zeier, "Impact of solvent treatment of the superionic argyrodite Li_6PS_5Cl on solid-state battery performance." *Adv. Energy Sustain. Res.*, **2**, 2000077 (2021).
83. A.-K. Hatz, R. Calaminus, J. Feijoo, F. Treber, J. Blahusch, T. Lenz, M. Reichel, K. Karaghiosoff, N. M. Vargas-Barbosa, and B. V. Lotsch, "Chemical stability and ionic conductivity of LGPS-type solid electrolyte tetra-Li_7SiPS_8 after solvent treatment." *ACS Appl. Energy Mater.*, **4**, 9932–9943 (2021).
84. W. Zhang, T. Leichtweiss, S. Culver, R. Koerver, D. Das, D. A. Weber, W. G. Zeier, and J. Janek, "The detrimental effects of carbon additives in solid-state batteries using $Li_{10}GeP_2S_{12}$ as solid electrolyte." *ACS Appl. Mater. Interf.*, **9**, 35888 (2017).

5.3 Publication 3 - Designing cathodes and cathodes active materials for solid state batteries.

While Publication 1 and Publication 2 identified bottlenecks in charge transport and factors such as particle size distribution and cathode active material (CAM) content, they focused on a very specific material combination and system. Naturally, this raised the question of whether cathode design can be related to the fundamental properties of solid electrolytes (SE) and CAMs, and how one could develop guidelines for CAM and cathode design based on the findings and available literature.

Most CAMs are designed to perform well in lithium-ion batteries (LIBs) with liquid electrolytes (LEs), and many of their properties are specifically tailored to meet the requirements of these systems. However, solid-state batteries (SSBs) have different needs, and CAM properties must be optimized accordingly. Unlike LEs, which can penetrate residual voids and establish intimate contact with CAMs through wetting, SEs must be designed to complement CAMs, accounting for volume changes, poor interface contact, and higher tortuosity in SSB cathodes.

Publication 3[34] provides an overview of important factors to consider when designing composite cathodes for SSBs. These factors are categorized into electrode level, particle level, and interface level, ranging from macroscopic to nanoscopic properties and effects. Based on the study's findings, the necessary properties of CAMs using intercalation (e.g., $LiNi_xCo_yMn_zO2$), insertion (e.g., LiFePO4), or conversion (e.g., CuS) chemistries were outlined. The study offers guidelines for addressing challenges related to chemical degradation, chemo-mechanical degradation, and percolation limitations for each system.

The particle size distribution of both CAM and SE is one of the most critical factors and requires careful attention. Furthermore, CAMs that exhibit high potentials demand interface protection strategies to prevent excessive SE oxidation. This work provides comprehensive design principles to improve SSB cathode performance through the customization of material properties.

The study design was developed by F. Strauss and me. F. Strauss and I contributed equally to this work. The manuscript was written by F. Strauss and me and edited by all contributing authors. Reprinted with permission under CC BY from:

Minnmann, P.; Strauss, F.; Bielefeld, A.; Ruess, R.; Adelhelm, P.; Burkhardt, S.; Dreyer, S. L.; Trevisanello, E.; Ehrenberg, H.; Brezesinski, T.; Richter, F. H.; Janek, J. Designing Cathodes and Cathode Active Materials for Solid-State Batteries. *Adv. Energy Mater.* **2022**, *12* (35), 2201425. https://doi.org/10.1002/aenm.202201425.

PERSPECTIVE

ADVANCED ENERGY MATERIALS

www.advenergymat.de

Designing Cathodes and Cathode Active Materials for Solid-State Batteries

Philip Minnmann, Florian Strauss, Anja Bielefeld, Raffael Ruess, Philipp Adelhelm, Simon Burkhardt, Sören L. Dreyer, Enrico Trevisanello, Helmut Ehrenberg, Torsten Brezesinski,* Felix H. Richter,* and Jürgen Janek*

Solid-state batteries (SSBs) currently attract great attention as a potentially safe electrochemical high-energy storage concept. However, several issues still prevent SSBs from outperforming today's lithium-ion batteries based on liquid electrolytes. One major challenge is related to the design of cathode active materials (CAMs) that are compatible with the superionic solid electrolytes (SEs) of interest. This perspective, gives a brief overview of the required properties and possible challenges for inorganic CAMs employed in SSBs, and describes state-of-the art solutions. In particular, the issue of tailoring CAMs is structured into challenges arising on the cathode-, particle-, and interface-level, related to micro-structural, (chemo-)mechanical, and (electro-)chemical interplay of CAMs with SEs, and finally guidelines for future CAM development for SSBs are proposed.

1. Introduction

The increasing demand for safe, reliable, and affordable energy-storage devices has stimulated extensive battery research and development in the last decade. While the development of conventional lithium-ion batteries (LIBs) using organic liquid electrolytes (LEs) is approaching physicochemical limits, solid-state batteries (SSBs) with high capacity anodes (e.g., Li metal) are considered as a promising alternative, and their commercialization within the near future is strongly anticipated.[1–3]

The key component of any battery, regardless of whether utilizing LEs or solid electrolytes (SEs), is the cathode active material (CAM) in its lithiated form, that is, as present in a discharged cell. In its delithiated form, when the cell is charged, it is the only cell component that is contributing to storing energy (in conjunction with a hypothetical in situ lithium-plated anode formed during charging), thus making it the material required to be present in large quantity to achieve a high-performing cell. All other components, which may be required for large scale processing, only decrease the specific energy of the cell and are, therefore, engineered to minimize their content without affecting the function of the cell. This is evident in the research efforts made to increase the CAM content in the cathode layer, decrease the separator thickness as much as possible, and the pursuit to plate lithium metal in situ (in "anode-free" cells, which are more correctly described as "zero excess lithium metal" cells) without the use of an anode active material.[4] Thus, the CAM type and content in the cell ultimately determine the maximum specific energy that the system can provide.

Moreover, the CAM contributes a significant proportion to the overall cell costs,[5] hence the necessity of steady tailoring toward reduced costs and higher energy density. So far, CAM development has mainly targeted performance optimization with LEs in LIBs. For instance, cathode electrolyte interface (CEI) formation,[6]

P. Minnmann, A. Bielefeld, R. Ruess, S. Burkhardt, E. Trevisanello,
F. H. Richter, J. Janek
Institute of Physical Chemistry
Justus-Liebig-University Giessen
Heinrich-Buff-Ring 17, 35392 Giessen, Germany
E-mail: juergen.janek@phys.chemie.uni-giessen.de;
felix.h.richter@phys.chemie.uni-giessen.de

P. Minnmann, A. Bielefeld, R. Ruess, S. Burkhardt, E. Trevisanello,
F. H. Richter, J. Janek
Center for Materials Research (ZfM)
Justus-Liebig-University Giessen
Heinrich-Buff-Ring 16, 35392 Giessen, Germany

The ORCID identification number(s) for the author(s) of this article can be found under https://doi.org/10.1002/aenm.202201425.

DOI: 10.1002/aenm.202201425

F. Strauss, S. L. Dreyer, T. Brezesinski, J. Janek
Battery and Electrochemistry Laboratory (BELLA)
Institute of Nanotechnology, Karlsruhe Institute
of Technology (KIT)
Hermann-von-Helmholtz-Platz 1, 76344 Eggenstein-Leopoldshafen,
Germany
E-mail: torsten.brezesinski@kit.edu

P. Adelhelm
Department of Chemistry – Electrochemistry
Humboldt-University Berlin
Brook-Taylor-Strasse 2, 14489 Berlin, Germany

P. Adelhelm
Joint Research Group Operando Battery Analysis
Helmholtz Centre for Materials and Energy
Hahn-Meitner-Platz 1, 14109 Berlin, Germany

H. Ehrenberg
Institute for Applied Materials (IAM)
Karlsruhe Institute of Technology (KIT)
Hermann-von-Helmholtz-Platz 1, 76344 Eggenstein-Leopoldshafen,
Germany

cracking of CAM particles,[7] transition metal dissolution,[8] and HF scavenging[9] have been identified and extensively studied, and rational materials design has allowed to overcome these challenges.[10] This resulted in today's state-of-the-art CAMs for LIBs, primarily referring to layered lithium metal oxides $LiMO_2$ (M = Ni, Co, Mn, Al, etc.). However, a transition from LIBs to SSBs is associated with different requirements for CAMs, which are rooted in the different properties of SEs (electrochemical stability, mechanical rigidity, etc.) as compared to LEs. Examples are different (electro-)chemical reactions at the electrolyte–CAM interface[6,9,11,12] and increasing importance of (chemo-) mechanical processes[13,14] or composite cathode fabrication.

The main types of solid lithium-ion conductors can be roughly divided into oxide-, sulfide-, halide-, and polymer-based SEs. Each of these material classes has distinct advantages and disadvantages, which have been summarized in several reviews elsewhere.[15–22] For instance, oxide-based SEs possess a high (oxidative) electrochemical stability, preventing decomposition when in contact with (high-voltage) CAMs. However, their maximum ionic conductivity (≈1 mS cm^{-1} at room temperature [r.t.]) appears too low to enable fast charge/discharge kinetics, which can only be realized if the materials are sintered. Unfortunately, CAM/SE decomposition reactions take place at lower temperatures than required for proper sintering.[23] In addition, their mechanical rigidity and brittle nature greatly complicate attaining and maintaining the required intimate contact with the CAM, especially when considering the volume changes occurring during cell cycling.[21]

In contrast, polymer-based SEs possess favorable mechanical properties and can be processed in solution or molten form, which allows simple implementation into existing roll-to-roll processing lines for LIB fabrication. However, their ionic conductivities are yet too low for reasonable room-temperature operation, and limited oxidative electrochemical stability presents additional challenges during cell cycling. Nevertheless, polymer-based cells with $LiFePO_4$ (LFP) as CAM are available and used in public transportation.[24]

The most prominent class of present-day SEs are sulfide-based materials, or in particular lithium thiophosphates, displaying exceptionally high r.t. ionic conductivities up to 25 mS cm^{-1}. They also have suitable mechanical properties (i.e., malleability and low Young's modulus), which makes them ideal candidates at first sight. However, they exhibit a narrow electrochemical stability window, and consequently, artificial protection layers avoiding direct contact with the CAM need to be implemented.[21,25]

Halide SEs have recently regained great research interest, mainly owing to their high oxidative electrochemical stability, allowing their use together with unprotected CAMs. Apart from that, their mechanical properties allow moderate ionic conductivities (1 mS cm^{-1}) to be achieved in a cold-pressed state. In addition, they may also serve as a protective coating on the CAM surface, provided they do not react with the catholyte.[26] As mostly rare-earth or other resource-critical metals are employed, their commercial use as catholyte is somewhat questionable.[22]

Please note, that there are cell concepts using more than one SE.

To sum up, independent of the employed SE, a strong interplay between CAM and SE most likely requires a complementary design of both materials to achieve maximum battery performance. In this perspective, we summarize specific issues regarding the application of inorganic CAMs in SSBs based on mainly sulfide and halide SEs. We elucidate the requirements of such CAMs to be addressed from a materials perspective and describe possible challenges and solutions. Building on this, we focus on proposed design principles toward improved CAMs, aiming to provide guidelines for rational CAM development for SSBs.

2. SSB Cathodes—Challenges

Composite cathodes in SSBs are generally composed of CAM and SE particles in combination with polymer binders and carbon-based additives, which improve the mechanical and electrical properties, respectively. In general, the fabrication of high-performance SSB cathodes presents challenges on different length scales, ranging from the micro- to the nano-scale which are related to the composite cathode, CAM particles, and interface between CAM and SE, respectively (**Figure 1**).[27] Besides optimizing the composite cathodes on a microscale level, the CAM itself needs to be tailored for application in SSBs to be (chemo-)mechanically compatible with the SE. In the following, we describe the different requirements for the CAM and composite cathodes from materials and processing perspectives. Although various parameters related to the different materials (SE, binder, conductive additives) in SSB cathodes influence the cell performance, we focus on the particular design parameters of the CAM, as this material is the integral constituent.

2.1. Cathode Microstructure and Charge Transport

First of all, SSB cathodes should possess high ionic and electronic partial conductivities together with a high loading of CAM to remain within several tens of Ω cm^2 of internal cell resistance and maximize both, energy and power density.[28] However, there is usually a trade-off between maximizing energy and power. For instance, a high content of CAM is necessary to increase the energy density of the cathode and in an ideal composite cathode, the CAM fraction approaches 100 %. This goes hand in hand with a lower content of SE, which in turn increases the tortuosity of ionic conduction pathways and limits the attainable power density.[29–33] Therefore, electrode engineering requires careful balancing of CAM volume fraction and electrode thickness. To date, experimental studies commonly use ≈50 vol% CAM fraction to ensure ionic percolation[14,31,33–35] and geometrical models suggest an optimal composition in terms of active surface area between 60 and 70 vol% CAM fraction depending on the porosity in homogeneously distributed composites.[36,37] We therefore anticipate, that, with tailored manufacturing techniques and liquid additives that reduce porosity and enable highly homogeneous particle distributions, commercial ASSBs, designed to provide high energy density, will target at least around 70 vol% CAM fraction. A detailed overview of experimentally achieved composite cathode loadings and the influence of kinetic transport limitations can be found elsewhere.[38]

In contrast to cathodes employed in LE-based LIBs, porosity is detrimental to SSB cathodes and should be reduced to a

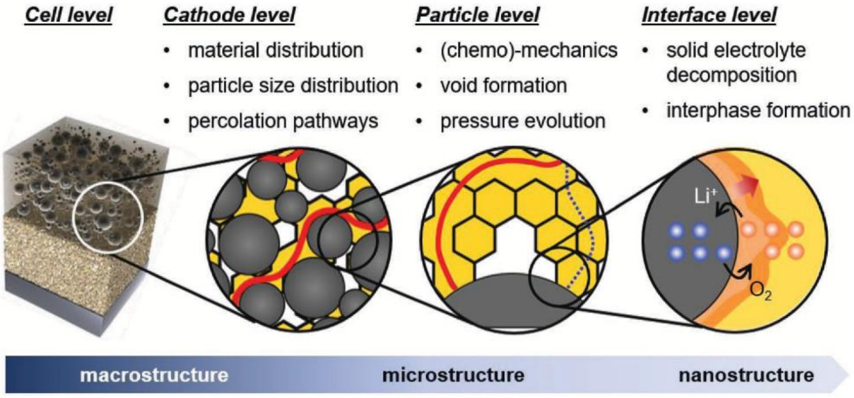

Figure 1. Schematic overview of the important processes occurring on different length scales in SSB cathodes, causing various challenges to the development of scalable fabrication processes and tailored materials properties.

minimum, as pores are neither electronically nor ionically conductive and negatively affect the charge transport.[39] Apart from the conductivity, pores prevent active interface between SE and CAM and, depending on surface coverage, pore size, and distribution models, predict a significant increase in overvoltage.[40] There is, of course, the possibility of introducing liquid ion conducting additives into the cathode to eliminate the pores, however, this concept leads to additional interfaces and needs further evaluation.

As a consequence, the charge-transport percolation, or in other words the ability to supply electrons and ions to all regions in the cathode, is a crucial condition when fabricating high-performance composite cathodes. Ionic and electronic percolation depends on several parameters, such as conducting-phase content,[29–31,41,42] particle-size ratio,[30,31,43,44] and processing conditions.[34,45–48] Recent studies have shown that partial conductivities are suitable descriptors for the charge-transport percolation, and several experimental setups have been developed to determine the transport properties in different cathodes architectures.[29,31,41,49,50]

The reader should note that SEs, different from LEs, possess their own microstructure, consisting of bulk and grain boundary, that can lead to ill-defined and non-uniform transport properties on the microscale (see **Figure 2**). Poorly conducting grain boundaries may further increase the "apparent tortuosity" of the ionic transport (as obtained from charge-transport measurements) beyond the "geometric tortuosity," which only considers the respective distribution of phases. Thus, the SE and CAM particle microstructures are crucial for the electrochemical performance and have been studied from a modeling perspective alone or in combination with experimental works.

In general, the motivation for modeling composite cathodes for SSBs is driven by explaining experimental observations and, more importantly, providing guidelines on how to optimize the cathode microstructure. This involves the identification of the optimum composition of the cathode relevant parameters, such as particle-size distribution (PSD) of CAM and SE, required SE conductivity, and phase fractions of the

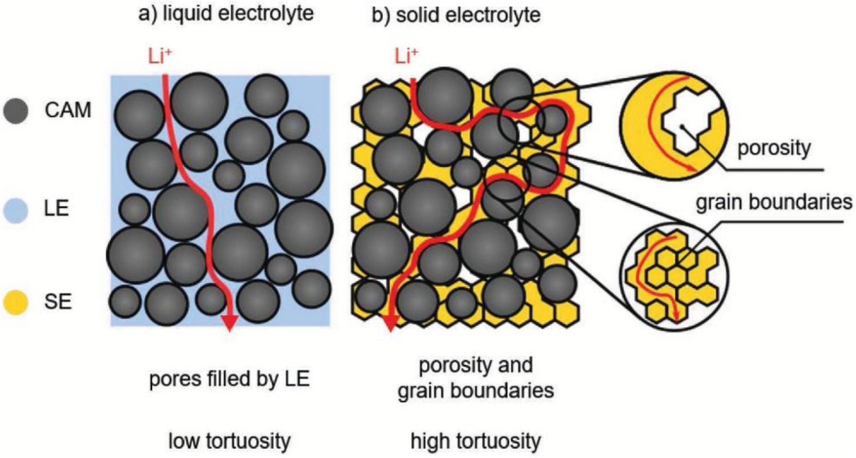

Figure 2. Comparison of composite cathodes using a a) liquid- or b) solid-electrolyte. A liquid electrolyte can infiltrate the cathode and penetrate pores, leading to both, a uniform distribution of charge transport pathways and a low tortuosity for ion transport (red line in [a]). In the case of the solid electrolyte, residual porosity and grain boundary resistances result in much more tortuous transport pathways and a higher overall tortuosity (red line in [b]).

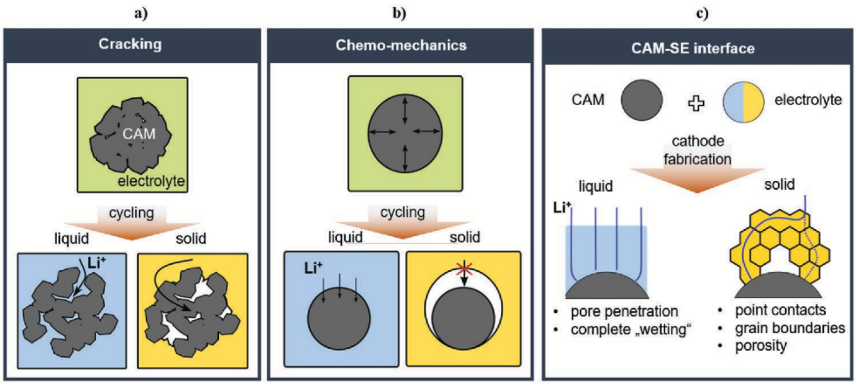

Figure 3. Schematic illustration of effects that come into play if changing the liquid electrolyte to a solid electrolyte. a) Cracking of CAMs induced by (chemo-)mechanical stress leads to reduced transport pathways in the case of a liquid electrolyte, because it can penetrate the newly formed pores. In case of a solid electrolyte, the transport pathways are increased in length. b) Large volume changes result in contact loss between CAM and SE and cause increased interface resistances. c) During cathode fabrication, a liquid electrolyte can penetrate the porous cathode and wet the free surface. A solid electrolyte is already part of the slurry before the cathode layer is fabricated. Although this may provide certain advantages in terms of reduction of processing steps, it is difficult to achieve intimate contact between CAM and SE, especially if the CAM possesses a complex surface morphology. Porosity and grain boundaries can affect the charge transfer and point contacts lead to current constriction and limit electrode kinetics.

respective constituents to achieve high energy and power densities while minimizing residual pore space. Most modeling studies rely on representing the cathode microstructure in voxels or simulate it using the finite-element method. To obtain a representative microstructure, voxel data are either directly imported from µ-computed tomography[51] or focused ion beam scanning electron microscopy[52] or reconstructed from SEM images.[30,32,36,37] This allows to extract PSDs, particle shapes, or material distributions. In addition, fully synthetic microstructures are used to examine the impact of particular design parameters.[30,36,37,45,53–57]

However, a challenge in the microstructure reconstruction is the high resolution that is required for binder and carbon additives, as these are much smaller in size and contrast to CAM and SE. Thus, most microstructure reconstructions do not take these components into account, with the exception of some recent studies reporting about the influence of the carbon black content in LFP/polyethylene oxide:LiTFSI composites,[45,54] the microstructure of the carbon additive in $LiNi_xCo_yMn_zO_2$ (NCM)/Li_6PS_5Cl (LPSCl) composites,[58] and the effect of nitrile butadiene rubber and polyvinylidene-fluoride binders in NCM/LPSCl composites.[32,37]

2.2. Chemo-Mechanics during Electrochemical Cycling

As all constituents of inorganic SSBs are solids and usually constrained by volume in the cell housing, (electro-)chemically driven volume or morphology changes during cycling have a profound effect on the performance and degradation. In the cathode, volume and/or morphology changes are in particular related to the CAM upon (de-)lithiation and are dependent on the state of charge (SOC). **Figure 3**a,b illustrates how common (chemo-)mechanical effects, such as interparticle stresses and CAM expansion/contraction, have to be taken into account when replacing a LE by a SE.

Since not all CAMs exhibit the largest volume change at the highest SOC, we focus on the maximum volume change ($\Delta V_{max}/V$) during cycling. Whereas conventional intercalation- or insertion-type CAMs mainly undergo volume changes in the range of several percent while maintaining the original crystal structure, conversion-type CAMs can undergo volume changes up to hundreds of percent, in addition to morphology changes due to the electrochemical conversion reaction. Please note, that volume changes are not necessarily isotropic[43] and the resulting strain can differ significantly along different crystallographic axes, leading to massive anisotropic stress and mechanical damage. Thus, there is a strong current research interest to understand the effect of (chemo-)mechanical processes on battery performance and to find strategies to mitigate degradation mechanisms. For instance, the combination of thiophosphate-based SE (e.g., β-Li_3PS_4 [LPS] or LPSCl) and polycrystalline (PC) Ni-rich NCM CAM is highly attractive and often reported. This is mainly triggered by the high ionic conductivity of Li-thiophosphate SEs in combination with their malleability (low Young's modulus), which allows to accommodate (electro-)chemically driven volume changes during battery operation to a certain extent.[21]

Such volume changes become more prominent if Ni-rich NCM or conversion-type CAMs are employed, leading to impedance increase and decreasing battery performance. However, modeling studies addressing (chemo-)mechanics remain largely elusive.[59] In particular, the volume changes of the CAM during cycling can lead to interparticle cracking (for PC CAM) and pore formation between the SE and CAM particles, causing contact loss and increased tortuosity.[13,14,48] In addition, it can be assumed that internal stress/strain generation in the cathode can cause cracking of the SE matrix (including the separator layer). This adversely affects the ionic and electronic percolation pathways, and ultimately results in poor electrochemical reversibility and capacity fading due to loss of contact to CAM upon prolonged cycling. While LEs can penetrate into these pores and cracks,[7] SEs are rigid and cannot do the same.[13] On a laboratory cell scale, these effects have usually been compensated for by applying external pressures of a few to tens of MPa to the SSB. Clearly, such high pressures are not suitable for large-scale commercial applications.[14,60] Consequently, it is important to find and develop materials combinations that allow to minimize or even avoid detrimental (chemo-)mechanical effects in SSB composite cathodes.

2.3. Interfacial Compatibility

In addition to the dominant role of (chemo-)mechanics, the interfacial compatibility between CAMs and SEs is another important issue. From a chemical perspective, the low chemical potential of lithium in the employed CAMs leads to oxidation of the SE. During oxidation, ionically poorly conductive phases are formed, for example, phosphites/phosphates, sulfites/sulfates, and polysulfides in the case of thiophosphate-based SEs. These narrow down transport pathways and cause an increased interfacial resistance, thereby impeding charge transfer.[12,49,61] Oxidative SE decomposition can either be addressed via the implementation of stable SEs (i.e., oxides or halides) or through the application of a protective surface coating to the CAM, preventing direct contact with the SE. The primary function of a surface coating is to act as an electron blocking but lithium-ion conducting layer, so that the SE does not experience the low chemical potential of lithium in the CAM. However, sufficient electronic transport through the protective coating between the particles needs to be ensured to enable (de-)lithiation of the CAM. Moreover, if the coating itself is too brittle, it can lose contact to the CAM during cycling due to the accompanying volume/morphology changes. In addition, the application of a surface coating introduces new interfaces, namely SE/coating and CAM/coating interfaces, which may have detrimental effects on the charge-transport properties of the composite cathode.

Switching from thiophosphate- to oxide-based SEs comes along with different challenges, as oxide SEs are much more rigid, thus achieving and maintaining intimate contact with the CAM (and other electrode constituents) remains challenging (see Figure 3c) and often requires high-temperature sintering.[23] In this regard, halide-based SEs (e.g., Li_3InCl_6 or Li_3YCl_6) may be a more suitable choice, as they combine high oxidation stability with favorable mechanical properties, but typically contain resource-critical and potentially costly elements.[22] If only minor amounts of these materials are used in the form of nanoscale coatings their material cost is less of an issue.

In summary, interface engineering requires tailored approaches depending on the type of CAM and SE used and presents specific challenges for the materials development.

3. SSB Cathodes—Requirements and Solutions

As shown in Figure 1, SSB cathodes need to be tailored on different length scales, pertaining to challenges in the composite cathode, CAM particles, and interface formation between CAM and SE. In the following, we describe the requirements going from the macroscale (cathode level) to the nanoscale (interface level), and outline possible optimization strategies for each level.

3.1. Cathode Level

To achieve high-performance SSB cathodes, careful balancing of the SE versus CAM content (and other additives) is required. Several experimental studies focused on tailoring these parameters, also addressing the charge transport and (chemo-)mechanical stability with the goal to increase cell performance.[30,31] However, the fact that inorganic SEs possess their own microstructure (and PSD) implies that the SE and CAM PSD should be adapted to one another in order to achieve the highest possible packing density, thereby avoiding pore space and increasing energy density. It has been reported that the use of small SE particles (large CAM/SE particle-size ratio) in combination with spherical CAM particles is favorable for a high packing density.[30,55,57] Moreover, for percolation modeling, experimental results indicate that NCM secondary particles with a diameter of 3–5 µm are beneficial for the interparticle connectivity, as they provide a sufficiently high specific surface area and many contact points with other NCM particles.[36,37] Additionally, CAM fractions above 60 vol% may even enable carbon-free cathode composites if the electronic conductivity of the CAM is sufficiently high.[31,36]

The most cost-effective way to fabricate SSB cathodes is to adopt already existing processes that are currently utilized in the production of LIBs, that is, slurry-based tape casting. However, new mixing strategies need to be developed, since the SE is usually already part of the slurry, and a uniform distribution of all electrode constituents after tape casting is required to maintain optimized charge percolation networks throughout the cathode.

A promising concept may be the application of gradient cathodes, in which a high electronic conductivity is achieved at the current collector and a high ionic conductivity is achieved at the separator side of the cathode.[40,62] A gradient architecture compensates for the heterogeneity of the respective network resistance throughout the cathode cross section. Although the total charge flux through the cathode is constant at every distance from the separator and current collector, the resistance is smaller for ions at the separator, while the electrons experience a smaller resistance at the current collector side and vice versa.[51,62] This can be understood in terms of a reaction zone model, where lithiation starts at the cathode side, at which the charge carrier experiencing the highest resistance is inserted. A detailed description is given by Usiskin et al.[62]

Conductivity gradients can be achieved by varying the CAM volume content, and it may also be possible to use particles with different properties in different parts of the cathode. For instance, small particles with short diffusion pathways could be employed at the current collector side and larger particles at the separator side, so that ionic transport limitations will be mitigated. To further increase the rate capability, consideration of the above requirements may be useful in the design of CAMs. Another issue related to manufacturing is the amount (and type) of binder needed to achieve mechanical integrity and to enable large-scale cell fabrication.[37,46] To date, binder-containing cathodes have shown limited performance, as polymer binders block active (free) surface and conduction paths.[35,63–65] There are approaches aiming at minimizing the binder content based on dry-processing using a PTFE-binder[66] or by selective removal from the electrode via heat treatment.[67] Dry processing has the advantage of excluding solvent from the production process, thereby eliminating the possibility of degradation reactions between CAM and solvent or SE and solvent. Additionally, high shear forces may be generated (extrusion) and could create sufficient contact points between the CAM and SE particles, provided the mechanical properties of the materials are tailored accordingly.

Another possibility is the liquid phase (melt) infiltration of the cathodes with subsequent SE crystallization, which can ideally result in a dense electrode.[68] However, this approach requires SEs of low melting points and high ionic conductivity (yet to be discovered/synthesized).

As described previously, many parameters can influence the resulting performance. Thus, tailoring SSB cathodes via design-of-experiment approaches or comparable computation-aided methods is well suited to reduce the number of experiments needed.[46]

3.2. CAM Particle Level

For the storage of lithium in the CAM, both electrons and ions need to be transported within a single particle, assuming that it is electronically and ionically well contacted, for example, by other CAM particles, conductive carbon (if added), and SE. It is essential to understand that the slowest process, either electronic or ionic transport, limits how much of the CAM is electrochemically addressed at a certain C-rate (in units of h^{-1}). Thus, the particle size L should be designed depending on the chemical diffusion coefficient $\tilde{D}_{Li}$ of lithium as a neutral component (note that $\tilde{D}_{Li} \approx \tilde{D}_{ion}$ if the CAM is a predominantly electronic conductor) for a targeted C-rate, according to Equation (1), in order to achieve at least 83% of the theoretical specific capacity of a spherical CAM particle.[69]

$$L \le \sqrt{\frac{3\tilde{D}_{Li}}{\mathrm{C-rate}}} \qquad (1)$$

Figure 4 provides an illustration of the particle size calculated from Equation (1) for the $\tilde{D}_{ion}$ in NCM and $\tilde{D}_{el}$ in LFP exemplarily. For conversion- and spinel-type materials, it is difficult to obtain $\tilde{D}_{Li}$, because most of these materials undergo several phase transitions, and two phases are present over a large range of SOC. We would like to note though that $\tilde{D}_{ion}$ in spinel-type materials should be higher than that of layered NCM CAMs.[70] Evidently, even for materials with high $\tilde{D}_{Li}$, such as NCM, the particle size should not exceed more than a few micrometers if high C-rates are to be achieved.

In this regard, small CAM particles are beneficial to achieve high capacities at a high C-rate. However, an optimum particle size exists, as too small particles compromise ionic partial conductivity and ionic percolation on the cathode level.[30,37,72] This is especially critical if also degradation at the CAM|SE interface is taken into account, which is more detrimental in the case of small particles due to the larger contact area.[37,49]

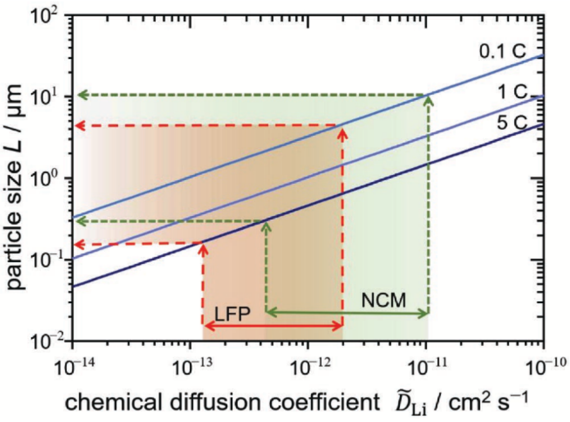

Figure 4. Maximum particle size according to Equation (1) for a C-rate of 0.1, 1, and 5 C depending on the range of the respective diffusion coefficient (colored areas). For NCM CAMs, the diffusion coefficient for ions was considered,[7] while for LFP and conversion-type materials, the diffusion coefficient for electrons was considered,[71] because they are mostly poor electronic conductors.

As mentioned above, the initial particle size of a certain CAM does, in most cases, change during cycling. The changes in lithium concentration within the CAM upon charging and discharging lead to volume changes of the primary particles that predominantly expand (e.g., $LiCoO_2$ [LCO]) or shrink (e.g., Li_2S or NCM) with delithiation. The volume changes are typically in the range of a few percent for intercalation-type CAMs, whereas for conversion-type CAMs, the volume changes are much larger, depending on the cell chemistry involved. Based on the electrochemical reaction formula during discharging, a theoretical volume expansion of 78% and 65% can be calculated for the conversion-type CAMs sulfur and iron disulfide, respectively. Although the relative volume change is independent of the particle size, it has to be taken into account that smaller particles show smaller absolute changes in L. **Figure** 5a shows the absolute change of the particle radius r (with $r = L/2$) as a function of the initial particle radius r_0 for several CAMs. For smaller particle sizes, smaller changes occur, which may be accommodated more easily by SE deformation. Yet, it is unclear to which extent SEs are capable of compensating the CAM volume change.

Importantly, the volume changes are correlated to the lithium concentration within the CAM, so that lithium concentration gradients, typically generated at high C-rates, as well as the anisotropy of the volume changes, lead to mechanical stress. This can result in the formation of cracks either between different grains in PC CAMs or within individual single-crystalline CAM domains. Such cracks within the CAM increase the electronic tortuosity throughout the composite cathode, since they effectively block electronic charge transport and increase the length of the electronic pathway. The increase in electronic tortuosity is even more pronounced if CAM particles close to the current

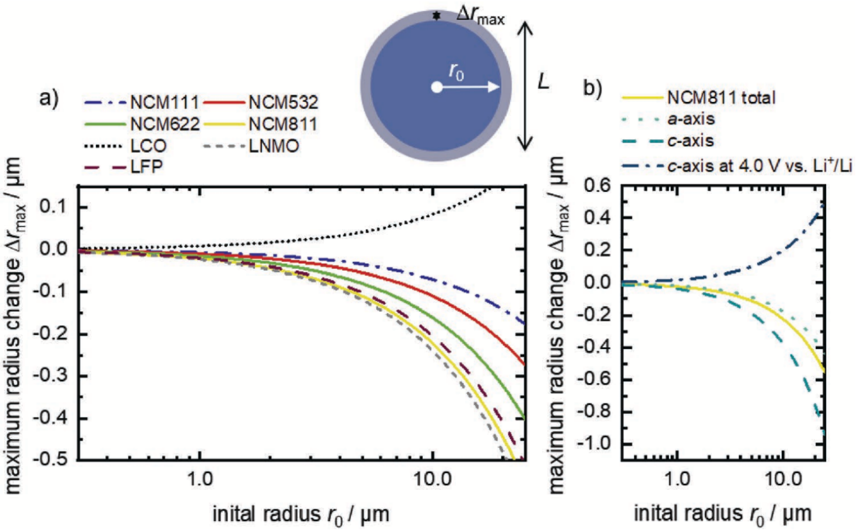

Figure 5. a) Calculated maximum radius change of spherical CAM particles as a function of the initial particle radius r_0.[14,73–75] The absolute maximum volume change is much smaller for smaller particle radii, and the differences between different types of CAMs become less pronounced. b) Deconvolution of the total volume change of NCM811 into *c*- and *a*-axis changes.[76] The *c*-axis first expands up to a potential of 4 V and subsequently contracts. The differences in the *c*- and *a*-axis change lead to internal stress and may cause anisotropic volume changes of SC CAMs. For conversion-type CAMs, more elaborate calculations would require knowledge of the phase nucleation geometry and are beyond the scope of this work.

collector crack, as this is accompanied by contact loss between CAM and current collector.

To mitigate interparticle cracking, the development of single-crystal (SC) CAMs appears to be a promising approach.[77] Nevertheless, SC CAMs still show an overall volume change during (de-)lithiation and will not change volume isotropically, due to different crystallographic orientations of the facets and the anisotropic changes in the *a*- and *c*-axis. Please note that the *c*-axis initially expands during delithiation due to increased Coulombic repulsion of the oxygen layers. At a certain Li-concentration (corresponding to around 4 V vs Li$^+$/Li) these layers collapse, and the *c*-axis exhibits substantial contraction (see Figure 5b). The contact loss along certain facets could be much more severe, than expected from the total volume change. Hence SC CAMs may not necessarily be an ideal solution to the chemo-mechanical problems in SSBs, unless the particle shapes can be tailored in a controlled way.[78] However, this point is quite unclear so far and needs further evaluation.

Thus, multiple other strategies have been developed, each with its own advantages and disadvantages. First, the use of zero- or low-strain materials eliminates the volume changes during battery operation directly. For instance, NCM CAMs showing virtually zero volume changes during charge/discharge have been developed via rational tailoring of the transition metal composition. This results in almost no pressure evolution on a cell level during cycling.[79] However, one again has to consider that such materials do undergo anisotropic volume changes along different crystallographic directions as mentioned above, yet these result in zero net changes upon (de-)lithiation. Thus, on the microscale, (chemo-)mechanical separation between SE and CAM may still occur.[79] Alternatively, the overall balancing of volume changes on the cell level has also been achieved by blending CAMs that shrink with CAMs that expand during delithiation (e.g., $LiNi_{0.8}Co_{0.1}Mn_{0.1}O_2$ [NCM811] and LCO)[14] or by combining expanding anodes with shrinking cathodes and vice versa.[80] However, in both aforementioned cases, the development of quasi zero-strain cathodes comes at the expense of decreased Ni content and thus, specific capacity.

Recently, it has been demonstrated that pressure changes and secondary particle fracture in SSBs can be mitigated via the application of “full-concentration gradient” NCM CAMs, which possess radially oriented rod-shaped primary crystallites, unlike conventional NCMs.[81] Apart from addressing pressure evolution through designing the CAM itself, this issue may be counterbalanced by the introduction of certain amounts of suitable polymer binders and/or additional polymer SEs into the cathode to buffer pressure changes during cycling and maintain mechanical integrity.

3.3. Interface Level

Although already several CAM design strategies to minimize detrimental (chemo-)mechanical effects in SSBs have been developed, the interface formation, that is, SE degradation remains problematic. To prevent side reactions that form high-impedance interphases, a common approach is the application of a protective surface layer to the CAM particles, usually with a thickness in the nanometer range. In principle, the primary requirement for such coatings is to act as an electron-blocking but ion-conducting layer while having high oxidative stability. To this end, various lithium transition metal oxides (e.g., $LiNbO_3$, $LiTaO_3$, and Li_2ZrO_3) have been studied in the past, and SE degradation could be strongly suppressed, ultimately leading to increased performance and long-term cycling stability.[64,82–84] Although usually specific coating compositions are aimed for, it has been recently shown that especially for Ni-rich NCM CAMs this may differ in reality. For instance, surface residuals, such as Li_2CO_3 and LiOH, are known to be present on NCM CAMs, which are eventually incorporated into the coating and may play an important role in stabilizing the as-formed interface.[85] Moreover, one has to consider that the volume changes of CAMs upon charging and discharging not only create mechanical stress in the CAM (and on the cell level), but also exert similar stress to the interface between CAM and coating. Thus, the contact between coating and CAM may be deteriorated with continuous (de-)lithiation so that the protective function decreases or even vanishes. Additionally, interfacial reactions can also cause significant volume changes due to the different specific volumes of educts and products. If the volume changes resulting from such interfacial reactions are sufficiently pronounced, they can even lead to contact loss between CAM and SE.[86] As a result, specific coating chemistries and tailored synthetic procedures need to be developed for different CAM types. A detailed discussion about the functionality of CAM coating properties can be found elsewhere.[25] Please note, that recently the potential of halide SEs and polymers as protective surface coatings has been evaluated.[22,87]

To conclude, different factors have to be considered when designing the CAM and CAM PSD, which are summarized in **Figure 6**. Charge transport percolation, diffusion pathways inside the CAM, and active interface area are critical parameters which are influenced by the particle size distributions of CAM and SE. To increase the cathode performance, these parameters need to be adjusted complementary. While smaller particles offer the advantage of percolation and shorter diffusion pathways, their high specific surface area can create additional challenges. Therefore, tailored PSDs of CAM and SE are necessary, and these PSDs may be different for every system/combination.

4. Design of Individual CAM Types

In the following, we highlight current research trends for the application of different types of CAMs in SSBs. In particular, we compare layered lithium transition metal oxides ($LiMO_2$), polyanionic LFP, spinel-type LiM_2O_4/$LiNi_{0.5}Mn_{1.5}O_4$ (LMO/LNMO), and conversion-type materials (M_aX_b) and consider the different reaction mechanisms. Moreover, we discuss advantages and limitations of design methodologies for each type of CAM regarding their application in SSBs and propose additional solutions, which go beyond the state-of-the art.

4.1. Intercalation-Type (Layered) CAMs

In intercalation-type materials, lithium is stored in between layers typically consisting of transition metal and oxygen ions, similar to cars being parked in a multi-level parking garage. During the intercalation process, lithium ions enter the material from SE contacts and the added positive charge is immediately compensated by transfer of an electron from electronic contacts, effectively leading to the incorporation of a neutral lithium atom. After transfer, lithium diffuses inside the CAM toward the center of the material due to its concentration gradient. During deintercalation, the process takes place in reversed direction. We like to note that this process needs to be described as "chemical diffusion" of lithium, that is, the diffusion coefficient $\tilde{D}_{Li}$ includes kinetic (diffusion coefficients of ions and electrons) and thermodynamic contributions (thermodynamic factor). It is a nonlinear function of the lithium concentration.[88,89]

Intercalation-type layered lithium transition metal oxide CAMs with the general formula $LiMO_2$ find widespread application in LE-based LIBs and are widely investigated to be employed in SSBs. Usually, mixed transition metals are introduced referring to NCM or NCA materials (e.g., NCM811 or $LiNi_{0.8}Co_{0.15}Al_{0.05}O_2$). The strong interest in this class of materials is mainly driven by their superior volumetric energy density over other CAMs. However, they display two main issues when it comes to their application in SSBs. First of all, they operate at potentials high enough to cause the electrochemical oxidation of many highly conductive (mostly thiophosphate) SEs, leading to the progressive growth of a resistive CEI.[85,90] Second, they show relatively large volume changes upon (de-)lithiation, causing mechanical degradation of the secondary particles and leading to severe contact loss between CAM and SE.[14,86,91] Additionally, NCM materials exhibit anisotropic expansion and contraction along the crystallographic *c* and *a* directions and these unit cell distortions are creating significant internal stresses. Thus, design strategies for this class of materials need to minimize 1) the interfacial reactivity in contact with the SE and 2) mitigate detrimental (chemo-)mechanical effects.

In the first case, protective coatings mostly based on lithium-containing oxides with Nb, Ta, Ti, Zr, Al, or B are employed to alleviate (electro-)chemical oxidation of the SE via preventing direct contact between CAM and SE.[25,64,83,92–97] Protective surface coatings are especially relevant when using SEs with a narrow stability window, such as lithium thiophosphates. It should be noted that thiophosphate-based SEs generally tend to react with oxides (including the coating itself), due to the formation of energetically favorable phosphite/phosphate and sulfite/sulfate compounds, and chemical reactions are not completely avoided by protective CAM coatings.[93] However, coatings with sufficiently low electronic conductivity can shield the low chemical potential of lithium in the CAM, which attenuates the oxidation of the SE and has been shown to be beneficial to the cathode stability. While usually simple stoichiometric compounds have been targeted for the coating, it has recently been shown that the chemical composition obtained after the coating process may actually deviate from the targeted composition. Specifically, Ni-rich layered oxides show a natural presence of surface impurities, such as Li_2CO_3 and LiOH. Although contradictory results have demonstrated that Li residuals alone are already capable of somewhat stabilizing the SE/CAM interface,[84,98–102] they can be incorporated into the coating during preparation and may be advantageous when included in a controlled manner.[82,84,85,98,101] This might also be the reason why nominally binary oxide-based coatings show beneficial properties if applied to NCM-type materials for SSB applications, as

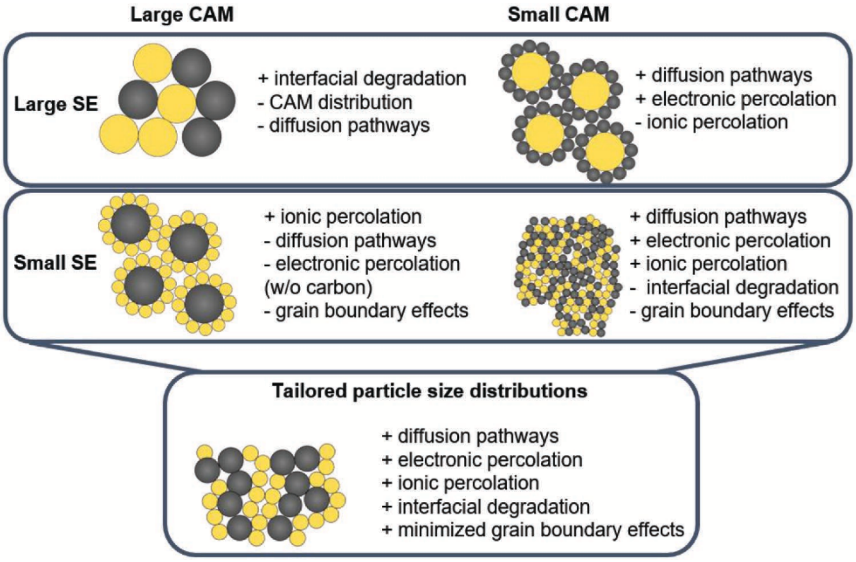

Figure 6. Influence of CAM and SE particle size on the different aspects of requirements for SSB cathodes. CAM particle size determines the properties on all three levels of composite cathodes and is an important design parameter for optimum cyclability in terms of kinetics and stability.

such oxides do not show significant lithium-ion conductivity.[103] Moreover, post processing of, for example, NCA can lead to significant improvement in performance, further emphasizing the role of surface residuals in Ni-rich layered oxide CAMs.[104] Apart from the development of customized coating compositions, the micro- and/or nano-structure of the coating itself may also play an important role.[105] This has been evidenced, among others, through the preparation of a high-quality coating on a Ni-rich NCM consisting of a carbonaceous (Li_2CO_3) layer and a ZrO_2 nanocrystal mono or bilayer. This kind of coating helped to improve considerably the cycling performance of thiophosphate-based SSBs.[106]

However, note that electronic percolation throughout the composite cathode still needs to be maintained by either plastic deformation of the coating during electrode calendaring or incomplete coverage of the coating with the combination of small CAM particles and (surface tailored) conductive carbon additives.[58] Besides the tailoring of the coating composition, the deposition technique itself will have a profound effect on the resulting CAM performance. Simple sol–gel approaches involving alkoxides are widely used in literature. However, the coating quality in terms of conformity and surface coverage is rather poor. Here, atomic layer deposition (ALD) may be an alternative route to produce coatings of uniform thickness and composition at the expense of costly equipment and processing. Combining the advantages of both sol–gel and ALD techniques, it has been demonstrated that by using highly reactive precursors in a liquid-phase process, ALD-like surface coatings can be achieved in the case of Al_2O_3.[107,108] Thus, we believe that properly adjusting precursor reactivities and taking into account the composition, reactivity, and functionalization of the CAM surface may lead to the development of simple, cost-effective approaches toward high-quality protective coatings.

On top of the (electro-)chemical instability at the SE/CAM interface, several irreversible changes take place in the CAM itself during (de-)lithiation. These involve detrimental phase transformations primarily at high SOC (e.g., from active layered into inactive rock-salt type structure) and (chemo-)mechanical degradation, such as contact loss and cracking of secondary particles. The aforementioned structural transformation is accompanied by the release of molecular oxygen, which can further react with the SE.[85,109,110] Such side reactions can additionally contribute to the buildup of a resistive SE/CAM interface and cause an increase in overpotential, which progressively lowers the cell performance. Traditionally, coating of CAM is pursued for mitigating both LE decomposition and rock-salt formation. However, in recent years, the focus has shifted toward bulk and surface doping, thereby preventing deleterious phase transformations via crystal lattice stabilization.[111,112] This can be achieved by substituting the redox-active transition metals with other redox-inactive elements, with NCA being the most prominent example.[113] As the substituent cannot be oxidized, some of the lithium in the structure cannot be extracted, thus preventing the formation of the rock-salt phase and lattice oxygen release.[113,114]

Apart from phase transformations, the (chemo-)mechanics of layered oxide-based CAMs during (de-)lithiation may cause detrimental effects. Pronounced volume changes occur when lithium is removed from the layered structure (e.g., $\Delta V_{max}/V \approx -5\%$ for NCM-811 at 4.3 V vs Li^+/Li).[76] This can lead to contact loss between CAM and SE or cracking of secondary CAM particles, which ultimately results in longer transport pathways and lower capacities (see Equation (1)).[86,91] In the case of LE-based LIBs, secondary particle fracture is not as harmful as for SSBs, because the LE can penetrate into the newly formed voids. Cracking even shortens the lithium-diffusion pathways and allows utilizing the full capacity of large

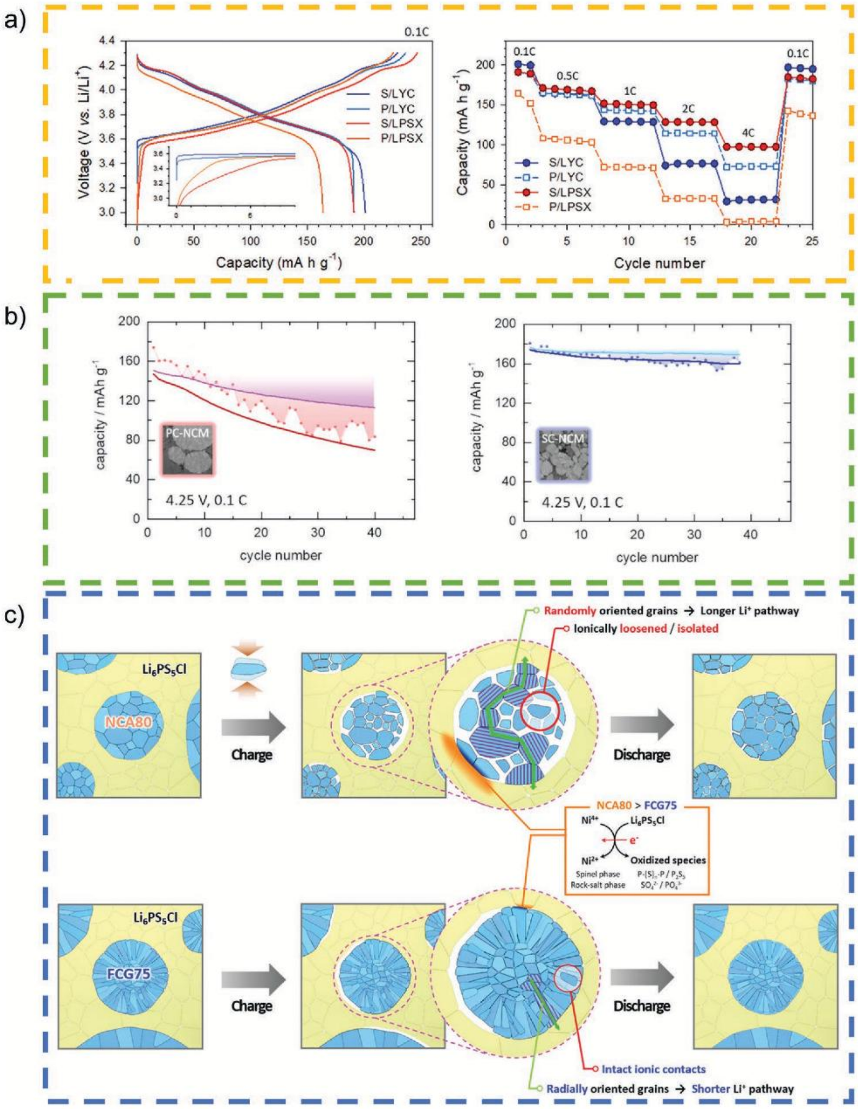

Figure 7. Strategies to overcome chemo-mechanical challenges in CAMs for SSBs: a) Influence of the choice of solid electrolyte (LYC = Li_3YCl_6, LPSX = Li_6PS_5Cl) on the performance of NCM with PC (P) or SC (S) particles. Reproduced with permission.[86] Copyright 2021, John Wiley and Sons. b) Influence of particle cracking on the cycling stability of SC and PC NCMs. Reproduced under terms of the CC-BY license.[91] Copyright 2021, The authors, published by IOP Publishing. c) Mitigating CAM particle cracking by the use of tailored "full concentration gradient" (FCG) CAM particles with rod-shaped crystallites. Reproduced with permission.[81] Copyright 2019, John Wiley and Sons.

(micrometer-sized) secondary CAM particles, which deliver lower specific capacities in SSBs.[7,13]

Addressing the issue of (chemo-)mechanical degradation, several strategies have been developed. One recently pursued approach is the development of SC NCM materials (**Figure 7**a,b).[86,91] Here, the major goal is the application of CAMs with monolithic grains. It is worth noting, that most of the investigated SC NCM materials do not exhibit a pure single crystalline morphology, but rather consist of agglomerates of micrometer-sized monolithic grains, as synthesizing fully separated single crystals is very challenging.[104,115,116] In theory, such SC NCM CAMs should prevent particle cracking but still be susceptible to loss of contact with the SE as a result of the unit-cell volume changes during (de-)lithiation. Indeed, several reports have shown the favorable mechanical behavior of SC CAMs in SSBs, leading to much improved morphological integrity and better capacity retention. Ni fractions of up to 88% with high capacity retention (96.8 % after 200 cycles)[86] as well as high specific capacities (210 mAh g^{-1})[117] have been realized in SSBs employing SC CAM so far. With a further increase in Ni content and additional facet engineering, even higher performance can be expected.[118,119]

The increased performance of SC CAMs is sometimes also explained by the smaller particle size compared with conventional PC secondary particles.[36] However, using PC CAMs with equally small secondary particles, which then have an even higher specific surface area, similar specific discharge capacities, and performance were found for NCM811, when setting the upper cutoff voltage to 4.15 V versus Li^+/Li. Only when it was increased to 4.35 V, thereby inducing secondary particle fracture, SC CAM outperformed the PC counterpart.[120] At the same time, depending on the mixing procedure and choice of SE, the use of small particles may lead to non-uniform spatial distribution of CAM in the cathode, resulting in SC particles touching and inducing strain on each other, thereby negating any initial benefits.[86] However, the particle size of SC materials can be controlled to some extent during the synthesis (and independently from the precursor particle size), thus optimization of both CAM size and CAM/SE particle-size ratio, as discussed before, can be achieved.[121]

The design of a cathode composite should also consider the excess lithium inventory required to compensate for side reactions at the anode. In LIBs, the capacity lost in the first cycle, linked to the kinetic limitations of the CAM at the end of discharge, is effectively used for the formation of the SEI. However, whether or not lithium excess is needed in SSBs depends greatly on the anode design. When such a compromise is not necessary, the particle size of the CAM can be tailored for high Coulomb efficiency in the first cycle. As previously discussed, by reducing the particle size of the layered oxide CAM, both a higher active surface area and shortened lithium diffusion length can be achieved, thereby improving the discharge capacity. Nevertheless, surface doping efforts toward structural stabilization have proven to be successful only for PC materials, with scarce literature about similar improvements for SC ones. Here, the required high-temperature processing might pose some challenges, with dopant diffusion inside the particle practically preventing selective surface modification.

Apart from the development of SC NCM CAMs, other crack mitigation strategies, such as the aforementioned gradient particles with rod-shaped primary particles (Figure 7c), have also been pursued.[81] Here, the primary crystallites are preferably grown along distinct crystallographic directions to counterbalance the anisotropic volume changes during (de-)lithiation and avoid cracking of the NCM secondary particles. Although contact loss between CAM and SE still occurs to some extent for this example, the overall cell pressure evolution and loss of active material are strongly reduced, thus improving the cell performance.

4.2. Insertion-Type CAMs

For insertion-type CAMs, lithium is stored on free lattice sites located within a rigid (3D) crystal framework, offering Li-ion conduction via vacancies and interstitial sites. Usually, the insertion/extraction of lithium causes minimal shrinkage or expansion of the host structure, hence a high structural stability of such CAMs during operation can be anticipated. In principle, two kinds of insertion-type CAMs have been investigated in SSBs so far, namely LFP (olivine structure) and LMO or LNMO (spinel structure). Due to their respective operating voltage of 3.5 and 4.5 V versus Li^+/Li, a much more severe SE decomposition occurs for LNMO, the higher voltage CAM. Although the redox potential of LFP seems suitable to be employed with most SEs without severe interfacial degradation, the main drawback lies in its intrinsic low electronic conductivity (in the range of 10^{-9} S cm^{-1} at r.t.). Thus, LFP is usually carbon coated or mixed with a large fraction of conductive additives to ensure sufficient electronic percolation, which creates issues in SSBs. Adding carbon has been shown to deteriorate cycling performance, especially in the case of thiophosphate-based SSBs.[58,122–124] This issue might be the reason why reports about LFP in inorganic SSBs are scarce, and LFP is usually combined with polymer-based SEs. Nevertheless, it has been claimed that the electronic conductivity of LFP can be significantly increased via doping on the Fe site (up to 10^{-3} S cm^{-1} at r.t.).[125] Yet, the performance of such doped CAMs in SSBs remains elusive. We believe that the intrinsically low partial electronic conductivity of polyanionic electrode materials may present the biggest hurdle toward their implementation in SSBs. Moreover, the application of LFP (or derivatives) in SSBs would most likely be cost-driven, as especially the gravimetric energy density is rather low compared to state-of-the-art NCM CAMs.

However, higher energy densities could possibly be achieved through the implementation of high-voltage spinel lithium manganese oxide-based CAMs (e.g., LMO or LNMO), which offer a redox potential of up to 4.7 V versus Li^+/Li. Nevertheless, according to published research data, it seems challenging to realize this potential advantage. Using LNMO together with, for example, lithium thiophosphates causes severe SE degradation and poor capacity retention.[126–129] To prevent such detrimental side reactions, conventional protective surface coatings have been applied to LNMO but without significant performance improvement. Normally, a specific discharge capacity of ≈80 mAh g^{-1} specific discharge capacity is achieved in literature for surface-protected LMO/LNMO CAMs in SSBs, which is relatively low compared to the theoretical specific capacity (147 mAh g^{-1} for LNMO). A recent study comparing different lithium transition metal oxide surface coatings on LNMO has shown that depending on the coating chemistry, an improvement over the pristine CAM can be achieved.[130] Additionally, the use of halide SEs, which offer a high oxidation stability may be another suitable alternative to enable high voltage CAMs such as LMO/LNMO in SSBs.

Achieving SSB performance close to the theoretical capacity of LMO-type CAMs needs further engineering on several parameters, which are generally important in the case of SSBs, such as the particle size, intragranular porosity, or the application of a protective surface layer.

4.3. Conversion-Type and In Situ Formed CAMs

Conversion-type CAMs undergo distinct phase changes during (de-)lithiation, that is, phases with very different physicochemical properties occur during cycling. This is different from intercalation- and insertion-type materials, which maintain their structure, that is, their overall properties remain similar during cycling. The key advantage of conversion-type CAMs (which, except for elemental sulfur, can be described as by M_aX_b, M: transition metal, X: anion) is their higher specific capacity while on the downside they show much larger volume changes. Typical values are several hundred mAh g^{-1} and several tens to a few hundred vol%, respectively. Additionally, the redox potential increases with the ionicity of the bond, that is, transition metal fluorides have the highest redox potentials. Among the transition metals, copper compounds show the highest redox potential. The "upper limit" is therefore found for CuF_2, which theoretically has a redox potential of 3.53 V versus Li^+/Li, that is, slightly below NCM CAMs. However, because the conversion reaction involves the formation of intermediate and amorphous phases, it is only partially reversible and typically (but not always, see below) leads to a nanoscopic structure comprising transition metal nanoparticles dispersed in an amorphous Li_cX matrix. Structural characterization of this nanoscopic/amorphous structure and theoretical description are more challenging than for other CAMs. Even for seemingly simple compounds, like FeF_3, FeS_2, CuS, Mn_3O_4, or MoS_2, the reaction mechanisms are still under debate.[131–136] Moreover, electrolyte decomposition takes place, leading to thick surface films and initial Coulomb efficiencies typically below 75%. Overall, the appearance of intermediates and the formation of nanoscopic/amorphous structures along with electrolyte decomposition lead to more sloping voltage profiles and often large voltage hysteresis (low energy efficiency).[137–140]

A challenge for using conversion-type CAMs in SSBs is often their poor electronic or ionic conductivity. Thus, conductive percolating networks cannot be created by the CAM alone, and additionally, the transport within the CAM particles limits the charge-transport kinetics. Hence, CAM nanosizing and addition of large amounts of conductive additive(s) are typically required, both of which is detrimental to the electrode capacity if SEs with a narrow electrochemical stability window are used.[41] Nevertheless, the use of SEs may overcome specific limitations of particular conversion reactions, such as the electrolyte instability or polysulfide solubility in the case of Li_2S or S_8 as CAMs. The confinement of the active material in a SE may also help to mitigate undesired particle growth during cycling. However, at the same time, the mechanical properties (hardness, volume expansion, etc.) become more important when designing conversion-type CAMs for SSB applications.

Several conversion-type CAMs have been explored for SSBs in the last years among FeS_2, CuS, and S_8. FeS_2 (pyrite) has a theoretical specific capacity and cell voltage of 894 mAh g^{-1} and 1.84 V, respectively. Similar to LE-based LIBs, the CAM performance in the experiment deviates from this ideal case.[141] Clear steps in the voltage profile are only observed at elevated temperatures or at very small currents, for example, using polymer electrolytes (120 °C)[142] or inorganic glass electrolytes (20–60 °C).[100,143] While there has been dispute over the active phases during cycling, Yersak et al. demonstrated that the application of SEs leads to significant improvements in cycle life compared to LEs.[100] The same authors also confirmed the formation of FeS_2 upon charging (along with non-stoichiometric FeS_y and sulfur), that is, a multiphase mixture is formed. At r.t., cell cycling still shows an issue due to high polarization although nanosizing of the active material can be a strategy to mitigate this.[144] The need for particularly careful electrode optimization, for example, regarding particle size in the case of FeS_2, is also obvious from its comparably high Mohs hardness (6.0–6.5) and large electrode expansion during initial lithiation (163%).

CuS (Covellite) is a naturally occurring mineral. Special aspects of using CuS as electrode material are the complex Cu–S phase diagram, which shows several non-stoichiometric compounds, such as $Cu_{2-x}S$. Compared to FeS_2, the energy density of CuS is lower, but it is much softer, shows a slightly higher cell voltage, and a smaller volume expansion. A key advantage is that copper sulfides are electronically conductive (e.g., 870 S cm^{-1} at r.t. for CuS)[133] and also show a high conductivity for Cu ions,[145] which can help to minimize the amounts of SE and conductive additives required in the SSB cathode. Among the compounds tested in conversion reactions, CuS is quite unique in that the material undergoes a displacement reaction, in contrast to the nanostructure formation seen for other conversion electrodes. This means that macroscopic copper forms during lithiation of CuS. This has been described in LE-based LIBs by Debart et al.[132] but recently also found to occur in SSBs.[146] In SSBs with LPS as SE, Aggunda et al. found a network of μm-sized Cu crystals after discharge, which were even visible by eye.[146] No conductive additive was used in this study.

Both metal sulfides discussed here show a mixed cationic (Fe/Cu) and anionic (S) redox chemistry. This is naturally different for pure sulfur, which is another promising conversion electrode for SSBs and has drawn great attention in the last years.[147–150] The main reason is the low cost of sulfur and its high theoretical specific capacity of 1672 mAh g^{-1}, providing a high specific energy (the advantage is less considerable with respect to volumetric energy density). The use of SEs prevents the well-known dissolution of soluble polysulfide intermediates that cause a shuttle mechanism and electrode degradation in cells with LEs. The lack of dissolution/precipitation processes during cell cycling also leads to a simpler, in this case very flat voltage profile of SSBs, compared to their analogues with LEs. In fact, experiments indeed show a flat voltage profile in agreement with the phase diagram (Li_2S being the only stable binary lithium-sulfur compound). The main challenge of using sulfur in SSBs is, next to the volume expansion of around 80%, that both the charge (sulfur) and discharge (Li_2S) products are electronic insulators. This requires nanosizing and the addition of large amounts of conductive additives compared to other conversion materials.

Another approach is to combine sulfur and transition metal sulfides in a single electrode, that is, using $CuS+S_8$ or FeS_2+S_8 composites as electrodes. This approach has been realized in 2003 already by Hayashi et al.,[151] but is nowadays more frequently applied.[152–154] Overall, the large number of conversion reactions and possible combinations in composite electrodes provide a versatile playground for developing conversion-type electrodes for SSBs. The three cases discussed here (FeS_2, CuS, and S_8) are especially appealing, as they show unique properties. Few grave challenges, however, apply to most of the conversion reactions. First, their large capacities are intrinsically coupled to large volume changes that need to be considered in the electrode and overall cell design. The mechanical properties of the CAM, SE, and composite probably need to be tailored accordingly. Second, in many cases, nanostructures form during cycling, which show a high surface area that can trigger severe side reactions with the SE, thus causing fast capacity decay. Third, in most studies on conversion electrodes, cells are assembled in the charged state. This means that lithium (or a lithiated compound) is needed as a counter electrode, which is a clear drawback for commercialization. It is therefore important to draw more attention on lithiated conversion-type CAMs, however, identifying and synthesizing such compounds is not trivial.

It is worth noting, that several other CAMs are being explored in SSBs. In a recent approach, a lithium argyrodite SE has been used in a simple SE/C composite as a precursor for the in situ formation of redox active sulfur and phosphorus phases, thus achieving another type of two-element redox activity.[155] Additionally, organic CAMs, in which multi-electron transfer reactions occur during (dis-)charging, have been used recently in SSBs.[156–158]

5. Guidelines in Short

So far, we have identified and reviewed several aspects that play a role in composite cathodes for SSBs, and have shown how these affect different types of CAMs. In the following, we summarize the essential aspects that need to be considered when designing CAMs on different length scales for SSBs.

5.1. Cathode Level

Effective electronic and ionic percolation as well as full active material utilization are of prime importance—often expressed by partial effective conductivities. CAM/SE PSDs and particle shapes should allow ideally close packing. For optimal charge transport, it is crucial to reduce porosity to a bare minimum and to increase the effective ionic conductivity of crystalline SEs through grain boundary design. Gradient cathodes may require different CAMs and/or CAM particle sizes at the current collector and separator side. In an ideal case, CAM and SE particle size and distribution are designed simultaneously.

5.2. Particle Level

Particle cracking and internal porosity in the CAM have to be avoided. Particle sizes and shapes have to be adjusted to the electronic and ionic transport properties, which ultimately determine the optimum size. Gradient particles may show benefits with respect to avoiding (chemo-)mechanical degradation. Doping grain boundaries may be an effective strategy to achieve more stability and/or adjust kinetics.

5.3. Interface Level

A stable CAM/SE interface has to be achieved, either by coating, by the formation of a native passivating CEI, or both. Coatings should be primarily lithium-ion conducting but allow sufficient electronic percolation within the electronic conduction pathways through the cathode generated by the CAM particles and, if required, conductive additives. Contact of SE and CAM even during volume changes has to be maintained, that is, the protective surface layer needs to show some flexibility. Also, interactions of the CAM surface with binder and/or solvents during processing have to be considered.

5.4. Modeling

Usually, modeling studies do not offer suggestions for improvements on the CAM level. Instead, they rather focus on optimizing the SE (i.e., achieving high ionic conductivity). In our opinion, this lowers the degree of freedom, and we encourage to rethink the CAM with other particle shapes, sizes, elastic properties etc., and to widen the range of materials to SC or conversion-type CAMs. In addition, sophisticated mechanical models that can be coupled to electrochemical and thermal models on the microstructure level are required to gain more insight into pressure and temperature effects.

6. Conclusions

In summary, we have outlined the specific challenges and resulting requirements for the application of inorganic CAMs in SSBs. In particular, we focused on compiling recent strategies to tailor specific CAMs with respect to certain requirements related to (chemo-)mechanics and interfacial degradation occurring upon cycling. However, we finally like to emphasize that the design of CAMs for SSB applications cannot be conducted without taking the nature of the utilized SE into account. More precisely, different types of CAMs may require different types of SEs with certain matching properties (i.e., hard CAM together with soft SE and vice versa). Thus, we believe that in the case of SSBs, novel approaches are needed to improve the performance of the respective composite cathodes, which may include large-scale machine-aided screening approaches to identify best possible material combinations. This becomes even more important as cathodes for SSBs not only need to be optimized from a materials perspective (i.e., intrinsic material properties and surface chemistry) but their integration into a composite cathode may lead to new effects on a cell level. Modeling approaches should also tackle (chemo-)mechanical and fabrication processes for SSB cathodes in order to mitigate stress and limit pore space as much as possible. Finally, we provide scientists in the field with a comprehensive CAM development guideline targeting improved (inorganic) SSBs.

Acknowledgements

P.M. and F.S. contributed equally to this work. This work has been partly funded by the BMBF cluster of competence for solid state batteries (FestBatt, Bundesministerium für Bildung und Forschung) grant identifiers 03XP0177A/03XP0430A (thiophosphate platform), 03XP0433A (characterization platform), and 03XP0180/03XP0431 (coordination project). F.S. thanks the Fond der Chemischen Industrie (FCI) for financial support through a Liebig fellowship. The authors thank Christian Grupe and Elisa Monte for graphical assistance.

Open access funding enabled and organized by Projekt DEAL.

Conflict of Interest

The authors declare no conflict of interest.

Keywords

chemo-mechanics, electrochemical energy storage, lithium-ion batteries, microstructures, NCM, particle sizes, thiophosphates

Received: April 26, 2022
Revised: July 3, 2022
Published online: July 28, 2022

[1] J. Janek, W. G. Zeier, *Nat Energy* **2016**, *1*, 16141.
[2] J. Chen, J. Wu, X. Wang, A. Zhou, Z. Yang, *Energy Storage Mater.* **2021**, *35*, 70.
[3] Y.-K. Sun, *ACS Energy Lett.* **2020**, *5*, 3221.
[4] S. Nanda, A. Gupta, A. Manthiram, *Adv. Energy Mater.* **2021**, *11*, 2000804.
[5] Q. Dai, J. C. Kelly, L. Gaines, M. Wang, *Batteries* **2019**, *5*, 48.
[6] Y. Qian, P. Niehoff, M. Börner, M. Grützke, X. Mönnighoff, P. Behrends, S. Nowak, M. Winter, F. M. Schappacher, *J. Power Sources* **2016**, *329*, 31.
[7] E. Trevisanello, R. Ruess, G. Conforto, F. H. Richter, J. Janek, *Adv. Energy Mater.* **2021**, *11*, 2003400.
[8] N. P. W. Pieczonka, Z. Liu, P. Lu, K. L. Olson, J. Moote, B. R. Powell, J.-H. Kim, *J. Phys. Chem. C* **2013**, *117*, 15947.
[9] W. Cho, S.-M. Kim, J. H. Song, T. Yim, S.-G. Woo, K.-W. Lee, J.-S. Kim, Y.-J. Kim, *J. Power Sources* **2015**, *282*, 45.
[10] T. Li, X.-Z. Yuan, L. Zhang, D. Song, K. Shi, C. Bock, *Electrochem. Energy Rev.* **2020**, *3*, 43.
[11] F. Walther, R. Koerver, T. Fuchs, S. Ohno, J. Sann, M. Rohnke, W. G. Zeier, J. Janek, *Chem. Mater.* **2019**, *31*, 3745.
[12] R. Koerver, F. Walther, I. Aygün, J. Sann, C. Dietrich, W. G. Zeier, J. Janek, *J. Mater. Chem. A* **2017**, *5*, 22750.
[13] R. Ruess, S. Schweidler, H. Hemmelmann, G. Conforto, A. Bielefeld, D. A. Weber, J. Sann, M. T. Elm, J. Janek, *J. Electrochem. Soc.* **2020**, *167*, 100532.
[14] R. Koerver, W. Zhang, L. de Biasi, S. Schweidler, A. O. Kondrakov, S. Kolling, T. Brezesinski, P. Hartmann, W. G. Zeier, J. Janek, *Energy Environ. Sci.* **2018**, *11*, 2142.
[15] R. C. Agrawal, G. P. Pandey, *J. Phys. D: Appl. Phys.* **2008**, *41*, 223001.
[16] J. C. Bachman, S. Muy, A. Grimaud, H.-H. Chang, N. Pour, S. F. Lux, O. Paschos, F. Maglia, S. Lupart, P. Lamp, L. Giordano, Y. Shao-Horn, *Chem. Rev.* **2016**, *116*, 140.
[17] T. Famprikis, P. Canepa, J. A. Dawson, M. S. Islam, C. Masquelier, *Nat. Mater.* **2019**, *18*, 1278.
[18] Z. Gao, H. Sun, L. Fu, F. Ye, Y. Zhang, W. Luo, Y. Huang, *Adv. Mater.* **2018**, *30*, e1705702.
[19] K. H. Park, Q. Bai, D. H. Kim, D. Y. Oh, Y. Zhu, Y. Mo, Y. S. Jung, *Adv. Energy Mater.* **2018**, *8*, 1800035.
[20] L. Long, S. Wang, M. Xiao, Y. Meng, *J. Mater. Chem. A* **2016**, *4*, 10038.
[21] K. J. Kim, M. Balaish, M. Wadaguchi, L. Kong, J. L. M. Rupp, *Adv. Energy Mater.* **2021**, *11*, 2002689.
[22] X. Li, J. Liang, X. Yang, K. R. Adair, C. Wang, F. Zhao, X. Sun, *Energy Environ. Sci.* **2020**, *13*, 1429.
[23] J. P. Beaupain, K. Waetzig, S.-K. Otto, A. Henss, J. Janek, M. Malaki, A. Pokle, J. Müller, B. Butz, K. Volz, M. Kusnezoff, A. Michaelis, *ACS Appl. Mater. Interfaces* **2021**, *13*, 47488.
[24] J. R. Nair, L. Imholt, G. Brunklaus, M. Winter, *Electrochem. Soc. Interface* **2019**, *28*, 55.
[25] S. P. Culver, R. Koerver, W. G. Zeier, J. Janek, *Adv. Energy Mater.* **2019**, *9*, 1900626.
[26] T. Koç, F. Marchini, G. Rousse, R. Dugas, J.-M. Tarascon, *ACS Appl. Energy Mater.* **2021**, *4*, 13575.
[27] S. Sun, C.-Z. Zhao, H. Yuan, Y. Lu, J.-K. Hu, J.-Q. Huang, Q. Zhang, *Mater. Futures* **2021**, *1*, 012101.
[28] S. Randau, D. A. Weber, O. Kötz, R. Koerver, P. Braun, A. Weber, E. Ivers-Tiffée, T. Adermann, J. Kulisch, W. G. Zeier, F. H. Richter, J. Janek, *Nat. Energy* **2020**, *5*, 259.
[29] N. Kaiser, S. Spannenberger, M. Schmitt, M. Cronau, Y. Kato, B. Roling, *J. Power Sources* **2018**, *396*, 175.
[30] T. Shi, Q. Tu, Y. Tian, Y. Xiao, L. J. Miara, O. Kononova, G. Ceder, *Adv. Energy Mater.* **2020**, *10*, 1902881.
[31] P. Minnmann, L. Quillman, S. Burkhardt, F. H. Richter, J. Janek, *J. Electrochem. Soc.* **2021**, *168*, 040537.
[32] J. Park, K. T. Kim, D. Y. Oh, D. Jin, D. Kim, Y. S. Jung, Y. M. Lee, *Adv. Energy Mater.* **2020**, *10*, 2001563.
[33] W. Zhang, D. A. Weber, H. Weigand, T. Arlt, I. Manke, D. Schröder, R. Koerver, T. Leichtweiss, P. Hartmann, W. G. Zeier, J. Janek, *ACS Appl. Mater. Interfaces* **2017**, *9*, 17835.
[34] J. Kim, M. Eom, S. Noh, D. Shin, *J. Power Sources* **2013**, *244*, 476.
[35] Y. J. Nam, D. Y. Oh, S. H. Jung, Y. S. Jung, *J. Power Sources* **2018**, *375*, 93.
[36] A. Bielefeld, D. A. Weber, J. Janek, *J. Phys. Chem. C* **2019**, *123*, 1626.
[37] A. Bielefeld, D. A. Weber, J. Janek, *ACS Appl. Mater. Interfaces* **2020**, *12*, 12821.
[38] G. Deysher, P. Ridley, S.-Y. Ham, J.-M. Doux, Y.-T. Chen, E. A. Wu, D. H. Tan, A. Cronk, J. Jang, Y. S. Meng, *Mater. Today Phys.* **2022**, *24*, 100679.
[39] D. Hlushkou, A. E. Reising, N. Kaiser, S. Spannenberger, S. Schlabach, Y. Kato, B. Roling, U. Tallarek, *J. Power Sources* **2018**, *396*, 363.
[40] A. Bielefeld, D. A. Weber, R. Rueß, V. Glavas, J. Janek, *J. Electrochem. Soc.* **2022**, *169*, 020539.
[41] G. F. Dewald, S. Ohno, J. G. C. Hering, J. Janek, W. G. Zeier, *Batteries Supercaps* **2021**, *4*, 183.
[42] T. Asano, S. Yubuchi, A. Sakuda, A. Hayashi, M. Tatsumisago, *J. Electrochem. Soc.* **2017**, *164*, A3960.
[43] F. Strauss, T. Bartsch, L. de Biasi, A.-Y. Kim, J. Janek, P. Hartmann, T. Brezesinski, *ACS Energy Lett.* **2018**, *3*, 992.
[44] C. Park, S. Lee, K. Kim, M. Kim, S. Choi, D. Shin, *J. Electrochem. Soc.* **2019**, *166*, A5318.
[45] V. Laue, N. Wolff, F. Röder, U. Krewer, *Energy Technol.* **2020**, *8*, 1801049.
[46] J. H. Teo, F. Strauss, Đ. Tripković, S. Schweidler, Y. Ma, M. Bianchini, J. Janek, T. Brezesinski, *Cell Rep. Phys. Sci.* **2021**, *2*, 100465.
[47] M. Ghidiu, J. Ruhl, S. P. Culver, W. G. Zeier, *J. Mater. Chem. A* **2019**, *7*, 17735.
[48] S. Ohno, R. Koerver, G. Dewald, C. Rosenbach, P. Titscher, D. Steckermeier, A. Kwade, J. Janek, W. G. Zeier, *Chem. Mater.* **2019**, *31*, 2930.
[49] S. Ohno, C. Rosenbach, G. F. Dewald, J. Janek, W. G. Zeier, *Adv. Funct. Mater.* **2021**, *31*, 2010620.
[50] M. Falco, S. Ferrari, G. B. Appetecchi, C. Gerbaldi, *Mol. Syst. Des. Eng.* **2019**, *4*, 850.
[51] A. Neumann, S. Randau, K. Becker-Steinberger, T. Danner, S. Hein, Z. Ning, J. Marrow, F. H. Richter, J. Janek, A. Latz, *ACS Appl. Mater. Interfaces* **2020**, *12*, 9277.

[52] M. Finsterbusch, T. Danner, C.-L. Tsai, S. Uhlenbruck, A. Latz, O. Guillon, *ACS Appl. Mater. Interfaces* **2018**, *10*, 22329.
[53] G. Bucci, T. Swamy, Y.-M. Chiang, W. C. Carter, *J. Mater. Chem. A* **2017**, *5*, 19422.
[54] C. S. Giménez, L. Helmers, C. Schilde, A. Diener, A. Kwade, *Chem. Eng. Technol.* **2020**, *43*, 819.
[55] S. Yamakawa, S. Ohta, T. Kobayashi, *Solid State Ionics* **2020**, *344*, 115079.
[56] A. Ohashi, M. Kodama, S. Xueying, S. Hori, K. Suzuki, R. Kanno, S. Hirai, *J. Power Sources* **2020**, *470*, 228437.
[57] M. B. Dixit, A. Parejiya, N. Muralidharan, R. Essehli, R. Amin, I. Belharouak, *Energy Storage Mater.* **2021**, *40*, 239.
[58] S. Randau, F. Walther, A. Neumann, Y. Schneider, R. S. Negi, B. Mogwitz, J. Sann, K. Becker-Steinberger, T. Danner, S. Hein, A. Latz, F. H. Richter, J. Janek, *Chem. Mater.* **2021**, *33*, 1380.
[59] D. Bistri, A. Afshar, C. V. Di Leo, *Meccanica* **2021**, *56*, 1523.
[60] J.-M. Doux, Y. Yang, D. H. S. Tan, H. Nguyen, E. A. Wu, X. Wang, A. Banerjee, Y. S. Meng, *J. Mater. Chem. A* **2020**, *8*, 5049.
[61] D. H. S. Tan, E. A. Wu, H. Nguyen, Z. Chen, M. A. T. Marple, J.-M. Doux, X. Wang, H. Yang, A. Banerjee, Y. S. Meng, *ACS Energy Lett.* **2019**, *4*, 2418.
[62] R. Usiskin, J. Maier, *J. Electrochem. Soc.* **2020**, *167*, 080505.
[63] D. Y. Oh, Y. J. Nam, K. H. Park, S. H. Jung, K. T. Kim, A. R. Ha, Y. S. Jung, *Adv. Energy Mater.* **2019**, *9*, 1802927.
[64] S. Ito, S. Fujiki, T. Yamada, Y. Aihara, Y. Park, T. Y. Kim, S.-W. Baek, J.-M. Lee, S. Doo, N. Machida, *J. Power Sources* **2014**, *248*, 943.
[65] T. Inada, *Solid State Ionics* **2003**, *158*, 275.
[66] F. Hippauf, B. Schumm, S. Doerfler, H. Althues, S. Fujiki, T. Shiratsuchi, T. Tsujimura, Y. Aihara, S. Kaskel, *Energy Storage Mater.* **2019**, *21*, 390.
[67] M. Yamamoto, Y. Terauchi, A. Sakuda, M. Takahashi, *Sci. Rep.* **2018**, *8*, 1212.
[68] Y. Xiao, K. Turcheniuk, A. Narla, A.-Y. Song, X. Ren, A. Magasinski, A. Jain, S. Huang, H. Lee, G. Yushin, *Nat. Mater.* **2021**, *20*, 984.
[69] R. E. Usiskin, J. Maier, *Phys. Chem. Chem. Phys.* **2018**, *20*, 16449.
[70] A. van der Ven, J. Bhattacharya, A. A. Belak, *Acc. Chem. Res.* **2013**, *46*, 1216.
[71] Y. Zhu, C. Wang, *J. Phys. Chem. C* **2010**, *114*, 2830.
[72] L. Froboese, J. F. van der Sichel, T. Loellhoeffel, L. Helmers, A. Kwade, *J. Electrochem. Soc.* **2019**, *166*, A318.
[73] S. Brutti, G. Greco, P. Reale, S. Panero, *Electrochim. Acta* **2013**, *106*, 483.
[74] D. Wang, X. Wu, Z. Wang, L. Chen, *J. Power Sources* **2005**, *140*, 125.
[75] Q. Liu, Y. Liu, F. Yang, H. He, X. Xiao, Y. Ren, W. Lu, E. Stach, J. Xie, *ACS Appl. Mater. Interfaces* **2018**, *10*, 4622.
[76] L. de Biasi, A. O. Kondrakov, H. Geßwein, T. Brezesinski, P. Hartmann, J. Janek, *J. Phys. Chem. C* **2017**, *121*, 26163.
[77] S. Payandeh, D. Goonetilleke, M. Bianchini, J. Janek, T. Brezesinski, *Curr. Opin. Electrochem.* **2022**, *31*, 100877.
[78] H. Jeon, D.-H. Kwon, H. Kim, J.-H. Lee, Y. Jun, J.-W. Son, S. Park, *Chem. Eng. J.* **2022**, *445*, 136828.
[79] F. Strauss, L. de Biasi, A.-Y. Kim, J. Hertle, S. Schweidler, J. Janek, P. Hartmann, T. Brezesinski, *ACS Mater. Lett.* **2020**, *2*, 84.
[80] A. Banerjee, X. Wang, C. Fang, E. A. Wu, Y. S. Meng, *Chem. Rev.* **2020**, *120*, 6878.
[81] S. H. Jung, U.-H. Kim, J.-H. Kim, S. Jun, C. S. Yoon, Y. S. Jung, Y.-K. Sun, *Adv. Energy Mater.* **2020**, *10*, 1903360.
[82] F. Strauss, J. H. Teo, J. Maibach, A.-Y. Kim, A. Mazilkin, J. Janek, T. Brezesinski, *ACS Appl. Mater. Interfaces* **2020**, *12*, 57146.
[83] W. Zhang, F. H. Richter, S. P. Culver, T. Leichtweiss, J. G. Lozano, C. Dietrich, P. G. Bruce, W. G. Zeier, J. Janek, *ACS Appl. Mater. Interfaces* **2018**, *10*, 22226.
[84] A.-Y. Kim, F. Strauss, T. Bartsch, J. H. Teo, J. Janek, T. Brezesinski, *Sci. Rep.* **2021**, *11*, 5367.
[85] F. Walther, F. Strauss, X. Wu, B. Mogwitz, J. Hertle, J. Sann, M. Rohnke, T. Brezesinski, J. Janek, *Chem. Mater.* **2021**, *33*, 2110.
[86] Y. Han, S. H. Jung, H. Kwak, S. Jun, H. H. Kwak, J. H. Lee, S.-T. Hong, Y. S. Jung, *Adv. Energy Mater.* **2021**, *11*, 2100126.
[87] S. Sen, E. Trevisanello, E. Niemöller, B.-X. Shi, F. J. Simon, F. H. Richter, *J. Mater. Chem. A* **2021**, *9*, 18701.
[88] M. Weiss, R. Ruess, J. Kasnatscheew, Y. Levartovsky, N. R. Levy, P. Minnmann, L. Stolz, T. Waldmann, M. Wohlfahrt-Mehrens, D. Aurbach, M. Winter, Y. Ein-Eli, J. Janek, *Adv. Energy Mater.* **2021**, *11*, 2101126.
[89] A. J. Merryweather, C. Schnedermann, Q. Jacquet, C. P. Grey, A. Rao, *Nature* **2021**, *594*, 522.
[90] S. Wang, R. Fang, Y. Li, Y. Liu, C. Xin, F. H. Richter, C.-W. Nan, *J. Materiomics* **2021**, *7*, 209.
[91] G. Conforto, R. Ruess, D. Schröder, E. Trevisanello, R. Fantin, F. H. Richter, J. Janek, *J. Electrochem. Soc.* **2021**, *168*, 070546.
[92] K. Takada, N. Ohta, L. Zhang, K. Fukuda, I. Sakaguchi, R. Ma, M. Osada, T. Sasaki, *Solid State Ionics* **2008**, *179*, 1333.
[93] Y.-Q. Zhang, Y. Tian, Y. Xiao, L. J. Miara, Y. Aihara, T. Tsujimura, T. Shi, M. C. Scott, G. Ceder, *Adv. Energy Mater.* **2020**, *10*, 1903778.
[94] R. S. Negi, P. Minnmann, R. Pan, S. Ahmed, M. J. Herzog, K. Volz, R. Takata, F. Schmidt, J. Janek, M. T. Elm, *Chem. Mater.* **2021**, *33*, 6713.
[95] Y. Zhao, K. Zheng, X. Sun, *Joule* **2018**, *2*, 2583.
[96] A. Gurung, J. Pokharel, A. Baniya, R. Pathak, K. Chen, B. S. Lamsal, N. Ghimire, W.-H. Zhang, Y. Zhou, Q. Qiao, *Sustainable Energy Fuels* **2019**, *3*, 3279.
[97] M. Yoon, Y. Dong, J. Hwang, J. Sung, H. Cha, K. Ahn, Y. Huang, S. J. Kang, J. Li, J. Cho, *Nat. Energy* **2021**, *6*, 362.
[98] A.-Y. Kim, F. Strauss, T. Bartsch, J. H. Teo, T. Hatsukade, A. Mazilkin, J. Janek, P. Hartmann, T. Brezesinski, *Chem. Mater.* **2019**, *31*, 9664.
[99] S. Deng, Q. Sun, M. Li, K. Adair, C. Yu, J. Li, W. Li, J. Fu, X. Li, R. Li, Y. Hu, N. Chen, H. Huang, L. Zhang, S. Zhao, S. Lu, X. Sun, *Energy Storage Mater.* **2021**, *35*, 661.
[100] T. A. Yersak, H. A. Macpherson, S. C. Kim, V.-D. Le, C. S. Kang, S.-B. Son, Y.-H. Kim, J. E. Trevey, K. H. Oh, C. Stoldt, S.-H. Lee, *Adv. Energy Mater.* **2013**, *3*, 120.
[101] Y. Zhang, X. Sun, D. Cao, G. Gao, Z. Yang, H. Zhu, Y. Wang, *Energy Storage Mater.* **2021**, *41*, 505.
[102] F. Strauss, S. Payandeh, A. Kondrakov, T. Brezesinski, *Mater. Futures* **2022**, *1*, 023501.
[103] D. Kitsche, Y. Tang, Y. Ma, D. Goonetilleke, J. Sann, F. Walther, M. Bianchini, J. Janek, T. Brezesinski, *ACS Appl. Energy Mater.* **2021**, *4*, 7338.
[104] R. Fantin, E. Trevisanello, R. Ruess, A. Pokle, G. Conforto, F. H. Richter, K. Volz, J. Janek, *Chem. Mater.* **2021**, *33*, 2624.
[105] S. Payandeh, F. Strauss, A. Mazilkin, A. Kondrakov, T. Brezesinski, *Nano Res. Energy* **2022**, *1*, https://doi.org/10.26599/NRE.2022.9120016.
[106] Y. Ma, J. H. Teo, F. Walther, Y. Ma, R. Zhang, A. Mazilkin, Y. Tang, D. Goonetilleke, J. Janek, M. Bianchini, T. Brezesinski, *Adv. Funct. Mater.* **2022**, *32*, 2111829.
[107] S. Neudeck, F. Strauss, G. Garcia, H. Wolf, J. Janek, P. Hartmann, T. Brezesinski, *Chem. Commun.* **2019**, *55*, 2174.
[108] R. S. Negi, S. P. Culver, A. Mazilkin, T. Brezesinski, M. T. Elm, *ACS Appl. Mater. Interfaces* **2020**, *12*, 31392.
[109] J. H. Teo, F. Strauss, F. Walther, Y. Ma, S. Payandeh, T. Scherer, M. Bianchini, J. Janek, T. Brezesinski, *Mater. Futures* **2022**, *1*, 015102.
[110] F. Strauss, J. H. Teo, A. Schiele, T. Bartsch, T. Hatsukade, P. Hartmann, J. Janek, T. Brezesinski, *ACS Appl. Mater. Interfaces* **2020**, *12*, 20462.
[111] A. Liu, N. Zhang, H. Li, J. Inglis, Y. Wang, S. Yin, H. Wu, J. R. Dahn, *J. Electrochem. Soc.* **2019**, *166*, A4025.

[112] A. Aishova, G.-T. Park, C. S. Yoon, Y.-K. Sun, *Adv. Energy Mater.* **2020**, *10*, 1903179.

[113] Z.-Y. Li, H. Guo, X. Ma, K. Sun, D. Chen, L. He, S. Han, *J. Phys. Chem. C* **2019**, *123*, 19298.

[114] H. Li, A. Liu, N. Zhang, Y. Wang, S. Yin, H. Wu, J. R. Dahn, *Chem. Mater.* **2019**, *31*, 7574.

[115] J. Langdon, A. Manthiram, *Energy Storage Mater.* **2021**, *37*, 143.

[116] A. Liu, N. Zhang, J. E. Stark, P. Arab, H. Li, J. R. Dahn, *J. Electrochem. Soc.* **2021**, *168*, 050506.

[117] C. Doerrer, I. Capone, S. Narayanan, J. Liu, C. R. M. Grovenor, M. Pasta, P. S. Grant, *ACS Appl. Mater. Interfaces* **2021**, *13*, 37809.

[118] J. Zhu, G. Chen, *J. Mater. Chem. A* **2019**, *7*, 5463.

[119] J. Zhu, S. Sharifi-Asl, J. C. Garcia, H. H. Iddir, J. R. Croy, R. Shahbazian-Yassar, G. Chen, *ACS Appl. Energy Mater.* **2020**, *3*, 4799.

[120] X. Liu, B. Zheng, J. Zhao, W. Zhao, Z. Liang, Y. Su, C. Xie, K. Zhou, Y. Xiang, J. Zhu, H. Wang, G. Zhong, Z. Gong, J. Huang, Y. Yang, *Adv. Energy Mater.* **2021**, *11*, 2003583.

[121] L. Zheng, J. C. Bennett, M. N. Obrovac, *J. Electrochem. Soc.* **2020**, *167*, 130536.

[122] F. Strauss, D. Stepien, J. Maibach, L. Pfaffmann, S. Indris, P. Hartmann, T. Brezesinski, *RSC Adv.* **2020**, *10*, 1114.

[123] F. Walther, S. Randau, Y. Schneider, J. Sann, M. Rohnke, F. H. Richter, W. G. Zeier, J. Janek, *Chem. Mater.* **2020**, *32*, 6123.

[124] W. Zhang, T. Leichtweiß, S. P. Culver, R. Koerver, D. Das, D. A. Weber, W. G. Zeier, J. Janek, *ACS Appl. Mater. Interfaces* **2017**, *9*, 35888.

[125] C. Wang, J. Hong, *Electrochem. Solid-State Lett.* **2007**, *10*, A65.

[126] J. Auvergniot, A. Cassel, J.-B. Ledeuil, V. Viallet, V. Seznec, R. Dedryvère, *Chem. Mater.* **2017**, *29*, 3883.

[127] H. Kitaura, A. Hayashi, K. Tadanaga, M. Tatsumisago, *J. Electrochem. Soc.* **2010**, *157*, A407.

[128] G. Oh, M. Hirayama, O. Kwon, K. Suzuki, R. Kanno, *Chem. Mater.* **2016**, *28*, 2634.

[129] S. Yubuchi, Y. Ito, T. Matsuyama, A. Hayashi, M. Tatsumisago, *Solid State Ionics* **2016**, *285*, 79.

[130] G. Liu, Y. Lu, H. Wan, W. Weng, L. Cai, Z. Li, X. Que, H. Liu, X. Yao, *ACS Appl. Mater. Interfaces* **2020**, *12*, 28083.

[131] L. Zhang, D. Sun, J. Kang, J. Feng, H. A. Bechtel, L.-W. Wang, E. J. Cairns, J. Guo, *Nano Lett.* **2018**, *18*, 1466.

[132] A. Débart, L. Dupont, R. Patrice, J.-M. Tarascon, *Solid State Sci.* **2006**, *8*, 640.

[133] B. Jache, B. Mogwitz, F. Klein, P. Adelhelm, *J. Power Sources* **2014**, *247*, 703.

[134] S.-H. Yu, X. Feng, N. Zhang, J. Seok, H. D. Abruña, *Acc. Chem. Res.* **2018**, *51*, 273.

[135] S. S. Zhang, D. T. Tran, *Electrochim. Acta* **2015**, *176*, 784.

[136] X. Hua, A. S. Eggeman, E. Castillo-Martínez, R. Robert, H. S. Geddes, Z. Lu, C. J. Pickard, W. Meng, K. M. Wiaderek, N. Pereira, G. G. Amatucci, P. A. Midgley, K. W. Chapman, U. Steiner, A. L. Goodwin, C. P. Grey, *Nat. Mater.* **2021**, *20*, 841.

[137] S.-H. Chung, A. Manthiram, *Adv. Mater.* **2019**, *31*, e1901125.

[138] Q. Pang, X. Liang, C. Y. Kwok, L. F. Nazar, *Nat. Energy* **2016**, *1*, 16132.

[139] S. Dörfler, H. Althues, P. Härtel, T. Abendroth, B. Schumm, S. Kaskel, *Joule* **2020**, *4*, 539.

[140] L. Medenbach, P. Adelhelm, in *Electrochemical Energy Storage* (Ed: R.-A. Eichel), Springer International Publishing, Cham **2019**, p. 101.

[141] L. Li, M. Cabán-Acevedo, S. N. Girard, S. Jin, *Nanoscale* **2014**, *6*, 2112.

[142] E. Strauss, *J. Power Sources* **2003**, *115*, 323.

[143] K. Takada, *Solid State Ionics* **1999**, *117*, 273.

[144] G. F. Dewald, Z. Liaqat, M. A. Lange, W. Tremel, W. G. Zeier, *Angew. Chem.* **2021**, *133*, 18096.

[145] K. Okamoto, S. Kawai, *Jpn. J. Appl. Phys.* **1973**, *12*, 1130.

[146] A. L. Santhosha, N. Nazer, R. Koerver, S. Randau, F. H. Richter, D. A. Weber, J. Kulisch, T. Adermann, J. Janek, P. Adelhelm, *Adv. Energy Mater.* **2020**, *10*, 2002394.

[147] H. Wang, X. Cao, W. Liu, X. Sun, *Front. Energy Res.* **2019**, *7*, 112.

[148] B. Ding, J. Wang, Z. Fan, S. Chen, Q. Lin, X. Lu, H. Dou, A. K. Nanjundan, G. Yushin, X. Zhang, Y. Yamauchi, *Mater. Today* **2020**, *40*, 114.

[149] N. H. H. Phuc, K. Hikima, H. Muto, A. Matsuda, *Crit. Rev. Solid State Mater. Sci.* **2021**, *47*, 283.

[150] S. Ohno, W. G. Zeier, *Acc. Mater. Res.* **2021**, *2*, 869.

[151] A. Hayashi, T. Ohtomo, F. Mizuno, K. Tadanaga, M. Tatsumisago, *Electrochem. Commun.* **2003**, *5*, 701.

[152] U. Ulissi, S. Ito, S. M. Hosseini, A. Varzi, Y. Aihara, S. Passerini, *Adv. Energy Mater.* **2018**, *8*, 1801462.

[153] A. Douglas, R. Carter, L. Oakes, K. Share, A. P. Cohn, C. L. Pint, *ACS Nano* **2015**, *9*, 11156.

[154] S. M. Hosseini, A. Varzi, S. Ito, Y. Aihara, S. Passerini, *Energy Storage Mater.* **2020**, *27*, 61.

[155] S. Wang, M. Tang, Q. Zhang, B. Li, S. Ohno, F. Walther, R. Pan, X. Xu, C. Xin, W. Zhang, L. Li, Y. Shen, F. H. Richter, J. Janek, C.-W. Nan, *Adv. Energy Mater.* **2021**, *11*, 2101370.

[156] W. Ji, X. Zhang, D. Zheng, H. Huang, T. H. Lambert, D. Qu, *Adv. Funct. Mater.* **2022**, *23*, 2202919.

[157] Z. Yang, F. Wang, Z. Hu, J. Chu, H. Zhan, X. Ai, Z. Song, *Adv. Energy Mater.* **2021**, *11*, 2102962.

[158] J. Zhang, Z. Chen, Q. Ai, T. Terlier, F. Hao, Y. Liang, H. Guo, J. Lou, Y. Yao, *Joule* **2021**, *5*, 1845.

6. Conclusions

Solid-state batteries still face significant challenges on their path to commercialization. Identifying and addressing these challenges at the lab scale is the first step toward developing strategies for higher energy density (design for range), higher power density (design for power), and reduced cost (design for cost).

This thesis investigates the kinetic limitations stemming from charge transport, charge transfer, and diffusion in composite cathodes. By identifying key microstructural features and charge transport properties, a better understanding of how to optimize material properties, cell architecture, and processing parameters was obtained. The determination and deconvolution of partial conductivities, using selectively blocking electrodes and electrochemical impedance spectroscopy, provide valuable metrics that can serve as straightforward characterization tools for screening and evaluating different electrode architectures.

In an ideal electrode, optimizing both electronic and ionic percolation – and, consequently, partial conductivities – it is essential to activate all cathode active material (CAM) particles. This task becomes more challenging as energy density increases, either through higher CAM content or greater electrode areal loading. The partial ionic conductivity of the composite, therefore, plays a crucial role and can be tailored by selecting the appropriate solid electrolyte (SE) particle size distribution. This not only leads to more homogeneous electrodes (lower tortuosity factors) but also reduces void space and increases the interface between CAM and SE. Reducing void space is critical for improving cathode kinetics, as voids block both ions and electrons.

Ultimately, matching SE and CAM properties is essential for achieving high-performance electrodes, and using "off-the-shelf" CAMs for solid-state battery applications is not a viable solution. Designing CAM and SE to complement each other, accounting for partial conductivities, interface compatibility, morphology, and diffusion pathways, can accelerate solid-state battery development and speed up commercialization.

However, many questions remain unanswered, and in the following, I will present several tasks for further investigation of the concepts explored in this work.

i) Chemo-mechanical behavior at low stack pressure operation

The results of the first two publications refer to charge transport measurements of electrodes that are freshly prepared, while in reality battery electrodes in consumer applications need to last (mostly unchanged) for many years and even decades, over thousands of cycles. Because of chemo-mechanical induced changes in the microstructure, originating from expansion and contraction of active materials during cycling, a change in the kinetics of the cathode can be anticipated[103,104]. Especially at the targeted high CAM-contents of $\varphi_{\mathrm{CAM}} > 70\%$, expansion of CAM will likely result in particle rearrangement and re-orientation, altering charge transport pathways. Interfacial reactions, taking place at $A_{\mathrm{CAM|SE}}$ can result in volume changes of the electrodes, due to different molar volumes of the reaction products compared to the educts[26,105]. At high CAM contents, these reaction products can narrow down even further the ionic charge transport pathways and increase tortuosity and cell impedance.

During contraction of CAM particles, contact loss between CAM and SE can occur, reducing the active interface area. This effect is of particular relevance for cells, which are operated under relatively low stack pressure of several 0.1 MPa[106]. Because the results of the first two publications were achieved using tens of MPa of pressure, they have only limited prediction capability for the behavior of cathode operated under lower pressure. Tracking cathode kinetics at high CAM contents over multiple cycles and low-pressure applications would consequently mark a next step in the design of cathodes towards improved performance.

ii) Improved manufacturing

As discussed in Chapter 4.3, pores play a crucial role in cathode kinetics. Reducing their presence by all possible means should be a primary focus of cathode optimization. For instance, controlling the particle size of solid electrolytes and avoiding re-agglomeration is essential during manufacturing. Additionally, achieving high coverage of CAM particles with SE is necessary, which requires homogeneous mixtures of (sub-)micron particles. De-agglomeration of particles through high shear forces could make extrusion a technique of interest[77,107]. Other promising approaches include (partial) coating of the CAM surface with SE via high shear mixers or wet coating methods[52].

Innovative strategies to reduce porosity might involve warm isostatic pressing, multi-step calendaring, or even a hybrid approach using low-viscosity additives, known as “pore-fillers.” These pore-fillers can be ionically conductive polymers or liquids[108,109]. The idea behind this concept is that even low ionic conductivity is preferable to none at all (as found in pores).

Additionally, any crack or void that forms during battery operation could theoretically be healed "operando" by the additive. However, introducing an additional component also adds more interfaces and increases the chemical complexity within the cathode[110,111]. Ensuring the long-term chemical stability of these interfaces is therefore crucial before adopting such approaches.

There are several key points where optimization can begin, and the methodology presented in this work can serve as a valuable tool for evaluating and optimizing these new manufacturing technologies.

iii) Gradients: Addressing kinetic limitations through targeted design of electrodes

All three publications have demonstrated that various processes impact cathode kinetics, many of which are determined by the material properties and microstructure of the cathode. Therefore, it is logical to consider tailoring and matching these properties and microstructures not only on a global component level but also locally. For instance, electronic transport requires pathways for electrons to travel from the current collector to each CAM particle and back. Consequently, limitations in electronic conductivity will have the highest impact if they occur in areas directly at the current collector. Here every electron needs to pass through and consequently conductivity needs to be highest. Similarly, the same principle applies to ionic transport pathways at the cathode side facing the separator.

Designing cathode architectures to incorporate gradients can be a powerful optimization strategy without compromising energy and power density.[45,51,112] As discussed in the third publication, small SE particles primarily enhance ionic percolation, while small CAM particles improve electronic percolation. Thus, using smaller CAM particles near the current collector and larger ones towards the separator should enhance both ionic and electronic transport[56].

Another example is designing the microstructure for diffusive transport. In cathodes where electronic transport is faster than ionic transport, particles will begin to (de-)lithiate at the separator side, while the process will be delayed at the current collector side. To address this, a cathode could be designed with CAM materials having high lithium diffusion coefficients (D_{Li}) at the kinetically inhibited location, i.e., near the current collector. This approach would homogenize the (de-)lithiation across the entire cathode, while reducing costs by not using the high D_{Li} material throughout the entire cathode.

This design approach can be applied to various parameters, such as volume changes of active materials, composition, diffusion coefficients, or particle morphology. Validating these strategies can be effectively achieved using the knowledge and methods presented in this work.

7. Literature

(1) Batteries and Secure Energy Transitions, 2024. https://www.iea.org/reports/batteries-and-secure-energy-transitions.

(2) Daniel, C.; Besenhard, J. O. *Handbook of Battery Materials*; Wiley: Weinheim, 2012.

(3) Battery Revolution to Evolution. *Nat. Energy* **2019**, *4* (11), 893–893. https://doi.org/10.1038/s41560-019-0503-2.

(4) Janek, J.; Zeier, W. G. A Solid Future for Battery Development. *Nat. Energy* **2016**, *1* (9), 1167. https://doi.org/10.1038/nenergy.2016.141.

(5) Janek, J.; Zeier, W. G. Challenges in Speeding up Solid-State Battery Development. *Nat. Energy* **2023**, *8* (3), 230–240. https://doi.org/10.1038/s41560-023-01208-9.

(6) Winter, M.; Brodd, R. J. What Are Batteries, Fuel Cells, and Supercapacitors? *Chem. Rev.* **2004**, *104* (10), 4245–4270. https://doi.org/10.1021/cr020730k.

(7) Pamidimukkala, A.; Kermanshachi, S.; Rosenberger, J. M.; Hladik, G. Barriers and Motivators to the Adoption of Electric Vehicles: A Global Review. *Green Energy Intell. Transp.* **2024**, *3* (2), 100153. https://doi.org/10.1016/j.geits.2024.100153.

(8) Frith, J. T.; Lacey, M. J.; Ulissi, U. A Non-Academic Perspective on the Future of Lithium-Based Batteries. *Nat. Commun.* **2023**, *14* (1), 420. https://doi.org/10.1038/s41467-023-35933-2.

(9) Kainat, S.; Anwer, J.; Hamid, A.; Gull, N.; Khan, S. M. Electrolytes in Lithium-Ion Batteries: Advancements in the Era of Twenties (2020's). *Mater. Chem. Phys.* **2024**, *313*, 128796. https://doi.org/10.1016/j.matchemphys.2023.128796.

(10) Weiss, M.; Ruess, R.; Kasnatscheew, J.; Levartovsky, Y.; Levy, N. R.; Minnmann, P.; Stolz, L.; Waldmann, T.; Wohlfahrt-Mehrens, M.; Aurbach, D.; Winter, M.; Ein-Eli, Y.; Janek, J. Fast Charging of Lithium-Ion Batteries: A Review of Materials Aspects. *Adv. Energy Mater.* **2021**, *11* (33), 2101126. https://doi.org/10.1002/aenm.202101126.

(11) Giffin, G. A. The Role of Concentration in Electrolyte Solutions for Non-Aqueous Lithium-Based Batteries. *Nat. Commun.* **2022**, *13* (1), 5250. https://doi.org/10.1038/s41467-022-32794-z.

(12) Deng, D. Li-ion Batteries: Basics, Progress, and Challenges. *Energy Sci. Eng.* **2015**, *3* (5), 385–418. https://doi.org/10.1002/ese3.95.

(13) Xiao, X.; Liu, Z.; Baggetto, L.; Veith, G. M.; More, K. L.; Unocic, R. R. Unraveling Manganese Dissolution/Deposition Mechanisms on the Negative Electrode in Lithium Ion Batteries. *Phys. Chem. Chem. Phys.* **2014**, *16* (22), 10398. https://doi.org/10.1039/c4cp00833b.

(14) Dose, W. M.; Li, W.; Temprano, I.; O'Keefe, C. A.; Mehdi, B. L.; De Volder, M. F. L.; Grey, C. P. Onset Potential for Electrolyte Oxidation and Ni-Rich Cathode Degradation in Lithium-Ion Batteries. *ACS Energy Lett.* **2022**, *7* (10), 3524–3530. https://doi.org/10.1021/acsenergylett.2c01722.

(15) Famprikis, T.; Canepa, P.; Dawson, J. A.; Islam, M. S.; Masquelier, C. Fundamentals of Inorganic Solid-State Electrolytes for Batteries. *Nat. Mater.* **2019**. https://doi.org/10.1038/s41563-019-0431-3.

(16) Li, Y.; Song, S.; Kim, H.; Nomoto, K.; Kim, H.; Sun, X.; Hori, S.; Suzuki, K.; Matsui, N.; Hirayama, M.; Mizoguchi, T.; Saito, T.; Kamiyama, T.; Kanno, R. A Lithium Superionic Conductor for Millimeter-Thick Battery Electrode. *Science* **2023**, *381* (6653), 50–53. https://doi.org/10.1126/science.add7138.

(17) Kato, Y.; Hori, S.; Saito, T.; Suzuki, K.; Hirayama, M.; Mitsui, A.; Yonemura, M.; Iba, H.; Kanno, R. High-Power All-Solid-State Batteries Using Sulfide Superionic Conductors. *Nat. Energy* **2016**, *1* (4), 652. https://doi.org/10.1038/nenergy.2016.30.

(18) Kamaya, N.; Homma, K.; Yamakawa, Y.; Hirayama, M.; Kanno, R.; Yonemura, M.; Kamiyama, T.; Kato, Y.; Hama, S.; Kawamoto, K.; Mitsui, A. A Lithium Superionic Conductor. *Nat. Mater.* **2011**, *10* (9), 682–686. https://doi.org/10.1038/nmat3066.

(19) Kraft, M. A.; Ohno, S.; Zinkevich, T.; Koerver, R.; Culver, S. P.; Fuchs, T.; Senyshyn, A.; Indris, S.; Morgan, B. J.; Zeier, W. G. Inducing High Ionic Conductivity in the Lithium Superionic Argyrodites $Li_{6+x}P_{1-x}Ge_xS_5I$ for All-Solid-State Batteries. *J. Am. Chem. Soc.* **2018**, *140* (47), 16330–16339. https://doi.org/10.1021/jacs.8b10282.

(20) Zhou, L.; Kwok, C. Y.; Shyamsunder, A.; Zhang, Q.; Wu, X.; Nazar, L. F. A New Halospinel Superionic Conductor for High-Voltage All Solid State Lithium Batteries. *Energy Environ. Sci.* **2020**, *13* (7), 2056–2063. https://doi.org/10.1039/D0EE01017K.

(21) Culver, S. P.; Koerver, R.; Krauskopf, T.; Zeier, W. G. Designing Ionic Conductors: The Interplay between Structural Phenomena and Interfaces in Thiophosphate-Based Solid-State Batteries. *Chem. Mater.* **2018**, *30* (13), 4179–4192. https://doi.org/10.1021/acs.chemmater.8b01293.

(22) Walther, F.; Koerver, R.; Fuchs, T.; Ohno, S.; Sann, J.; Rohnke, M.; Zeier, W. G.; Janek, J. Visualization of the Interfacial Decomposition of Composite Cathodes in Argyrodite-Based All-Solid-State Batteries Using Time-of-Flight Secondary-Ion Mass Spectrometry. *Chem. Mater.* **2019**, *31* (10), 3745–3755. https://doi.org/10.1021/acs.chemmater.9b00770.

(23) Wenzel, S.; Sedlmaier, S. J.; Dietrich, C.; Zeier, W. G.; Janek, J. Interfacial Reactivity and Interphase Growth of Argyrodite Solid Electrolytes at Lithium Metal Electrodes. *Solid State Ion.* **2018**, *318*, 102–112. https://doi.org/10.1016/j.ssi.2017.07.005.

(24) Wenzel, S.; Randau, S.; Leichtweiß, T.; Weber, D. A.; Sann, J.; Zeier, W. G.; Janek, J. Direct Observation of the Interfacial Instability of the Fast Ionic Conductor $Li_{10}GeP_2S_{12}$ at the Lithium Metal Anode. *Chem. Mater.* **2016**, *28* (7), 2400–2407. https://doi.org/10.1021/acs.chemmater.6b00610.

(25) Dewald, G. F.; Ohno, S.; Kraft, M. A.; Koerver, R.; Till, P.; Vargas-Barbosa, N. M.; Janek, J.; Zeier, W. G. Experimental Assessment of the Practical Oxidative Stability of Lithium Thiophosphate Solid Electrolytes. *Chem. Mater.* **2019**, *31* (20), 8328–8337. https://doi.org/10.1021/acs.chemmater.9b01550.

(26) Aktekin, B.; Kataev, E.; Riegger, L. M.; Garcia-Diez, R.; Chalkley, Z.; Becker, J.; Wilks, R. G.; Henss, A.; Bär, M.; Janek, J. Operando Photoelectron Spectroscopy Analysis of Li_6PS_5Cl Electrochemical Decomposition Reactions in Solid-State Batteries. *ACS Energy Lett.* **2024**, *9* (7), 3492–3500. https://doi.org/10.1021/acsenergylett.4c01072.

(27) Culver, S. P.; Koerver, R.; Zeier, W. G.; Janek, J. On the Functionality of Coatings for Cathode Active Materials in Thiophosphate–Based All–Solid–State Batteries. *Adv. Energy Mater.* **2019**, *9* (24), 1900626. https://doi.org/10.1002/aenm.201900626.

(28) Nakamura, T.; Amezawa, K.; Kulisch, J.; Zeier, W. G.; Janek, J. Guidelines for All-Solid-State Battery Design and Electrode Buffer Layers Based on Chemical Potential Profile Calculation, 2019. https://pubs.acs.org/doi/10.1021/acsami.9b03053#.

(29) Albertus, P.; Anandan, V.; Ban, C.; Balsara, N.; Belharouak, I.; Buettner-Garrett, J.; Chen, Z.; Daniel, C.; Doeff, M.; Dudney, N. J.; Dunn, B.; Harris, S. J.; Herle, S.; Herbert, E.; Kalnaus, S.; Libera, J. A.; Lu, D.; Martin, S.; McCloskey, B. D.; McDowell, M. T.; Meng, Y. S.; Nanda, J.; Sakamoto, J.; Self, E. C.; Tepavcevic, S.; Wachsman, E.; Wang, C.; Westover, A. S.; Xiao, J.; Yersak, T. Challenges for and Pathways toward Li-Metal-Based All-Solid-State Batteries. *ACS Energy Lett.* **2021**, 1399–1404. https://doi.org/10.1021/acsenergylett.1c00445.

(30) Randau, S.; Weber, D. A.; Kötz, O.; Koerver, R.; Braun, P.; Weber, A.; Ivers-Tiffée, E.; Adermann, T.; Kulisch, J.; Zeier, W. G.; Richter, F. H.; Janek, J. Benchmarking the Performance of All-Solid-State Lithium Batteries. *Nat. Energy* **2020**, *5* (3), 259–270. https://doi.org/10.1038/s41560-020-0565-1.

(31) Minnmann, P.; Quillman, L.; Burkhardt, S.; Richter, F. H.; Janek, J. Editors' Choice—Quantifying the Impact of Charge Transport Bottlenecks in Composite Cathodes of All-Solid-State Batteries. *J. Electrochem. Soc.* **2021**, *168* (4), 040537. https://doi.org/10.1149/1945-7111/abf8d7.

(32) Bielefeld, A.; Weber, D. A.; Janek, J. Microstructural Modeling of Composite Cathodes for All-Solid-State Batteries. *J. Phys. Chem. C* **2019**, *123* (3), 1626–1634. https://doi.org/10.1021/acs.jpcc.8b11043.

(33) Minnmann, P.; Schubert, J.; Kremer, S.; Rekers, R.; Burkhardt, S.; Ruess, R.; Bielefeld, A.; Richter, F. H.; Janek, J. Editors' Choice—Visualizing the Impact of the Composite Cathode Microstructure and Porosity on Solid-State Battery Performance. *J. Electrochem. Soc.* **2024**, *171* (6), 060514. https://doi.org/10.1149/1945-7111/ad510e.

(34) Minnmann, P.; Strauss, F.; Bielefeld, A.; Ruess, R.; Adelhelm, P.; Burkhardt, S.; Dreyer, S. L.; Trevisanello, E.; Ehrenberg, H.; Brezesinski, T.; Richter, F. H.; Janek, J. Designing Cathodes and Cathode Active Materials for Solid-State Batteries. *Adv. Energy Mater.* **2022**, *12* (35), 2201425. https://doi.org/10.1002/aenm.202201425.

(35) Xu, H.; Zhu, J.; Finegan, D. P.; Zhao, H.; Lu, X.; Li, W.; Hoffman, N.; Bertei, A.; Shearing, P.; Bazant, M. Z. Guiding the Design of Heterogeneous Electrode Microstructures for Li–Ion Batteries: Microscopic Imaging, Predictive Modeling, and Machine Learning. *Adv. Energy Mater.* **2021**, *11* (19), 2003908. https://doi.org/10.1002/aenm.202003908.

(36) Lu, X.; Zhang, X.; Tan, C.; Heenan, T. M. M.; Lagnoni, M.; O'Regan, K.; Daemi, S.; Bertei, A.; Jones, H. G.; Hinds, G.; Park, J.; Kendrick, E.; Brett, D. J. L.; Shearing, P. R. Multi-Length Scale Microstructural Design of Lithium-Ion Battery Electrodes for Improved Discharge Rate Performance. *Energy Environ. Sci.* **2021**, *14* (11), 5929–5946. https://doi.org/10.1039/D1EE01388B.

(37) Naik, K. G.; Vishnugopi, B. S.; Mukherjee, P. P. Kinetics or Transport: Whither Goes the Solid-State Battery Cathode? *ACS Appl. Mater. Interfaces* **2022**, *14* (26), 29754–29765. https://doi.org/10.1021/acsami.2c04962.

(38) Ashby, M. F. Composite Materials, Microstructural Design Of. In *Encyclopedia of Materials: Science and Technology*; Elsevier, 2001; pp 1357–1361. https://doi.org/10.1016/B0-08-043152-6/00253-9.

(39) *Neutrons and Synchrotron Radiation in Engineering Materials Science: From Fundamentals to Applications*, 1st ed.; Staron, P., Schreyer, A., Clemens, H., Mayer, S., Eds.; Wiley, 2017. https://doi.org/10.1002/9783527684489.

(40) Kato, Y.; Shiotani, S.; Morita, K.; Suzuki, K.; Hirayama, M.; Kanno, R. All-Solid-State Batteries with Thick Electrode Configurations. *J. Phys. Chem. Lett.* **2018**, *9* (3), 607–613. https://doi.org/10.1021/acs.jpclett.7b02880.

(41) Kasap, S. O. *Principles of Electronic Materials and Devices*, Fourth edition.; McGraw-Hill Education: New York, 2018.

(42) Choi, W.; Ku, J. H.; Kim, Y.; Gwon, H.; Yoon, G.; Yu, D.; Kim, J.-S. Formulating Interfacial Impedances for Designing High-Energy and High-Power All-Solid-State Battery Cathodes. *ACS Appl. Mater. Interfaces* **2024**, *16* (20), 26066–26078. https://doi.org/10.1021/acsami.4c01322.

(43) Amin, R.; Chiang, Y.-M. Characterization of Electronic and Ionic Transport in $Li_{1-x}Ni0_{.33}Mn_{0.33}Co_{0.33}O_2$ (NMC333) and $Li_{1-x}Ni_{0.50}Mn_{0.20}Co_{0.30}O_2$ (NMC523) as a Function of Li Content. *J. Electrochem. Soc.* **2016**, *163* (8), A1512–A1517. https://doi.org/10.1149/2.0131608jes.

(44) Zahnow, J.; Bernges, T.; Wagner, A.; Bohn, N.; Binder, J. R.; Zeier, W. G.; Elm, M. T.; Janek, J. Impedance Analysis of NCM Cathode Materials: Electronic and Ionic Partial Conductivities and the Influence of Microstructure. *ACS Appl. Energy Mater.* **2021**, *4* (2), 1335–1345. https://doi.org/10.1021/acsaem.0c02606.

(45) Usiskin, R. E.; Maier, J. Guidelines for Optimizing the Architecture of Battery Insertion Electrodes Based on the Concept of Wiring Lengths. *Phys. Chem. Chem. Phys.* **2018**, *20* (24), 16449–16462. https://doi.org/10.1039/c8cp01946k.

(46) Nguyen, T.-T.; Demortière, A.; Fleutot, B.; Delobel, B.; Delacourt, C.; Cooper, S. J. The Electrode Tortuosity Factor: Why the Conventional Tortuosity Factor Is Not Well Suited for Quantifying Transport in Porous Li-Ion Battery Electrodes and What to Use Instead. *Npj Comput. Mater.* **2020**, *6* (1). https://doi.org/10.1038/s41524-020-00386-4.

(47) Tjaden, B.; Cooper, S. J.; Brett, D. J. L.; Kramer, D.; Shearing, P. R. On the Origin and Application of the Bruggeman Correlation for Analysing Transport Phenomena in Electrochemical Systems. *Curr. Opin. Chem. Eng.* **2016**, *12*, 44–51. https://doi.org/10.1016/j.coche.2016.02.006.

(48) Usseglio-Viretta, F. L. E.; Colclasure, A.; Mistry, A. N.; Claver, K. P. Y.; Pouraghajan, F.; Finegan, D. P.; Heenan, T. M. M.; Abraham, D.; Mukherjee, P. P.; Wheeler, D.; Shearing, P.; Cooper, S. J.; Smith, K. Resolving the Discrepancy in Tortuosity Factor Estimation for Li-Ion Battery Electrodes through Micro-Macro Modeling and Experiment. *J. Electrochem. Soc.* **2018**, *165* (14), A3403–A3426. https://doi.org/10.1149/2.0731814jes.

(49) Bruggeman, D. A. G. Berechnung Verschiedener Physikalischer Konstanten von Heterogenen Substanzen. I. Dielektrizitätskonstanten Und Leitfähigkeiten Der Mischkörper Aus Isotropen Substanzen. *Ann. Phys.* **1935**, *416* (7), 636–664. https://doi.org/10.1002/andp.19354160705.

(50) Dixit, M. B.; Parejiya, A.; Muralidharan, N.; Essehli, R.; Amin, R.; Belharouak, I. Understanding Implications of Cathode Architecture on Energy Density of Solid-State Batteries. *Energy Storage Mater.* **2021**, *40*, 239–249. https://doi.org/10.1016/j.ensm.2021.05.001.

(51) Bielefeld, A.; Weber, D. A.; Rueß, R.; Glavas, V.; Janek, J. Influence of Lithium Ion Kinetics, Particle Morphology and Voids on the Electrochemical Performance of Composite Cathodes for All-Solid-State Batteries. *J. Electrochem. Soc.* **2022**, *169* (2), 020539. https://doi.org/10.1149/1945-7111/ac50df.

(52) Nakamura, H.; Kawaguchi, T.; Masuyama, T.; Sakuda, A.; Saito, T.; Kuratani, K.; Ohsaki, S.; Watano, S. Dry Coating of Active Material Particles with Sulfide Solid Electrolytes for an All-Solid-State Lithium Battery. *J. Power Sources* **2020**, *448*, 227579. https://doi.org/10.1016/j.jpowsour.2019.227579.

(53) Bisquert, J. Influence of the Boundaries in the Impedance of Porous Film Electrodes. *Phys. Chem. Chem. Phys.* **2000**, *2* (18), 4185–4192. https://doi.org/10.1039/B001708F.

(54) Kaiser, N.; Spannenberger, S.; Schmitt, M.; Cronau, M.; Kato, Y.; Roling, B. Ion Transport Limitations in All-Solid-State Lithium Battery Electrodes Containing a Sulfide-Based Electrolyte. *J. Power Sources* **2018**, *396*, 175–181. https://doi.org/10.1016/j.jpowsour.2018.05.095.

(55) Ohno, S.; Rosenbach, C.; Dewald, G. F.; Janek, J.; Zeier, W. G. Linking Solid Electrolyte Degradation to Charge Carrier Transport in the Thiophosphate–Based Composite Cathode toward Solid–State Lithium–Sulfur Batteries. *Adv. Funct. Mater.* **2021**, *31* (18), 2010620. https://doi.org/10.1002/adfm.202010620.

(56) Kim, J. Y.; Kim, J.; Kang, S. H.; Shin, D. O.; Lee, M. J.; Oh, J.; Lee, Y.; Kim, K. M. Efficient Cell Design and Fabrication of Concentration–Gradient Composite Electrodes for High–Power and High–Energy–Density All–Solid–State Batteries. *ETRI J.* **2020**, *42* (1), 129–137. https://doi.org/10.4218/etrij.2019-0176.

(57) Landesfeind, J.; Ebner, M.; Eldiven, A.; Wood, V.; Gasteiger, H. A. Tortuosity of Battery Electrodes: Validation of Impedance-Derived Values and Critical Comparison with 3D Tomography. *J. Electrochem. Soc.* **2018**, *165* (3), A469–A476. https://doi.org/10.1149/2.0231803jes.

(58) Landesfeind, J.; Eldiven, A.; Gasteiger, H. A. Influence of the Binder on Lithium Ion Battery Electrode Tortuosity and Performance. *J. Electrochem. Soc.* **2018**, *165* (5), A1122–A1128. https://doi.org/10.1149/2.0971805jes.

(59) Dewald, G. F.; Ohno, S.; Hering, J. G. C.; Janek, J.; Zeier, W. G. Analysis of Charge Carrier Transport Toward Optimized Cathode Composites for All–Solid–State Li-S Batteries. *Batter. Supercaps* **2021**, *4* (1), 183–194. https://doi.org/10.1002/batt.202000194.

(60) Strauss, F.; Bartsch, T.; de Biasi, L.; Kim, A.-Y.; Janek, J.; Hartmann, P.; Brezesinski, T. Impact of Cathode Material Particle Size on the Capacity of Bulk-Type All-Solid-State Batteries. *ACS Energy Lett.* **2018**, *3* (4), 992–996. https://doi.org/10.1021/acsenergylett.8b00275.

(61) Siroma, Z.; Sato, T.; Takeuchi, T.; Nagai, R.; Ota, A.; Ioroi, T. AC Impedance Analysis of Ionic and Electronic Conductivities in Electrode Mixture Layers for an All-Solid-State Lithium-Ion Battery. *J. Power Sources* **2016**, *316*, 215–223. https://doi.org/10.1016/j.jpowsour.2016.03.059.

(62) Jung, S.-K.; Gwon, H.; Lee, S.; Kim, H.; Lee, J. C.; Chung, J.; Park, S.; Aihara, Y.; Im, D. Understanding on the Effects of Chemical Reaction at Cathode-Electrolyte Interface in Sulfide Based All-Solid-State Batteries. *J Mater Chem A* **2019**, *7* (40). https://doi.org/10.1039/C9TA08517C.

(63) Hendriks, T. A.; Lange, M. A.; Kiens, E. M.; Baeumer, C.; Zeier, W. G. Balancing Partial Ionic and Electronic Transport for Optimized Cathode Utilization of High-Voltage $LiMn_2O_4/Li_3InCl_6$ Solid-State Batteries. *Batter. Supercaps* **2023**, *6* (4), e202200544. https://doi.org/10.1002/batt.202200544.

(64) Schlautmann, E.; Weiß, A.; Maus, O.; Ketter, L.; Rana, M.; Puls, S.; Nickel, V.; Gabbey, C.; Hartnig, C.; Bielefeld, A.; Zeier, W. G. Impact of the Solid Electrolyte Particle Size Distribution in Sulfide-Based Solid-State Battery Composites. *Adv. Energy Mater.* **2023**, 2302309. https://doi.org/10.1002/aenm.202302309.

(65) Scharf, J.; Chouchane, M.; Finegan, D. P.; Lu, B.; Redquest, C.; Kim, M.; Yao, W.; Franco, A. A.; Gostovic, D.; Liu, Z.; Riccio, M.; Zelenka, F.; Doux, J.-M.; Meng, Y. S. Bridging Nano- and Microscale X-Ray Tomography for Battery Research by Leveraging Artificial Intelligence. *Nat. Nanotechnol.* **2022**, *17* (5), 446–459. https://doi.org/10.1038/s41565-022-01081-9.

(66) Le Houx, J.; Kramer, D. X-Ray Tomography for Lithium Ion Battery Electrode Characterisation — A Review. *Energy Rep.* **2021**, *7*, 9–14. https://doi.org/10.1016/j.egyr.2021.02.063.

(67) *Focused Ion Beam Systems: Basics and Applications*, 1. publ., 1. paperb. ed.; Yao, N., Ed.; Cambridge Univ. Press: Cambridge, 2010.

(68) Cooper, S. J.; Roberts, S. A.; Liu, Z.; Winiarski, B. Methods—Kintsugi Imaging of Battery Electrodes: Distinguishing Pores from the Carbon Binder Domain Using Pt Deposition. *J. Electrochem. Soc.* **2022**, *169* (7), 070512. https://doi.org/10.1149/1945-7111/ac7a68.

(69) Ates, T.; Keller, M.; Kulisch, J.; Adermann, T.; Passerini, S. Development of an All-Solid-State Lithium Battery by Slurry-Coating Procedures Using a Sulfidic Electrolyte. *Energy Storage Mater.* **2019**, *17*, 204–210. https://doi.org/10.1016/j.ensm.2018.11.011.

(70) Conforto, G.; Ruess, R.; Schröder, D.; Trevisanello, E.; Fantin, R.; Richter, F. H.; Janek, J. Editors' Choice—Quantification of the Impact of Chemo-Mechanical Degradation on the Performance and Cycling Stability of NCM-Based Cathodes in Solid-State Li-Ion Batteries. *J. Electrochem. Soc.* **2021**, *168* (7), 070546. https://doi.org/10.1149/1945-7111/ac13d2.

(71) Asano, T.; Yubuchi, S.; Sakuda, A.; Hayashi, A.; Tatsumisago, M. Electronic and Ionic Conductivities of $LiNi_{1/3}Mn_{1/3}Co_{1/3}O_2$ -Li_3PS_4 Positive Composite Electrodes for All-

Solid-State Lithium Batteries. *J. Electrochem. Soc.* **2017**, *164* (14), A3960–A3963. https://doi.org/10.1149/2.1501714jes.

(72) Hakari, T.; Sato, Y.; Yoshimi, S.; Hayashi, A.; Tatsumisago, M. Favorable Carbon Conductive Additives in Li_3PS_4 Composite Positive Electrode Prepared by Ball-Milling for All-Solid-State Lithium Batteries. *J. Electrochem. Soc.* **2017**, *164* (12), A2804–A2811. https://doi.org/10.1149/2.1831712jes.

(73) Choi, S.; Jeon, M.; Kim, B.-K.; Sang, B.-I.; Kim, H. Electrochemical Behaviors of Li-Argyrodite-Based All-Solid-State Batteries under Deep-Freezing Conditions. *Chem Commun Camb Chem. Commun. Camb. Engl.* **2018**, *54* (100), 14116–14119. https://doi.org/10.1039/c8cc08030e.

(74) Doux, J.-M.; Yang, Y.; Tan, D. H. S.; Nguyen, H.; Wu, E. A.; Wang, X.; Banerjee, A.; Meng, Y. S. Pressure Effects on Sulfide Electrolytes for All Solid-State Batteries. *J Mater Chem A* **2020**, *8* (10), 5049–5055. https://doi.org/10.1039/C9TA12889A.

(75) Jiang, W.; Zhu, X.; Huang, R.; Zhao, S.; Fan, X.; Ling, M.; Liang, C.; Wang, L. Revealing the Design Principles of Ni-Rich Cathodes for All-Solid-State Batteries. *Adv. Energy Mater.* **2022**, *12* (13), 2103473. https://doi.org/10.1002/aenm.202103473.

(76) Doerrer, C.; Capone, I.; Narayanan, S.; Liu, J.; Grovenor, C. R. M.; Pasta, M.; Grant, P. S. High Energy Density Single-Crystal NMC/Li_6PS_5Cl Cathodes for All-Solid-State Lithium-Metal Batteries. *ACS Appl. Mater. Interfaces* **2021**, *13* (31), 37809–37815. https://doi.org/10.1021/acsami.1c07952.

(77) Hippauf, F.; Schumm, B.; Doerfler, S.; Althues, H.; Fujiki, S.; Shiratsushi, T.; Tsujimura, T.; Aihara, Y.; Kaskel, S. Overcoming Binder Limitations of Sheet-Type Solid-State Cathodes Using a Solvent-Free Dry-Film Approach. *Energy Storage Mater.* **2019**. https://doi.org/10.1016/j.ensm.2019.05.033.

(78) Lee, Y.-G.; Fujiki, S.; Jung, C.; Suzuki, N.; Yashiro, N.; Omoda, R.; Ko, D.-S.; Shiratsuchi, T.; Sugimoto, T.; Ryu, S.; Ku, J. H.; Watanabe, T.; Park, Y.; Aihara, Y.; Im, D.; Han, I. T. High-Energy Long-Cycling All-Solid-State Lithium Metal Batteries Enabled by Silver–Carbon Composite Anodes. *Nat. Energy* **2020**, *5* (4), 299–308. https://doi.org/10.1038/s41560-020-0575-z.

(79) Shi, T.; Tu, Q.; Tian, Y.; Xiao, Y.; Miara, L. J.; Kononova, O.; Ceder, G. High Active Material Loading in All–Solid–State Battery Electrode via Particle Size Optimization. *Adv. Energy Mater.* **2019**, *2*, 1902881. https://doi.org/10.1002/aenm.201902881.

(80) Rana, M.; Rudel, Y.; Heuer, P.; Schlautmann, E.; Rosenbach, C.; Ali, M. Y.; Wiggers, H.; Bielefeld, A.; Zeier, W. G. Toward Achieving High Areal Capacity in Silicon-Based Solid-State Battery Anodes: What Influences the Rate-Performance? *ACS Energy Lett.* **2023**, *8* (7), 3196–3203. https://doi.org/10.1021/acsenergylett.3c00722.

(81) Walther, F.; Randau, S.; Schneider, Y.; Sann, J.; Rohnke, M.; Richter, F. H.; Zeier, W. G.; Janek, J. Influence of Carbon Additives on the Decomposition Pathways in Cathodes of Lithium Thiophosphate-Based All-Solid-State Batteries. *Chem. Mater.* **2020**, *32* (14), 6123–6136. https://doi.org/10.1021/acs.chemmater.0c01825.

(82) Strauss, F.; Stepien, D.; Maibach, J.; Pfaffmann, L.; Indris, S.; Hartmann, P.; Brezesinski, T. Influence of Electronically Conductive Additives on the Cycling Performance of Argyrodite-Based All-Solid-State Batteries. *RSC Adv.* **2020**, *10* (2), 1114–1119. https://doi.org/10.1039/C9RA10253A.

(83) Zhang, W.; Leichtweiß, T.; Culver, S. P.; Koerver, R.; Das, D.; Weber, D. A.; Zeier, W. G.; Janek, J. The Detrimental Effects of Carbon Additives in $Li_{10}GeP_2S_{12}$-Based Solid-State Batteries. *ACS Appl. Mater. Interfaces* **2017**, *9* (41), 35888–35896. https://doi.org/10.1021/acsami.7b11530.

(84) Randau, S.; Walther, F.; Neumann, A.; Schneider, Y.; Negi, R. S.; Mogwitz, B.; Sann, J.; Becker-Steinberger, K.; Danner, T.; Hein, S.; Latz, A.; Richter, F. H.; Janek Jürgen. On

the Additive Microstructure in Composite Cathodes and Alumina-Coated Carbon Microwires for Improved All-Solid-State Batteries. *Chem. Mater.* **2021**.

(85) Hlushkou, D.; Reising, A. E.; Kaiser, N.; Spannenberger, S.; Schlabach, S.; Kato, Y.; Roling, B.; Tallarek, U. The Influence of Void Space on Ion Transport in a Composite Cathode for All-Solid-State Batteries. *J. Power Sources* **2018**, *396*, 363–370. https://doi.org/10.1016/j.jpowsour.2018.06.041.

(86) Kodama, M.; Takeuchi, A.; Uesugi, M.; Miyuki, T.; Yasuda, H.; Hirai, S. Nanoscale Pore Measurements in an All-Solid-State Lithium-Ion Battery with Ultra-Small-Angle X-Ray Scattering (USAXS). *J. Power Sources Adv.* **2021**, *12*, 100076. https://doi.org/10.1016/j.powera.2021.100076.

(87) Clausnitzer, M.; Mücke, R.; Al-Jaljouli, F.; Hein, S.; Finsterbusch, M.; Danner, T.; Fattakhova-Rohlfing, D.; Guillon, O.; Latz, A. Optimizing the Composite Cathode Microstructure in All-Solid-State Batteries by Structure-Resolved Simulations. *Batter. Supercaps* **2023**, e202300167. https://doi.org/10.1002/batt.202300167.

(88) Yamamoto, M.; Terauchi, Y.; Sakuda, A.; Kato, A.; Takahashi, M. Effects of Volume Variations under Different Compressive Pressures on the Performance and Microstructure of All-Solid-State Batteries. *J. Power Sources* **2020**, *473*, 228595. https://doi.org/10.1016/j.jpowsour.2020.228595.

(89) Kodama, M.; Ohashi, A.; Adachi, H.; Miyuki, T.; Takeuchi, A.; Yasutake, M.; Uesugi, K.; Kaburagi, T.; Hirai, S. Three-Dimensional Structural Measurement and Material Identification of an All-Solid-State Lithium-Ion Battery by X-Ray Nanotomography and Deep Learning. *J. Power Sources Adv.* **2021**, *8*, 100048. https://doi.org/10.1016/j.powera.2021.100048.

(90) Moyassari, E.; Kücher, S.; Jobst, N. M.; Chang, C.-C.; Hou, S.-C.; Spingler, F. B.; Wohlfahrt-Mehrens, M.; Jossen, A. Influence of Initial Porosity on the Expansion Behavior of Electrodes in Lithium-Ion Batteries. *J. Electrochem. Soc.* **2023**, *170* (5), 050528. https://doi.org/10.1149/1945-7111/acd2fe.

(91) Sakuda, A.; Hayashi, A.; Tatsumisago, M. Sulfide Solid Electrolyte with Favorable Mechanical Property for All-Solid-State Lithium Battery. *Sci. Rep.* **2013**, *3* (1), 2261. https://doi.org/10.1038/srep02261.

(92) Yamamoto, M.; Takahashi, M.; Terauchi, Y.; Sakuda, A.; Kobayashi, Y.; Ikeda, S.; Sakuda, A. Fabrication of Composite Positive Electrode Sheet with High Active Material Content and Effect of Fabrication Pressure for All-Solid-State Battery. *J. Ceram. Soc. Jpn.* **2017**, *125* (5), 391–395. https://doi.org/10.2109/jcersj2.16321.

(93) Zahiri, B.; Patra, A.; Kiggins, C.; Yong, A. X. B.; Ertekin, E.; Cook, J. B.; Braun, P. V. Revealing the Role of the Cathode–Electrolyte Interface on Solid-State Batteries. *Nat. Mater.* **2021**, *20* (10), 1392–1400. https://doi.org/10.1038/s41563-021-01016-0.

(94) König, C.; Miß, V.; Janin, L.; Roling, B. Mitigating the Ion Transport Tortuosity in Composite Cathodes of All-Solid-State Batteries by Wet Milling of the Solid Electrolyte Particles. *ACS Appl. Energy Mater.* **2023**, *6* (18), 9356–9362. https://doi.org/10.1021/acsaem.3c01242.

(95) Yamada, Y.; Watanabe, K.; Kim, H.; Suzuki, K.; Hori, S.; Kanno, R.; Hirayama, M. Microstructure Control of $LiCoO_2$ -$Li_{10}GeP_2S_{12}$ Composite Cathodes by Adjusting the Particle Size Distribution for the Enhancement of All-Solid-State Batteries. *Batter. Supercaps* **2023**, e202300261. https://doi.org/10.1002/batt.202300261.

(96) Cronau, M.; Duchardt, M.; Szabo, M.; Roling, B. Ionic Conductivity versus Particle Size of Ball-Milled Sulfide-Based Solid Electrolytes: Strategy Towards Optimized Composite Cathode Performance in All-Solid-State Batteries. *Batter. Supercaps* **2022**, *5* (6). https://doi.org/10.1002/batt.202200041.

(97) Jeon, H.; Kwon, D.-H.; Kim, H.; Lee, J.-H.; Jun, Y.; Son, J.-W.; Park, S. Tailoring Shape and Exposed Crystal Facet of Single-Crystal Layered-Oxide Cathode Particles for All-

Solid-State Batteries. *Chem. Eng. J.* **2022**, *445*, 136828. https://doi.org/10.1016/j.cej.2022.136828.

(98) Trevisanello, E.; Ruess, R.; Conforto, G.; Richter, F. H.; Janek, J. Polycrystalline and Single Crystalline NCM Cathode Materials—Quantifying Particle Cracking, Active Surface Area, and Lithium Diffusion. *Adv. Energy Mater.* **2021**, *11* (18), 2003400. https://doi.org/10.1002/aenm.202003400.

(99) Payandeh, S.; Njel, C.; Mazilkin, A.; Teo, J. H.; Ma, Y.; Zhang, R.; Kondrakov, A.; Bianchini, M.; Brezesinski, T. The Effect of Single versus Polycrystalline Cathode Particles on All-Solid-State Battery Performance. *Adv. Mater. Interfaces* **2023**, *10* (3), 2201806. https://doi.org/10.1002/admi.202201806.

(100) Payandeh, S.; Goonetilleke, D.; Bianchini, M.; Janek, J.; Brezesinski, T. Single versus Poly-Crystalline Layered Oxide Cathode Materials for Solid-State Battery Applications - a Short Review Article. *Curr. Opin. Electrochem.* **2022**, *31*, 100877. https://doi.org/10.1016/j.coelec.2021.100877.

(101) Han, Y.; Jung, S. H.; Kwak, H.; Jun, S.; Kwak, H. H.; Lee, J. H.; Hong, S.; Jung, Y. S. Single– or Poly–Crystalline Ni–Rich Layered Cathode, Sulfide or Halide Solid Electrolyte: Which Will Be the Winners for All–Solid–State Batteries? *Adv. Energy Mater.* **2021**, 2100126. https://doi.org/10.1002/aenm.202100126.

(102) Ruess, R.; Schweidler, S.; Hemmelmann, H.; Conforto, G.; Bielefeld, A.; Weber, D. A.; Sann, J.; Elm, M. T.; Janek, J. Influence of NCM Particle Cracking on Kinetics of Lithium-Ion Batteries with Liquid or Solid Electrolyte. *J. Electrochem. Soc.* **2020**, *167* (10), 100532. https://doi.org/10.1149/1945-7111/ab9a2c.

(103) Koerver, R.; Aygün, I.; Leichtweiß, T.; Dietrich, C.; Zhang, W.; Binder, J. O.; Hartmann, P.; Zeier, W. G.; Janek, J. Capacity Fade in Solid-State Batteries: Interphase Formation and Chemomechanical Processes in Nickel-Rich Layered Oxide Cathodes and Lithium Thiophosphate Solid Electrolytes. *Chem. Mater.* **2017**, *29* (13), 5574–5582. https://doi.org/10.1021/acs.chemmater.7b00931.

(104) Koerver, R.; Zhang, W.; de Biasi, L.; Schweidler, S.; Kondrakov, A. O.; Kolling, S.; Brezesinski, T.; Hartmann, P.; Zeier, W. G.; Janek, J. Chemo-Mechanical Expansion of Lithium Electrode Materials – on the Route to Mechanically Optimized All-Solid-State Batteries. *Energy Environ. Sci.* **2018**, *11* (8), 2142–2158. https://doi.org/10.1039/c8ee00907d.

(105) Riegger, L. M.; Otto, S.-K.; Sadowski, M.; Jovanovic, S.; Kötz, O.; Harm, S.; Balzat, L. G.; Merz, S.; Burkhardt, S.; Richter, F. H.; Sann, J.; Eichel, R.-A.; Lotsch, B. V.; Granwehr, J.; Albe, K.; Janek, J. Instability of the Li_7SiPS_8 Solid Electrolyte at the Lithium Metal Anode and Interphase Formation. *Chem. Mater.* **2022**, *34* (8), 3659–3669. https://doi.org/10.1021/acs.chemmater.1c04302.

(106) Gao, X.; Liu, B.; Hu, B.; Ning, Z.; Jolly, D. S.; Zhang, S.; Perera, J.; Bu, J.; Liu, J.; Doerrer, C.; Darnbrough, E.; Armstrong, D.; Grant, P. S.; Bruce, P. G. Solid-State Lithium Battery Cathodes Operating at Low Pressures. *Joule* **2022**, *6* (3), 636–646. https://doi.org/10.1016/j.joule.2022.02.008.

(107) Kim, S.; Chart, Y. A.; Narayanan, S.; Pasta, M. Thin Solid Electrolyte Separators for Solid-State Lithium–Sulfur Batteries. *Nano Lett.* **2022**, *22* (24), 10176–10183. https://doi.org/10.1021/acs.nanolett.2c04216.

(108) Woolley, H. M.; Vargas-Barbosa, N. M. Hybrid Solid Electrolyte-Liquid Electrolyte Systems for (Almost) Solid-State Batteries: Why, How, and Where To? *J. Mater. Chem. A* **2023**, *11* (3), 1083–1097. https://doi.org/10.1039/D2TA02179J.

(109) Oh, D. Y.; Nam, Y. J.; Park, K. H.; Jung, S. H.; Kim, K. T.; Ha, A. R.; Jung, Y. S. Slurry-Fabricable Li+ -Conductive Polymeric Binders for Practical All-Solid-State Lithium-Ion Batteries Enabled by Solvate Ionic Liquids. *Adv. Energy Mater.* **2019**, *22*, 1802927. https://doi.org/10.1002/aenm.201802927.

(110) Weiss, M.; Simon, F. J.; Busche, M. R.; Nakamura, T.; Schröder, D.; Richter, F. H.; Janek, J. From Liquid- to Solid-State Batteries: Ion Transfer Kinetics of Heteroionic Interfaces. *Electrochem. Energy Rev.* **2020**, *3* (2), 221–238. https://doi.org/10.1007/s41918-020-00062-7.

(111) Simon, F. J.; Hanauer, M.; Henss, A.; Richter, F. H.; Janek, J. Properties of the Interphase Formed between Argyrodite-Type Li_6PS_5Cl and Polymer-Based PEO $_{10}$:LiTFSI. *ACS Appl. Mater. Interfaces* **2019**, *11* (45), 42186–42196. https://doi.org/10.1021/acsami.9b14506.

(112) Kim, M.-J.; Park, J.-W.; Kim, B. G.; Lee, Y.-J.; Ha, Y.-C.; Lee, S.-M.; Baeg, K.-J. Facile Fabrication of Solution-Processed Solid-Electrolytes for High-Energy-Density All-Solid-State-Batteries by Enhanced Interfacial Contact. *Sci. Rep.* **2020**, *10* (1), 11923. https://doi.org/10.1038/s41598-020-68885-4.

8. Appendix

Supplementary Information: Quantifying the Impact of Transport Bottlenecks in Composite Cathodes of All-Solid-State Batteries

Philip Minnmann[1,2], Lars Quillman[1,2], Simon Burkhardt[1,2], Felix H. Richter[1,2], Jürgen Janek[1,2]*

[1]*Institute of Physical Chemistry, Justus-Liebig-University Giessen,*
Heinrich-Buff-Ring 17, D-35392 Giessen, Germany.

[2]*Center for Materials Research (LaMa), Justus-Liebig-University Giessen,*
Heinrich-Buff-Ring 16, D-35392 Giessen, Germany.

E-Mail: juergen.janek@pc.jlug.de

1. Transmission line model

The transmission line model (TLM) is commonly used for the modelling of porous electrodes, in which a species can diffuse through the interconnected pores and where a second charge transport pathway (the porous matrix) is accessible in parallel.[1] Charge transfer between these pathways can take place across their joint interface.[2] Each transport pathway is assumed to contain certain impedance elements representing the microscopic transport processes with characteristic relaxation times. By multiple repetition of these elements, a macroscopic model of the composite is derived. Thus, careful evaluation of the EIS measurement allows a general investigation of the charge transport and the influence of protective coatings, binders, conductive additives, particle size or particle morphology on charge transport processes.[3]

The transmission line equivalent circuit employed in this study models the complex impedance of a composite cathode under symmetric contact conditions. A "T-type connection" TLM representing a composite cathode between electronically conducting and ionically blocking electrodes, was used to describe and analyze the experimental data.[4]

The general mathematical description (Equation S1) of such a TLM was derived by Siroma *et al.*[5] For convenience, we follow their nomenclature and use lower case letters (e.g. z_{ion}, r_{ion}) for impedance elements used in the TLM and capital letters (e.g Z_{CC}, R_{ion}) for the macroscopic physical quantities of the equivalent circuit elements.

$$Z_{CC}(\omega) = \frac{z_{\text{ion}} z_{\text{el}}}{z_{\text{ion}} + z_{\text{el}}} \mathrm{L} + \frac{2\, {z_{\text{el}}}^{2} \sqrt{z_{\text{int}}}}{(z_{\text{ion}} + z_{\text{el}})^{\frac{3}{2}}} \cdot \frac{\cosh\left(L\sqrt{\frac{z_{\text{ion}} + z_{\text{el}}}{z_{\text{int}}}}\right) - 1}{\sinh\left(L\sqrt{\frac{z_{\text{ion}} + z_{\text{el}}}{z_{\text{int}}}}\right)}, \qquad \text{(S1)}$$

The impedance z_{ion} of ionic pathway was modelled by a simple resistor representing the ionic bulk resistance (r_{ion} (Ω m)) of the solid electrolyte.

$$\mathrm{z}_{\text{ion}} = r_{\text{ion}} \qquad \text{(S2)}$$

For the modelling of the impedance z_{el} of the electronic pathway, a serial combination of a single resistor representing the electronic bulk resistance ($r_{\mathrm{el,\,bulk}}$ ($\Omega\ \mathrm{m}^{-1}$)) of the cathode active material (CAM) and a R-CPE parallel unit representing the interfacial impedance at the NCM-NCM particle contacts were used, as proposed by Siroma *et al.* The total impedance z_{el} of the electronically conducting pathway is the sum of the electronic bulk impedance $z_{\mathrm{el,\,bulk}}$ and the electronic interface impedance $z_{\mathrm{el,\,int}}$.

$$z_{\mathrm{el}} = z_{\mathrm{el,\,bulk}} + z_{\mathrm{el,\,int}} \tag{S3}$$

The impedance $z_{\mathrm{el,\,int}}$ of the R-CPE unit is described by:

$$z_{\mathrm{el,\ int}} = \frac{r_{\mathrm{el,\,int}}}{1 + r_{\mathrm{el,int}}\left(\mathrm{j}\omega Q_{\mathrm{el,int}}\right)^{\alpha_{el,int}}} \tag{S4}$$

With the imaginary one (j), the angular frequency (ω (s^{-1})), the interfacial contact resistance ($r_{\mathrm{el,\,int}}$ ($\Omega\ \mathrm{m}^{-1}$)) the capacitance constant (Q (($\mathrm{S\ m\ s}^{-1})^{1/\alpha}$)) and the dimensionless ideality exponent α ($0 < \alpha < 1$). The interfacial contact resistance $r_{\mathrm{el,\,int}}$ might originate from surface contaminations and degradation occurring during cathode preparation.

A constant phase element (CPE) (Equation S5) was chosen to model a non-faradaic behavior (blocking) of the impedance z_{int} of the interface between the CAM and the solid electrolyte (SE). The scaling parameter (L (m)) describes the length of the respective transmission line model, i.e. the thickness of the composite cathode.

Since the CAM used was fully lithiated, charge and mass transport across the interface was neglected.

$$z_{\mathrm{int}} = \frac{1}{(\mathrm{j}\omega\ Q_{\mathrm{int}})^{\alpha_{int}}} \tag{S5}$$

The impedance spectra were fitted using Equations S1-S5. To evaluate the results, R_{el} and R_{ion} were determined by Equations S6 and S7:

$$R_{\mathrm{el}} = L\ (\mathrm{r}_{\mathrm{el,bulk}} + r_{\mathrm{el,int}}) \tag{S6}$$

$$R_{\mathrm{ion}} = L\ r_{ion} \tag{S7}$$

2. Influence of In/(InLi)$_x$ anodes

For the cells with electron-blocking contact materials, the influence of the SE separators and the In/(InLi)$_x$|SE interface was determined, by building a symmetric cell with a SE layer in the center, and an In/(InLi)$_x$ electrode attached to each side of the SE layer, as illustrated in Figure S1.

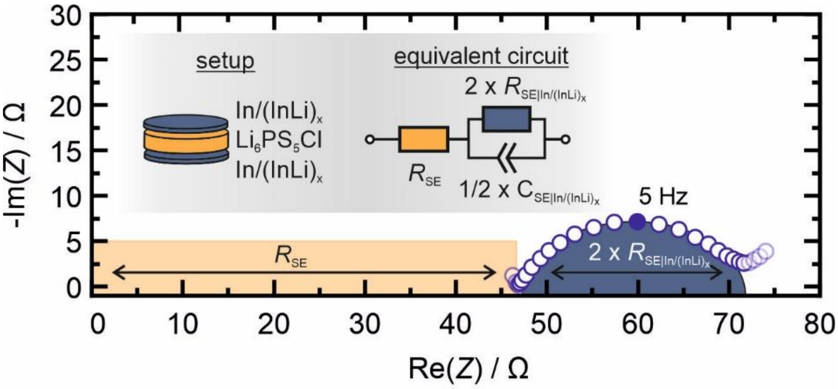

Figure S1: Impedance spectra, measurement setup and equivalent circuit used to determine the contribution of the SE separators and SE|In/(InLi)$_x$ *interfacial contribution to the impedance of the cells with electron blocking contact materials. The ionic resistivity of the solid electrolyte layer* R_{SE} *and the impedance response of the R-CPE unit are schematically illustrated as a guide to the eye. Low and high frequency data points are not used for the analysis and thus depicted in a lighter shade.*

Impedance spectroscopy was carried out and the resulting data were fitted to an equivalent circuit consisting of a single resistor R_{SE} representing the SE layer in series to a parallel arrangement of a single resistor $R_{\mathrm{SE|In/InLi}}$ and a CPE. The impedance contribution of both In/(InLi)$_x$|SE interfaces should be identical. Therefore, the impedance response of both interfaces can be fitted with a single equivalent circuit element. However, this means that the fit values for the resistance $R_{\mathrm{SE|In/InLi}}$ are twice as large as the resistance of a single interface, while the capacitance $C_{\mathrm{SE|In/InLi}}$ is only half as large as the capacitance of a single interface.

3. Determination and influence of porosity

While in most reported solid-state battery research weight fractions of CAM and SE are used to describe composite cathodes, it is much more relevant to consider volume fractions when investigating charge transport. Volume fractions describe the total volume, which is occupied by one phase, and are not affected by differences in density of the different CAM and solid electrolytes.

All compositions used for the charge transport investigations in this study are given in Table S1. The composite cathodes are not completely dense, as residual porosity is hardly avoidable. The reasons are difficulties in the processing of the cathode composites, as these are pure powder mixtures. All determined porosities are susceptible to errors, as high as 10 %, due to the inaccurate determination of the composite cathode thickness. While it has to be assumed that porosity is also present in the samples of pure CAM and pure SE, reducing the experimentally determined conductivity, the tortuosity factor of the pure materials has been set to unity to allow a simplification of the analysis.

The porosity Φ_{Porosity}, *i.e.* the volume fraction of pores, was determined as the difference between the experimentally determined volume V_{meas} and the theoretical volume V_{theo} calculated from the respective densities and masses of the SE and the CAM:

$$\Phi_{\mathrm{Porosity}} = \frac{V_{\mathrm{meas}} - V_{\mathrm{theo}}}{V_{\mathrm{meas}}} \qquad \text{(S8)}$$

Real volume fractions Φ_i of the respective components i (CAM and SE) were calculated by correcting the nominal volume fraction $\Phi_{i,\text{ nom}}$, as determined by the masses and densities of the components, using an average density of 14 % (Equation S8)

$$\Phi_i = (1 - \Phi_{\text{Porosity}}) \cdot \Phi_{i,\text{ nom}} \tag{S9}$$

Table S1: Overview of the used compositions of the composite cathodes. A total of 100 mg was prepared for each composite cathode. Listed are the masses m, the experimentally determined and theoretically calculated volumes V_{meas} *and* V_{theo}*, the calculated porosity* Φ_{Porosity} *and the calculated volume fraction of NCM and solid electrolyte* Φ_{NCM} *and* Φ_{SE} *with an assumed average porosity of 14%.*

m_{NCM} / mg	m_{SE} / mg	V_{theo} / mm^3	V_{meas} / mm^3	Φ_{Porosity} / %	Average Φ_{Porosity} / %*	Φ_{NCM} / %	Φ_{SE} / %
50	50	37.2	40.3	7.6	14	25	61
60	40	33.9	39.0	13	14	33	53
70	30	30.7	36.9	17	14	42	44
80	20	27.4	32.9	17	14	53	33
86	14	25.5	29.8	15	14	61	25

**average value of the five measured* Φ_{Porosity} *values*

Table S2: Volume fractions of SE an CAM and determined effective conductivities σ_{eff} and tortuosity factors τ^2 of the electronic and ionic transport pathway. Tortuosity factors have been set to unity for the pure components for a simplification of the analysis.

Φ_{NCM} / %	**Φ_{SE} / %**	**$\sigma_{el, eff}$ / S cm^{-1}**	**τ_{el}^2**	**$\sigma_{ion, eff}$ / S cm^{-1}**	**τ_{ion}^2**
0	100 (nominal)	-	-	$1.60 \cdot 10^{-3}$	1.00
25	61	$2.06 \cdot 10^{-5}$	120	$4.08 \cdot 10^{-4}$	2.40
33	53	$2.36 \cdot 10^{-4}$	13.7	$2.66 \cdot 10^{-4}$	3.23
42	44	$5.56 \cdot 10^{-4}$	7.44	$1.66 \cdot 10^{-4}$	4.27
53	33	$1.11 \cdot 10^{-3}$	4.77	$3.45 \cdot 10^{-5}$	15.3
61	25	$1.43 \cdot 10^{-3}$	4.29	$3.06 \cdot 10^{-6}$	130
61	25 (fine SE)	$6.97 \cdot 10^{-4}$	8.79	$1.17 \cdot 10^{-5}$	33.8
100 (nominal)	0	$1.00 \cdot 10^{-2}$	1	-	-

4. Cycling Data

Table S3: Overview of the areal loadings of NCM per square centimeter and the resulting areal capacity for the volume fractions of NCM used in the ASSB cell cycling experiments. All composite cathodes have a mass of 12 mg. For the calculation of the areal capacity, a specific capacity of 200 mAh g^{-1} is assumed.

Φ_{NCM} / %	**Areal loading / mg$_{NCM}$ cm^{-2}**	**Areal Capacity / mAh cm^{-2}**
33	9.17	1.83
42	10.7	2.14
47	11.5	2.29
58	12.8	2.55
61	13.1	2.62

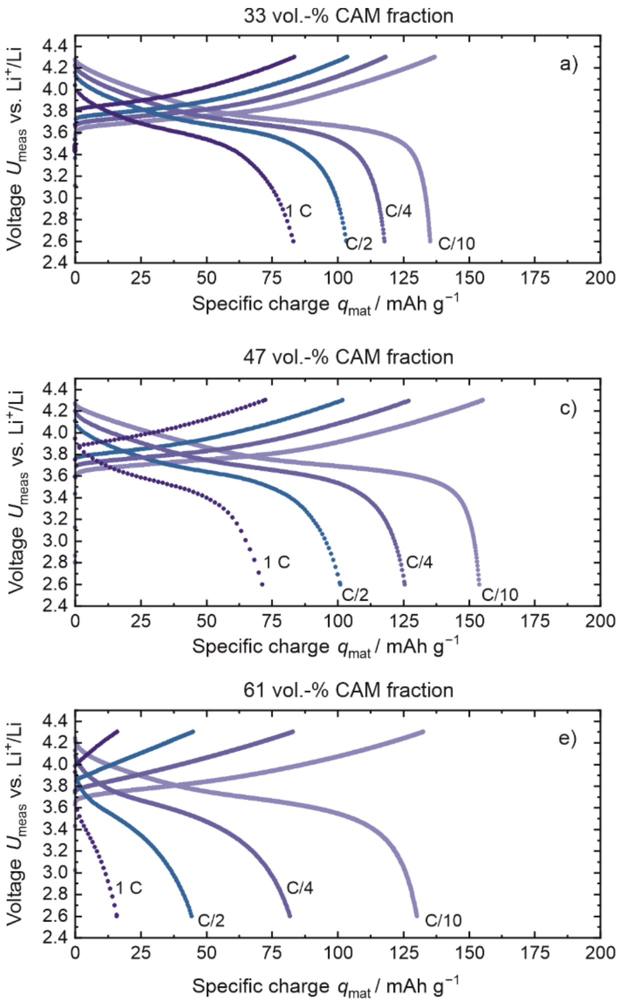

Figure S2: Charge-Discharge curves of full cells with CAM fractions of a) 33 vol.-%, b) 42 vol.-%, c) 47 vol.%, d) 58 vol.-% and e) 61 vol.-%. The measured cell voltage U_{meas} is plotted against the CAM-specific charge $q_{mat.}$ Displayed are the cycling curves at the four tested C-rates C/10 (0.1 C), C/4 (0.25 C), C/2 (0.5 C) and 1C. While at low CAM fractions the electronic limitation results in lower CAM specific charges at low C-rates, the ionic imitation, displayed by the cell average potential at higher C-rates, is less pronounced than in cells with high CAM fraction.

5. Charge-discharge capacities – Comparison with and w/o VGCF

Table S4: Overview of specific charges Q for the steps with and without (w/o) conductive additives at different C-rates for ASSB cells with 25 vol.-% (top) and 61 vol.-% (bottom) CAM. Listed are charge (chg) and discharge (dis) steps. Additionally, the differences ΔQ are listed.

C-rate / h^{-1}	Q_{chg} w/o VGCF / mAh g^{-1}	Q_{chg} with VGCF / mAh g^{-1}	ΔQ_{chg} / mAh g^{-1}	Q_{dis} w/o VGCF / mAh g^{-1}	Q_{dis} with VGCF / mAh g^{-1}	ΔQ_{dis} / mAh g^{-1}
25 vol.-% CAM						
0.1	137	159	22	135	157	22
0.25	118	140	22	118	140	22

0.5	104	119	15	103	119	16
1	83.4	93.4	10	83.0	93.0	10
61 vol.-% CAM						
0.1	132	132	0	132	130	-2.0
0.25	82.8	74.2	-8.6	80.2	71.5	8.8
0.5	44.9	33.5	-11	43.2	32.9	-7.3
1	16.0	8.00	-8.0	15.9	7.7	-8.2

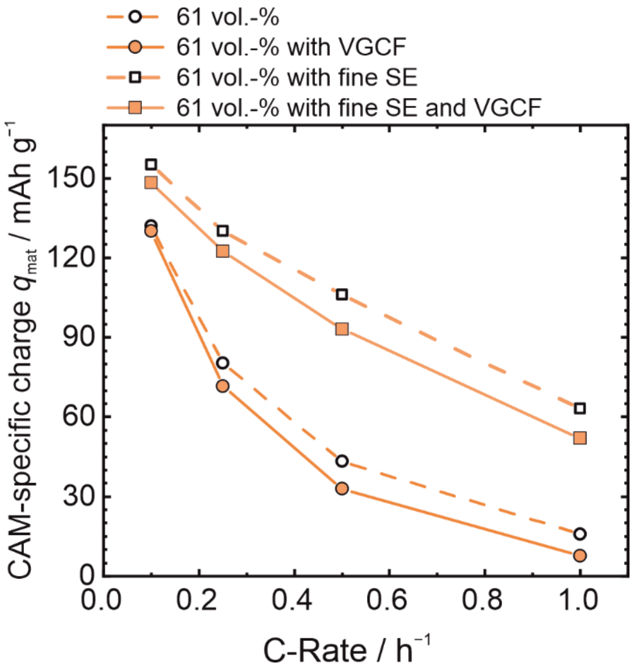

Figure S3: Direct comparison of the performance of cells with a high CAM fraction (61 vol.-%) and different cathode compositions. An increase of the CAM-specific charge especially at higher C-rates can be observed for the cells containing a fine SE. Carbon additives (VGCF), however, have a detrimental influence, demonstrating, that the performance limitation at high CAM-fractions is not caused by electronic charge-transport.

6. Particle size reduction

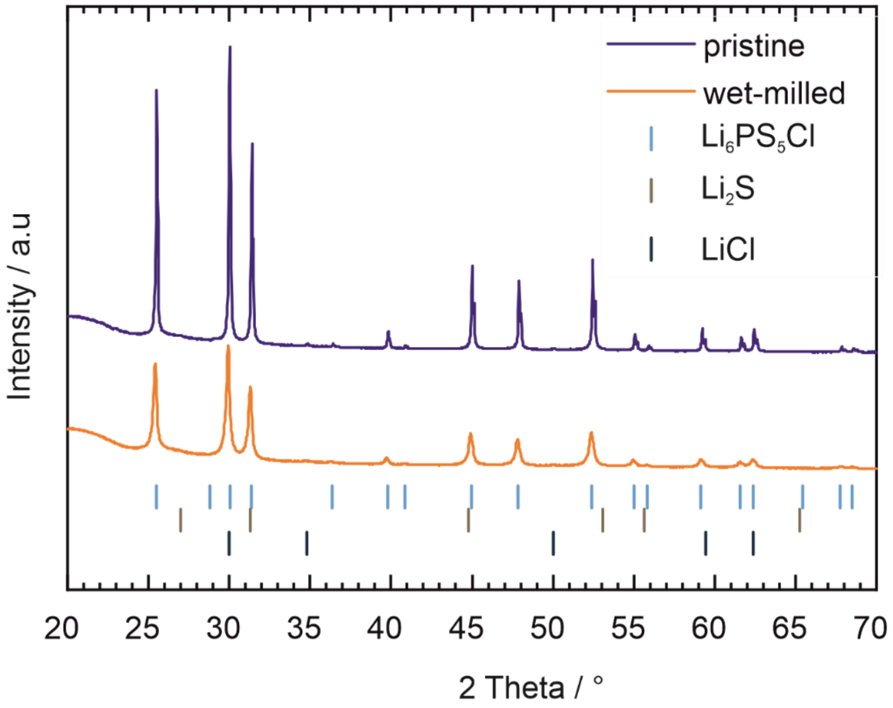

Figure S4: X-ray diffractograms of the SE before (pristine) and after (wet milled) the wet milling process aimed to reduce the particle size. Samples were measured under inert gas atmosphere, by applying a silicon zero-background holder and sealing the samples with a piece of Kapton® foil. Reference pattern for the Li_6PS_5Cl, Li_2S and LiCl are displayed below the pattern. The y-axis offset between the wet milled and the pristine sample has been generated manually, to avoid overlapping of the pattern and allow better comparison.

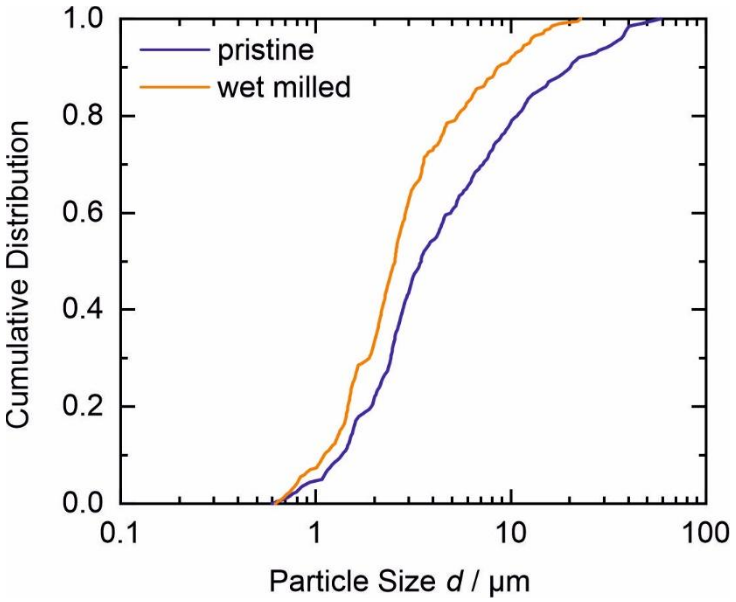

Figure S5: Cumulative particle size analysis of the pristine (blue) and wet milled (orange) sample of the solid electrolyte. A clear reduction in the average particle size is observed. We like to note that particularly the fraction of particles > 10 µm is strongly reduced.

Table S5: 50 % and 90 % median particle size values of solid electrolyte samples before (pristine) and after (wet-milled) the wet-milling process. While the D50 value only displays a slight change, the drastic decrease in the D90 value demonstrates the effective reduction of SE particles with particle sizes > 10 µm.

Value	**Pristine**	**Wet-Milled**
D_{50} / µm	3.45	2.45
D_{90} / µm	20.05	8.57

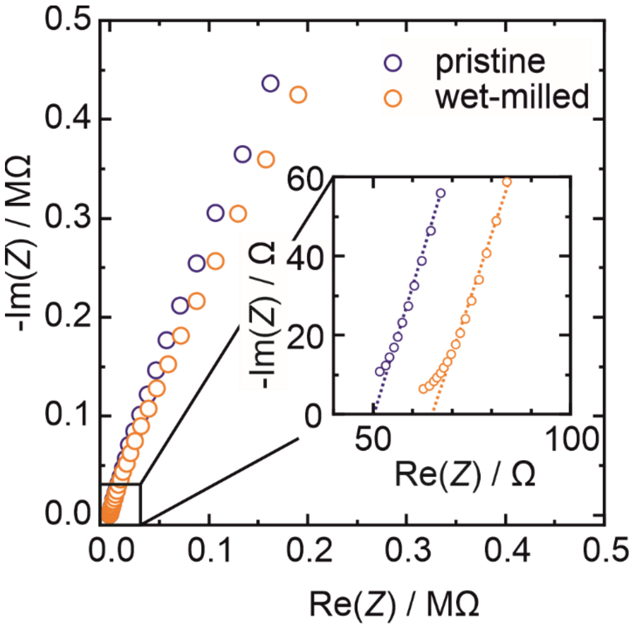

Figure S6: Impedance spectra of pure SE samples prior to (pristine) and after wet milling and subsequent drying. Samples were tested with stainless steel electrodes at an applied pressure of ca. 40 MPa. A slight reduction in the ionic conductivity can be observed after the wet-milling process, indicating either a slight amorphization, or a decomposition during the wet-milling process.

Table S5: Overview of specific charges Q for the steps with coarse and fine solid electrolyte particles at different C-rates for ASSB cells 61 vol.-% CAM. Listed are charge (chg) and discharge (dis) steps. Additionally, the differences ΔQ are listed.

C-rate / h^{-1}	**Q_{chg} coarse SE / mAh g^{-1}**	**Q_{chg} fine SE / mAh g^{-1}**	**ΔQ_{chg} / mAh g^{-1}**	**Q_{dis} coarse SE / mAh g^{-1}**	**Q_{dis} fine SE / mAh g^{-1}**	**ΔQ_{dis} / mAh g^{-1}**
0.1	137	159	22	135	157	22
0.25	118	140	22	118	140	22
0.5	104	119	15	103	119	16

1	83.4	93.4	10	83.0	93.0	10

References

1. J. Bisquert, *Phys. Chem. Chem. Phys.,* **2**(18), 4185–4192 (2000).

2. D. Pritzl, A. E. Bumberger, M. Wetjen, J. Landesfeind, S. Solchenbach and H. A. Gasteiger, *J. Electrochem. Soc.,* **166**(4), A582-A590 (2019).

3. P. Braun, C. Uhlmann, M. Weiss, A. Weber and E. Ivers-Tiffée, *Journal of Power Sources,* **393,** 119–127 (2018).

4. Z. Siroma, T. Sato, T. Takeuchi, R. Nagai, A. Ota and T. Ioroi, *Journal of Power Sources,* **316,** 215–223 (2016).

5. Z. Siroma, N. Fujiwara, S. Yamazaki, M. Asahi, T. Nagai and T. Ioroi, *Electrochimica Acta,* **160,** 313–322 (2015).

Supplementary Information: Visualizing the Impact of the Composite Cathode Microstructure and Porosity on Solid-State Battery Performance

Philip Minnmann[1,2]*, Johannes Schubert[1,2]*, Sascha Kremer[1,2], René Rekers[1,2], Simon Burkhardt[1,2], Raffael Ruess[1,2], Anja Bielefeld[1,2], Felix H. Richter[1,1], Jürgen Janek[1,2,3*,#]

[1] *Institute for Physical Chemistry, Justus-Liebig-University Giessen, Germany*

[2] *Center for Materials Research, Justus-Liebig-University Giessen, Germany*

[3] *BELLA, Institute for Nanotechnology, Karlsruhe Institute of Technology, Karlsruhe, Germany*

[*] *corresponding author*

[#] *lead contact*

S1. Impedance spectroscopy

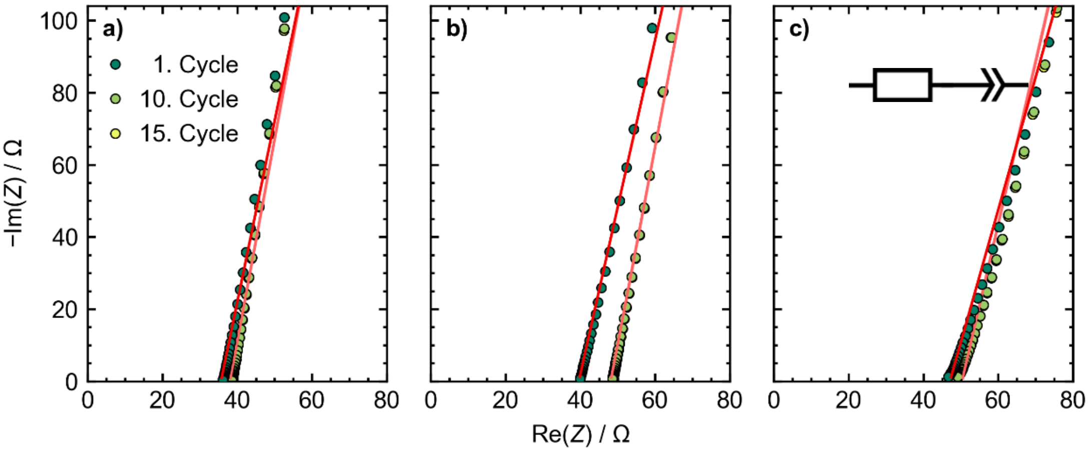

Figure S7: Impedance spectra (ion blocking symmetric cell configuration) for 1.5Li_2S-0.5P_2S_5-LiI solid electrolyte ball milled with a) 10 mm, b) 3 mm and c) 1 mm milling media. For determination of the ionic conductivity spectra were fitted with an equivalent circuit containing a resistor corresponding to the ionic resistance and a CPE addressing capacitive charging (polarisation) at low frequencies.

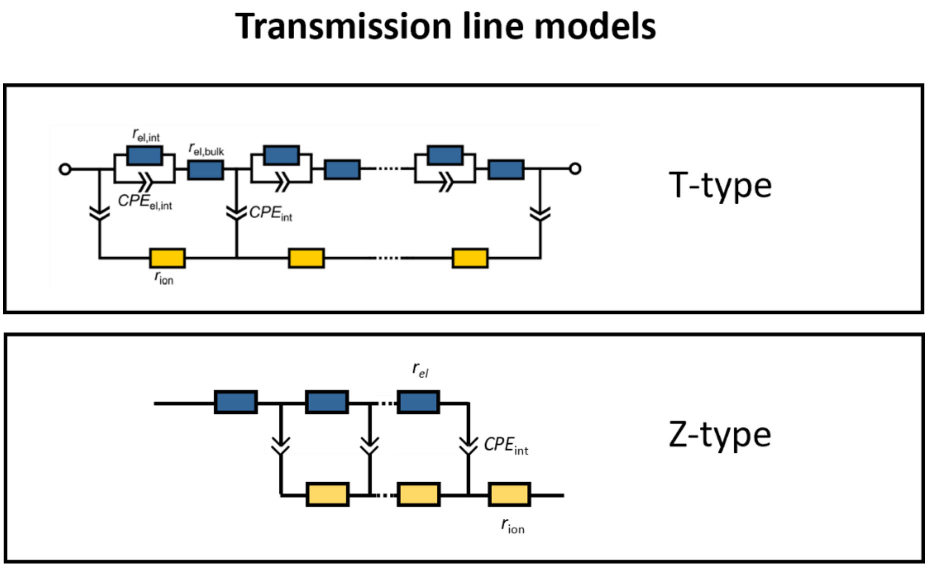

Figure S2: Transmission line models used for determining the ionic and electronic partial conductivities of composite cathodes. T-Type models were used for the impedance spectra with ion-blocking electrodes, while the Z-type model was used for the full-blocking cell setup.

S2. Tomography Image Acquisition

For the acquisition of the tomography data, the sample pellet was fractured inside of a glovebox and fragments were fixed on a sample holder by adhesive copper tape. Afterwards the sample was transferred into a sputter chamber using a vacuum transfer system LEICA VCT (Leica, Wetzlar, Germany). 4 nm of platinum were sputtered onto the sample to increase surface conductivity of the sample and to decrease charging effects during the preparation and image acquisition process. Afterwards, the sample was transferred into a Plasma-FIB-SEM (Xeia, TESCAN). Another layer of platinum roughly 120x120 µm in size and 5 µm thickness was deposited onto the region of interest by the FIB-gun using 10 kV acceleration voltage. Images were obtained with a tilting angle of 55° and images were geometrically transformed accordingly.

FIB cutting consisted of three sequential processes. First, a U-shaped trench was milled using 30 kV acceleration voltage and 2 µA current. Subsequently the obtained cross section was polished twice using a 300 nA and a 100 nA current respectively. For tomography data, the acquisition wizard was being used and the procedure consisted of alternating cutting (at 100 nA) and image acquisition of both BSE and SE images. Due to curtaining effects at the edges of the cross section, the imaging area was selected manually, resulting in different dimensions of the three sample reconstructions.

S3. Image Segmentation

The segmentation model is based on a consecutive implementation of a convolutional neural network (CNN) for feature extraction and a random forest classifier for pixelwise classification. It is able to process a single image and individual segmentations of BSE and SE images were generated. As both image types provide complementary information, i.e. in particular high material contrast in BSE images and pronounced topography in SE images, they are suited differently for segmentation of specific phases. Therefore, a third segmentation, including information of both image types, was generated by combination of the predicted phase of both image types.

First, a small number of BSE images were selected, and pores, CAM and ISE were manually labelled. The images were then fed to the two convolutional layers resulting in 64 feature maps for each image. By initialization of the two convolutional layers with trained weights obtained from the *ImageNet* online database separate training of the layers was avoided and, hence, the amount of training data and computational effort was reduced.[1] Subsequently, the random forest classifier was trained with this dataset (64 feature maps and respective labelled images) and the entire process was repeated with the respective SE images. In order to use both image types complementarily the obtained probabilities with which a pixel can be assigned to pores, CAM or ISE were pooled for both image types and the pixel was assigned to the respective phase on basis of the overall highest probability. In addition, this approach allows weighting of the probabilities and thus adjusting which image type should be primarily used for prediction of a phase which proofed to be particularly useful to optimize segmentation of pores since they are significantly stronger visible in SE images. Therefore, the respective probabilities were multiplied with a weighting factor which was determined by trial and error until the obtained segmentation was satisfactory. The segmentation resulting from the complementary use of both image types is shown in Figure S3.

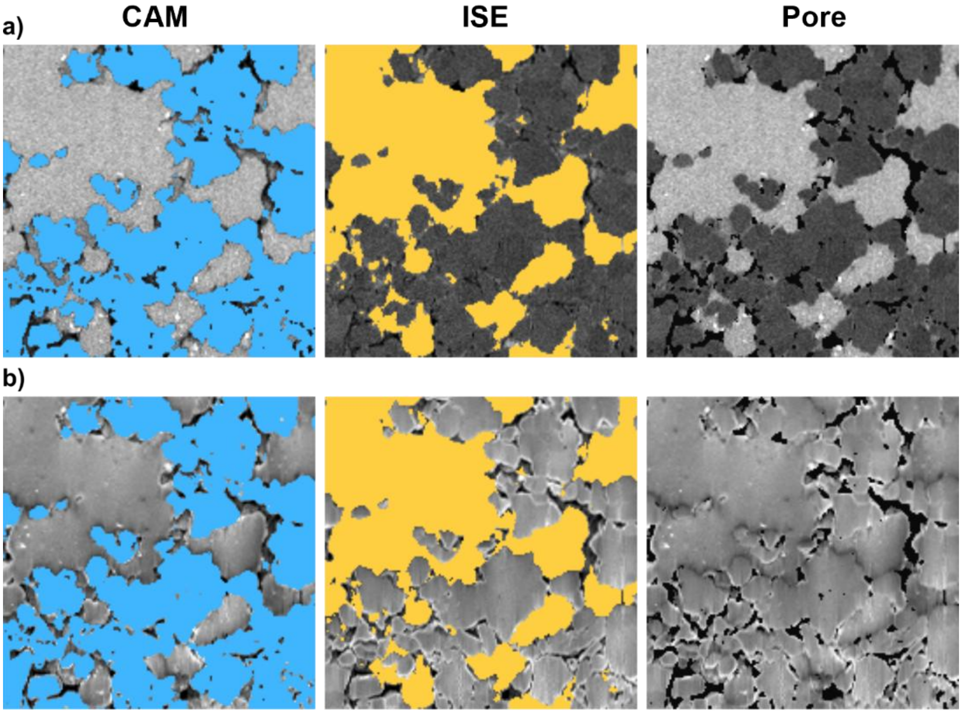

Figure S3: Identified regions of CAM (NCM, blue), ISE (Li_3PS_4-0.5LiI, yellow) and pore (black) on a) BSE images and b) SE images.

While SE images are beneficial for the segmentation of porosity, the low material contrast in combination with shadow effects can lead to a significant number of pixels falsely classified as “pore”. In contrast, the high material contrast in the BSE images allows for reliable segmentation of CAM and SE but material shining through the pores results in an underestimation of the true porosity. As the employed complementary segmentation is based on probabilities, a pixel may be e.g. falsely classified as “pore” in the segmentation of the SE image, in the complementary segmentation, however, that pixel may be correctly assigned to CAM or ISE if the respective probability is higher. Secondly, due to the intensity gradient at interfaces of bright and dark regions, conventional grey-value based techniques result in a false assignment of pixels to the phase of mean intensity. Since in the employed method pixels are not only classified based on the grey-value but on 64 feature maps, a flawless segmentation of interface of pores and ISE was ensured.

A direct comparison of BSE and SE image shows that the employed method is beneficial in terms of segmentation of porosity because pores are identified which are not visible in the BSE image.

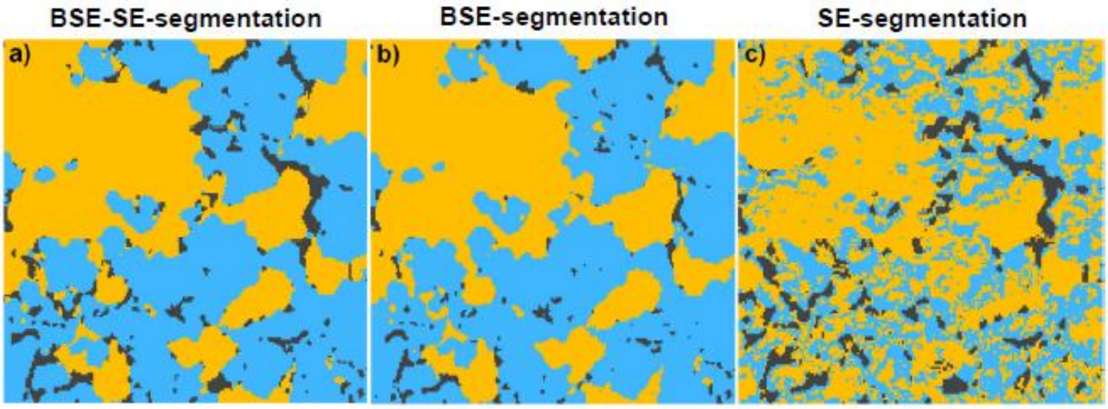

Figure S4: Comparison of different segmentation approaches. While segmentation from (a) both, SE and BSE, image leads to good identification of all three phases, (b) BSE segmentation does not detect all pores and (c) SE segmentation leads to insufficient detection of CAM and ISE phases.

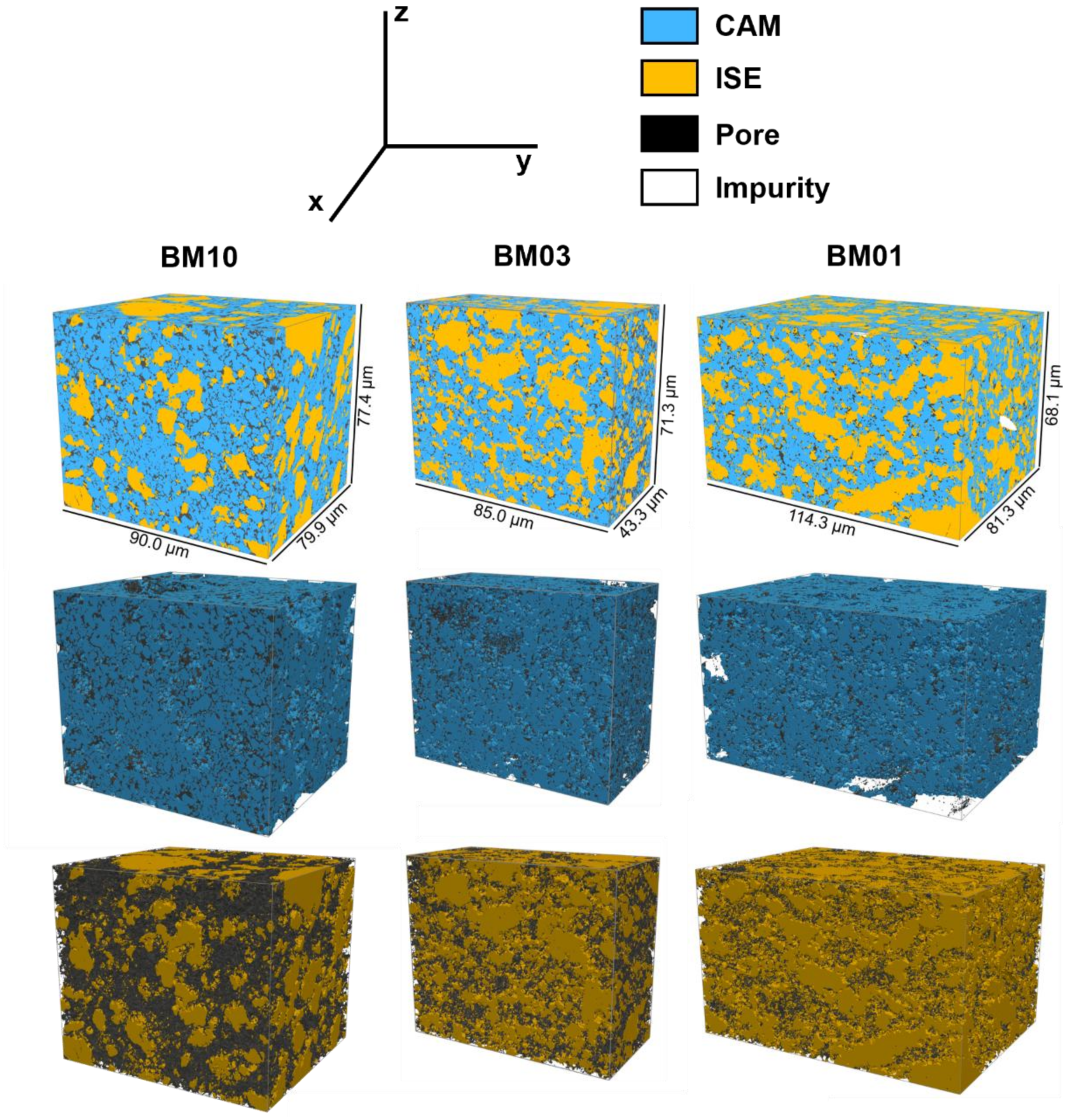

Figure S5: Segmented images of BM10, BM03 and BM01 samples showing the distribution of CAM (blue), ISE (yellow) and pore (black) phases respectively.

S4. Determination of Volume Fractions and Porosity

For the determination of the geometric volume fraction of pores φ_{pore}, the geometric dimensions of the sample (area A and thickness d) and the theoretical volume of the sample, calculated from the respective mass m and density ρ of the phases were used, according to Equation S1:

$$\varphi_{\text{pore}} = 1 - \frac{\frac{m_{CAM}}{\rho_{CAM}} + \frac{m_{ISE}}{\rho_{ISE}}}{A \cdot d} \qquad \text{(S1)}$$

The volume fraction of the CAM and ISE phase can be calculated according to Equation S2:

$$\varphi_{\mathrm{vol,CAM}} = \left(\frac{\frac{m_{\mathrm{CAM}}}{\rho_{\mathrm{CAM}}}}{\frac{m_{\mathrm{CAM}}}{\rho_{\mathrm{CAM}}}+\frac{m_{\mathrm{ISE}}}{\rho_{\mathrm{ISE}}}}\right)\cdot\left(1-\varphi_{\mathrm{pore}}\right) = \frac{\frac{m_{CAM}}{\rho_{CAM}}}{A\cdot d} \qquad \text{(S2)}$$

For the CAM, a density of $\rho_{\mathrm{CAM}} = 4.65\ \mathrm{g\ cm^{-3}}$ and for the ISE, a density of $\rho_{\mathrm{ISE}} = 2.1\ \mathrm{g\ cm^{-3}}$ was used.

S5. Charge Transport Simulations

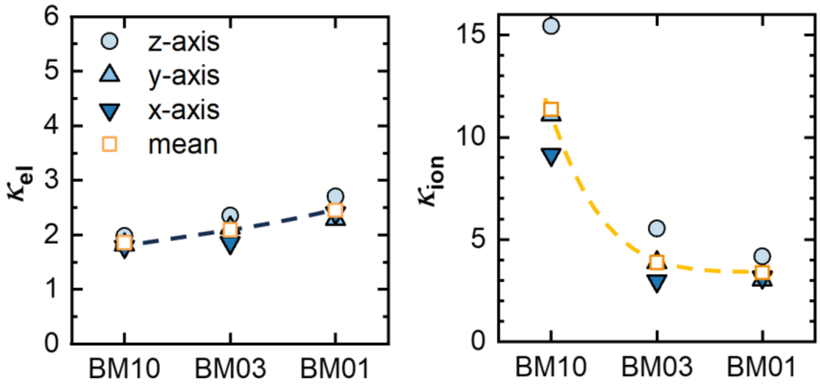

Figure S6: Determined tortuosity values along all three dimensions for electronic (left) and ionic (right) charge carriers.

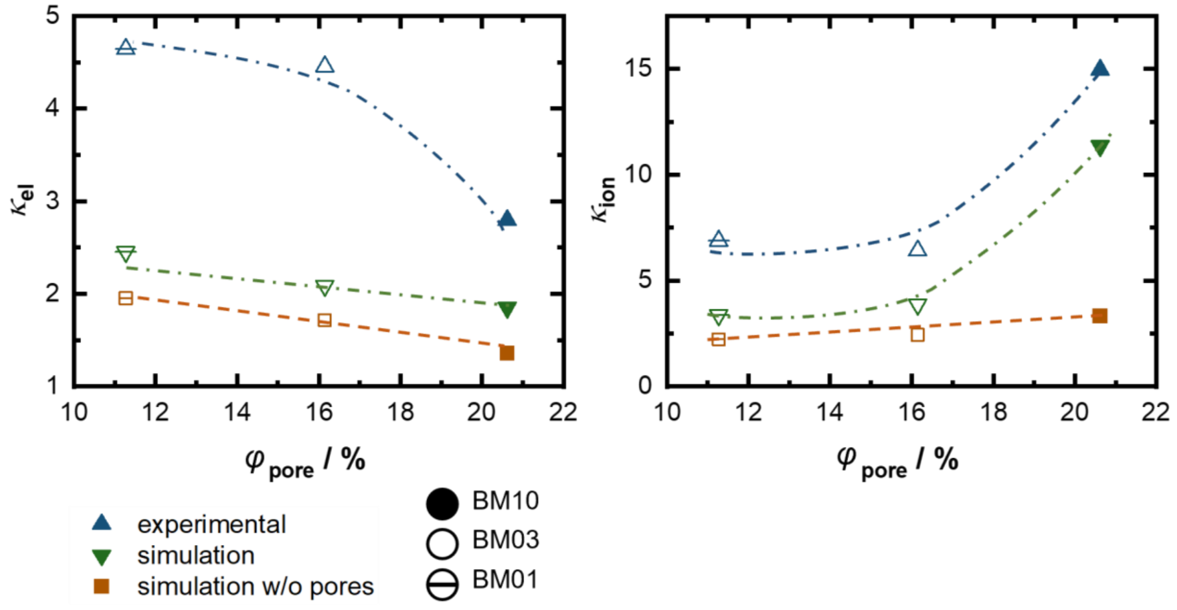

Figure S7: Tortuosity factors as a function of the measured porosity value for experimental data (blue triangle), and random walk simulations with (green inverse triangle) and without (brown square) porosity.

S6. Determination of the CAM Utilization

The equilibrium OCP is a function of the lithium content x and can, therefore, be determined if the respective OCP(x) dependence is known. Consequently, the active mass m_{act} can be obtained by Equation S1 considering the lithium content before and after discharging, which provides the actual specific capacity q_{act}, and the measured discharge capacity Q_{meas}.

$$m_{\mathrm{act}} = \frac{Q_{\mathrm{meas}}}{q_{\mathrm{act}}} \tag{S1}$$

The determination of m_{act} from the relaxed OCP before and after discharging is exemplarily shown for a full cell with 5 mg BM01 composite material in **Figure S9.** The difference of the lithium content Δx before and after discharging, and hence, the specific capacity q_{act} can be determined by comparison of the relaxed OCP after 5 h before (blue) and 5 h after discharging (red) (left) and the OCP as a function of x in a cell with liquid electrolyte (center). The active mass can then be calculated from the measured discharge capacity Q_{meas} (right). More information can be found elsewhere.[2]

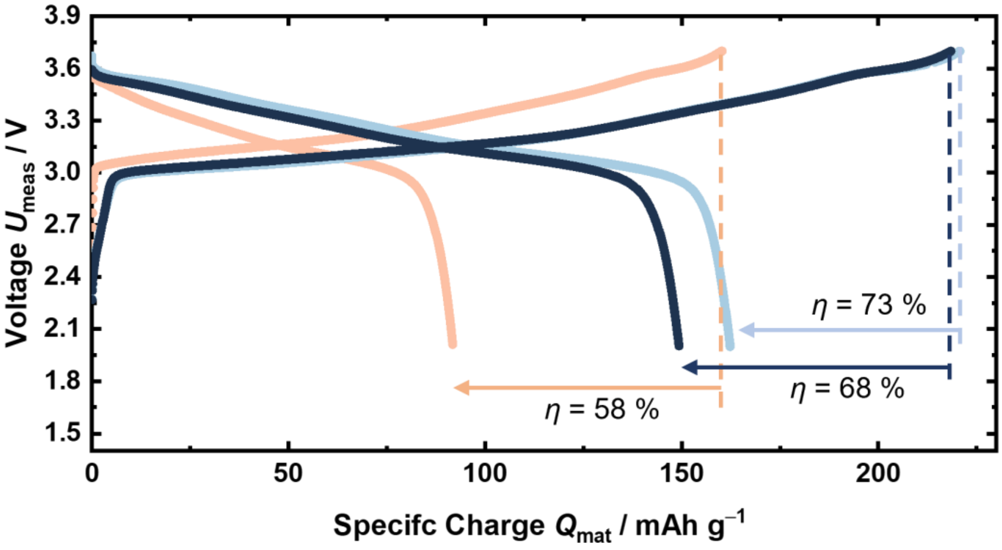

Figure S8: First cycle charge discharge curves and corresponding Coulombic efficiency for cells using BM10, BM03 and BM01 composite cathodes.

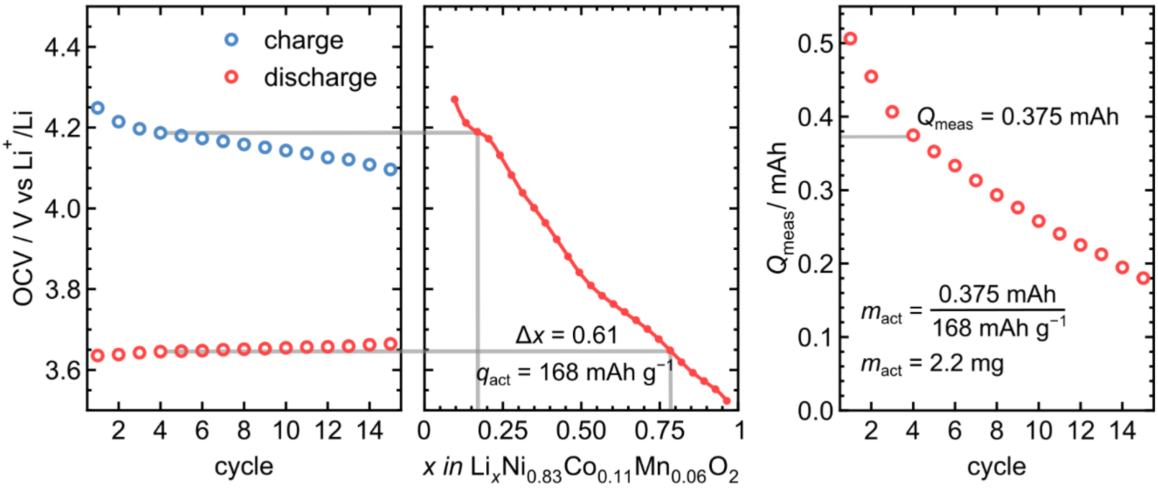

Figure S9: Determination of the electrochemically active mass of the CAM using a comparative measurement of the OCP as a function of lithium content *x*.

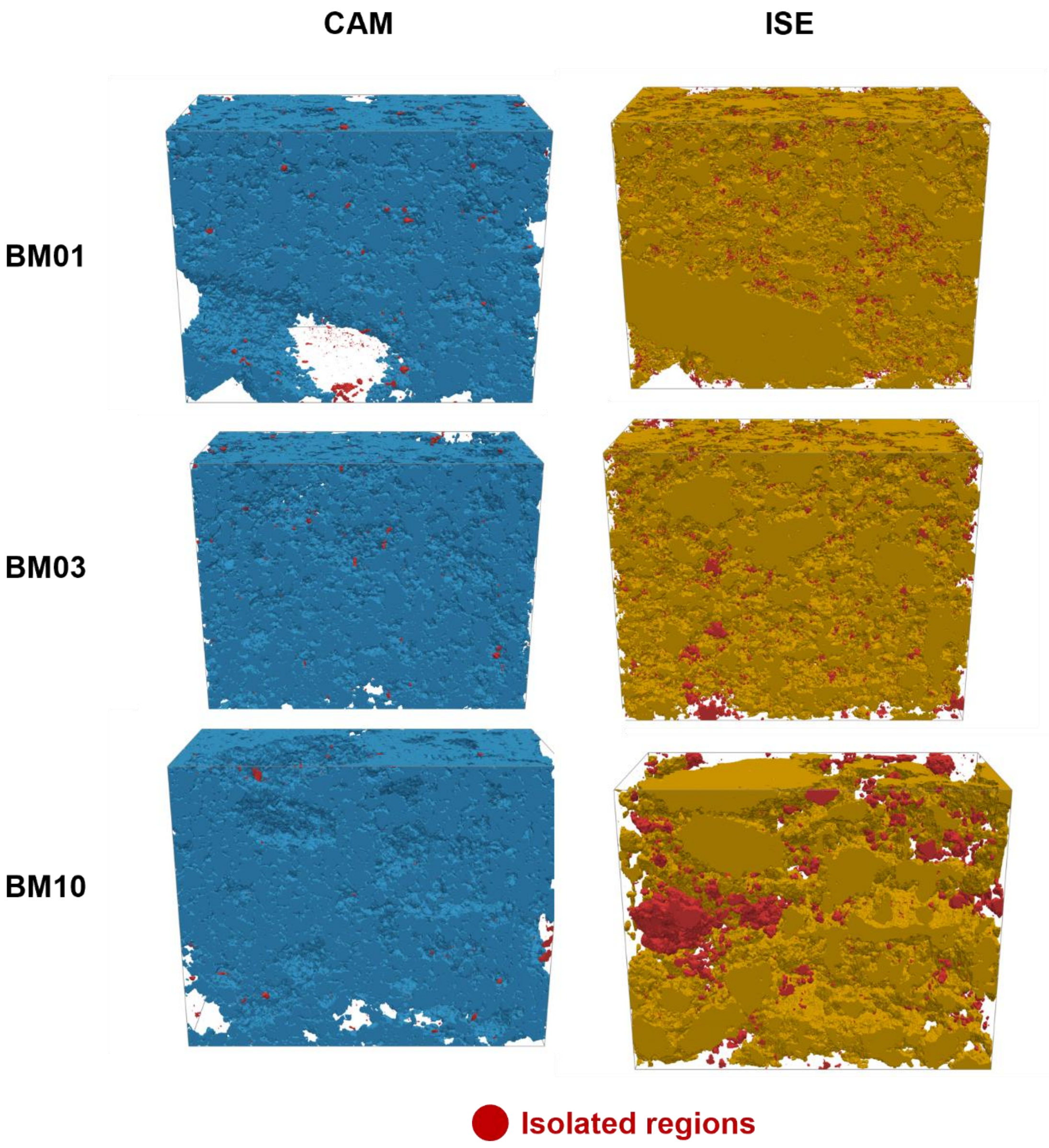

Figure S10: Isolated regions of CAM (left) and ISE (right) particles. Isolated regions are electrochemically inactive as they have no connection to percolating networks.

[1] Deng, J., Dong, W., Socher, R., Li, L.-J., Li, K., & Fei-Fei, L. (2009). Imagenet: A large-scale hierarchical image database. *IEEE conference on computer vision and pattern recognition,* **2009** 248–255)

Supplementary Information Figure 5

Table A1: Calculation Parameters Figure 5

Parameter	**Value**
Density NCM / g cm^{-3}	4.85
Density Li_6PS_5Cl / g cm^{-3}	1.8
Specific Capacity NCM811 Q / mAh g^{-1}	200
Average Cell Voltage / V	3.7
Separator thickness / µm	30
Cu foil thickness / µm	9
Al foil thickness / µm	12
Lithium thickness / µm/ mAh^{-1}	4.71

9. Scientific Contributions

List of Oral and Poster Presentations

ECS Atlanta 2022 (Poster) - Designing Cathodes and Cathode Active Materials

IBA 2022 (Poster) - Designing Cathodes and Cathode Active Materials

Bunsen Kolloqium 2022 (Oral Presentation) – Cathode Microstructure and Charge Transport in Solid State Batteries

SSB V Frankfurt 2022 (Poster) – Designing Cathodes and Cathode Active Materials

LLZO4W Conference 2023 (Poster) - Microstructure and Charge Transport of Composite Cathodes for Solid State Batteries

List of Publications:

First Author:

[1] Philip Minnmann, Lars Quillman, Simon Burkhardt, Felix Hermann Richter, Jürgen Janek: Editors' Choice – Quantifying the Impact of Charge Transport Bottlenecks in Composite Cathodes of All-Solid State Batteries. *J. Electrochem. Soc.* **2021**, *168* (4), 040537. https://doi.org/10.1149/19457111/abf8d7

[2] Philip Minnmann, Johannes Schubert, Sascha Kremer, René Rekers, Simon Burkhardt, Raffael Ruess, Anja Bielefeld, Felix Hermann Richter, Jürgen Janek: Editors' Choice Visualizing the Impact of the Composite Cathode Microstructure and Porosity on Solid-State Battery Performance. *J. Electrochem. Soc.* **2024**, *171* (6), 060514. https://doi.org/10.1149/1945-7111/ad510e.

[3] Philip Minnmann, Florian Strauss, Anja Bielefeld, Raffael Ruess, Philipp Adelhelm, Simon Burkhardt, Sören Lukas Dreyer, Enrico Trevisanello, Helmut Ehrenberg, Torsten Brezesinski, Felix Hermann Richter, Jürgen Janek: Designing Cathodes and Cathode Active Materials for Solid-State Batteries. *Adv. Energy Mater.* **2022**, *12* (35), 2201425. https://doi.org/10.1002/aenm.202201425

Co-Authored

[4] Manuel Weiss, Raffael Ruess, Johannes Kasnatscheew, Yehonatan Levartovsky, Natasha Ronith Levy**, Philip Minnmann**, Lukas Stolz, Thomas Waldmann, Margret Wohlfahrt-Mehrens, Doron Aurbach, Martin Winter, Yair Ein-Eli, Jürgen Janek: Fast charging of lithium-ion batteries: a review of material aspects. *Adv. Energy Mater.* ***2021****, 11 (33), 2101126*

[5] Rajendra S Negi, **Philip Minnmann**, Ruijun Pan, Shamail Ahmed, Marcel J. Herzog, Kerstin Volz, Ryo Takata, Franz Schmidt, Jürgen Janek, Matthias T Elm: Stabilizing the cathode/electrolyte interface using a dry-processed lithium titanate coating for all-solid-state batteries, *Chem. Mater*. **2021***, 33* (17)*,* 6713-6723

[6] Hanyu Huo, Ming Jiang, Boris Mogwitz, Joachim Sann, Yuriy Yusim, Tong-Tong Zuo, Yannik Moryson, **Philip Minnmann**, Felix H Richter, Chandra Veer Singh, Jürgen Janek: Interface Design Enabling Stable Polymer/Thiophosphate Electrolyte Separators for Dendrite-Free Lithium Metal Batteries, *Angew. Chemie. Int. Edition* **2023,** *62* (14), e202218044

[7] Janis K Eckhardt, Sascha Kremer, Till Fuchs, **Philip Minnmann**, Johannes Schubert, Simon Burkhardt, Matthias T Elm, Peter J Klar, Christian Heiliger, Jürgen Janek: Influence of Microstructure on the Material Properties of LLZO Ceramics Derived by Impedance Spectroscopy and Brick Layer Model Analysis, *ACS Applied Materials & Interfaces* **2023**, *15* (40), 47260-47277

[8] Jian Duan, Till Fuchs, Boris Mogwitz, **Philip Minnmann**, Tong-Tong Zuo, Anja Henss, Jürgen Janek: Solid electrolyte cracking due to lithium filament growth and concept of mechanical reinforcement–An operando study, *Materials Today* **2023**, *70*, 33-43

[9] Christoph D Alt, Nadia UCB Müller, Luise M Riegger, Burak Aktekin, **Philip Minnmann**, Klaus Peppler, Jürgen Janek: Quantifying multiphase SEI growth in sulfide solid electrolytes, *Joule* **2024**, https://doi.org/10.1016/j.joule.2024.07.006

[10] Sebastian Puls, Elina Nazmutdinova, Fariza Kalyk, Henry M Woolley, Jesper Frost Thomsen, Zhu Cheng, Adrien Fauchier-Magnan, Ajay Gautam, Michael Gockeln, So-Yeon Ham, Md Toukir Hasan, Min-Gi Jeong, Daiki Hiraoka, Jong Seok Kim, Tobias Kutsch, Barthélémy Lelotte, **Philip Minnmann**, Vanessa Miß, Kota Motohashi, Douglas Lars Nelson, Frans Ooms, Francesco Piccolo, Christian Plank, Maria Rosner, Stephanie E Sandoval, Eva Schlautmann, Robin Schuster, Dominic Spencer-Jolly, Yipeng Sun, Bairav S Vishnugopi, Ruizhuo Zhang, Huang Zheng, Philipp Adelhelm, Torsten Brezesinski, Peter G Bruce, Michael Danzer, Mario El Kazzi, Hubert Gasteiger, Kelsey B Hatzell, Akitoshi Hayashi, Felix Hippauf, Jürgen Janek, Yoon Seok Jung, Matthew T McDowell, Ying Shirley Meng, Partha P Mukherjee, Saneyuki Ohno, Bernhard Roling, Atsushi Sakuda, Julian Schwenzel, Xueliang Sun, Claire Villevieille, Marnix Wagemaker, Wolfgang G Zeier, Nella M Vargas-Barbosa: Benchmarking the reproducibility of all-solid-state battery cell performance, *Nature Energy* **2024**, https://doi.org/10.1038/s41560-024-01634-3

[11] Christoph D. Alt, Sören Keuntje, Inga L. Schneider, Johannes Westphal**, Philip Minnmann**, Janis K. Eckhardt, Klaus Peppler, Jürgen Janek: In–Li Counter Electrodes in Solid-State Batteries – A Comparative Approach on Kinetics, Microstructure, and Chemomechanics, *Adv. Energy Mater.* **2024**, https://doi.org/10.1002/aenm.202404055

10. Acknowledgement

Die Entstehung der vorliegende Arbeit wäre ohne die Unterstützung, Förderung und Toleranz vieler wunderbarer Menschen nicht möglich gewesen. Ganz besonders Danken möchte ich Prof. Dr. Jürgen Janek, für die Möglichkeit dies Arbeit überhaupt erstellen zu können, die herzliche Aufnahme in die Arbeitsgruppe, die fachliche Expertise und Betreuung und die Möglichkeit trotz voller Terminkalender immer wieder 5 Minuten Diskussion zu ermöglichen. Außerdem für einige wundervolle Winetastings und Weihnachtsfeiern mit der Arbeitsgruppe.

Des weiteren Prof. Nella-Vargas-Barbosa für die Übernahme der Rolle der Zweitgutachterin., sowie den weiteren Mitgliederinnen meiner Prüfungskommission Prof. Dr. Anja Henß und Prof. Dr. Maren Lepple. Ebenfalls Bedanken möchte ich mich bei Felix Richter für eine intensive und angenehme Betreuung, gerade zur Anfangszeit, für das Stellen der richtigen Fragen und dem immer präsenten Blick auf den roten Faden der Forschungsarbeit.

Allen Menschen der Arbeitsgruppe Janek/Zeier sowie des FestBatt Kompetenzclusters, die während meiner Zeit in Gießen gezeigt haben, dass eine harmonische Arbeitsatmosphäre einhergeht mit herausragenden Forschungsergebnissen. Mein besonderer Dank gilt:

Simon Burkhardt, Felix Hartmann und Adrian Schürmann für die tolle Zusammenarbeit und exzellente Organisation innerhalb des FestBatt Clusters. Bjoern Luerßen, Marcus Rohnke, Ljerka Majdandzic, Boris Mogwitz, Joachim Sann und Klaus Peppler, für die Hilfsbereitschaft und Unterstützung bei sämtlichen Fragestellungen, die während einer Promotion einmal auftreten können.

Johannes Schubert, Christoph Alt, Sascha Kremer, Justine Ruhl, Luise Riegger und Anja Bielefeld für die tolle Zusammenarbeit, und die Bereitschaft auch herausfordernde Fragestellungen gemeinsam anzugehen. Meiner Office-Crew, Jian Duan, Zhixuan Zhang, Raffael Ruess, Clarissa Glaser und Yuriy Yusim, für eine freundliche Atmosphäre, ausufernde Diskussionen und ein stets offenes Ohr bei Fragestellungen. Zudem Lars Quillmann, Marc Uhlherr, Dirk Hunstock, Antonio Carnevali, Rene Rekers und Nadia Müller, für die hervorragende Laborarbeit und Unterstützung bei der experimentellen Durchführung.

Meiner Gießener Crew, Julian Zahnow, Laura Goodwin, Jonas Hertle, Lena Krause und Marcus Ellburg Kvien, für die unvergesslichen und facettenreichen Stunden, Tage, Wochen, die wir in unsere Freizeit hatten. Ohne euch wäre Gießen ein ganzes Stück farbloser gewesen.

Meiner Aachener Crew, Rina Schmidt, Simon Schlagintweit, Simon Kusmierz, Tina Koll, Katrin Pingen, Niklas Bremer und Sophie Bremer, die mich durchs Studium und danach begleitet haben und für die viele schöne gemeinsame Erinnerungen.

Abschließend möchte ich mich bei den Menschen bedanken, die die Grundlage meines Lebens bilden. Meiner Eltern, für die ununterbrochene Unterstützung, die Förderung meiner Neugier und Motivation von Kindheit an und dafür, dass sie immer mit der einen oder anderen kulinarischen Ablenkung zur Stelle waren. Meinem Bruder Florian, dafür, dass er trotz einer langen Reise immer an mich geglaubt hat und für die dauerhafte Nachfrage, wann er mich denn Doktor nennen darf. Meiner Freundin Denise, für Ihr Verständnis, ihre Unterstützung gerade während der Schreibphase, und dafür, dass sie trotz antizyklischer Arbeitsrhythmen immer für mich da war.